Density Functional Theory and the Quantum Chemistry of Gas Separation, Magnetism, and Catalysis in Metal–Organic Frameworks

A DISSERTATION
SUBMITTED TO THE GRADUATE SCHOOL OF THE
UNIVERSITY OF MINNESOTA
BY

Pragya Verma

IN PARTIAL FULFILLMENT OF THE REQUIREMENTS
FOR THE DEGREE OF
DOCTOR OF PHILOSOPHY

Advisor: Prof. Donald G. Truhlar

September, 2017

Acknowledgments

This research was carried out under the guidance of Prof. Donald G. Truhlar. I thank him for his support, kindness, encouragement, great respect, and remarkable ability to find time in spite of being very busy whenever I have approached him to discuss anything. Don is extraordinary in many ways, and I had the great opportunity to interact with him and gain knowledge from him not just on scientific matters, but also non-scientific matters.

During my PhD, I had the opportunity to interact with a number of Truhlar group members. In particular, I am grateful to Kaining Duanmu, Laura E. Fernandez, Xiao He, Shuping Huang, Sijie Luo, Kamal Sharkas, Zoltan Varga, Bo Wang, Xuefei Xu, Haoyu S. Yu, and Wenjing Zhang, for their contributions to various projects on which I have worked with them. My interactions with each one of them have been very fruitful, and I had the chance to learn numerous things from them that has enriched my knowledge in the field.

I would also like to extend my gratitude to collaborators outside the Truhlar group, particularly the Gagliardi group. Members of Gagliardi group with whom I have interacted closely are Remi Maurice and Joshua Broycz, and I thank them for their useful insights in various projects.

I want to thank the staff at Minnesota Supercomputing Institute (MSI) whom I have emailed quite often with my queries regarding MSI, and I have very often received a helpful response from them.

Finally, this research would not have been successful without the generous financial help from various organizations and funding agencies. A major part of this research was supported by the U.S. Department of Energy (grant no. DE-FG02-12ER16362), a Phillips 66 Excellence Fellowship, a Graduate School Doctoral Dissertation Fellowship, and the Richard D. Amelar & Arthur S. Lodge Fellowship.

Abstract

This dissertation uses theoretical and computational methods, mainly the quantum mechanical density functional theory of electronic structure, to explore three functionalities of metal-organic frameworks (MOFs), namely, purification and separation of gaseous mixtures, catalysis of C–H bond activation, and potential use of MOFs as magnetic materials. The dissertation also includes the development and analysis of computationally efficient quantum mechanical and molecular mechanical methods that are more accurate than previously available methods.

Table of Contents

List of figures

List of tables

List of abbreviations and acronyms

AFM	antiferromagnetic
B3LYP	Becke 3-parameter Lee–Yang–Parr
BJ	Becke-Johnson
btc	1,3,5-benzenetricarboxylate
B-TCNE	benzene–tetracyanoethylene
CASPT2-CP	complete active space second-order perturbation theory with counterpoise corrections
CM5	charge model 5
CT	charge transfer
DD3S	damped dispersion based on D3 and SAPT
def2-TZVP	second-default triplet-zeta valence polarized
def2-QZVP	second-default quadruple-zeta valence polarized
DFT+U	density functional theory with Hubbard U correction
DMABN	dimethylaminobenzonitrile
dobdc	2,5–dioxido-1,4–benzenedicarboxylate
EER	exchange-enhanced reactivity
Expt.	experiment
FF	force field
FM	ferromagnetic
GA	gradient approximation
GAM	gradient approximation for molecules
GGA	generalized gradient approximation
HDV	Heisenberg-Dirac-van Vleck
HF	Hartree–Fock
HLE	high local exchange
HOMO	highest occupied molecular orbitals
HS	high-spin
HSE	Heyd–Scuseria–Ernzerhof
IS	intermediate-spin
KS-DFT	Kohn-Sham density functional theory
LoProp	local properties
LPNO-CCSD	local-pair natural-orbital coupled cluster theory with single and double excitations
LR-TDDFT	linear-response time-dependent DFT
LUMO	lowest unoccupied molecular orbital
MAD	mean absolute deviation
MM	molecular mechanics
MN-GFM	Minnesota-Gaussian Functional Module
MN-VFM	Minnesota-VASP Functional Module
MOF	metal–organic framework

MUE	mean unsigned error
NAO	natural atomic orbital
NBO	natural bond orbital
NGA	nonseparable gradient approximation
NMGC	Nanoporous Materials Genome Center
NN	nearest-neighbor
NNN	next-nearest-neighbor
PAW	projector-augmented-wave
PBC	periodic boundary conditions
PBE	Perdew–Burke–Ernzerhof
PNA	para-nitroaniline
QM	quantum mechanics
SAPT	symmetry-adapted perturbation theory
SCF	self-consistent field
SSR	single-state reactivity
TM	transition metal
TMG_3tren	tris(2-(tetramethylguanidino)ethyl)amine
TPSS	Tao–Perdew–Staroverov–Scuseria
TS	transition state
TSR	two-state reactivity
VASP	*Vienna Ab initio Simulation Package*
WFT	wave function theory
xc	exchange-correlation

1 Introduction

1.1 Synopsis

Metal–organic frameworks (MOFs) are porous materials with metal-containing nodes joined by organic linkers; they offer many possibilities for controlling their properties by the design of nodes, linkers, and three-dimensional architecture. They have attracted a lot of attention recently owing to their versatility as porous materials, and they exhibit a number of properties based on their behavior as molecular sieves, they can be used in catalysis, and they have a potential role as porous magnetic materials. MOFs constitute an emerging area of research with applications in industry, but their potential is yet to be fully exploited. This work explores several functionalities of MOFs using state-of-the-art quantum mechanical and molecular mechanical methods. The knowledge gained from theoretically studying experimentally known MOFs will allow tuning them and designing new MOFs for a variety of properties and applications. Furthermore, this thesis contains new methods that can provide increased accuracy for studying MOFs and a better understanding of their functionalities and capabilities.

1.2 Metal–Organic Frameworks (MOFs)

The Nanoporous Materials Genome Center (NMGC) at the University of Minnesota[1] employs both experimental and computational tools for synthesizing and predicting new materials such as metal–organic frameworks (MOFs) that can exhibit a wide variety of properties and applications. An important part of the vision of the NMGC is to develop and use theoretical methods to enable greater understanding of these novel materials and design them for specific applications, of which we consider four: (1) discovering porous materials that can separate gases more efficiently, faster, and using lower setup-costs than currently used in industry is an important research problem that has high societal impact, (2) chemical industry relies heavily on catalysis, and MOFs provide opportunities for designing new catalysts with unique capabilities, (3) studying the magnetic applications of MOFs can be helpful in developing chemical sensors and bulk magnets, and (4) developing quantum mechanical and molecular mechanical methods that are computationally more efficient and accurate than the existing methods for treating MOFs.

Porous materials are widely used for efficient gas storage and gas separation, and MOFs are one class of porous materials that have gained popularity recently.[2,3,4] MOFs are a new class of porous materials that are composed of metal ions or clusters of metal ions and organic ligands. The metal ions or metal ion clusters are connected to each other via bridging organic ligands. Figure 1.1 shows an example of the extended structure of an MOF along with its building blocks − metal centers connected via organic ligands. A variety of choices for either the metal ion or the organic ligand has led to the synthesis of a large number of structures of MOFs that have interesting chemistry and applications.[5] Even more interesting perhaps is a large number of structures that are yet-to-be-synthesized and potentially have interesting properties and applications in industries[6,7] and have generated a great deal of interest for their ability to display numerous properties. MOFs occur in a variety of shapes and exhibit numerous properties depending upon the shape and the choice of components – metal ion and linker, and they can be tailored for applications such as gas storage, gas separation, heterogeneous catalysis, magnetism, conductivity, etc. Therefore, a fundamental understanding of the relationship between structure and properties is required.

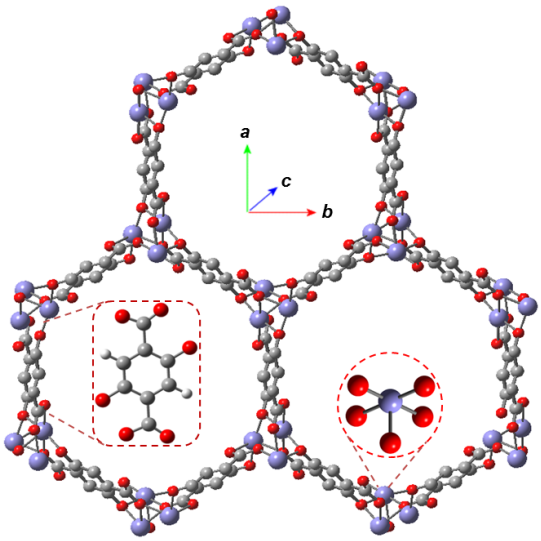

Figure 1.1 Structure of Fe_2(dobdc) displaying its building blocks.
The two building blocks, the Fe(II) ion (with its pentacoordinate environment) and the 2,5–dioxido-1,4–benzenedicarboxylate ($dobdc^{4-}$) linker, are shown in the insets. The hexagonal channels along the *c* axis are lined by Fe(II) ions at the vertices and the organic linker ($dobdc^{4-}$) on the sides. [Color code: Violet = Fe, Red = O, Gray = C, and White = H]

Applications of MOFs for gas separation include carbon capture,[8,9] separation of a mixture of hydrocarbons,[10] separation of oxygen and nitrogen present in the air,[11,12] etc. MOFs also provide unique opportunities to perform catalysis by using their metallic sites as catalysts or by using the MOF itself as support materials.[13,14,15,16,17,18,19,20,21] In these ways, they provide an alternative to widely employed zeolites for reactions such as hydrogenation, dehydrogenation, alkylation, and oxidation of inert materials such as hydrocarbons and their derivatives. The efficiency and selectivity of these catalytic processes depend on the composition, size, shape, and atomic-level structure of the catalyst and support material, and understanding how tuning these parameters affects the catalytic property such as percentage yield, catalytic turnover, etc., is important. Moreover, catalysis can happen at the metal site or the node, at the linker, or within the pore.[22,23] Also noteworthy is the role of the active site or open metal site in catalysis.[24]

One promising family of MOFs that has been synthesized and widely studied theoretically is M-MOF-74[25] with stoichiometry M_2(dobdc) (where M can be Mg(II) or any metal ion from Mn(II) to Zn(II) in the 3*d* series, and $dobdc^{4-}$ is 2,5–dioxido-1,4–benzenedicarboxylate). In M_2(dobdc), the metal atom has oxidation number +2, and the linker formally has four units of negative charge, therefore the stoichiometry, M_2(dobdc), leads to a neutral MOF. The metal lies on helical chains along the *c* axis and the linkers form the wall of the hexagonal channel of the MOF (see Figure 1.1). Each metal atom is pentacoordinate, is surrounded by five oxygen atoms, and has one vacant site that points toward the channel. The presence of open-metal sites in these MOFs makes them attractive for numerous properties. Of particular interest in this family is Fe_2(dobdc).

Fe_2(dobdc) has been found experimentally to be useful for separating a mixture of hydrocarbons and for separating the constituents of air.[10,12] Its magnesium-diluted analog has also been found useful for converting ethane to ethanol in the presence of N_2O molecules, which occurs via the formation of an Fe^{IV}=O intermediate.[26] Another property of Fe_2(dobdc) that has attracted attention is its potential ability to behave as a magnetic material.[27,28,29,30] To understand these properties, simulations are often used to obtain valuable information, and such theoretical modeling is the focus of the current work, with a special emphasis on density functional theory for quantum mechanical modeling of electronic structure.

1.3 Models

To study MOFs one can use either a cluster model or a periodic model. Both types of models have their advantages and limitations. The choice of the model depends on several factors such as the quantum mechanical or molecular mechanical method one is interested in applying and the kind of property one is interested in calculating. Calculations on a periodic model can be more expensive than those on a cluster model because one has to also take into account the six lattice parameters of the crystal structure. Additionally, calculations on periodic systems with hybrid density functionals may not be practical with plane-wave basis sets, while a greater variety of electronic structure methods can be used with cluster calculations. However, cluster models can have limitations owing to their size, and the ones that are small enough to provide inexpensive calculations may be deficient in capturing all the interactions in the MOF, particularly long-range interactions and steric effects.

Both these kinds of models allow us to determine properties such as the ground spin states, the nature and strength of interaction of MOFs with adsorbates, isotropic and anisotropic spin coupling constants, and mechanism of reactions occurring via the MOF.

1.3.1 Cluster Models

The cluster model used for a given application should be chosen to be large enough to represent the main interactions at a central site without appreciable edge effects while being small enough to lead to conveniently affordable high-level quantum mechanical calculations. Cluster models allow one to treat the MOF like a molecule and have the advantage that one can apply a greater a variety of methods to them, especially expensive quantum mechanical methods that can be more accurate than the density functional methods that form the workhorses of periodic calculations. Furthermore, even some of the more accurate density functional methods are more affordable in cluster calculations than in periodic ones.

Cluster models can be carved out of either the experimental crystal structure of the MOF or the periodic DFT optimized structure when the experimental crystal structure is not known or when the experimental crystal structure is distorted or has defects. A detailed description of the design of two cluster models of Fe_2(dobdc) consisting of 88 and 106 atoms is given in Ref. 31. Both these cluster models (shown

in Figure 1.2) were designed to be neutral because the MOF is neutral. This was achieved by adding the required number of hydrogen atoms to the dangling bonds at the periphery of the cluster. To obtain the cluster, it is important to consider where the periodic structure of the MOF should be truncated, and therefore the two models have been used to see the effect of the size of the models, which will be discussed in later sections. The bare 88-atom and 106-atom clusters are denoted by Fe3 and Fe5, respectively. The binding of adsorbate was studied only on the smaller model (Fe3). If only one adsorbate is bound to the central iron of Fe3, it is referred to as Fe3–adsorbate, and if one adsorbate is bound to each iron center of Fe3, it is referred to as Fe3–3adsorbate.

The three iron(II) centers of the 88-atom cluster are labeled *a*, *b*, and *c* from left to right in Figure 1.2(a) and the five iron(II) centers of the 106-atom cluster are labeled *e*, *a*, *b*, *c*, and *d* from left to right in Figure 1.2(b). For both the clusters, the central iron (Fe_b) gives the most accurate representation of an iron atom in the experimental crystal structure. For most of the work presented here, these clusters were carved from the experimental structure[10] of Fe_2(dobdc). In the 88-atom cluster, there exist 3.00 Å separations between the nearest-neighbour (NN) iron centers (*ab* and *bc* in Figure 1.2(a)) and 4.96 Å separation between the next-nearest-neighbor (NNN) iron centers (*ac* in Figure 1.2(a)). In the 106-atom cluster, the NN and NNN distances are the same as the 88-atom cluster, and there exists 6.84 Å and 9.33 Å separation between next-to-next nearest neighbors (*ec* and *ad* in Figure 1.2(b)) and the two farthest metal centers (*ed* in Figure 1.2(b)), respectively. The immediate environment of the three central iron atoms of the 106-atom cluster is closer to the experimental structure than that of the 88-atom cluster. Therefore, one can expect the 106-atom cluster model to give more accurate results than the 88-atom cluster.

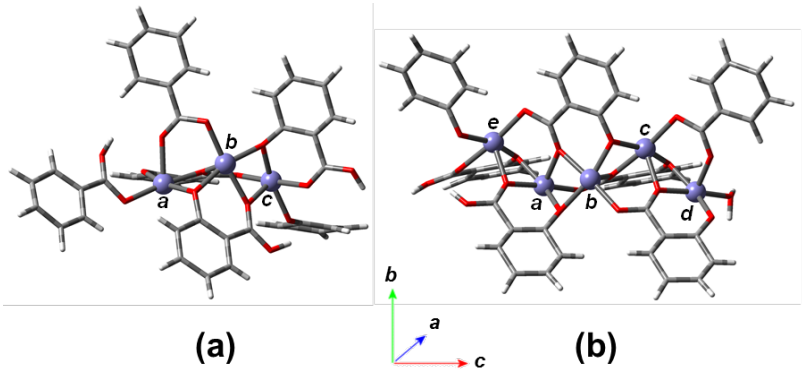

Figure 1.2. (a) The 88-atom and (b) the 106-atom cluster models of Fe_2(dobdc).

The clusters are viewed perpendicular to the *c* axis shown in Figure 1.1. [Color code: Violet = Fe, Red = O, Gray = C, and White = H]

Special notations are used to describe the level of optimization of cluster models. The notation is //opt*N* if *N* atoms of the MOF are optimized and *N* with values 0, 1, 3, 6, 12, and 14 have been tested. When *N* is 0, no atom of the MOF is optimized; when *N* is 1, the central iron (Fe_b) is optimized; when *N* is 3, all three Fe centers are optimized; when *N* is 6, the first coordination sphere (Fe_b + 5 O) of Fe_b is optimized; when *N* is 12 the extended coordination sphere (Fe_b + 2 O^- + 3 COO^-) of Fe_b is optimized; and when *N* is 14, the first coordination sphere of all three iron centers is optimized. This number comes out to be 14 rather than 18 because two pairs of oxygens are bridging atoms between the iron centers. Note that for all the levels of optimization, the adsorbate, if present, is always optimized.

1.3.2 Periodic Models

The unit cell of the periodic model of Fe_2(dobdc) is shown in Figure 1.3. It consists of 54 atoms of which six are iron atoms. There are two chains of iron atoms with three iron atoms in each chain. If adsorbates such as ethane or ethylene are present, the number of atoms in the unit cell increases. For example, Fe_2(dobdc) with ethane or ethylene at every iron site of the unit cell has 102 or 90 atoms, respectively (not shown in Figure 1.3). The periodic models allow one to compute not only the nearest-neighbor and next-nearest neighbor magnetic couplings but also interchain magnetic coupling.

For all periodic calculations in this work, the entire unit cell was optimized or single-point calculations were performed on optimized structures; therefore, in contrast to the cluster models discussed in the previous subsection, special notations are not necessary to indicate the level of optimization of periodic models.

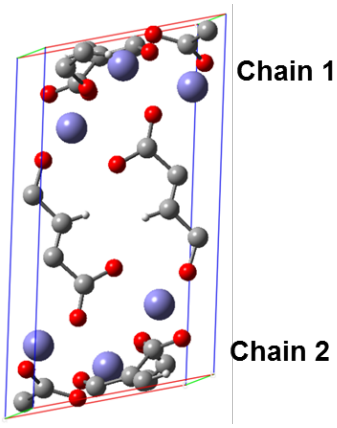

Figure 1.3. The unit cell of Fe_2(dobdc).
It consists of two chains of iron atoms. [Color code: Violet = Fe, Red = O, Gray = C, and White = H]

1.4 Method Development

Kohn-Sham density functional theory[32] has become the method of choice for treating the electronic structure of complex atomic, molecular, and solid-state systems at a reasonable computational cost. It can accurately treat both ground state and excited state properties of these systems, and it is the most widely used electronic structure method for treating not only main-group elements but also transition metals.[33] Since its inception in 1965, it has undergone significant improvements leading to state-of-the-art exchange-correlation functionals that are widely in use currently in all areas of research. The theory may be viewed as an alternative to solving the Schrödinger equation,[34] and is in principle exact, but only if one uses the exact exchange-correlation functional; however, this density functional is unknown.[35] Therefore one must use approximate exchange-correlation functionals. Although the MOF applications in this thesis used pre-existing density functional approximations,[36] another part of this thesis work has been the development of new density functional approximations. Because hybrid exchange-correlation functionals can be computationally very expensive for large systems such as MOFs, this work focuses on the development of computationally more efficient local approximations to exchange-correlation functionals, with emphasis on accurate prediction of those properties that are difficult to obtain with local functionals.

Although DFT is an important quantum mechanical tool for studying large systems, it can still be expensive for multi-scale modeling and studying materials with large unit cells or screening databases with thousands of structures. For such purposes, methods that allow initial screening at low computational costs are desired.

A method that has low computational cost and that has been applied recently to MOFs is molecular mechanics.[37] One of the major components of interaction energy, when an adsorbate is physisorbed on MOF, is dispersion energy, and the final chapter of this thesis analyses the treatment of dispersion interactions in molecular mechanics and presents a new method that can be broadly and conveniently applied across the periodic table for calculating dispersion energy.

1.5 Organization of the Thesis

This thesis is organized as follows. Chapter 2 discusses the ability of MOFs with open-metal sites to efficiently separate a mixture hydrocarbons, to separate dinitrogen from methane occurring in natural gas, and to fractionate air into its components (dinitrogen and dioxygen). Chapter 3 discusses the ability of a magnesium-diluted iron-based MOF to activate the strong C–H bonds of ethane. Chapter 4 discusses the magnetic properties of bare MOFs and MOFs with physisorbed and chemisorbed adsorbates. Chapters 5 and 6 discuss the development of quantum mechanical and molecular mechanical methods, respectively. Finally, Chapter 7 gives all the references cited in this thesis.

2 Gas Separation

2.1 Synopsis

Gas separations with porous materials are economically important and provide a unique challenge to fundamental materials design, as adsorbent properties can be altered to achieve selective gas adsorption. Metal–organic frameworks represent a rapidly expanding new class of porous adsorbents with a large range of possibilities for designing materials with desired functionalities. Given the large number of possible framework structures that can be generated, quantum mechanical computations can provide useful guidance in prioritizing the synthesis of the most useful materials for a given application. Here, we show that such calculations can help understand the separation of hydrocarbons present in natural gas, separation of air into its components, and predict a new metal-organic framework of potential utility for the separation of dinitrogen from methane, a particularly challenging separation of critical value for utilizing natural gas. An open Fe(II) or V(II) site incorporated into a metal–organic framework can be used to efficiently separate a mixture of gases into its components and can provide a material with a considerably higher enthalpy of adsorption for one of the components.

2.2 Introduction

Metal–organic frameworks have attracted attention in recent years due to their application for gas separation.[10,31,38,39,40,41,42,43,44,45] The M-MOF-74 MOFs have been widely studied experimentally and theoretically for their applications in gas storage,[46,47,48] isolation of CO_2 from various gaseous mixtures,[49,50,51] and fractionation of hydrocarbon mixtures.[31,39,41,52,53,54,55,56]

The separation of a mixture of hydrocarbons is a commercially important process that has a wide range of applications in the chemical industry. For example, saturated hydrocarbons find application as fuels, and unsaturated hydrocarbons are widely used in the polymer industry. Current methods of separation, such as cryogenic distillation, which is used to separate a gaseous mixture based on the difference in the boiling points of the constituents, have high-energy costs due to their requirement of low temperatures and high pressure. The recently synthesized iron-based MOF, Fe-MOF-74, has been found to be highly efficient in fractionating C1–

C3 hydrocarbon mixtures, at temperatures higher than those currently employed in cryogenic distillation.[10] In this work, our goal is to understand the structure and binding of C1–C3 hydrocarbon molecules to Fe-MOF-74 using Kohn-Sham density functional theory (KS-DFT) calculations.[31]

Another property of interest in the present work is the efficient separation of N_2 and O_2 gas molecules present in air. The MOF, Fe_2(dobdc), which is air sensitive, has been shown to be capable of separating O_2 from N_2 in air[12] due to its ability to bind O_2 more strongly than N_2 under ambient conditions. Another MOF that has been experimentally demonstrated to selectively bind O_2 over N_2 is $Cr_3(btc)_2$, where btc is 1,3,5-benzenetricarboxylate.[57] The present study elucidates the reasons behind the preference of Fe_2(dobdc) for O_2 over N_2 and thus identify the factors that make the separation possible. Two theoretical studies[58,59] have been reported for O_2 adsorption on Fe_2(dobdc). The previous studies of O_2 adsorption on Fe-MOF-74 used periodic boundary conditions; one, by Maximoff and Smit[59] on O_2 adsorption was based on KS-DFT modified by empirical intra-atomic Coulomb and exchange interactions (a method called PBE+U),[60] and the other, by Parkes *et al.*[58] on O_2 and N_2 adsorption utilized KS-DFT augmented with empirical damped-dispersion interactions (a method called PBE-D2).[60,61] The calculations by Maximoff and Smit were primarily addressed to the irreversible process that occurs when the MOF is dosed at high temperature; the present calculations are addressed to the low-temperature reversible adsorption. The calculations by Parkes *et al.* screened two families of MOFs, namely M_2(dobdc) and $M_3(btc)_2$ (M = Be, Mg, Sc–Zn, Mo, and Ru), for their ability to separate O_2 and N_2. They found that the identity of the metal is more important than the structure of the MOF, with the early transition metals better suited for separation than the late ones. The main objective of the present work is to rationalize the experimentally observed[12] preferential binding of O_2 over N_2 on Fe_2(dobdc) using KS-DFT.[30]

Finally, we would like to understand if it is possible to do dinitrogen/methane separation using the family of MOFs mentioned above. For example, Mg-MOF-74 displays CH_4 and N_2 adsorption enthalpies of 4.4[48] and 5.0[62] kcal/mol, respectively. As the synthesis of pure M-MOF-74 phases is often quite challenging, it would be advantageous to know *a priori* which variations are the best candidates for a given gas

separation application. This is a predictive challenge appropriate for the application of computational quantum chemistry, which can be used to pinpoint which cations might be anticipated to have interactions of significantly different strengths with competing guests. The interactions between M-MOF-74, corresponding to different M, and various adsorbates were investigated theoretically, which suggested that V-MOF-74 could be promising in the N_2/CH_4 separation. Here, we show that selective back bonding interactions from the V(II) cation centers in V-MOF-74 to the unoccupied π^* orbitals of N_2 can be used to separate N_2/CH_4 mixtures. To put this prediction on a quantitative basis we compare our calculations with the experimentally characterized Fe-MOF-74.

2.3 Methodology

To treat the adsorption process reliably, we use electronic structure methods that include dynamical correlation, especially attractive medium-range noncovalent forces. Most exchange-correlation (xc) functionals currently used in DFT do not treat such medium-range correlation energy accurately; however, here we use two kinds of density functionals that overcome this limitation. (1) The Rutgers-Chalmers van der Waals density functionals[63] use a nonlocal formulation of the correlation part of the xc functional and can treat attractive van der Waals interactions both at medium range and long range. We use the vdW-DF2+U functional[64] of this type with Hubbard *U* corrections,[65] where *U* is a parameter for metal *d* electrons that is determined to reproduce oxidation energies. (2) The Minnesota functionals include the local kinetic energy density in the xc functional and have been shown to yield accurate noncovalent attraction at van der Waals distances;[66] we employ three such functionals, M06-L,[162] M06,[140] and M11-L,[164] because they are based on very different approaches: M06-L is a well-validated local functional with global parameters, M11-L is a recent local functional employing different exchange and correlation parameters for short and long interelectronic distances, and M06 employs 27% Hartree–Fock exchange, as justified by adiabatic connection arguments[67] to reduce DFT self-interaction error.

We also employ two wave function theory (WFT) methods, in particular, local-pair natural-orbital coupled cluster theory with single and double excitations[68]

(LPNO-CCSD) and complete active space second-order perturbation theory with counterpoise corrections (CASPT2-CP).[69] The latter method has been shown to yield accurate energetics in systems containing transition metal compounds.[70,71]

The DFT and WFT methods used here involve approximations that impose limits on their accuracy. Because they represent very different approaches to the electronic structure problem, confidence in the utility of their quantitative predictions is significantly increased when different models agree, even if the nature of the various approximations employed makes it unclear which model is most accurate within the remaining variation.

Orbitals, spin states, cores, relativistic effects, and metal ions. In Kohn-Sham calculations and in the reference state for LPNO-CCSD, the V and Fe ions are in high-spin states (quartet and quintet, respectively), and all other orbitals are doubly occupied. For the CASPT2-CP calculation on the 88-atom cluster, the two outer metal ions were replaced by closed-shell Zn(II) ions and the central metal was treated in the active space. (None of the DFT calculations involve this Zn substitution.) The vdW-DF2 calculations with the Hubbard *U* correction employ the all-electron projector-augmented wave (PAW) method for scalar relativistic core electrons and ionic potentials; all other calculations treat all electrons explicitly. The CASPT2-CP calculations use the Douglas-Kroll-Hess relativistic approximation. All other calculations are nonrelativistic.

Basis sets. All the vdW-DF2+U calculations employed a plane-wave basis with a 1000 eV kinetic energy cutoff. All other DFT calculations employed the def2-TZVP basis set. The LPNO-CCSD calculations are extrapolated to a complete basis set from def2-TZVP and def2-QZVP. The CASPT2-CP calculations for the small model employed the ANO-RCC-TZVP basis for all atoms, and for the 88-atom cluster, they employed the ANO-RCC-DZVP basis for all atoms.

Charges and spin densities. Partial atomic charges were calculated by charge model 5 (CM5)[72,73] and spin densities were calculated by Hirshfeld population analysis.[74]

Coordinates. A triclinic primitive unit cell containing 54 atoms including six metal centers was used and involved simultaneous optimization of the lattice vectors and the atomic positions in the unit cell with variable cell dynamics with PBE+U for bare MOFs and with vdW-DF2+U for adsorbates. The 88-atom clusters were taken

out of these periodic structures. Optimization of the binding geometry of adsorbates in the periodic MOFs and on the 88-atom cluster involved freezing the MOF and optimizing only the coordinates of the adsorbate; this was carried out with all DFT calculations. The structure of the small model was fully optimized by M06-L and these structures were used for the LPNO-CCSD and CASPT2-CP calculations.

The starting geometries for the periodic model were based on the experimental structures of M-MOF-74 (Figure 1.1) and further optimized by DFT. We defined two other models of M-MOF-74 to be studied at additional levels of theory. The cluster (Figure 1.2(a)) has 88 atoms, including three metal centers, and it was designed to retain the local structure of MOF-74 about the central metal ion while remaining small enough for high-level electronic structure calculations. The small model has 19 atoms, including one metal center and is small enough to conduct calculations by expensive wave function methods for comparison.

All iron and vanadium ions were modeled in their respective ground (high-spin) state. To maintain charge neutrality with all oxide ligands in the small model, we included a *trans* carbonyl ligand. Although carbonyl groups are usually considered to be strong-field ligands, the small model nevertheless maintains a high-spin ground state and an electronic structure consistent with the larger model. Indeed, the insensitivity of our conclusions to the nature of the *trans* ligand in the M-MOF-74 model provides particularly strong support for our analysis.

Software. Minnesota functionals: *Gaussian 09*;[75] vdW-DF2+U: *VASP*;[76,77] LPNO-CCSD: *ORCA 2.9.1*;[78] CASPT2-CP: *Molcas 7.8*.[79]

2.4 Results and Discussion

The next three subsections discuss results obtained using quantum mechanical calculations for C1–C3 hydrocarbon separation, separation of O_2 and N_2 from air, and separation of N_2 and CH_4 present in natural gas.

2.4.1 Hydrocarbon Separation

Structures of unoptimized and optimized cluster models. The following notations are used to describe each of the optimized and unoptimized structures (all unoptimized coordinates are taken from the experimental crystal structure). Fe3opt0 stands for the 88-atom cluster where no atom is optimized (all atoms are frozen). In Fe3opt1, only

one atom, which is the central iron ion, is optimized and the remaining 87 atoms are frozen during geometry optimization. In Fe3opt12, twelve atoms are optimized; these include the central iron ion and eleven atoms of the groups in the first coordination sphere (three carboxylates and two oxidos in the first coordination sphere of the central iron), and the remaining 76 atoms are kept frozen during geometry optimization. When any of the above structures is optimized along with the guest molecule (which is a C1–C3 hydrocarbon), whose coordinates are always optimized, the structures are called Fe3opt0-guest, Fe3opt1-guest, and Fe3opt12-guest, respectively.

In Figure 2.1, it can be observed that, as the number of optimized atoms in the cluster increases from 0 to 1 (Fe3opt0 and Fe3opt1 systems, respectively), the central iron ion moves away from its position asymmetrically with respect to the neighboring iron ions as shown by a difference in bond distances of the central iron ion from the peripheral iron ions in Figure 2.1b. This phenomenon can also be observed in the presence of a guest molecule (see Figure 2.2b–2.7b). For the Fe3opt12 systems, the central iron ion moves more or less symmetrically with respect to the peripheral iron ions. The maximum difference in the bond distances for Fe3opt12 systems is 0.02 Å, which is observed for Fe3opt12-C_3H_8 (Figure 2.6c).

In Figure 2.2, 2.3, and 2.6, it can be observed that the three saturated hydrocarbons (methane, ethane, and propane) are bound to the central iron ion through their C–H bonds. Moreover, the distances of the central iron ion from the nearest hydrogen atoms are unequal. This result is consistent with all the three levels of optimization. The C–H bonds of methane, ethane, and propane directed towards the iron center become slightly elongated compared to the length optimized for the free hydrocarbon. This elongation is ~0.003 Å for the three C–H bonds of methane. For ethane and propane, we center attention on the two hydrogens closest to Fe. The C–H bond lengths of these hydrogens elongate by ~0.003 Å–0.004 Å in ethane and by 0.003 Å–0.005 Å in propane.

The unsaturated hydrocarbons are bound to the central iron ion by their C–C double or triple bonds rather than through C–H bonds. For acetylene and ethylene, the distances of the central iron ion from the two carbon atoms are almost equal (Figure 2.4 and 2.5). The Fe–C distances for ethylene, acetylene, and propylene are intermediate between standard single bond lengths[16] (1.24 + 0.75 = 1.99 Å) and van der Waals distances[16] (2.04 + 1.70 = 3.74 Å), and this situation is also observed

experimentally.[6] The Fe–C distances of propylene in the Fe3opt1 model agree with the experimentally reported results better than do the Fe–C distances of ethylene and acetylene. A decrease in the Fe–C distance is observed upon increasing the number of atoms being optimized within the cluster (Figure 2.4c, 2.5c, and 2.7c). This is because relaxation of more atoms within the cluster causes stronger binding, and hence brings the unsaturated hydrocarbon closer to the metal ion. The lengths of the C–C multiple bonds have been found to increase upon binding to Fe and also upon increasing the extent of optimization from Fe3opt0 to Fe3opt12. For example, the C–C double bond in ethylene increases from 1.32 Å when free to 1.33 Å for Fe3opt0-C_2H_4, to 1.35 Å for Fe3opt1-C_2H_4, and to 1.36 Å for Fe3opt12-C_2H_4. The C–C triple bond in acetylene increases from 1.20 Å in free acetylene and Fe3opt0-C_2H_2, to 1.22 Å in Fe3opt1-C_2H_2, and to 1.23 Å in Fe3opt12-C_2H_2. In case of propylene, the C–C double bond increases from 1.32 Å when free to 1.33 Å for Fe3opt0-C_3H_6, to 1.34 Å for Fe3opt1-C_3H_6, and to 1.35 Å for Fe3opt12-C_3H_6. Along with the increasing number of optimized atoms, the stronger electron back donation from the 3*d* orbitals of the central metal ion to C–C π antibonding orbital of unsaturated guest molecules is observed as discussed later in natural bond orbital (NBO) analysis section. This is why there is an increase in C–C multiple bond length with increasing level of optimization.

The experimental Fe–H distances are 2.6 Å for two hydrogen atoms of ethane directed towards iron, and 2.9 and 2.2 Å for the two hydrogen atoms in propane directed towards the iron center.[6] Comparison to Figure 2.3 and 2.6 shows good agreement with experimental distances for all three levels of optimization for ethane, but theory leads to Fe–H bonds for propane somewhere in between 2.2 and 2.9 Å. The experimental Fe–C distances are respectively 2.4, 2.5, and 2.6 Å in ethylene, acetylene, and propylene. Comparison to Figure 2.4, 2.5, and 2.7 shows the best agreement with opt1 structures in two cases and with opt0 in the other; in contrast, the opt12 structures are too tightly bound by 0.1, 0.4, and 0.2 Å, respectively.

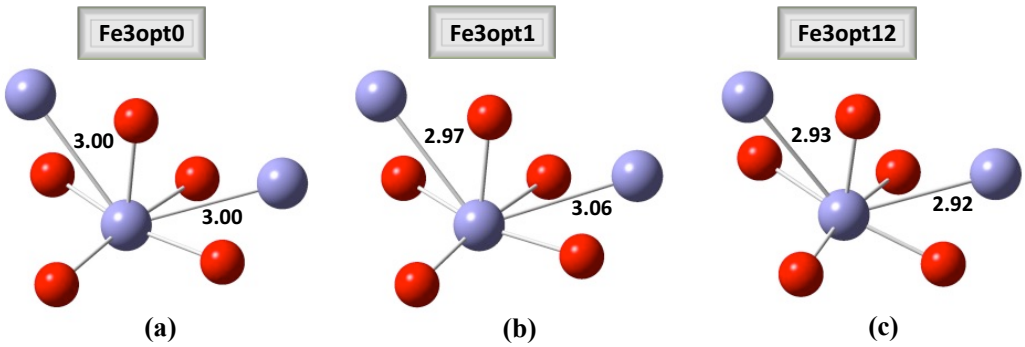

Figure 2.1 Structures of Fe3opt0, Fe3opt1, and Fe3opt12.
(a) Fe3opt0: no atom is optimized, (b) Fe3opt1: only the central iron ion is optimized, and (c) Fe3opt12: the central iron ion and eleven atoms in the first coordination shell of iron ion are optimized. Some distances are given in Å. [Color code: Violet = iron, Red = oxygen, Gray = carbon]

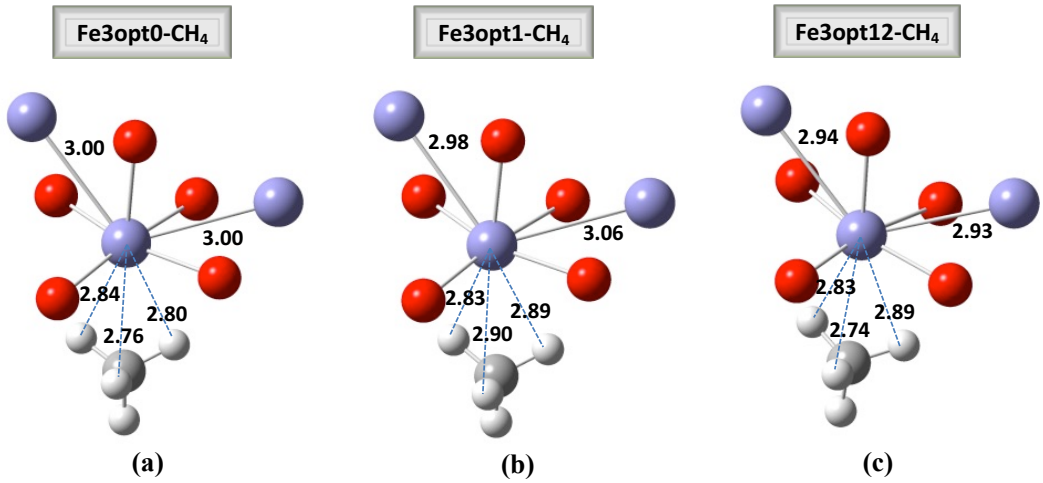

Figure 2.2 Structures of Fe3opt0-CH_4, Fe3opt1-CH_4, and Fe3opt12-CH_4.
(a) Fe3opt0-CH_4: only methane is optimized and no atom of the cluster is optimized, (b) Fe3opt1-CH_4: only the central iron ion of the cluster and methane bound to it are optimized, and (c) Fe3opt12-CH_4: the central iron, eleven atoms in the first coordination shell of the central iron ion, and methane bound to the central iron ion are optimized. Some distances are given in Å. [Color code: Violet = iron, Red = oxygen, Gray = carbon, White = hydrogen]

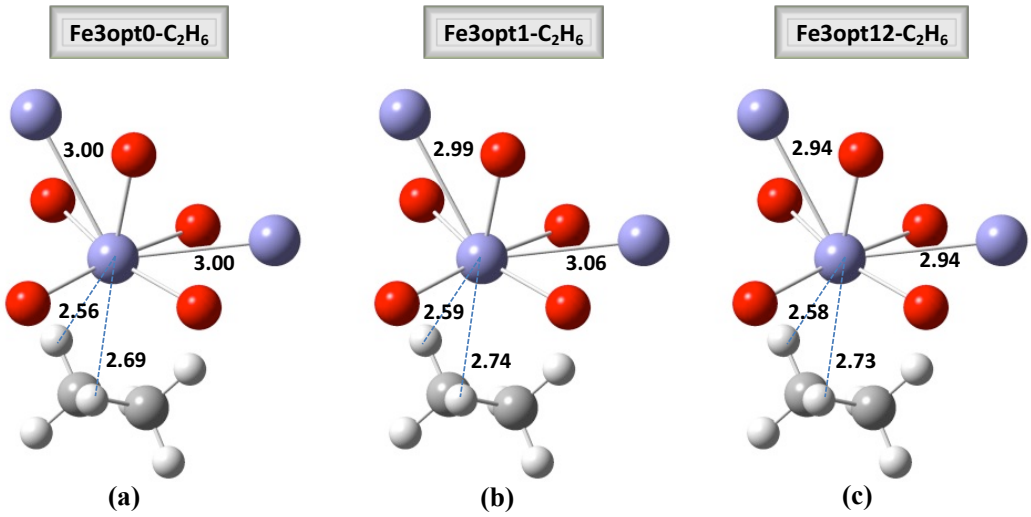

Figure 2.3 Structures of Fe3opt0-C_2H_6, Fe3opt1-C_2H_6, and Fe3opt12-C_2H_6. (a) Fe3opt0-C_2H_6: only ethane is optimized and no atom of the cluster is optimized, (b) Fe3opt1-C_2H_6: only the central iron ion of the cluster and ethane bound to it are optimized, and (c) Fe3opt12-C_2H_6: the central iron, eleven atoms in the first coordination shell of the central iron ion, and ethane bound to the central iron ion are optimized. Some distances are given in Å. [Color code: Violet = iron, Red = oxygen, Gray = carbon, White = hydrogen]

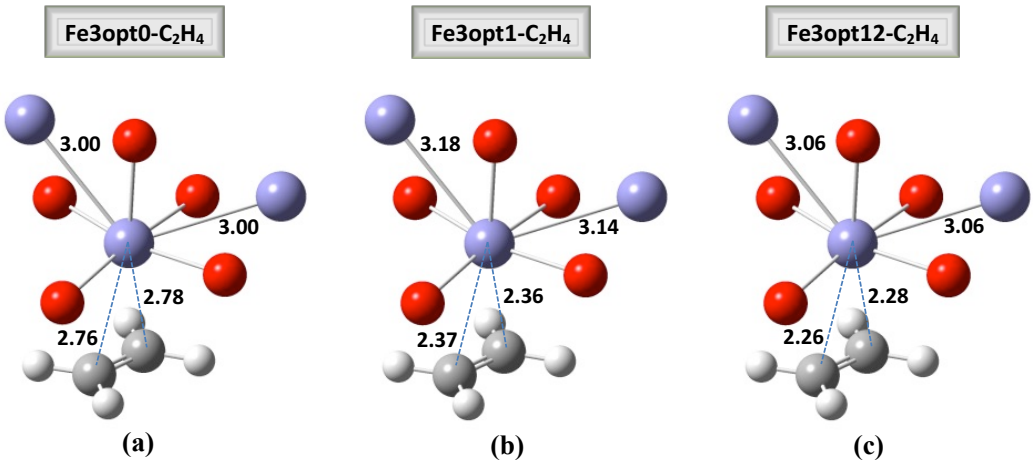

Figure 2.4 Structures of Fe3opt0-C_2H_4, Fe3opt1-C_2H_4, and Fe3opt12-C_2H_4. (a) Fe3opt0-C_2H_4: only ethylene is optimized and no atom of the cluster is optimized, (b) Fe3opt1-C_2H_4: only the central iron ion of the cluster and ethylene bound to it are optimized, and (c) Fe3opt12-C_2H_4: the central iron, eleven atoms in the first coordination shell of the central iron ion, and ethylene bound to the central iron ion are optimized. Some distances are given in Å. [Color code: Violet = iron, Red = oxygen, Gray = carbon, White = hydrogen]

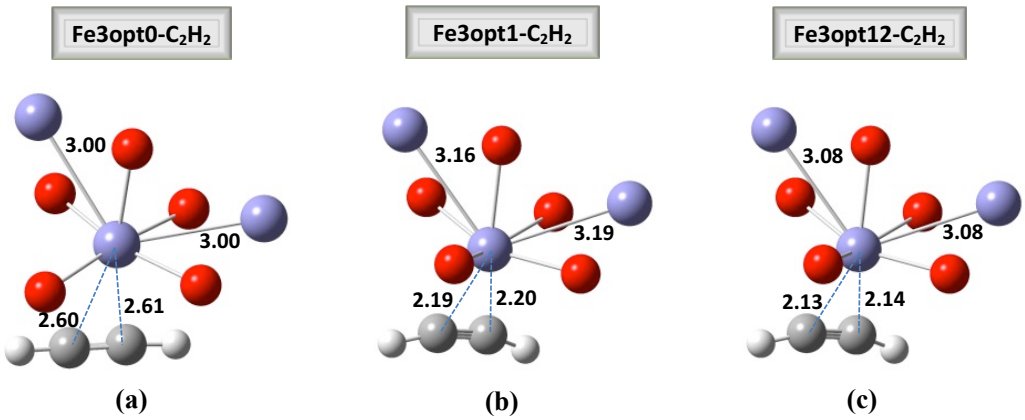

Figure 2.5 Structures of Fe3opt0-C_2H_2, Fe3opt1-C_2H_2, and Fe3opt12-C_2H_2.
(a) Fe3opt0-C_2H_2: only acetylene is optimized and no atom of the cluster is optimized, (b) Fe3opt1-C_2H_2: only the central iron ion of the cluster and acetylene bound to it are optimized, and (c) Fe3opt12-C_2H_2: the central iron, eleven atoms in the first coordination shell of the central iron ion, and acetylene bound to the central iron ion are optimized. Some distances are given in Å. [Color code: Violet = iron, Red = oxygen, Gray = carbon, White = hydrogen]

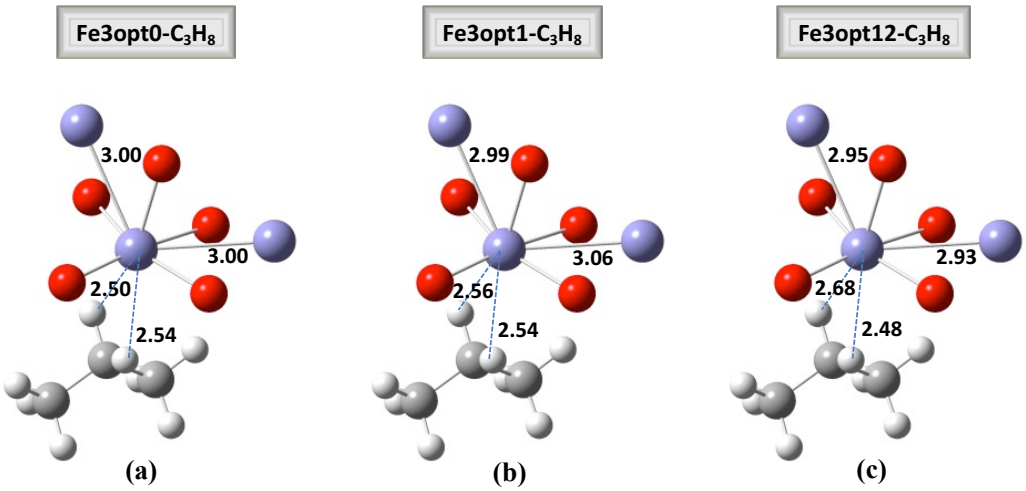

Figure 2.6 Structures of Fe3opt0-C_3H_8, Fe3opt1-C_3H_8, and Fe3opt12-C_3H_8.
(a) Fe3opt0-C_3H_8: only propane is optimized and no atom of the cluster is optimized, (b) Fe3opt1-C_3H_8: only the central iron ion of the cluster and propane bound to it are optimized, and (c) Fe3opt12-C_3H_8: the central iron, eleven atoms in the first coordination shell of the central iron ion, and propane bound to the central iron ion are optimized. Some distances are given in Å. [Color code: Violet = iron, Red = oxygen, Gray = carbon, White = hydrogen]

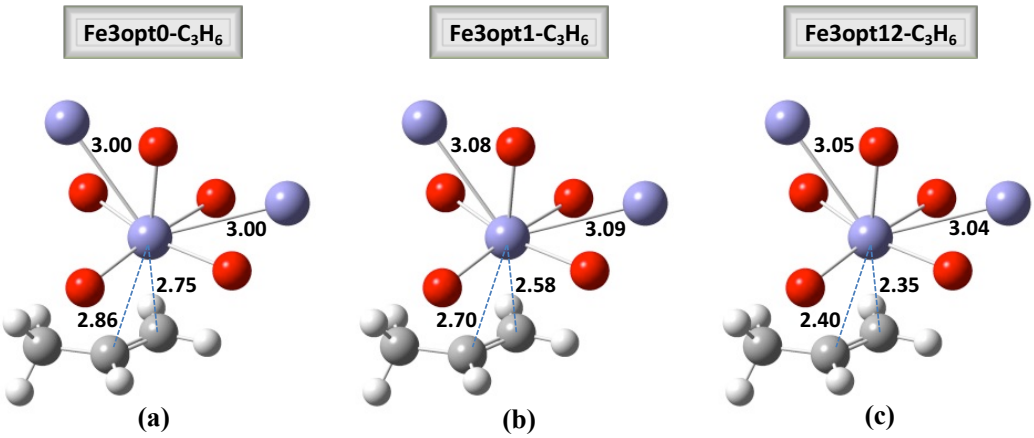

Figure 2.7 Structures of Fe3opt0-C_3H_6, Fe3opt1-C_3H_6, and Fe3opt12-C_3H_6. (a) Fe3opt0-C_3H_6: only propylene is optimized and no atom of the cluster is optimized, (b) Fe3opt1-C_3H_6: only the central iron ion of the cluster and propylene bound to it are optimized, and (c) Fe3opt12-C_3H_6: the central iron, eleven atoms in the first coordination shell of the central iron ion, and propylene bound to the central iron ion are optimized. Some distances are given in Å. [Color code: Violet = iron, Red = oxygen, Gray = carbon, White = hydrogen]

Binding enthalpies. Four spin states of the 88-atom cluster model were studied by considering each of the possible combinations of local quintet states on each of the three iron ions. Enthalpies for binding of both saturated and unsaturated hydrocarbons at the central iron ion were computed. We computed only the binding enthalpies at both 298.15 and 318 K and not the Gibbs free energies and entropies because the experimental data[10] is available only for enthalpies of adsorption. Furthermore, free energy and entropy calculations involve additional uncertainties that are beyond the scope of the present work. Hence, we confine ourselves to discussions of binding energies and binding enthalpies.

Table 2.1 gives results only for the 222 spin state because it is the lowest-energy spin state of the MOF. At 318 K, the binding enthalpies for other spin states always agree with those for the 222 spin state within 0.1 kcal/mol for ethane, within 0.3 kcal/mol for propylene, and within 0.4 kcal/mol for methane, but the deviations are much larger—up to 1.2 kcal/mol—for ethane and ethylene. Also, the unsaturated hydrocarbons bind more strongly to the central metal ion than do the saturated ones. Since different hydrocarbons bind to the metal centers with different strengths, a mixture of such hydrocarbons when passed through Fe-MOF-74 can be separated based on their differential adsorption within the pore of the MOF. Table 2.1 also

indicates that binding via C–C double or triple bond to the iron center is stronger than that occurring through C–H bond.

The values obtained by the M06-L/def2-TZVP method agree well with the experimental values[10] for the opt0 and opt1 structures, each having a mean absolute deviation (MAD) from the experiment of only 1.0 kcal/mol (average over six cases). Comparison of the binding enthalpies for methane in Table 2.1 indicates that as more atoms of the 88-atom cluster are optimized, the values get closer to the experimental value of 4.8 kcal/mol. This can also be seen for propane (which is interesting in light of the discrepancy with experiment for Fe–H distances), but for ethane, there is no significant change in binding enthalpies from Fe3opt1 to Fe3opt12. For the unsaturated hydrocarbons ethylene, acetylene, and propylene, the binding is strongest for the Fe3opt12 case because the unsaturated carbon atoms get closer to the central iron ion as can be seen in Figure 2.4, 2.5, and 2.7. However, the Fe3opt12 results of all three unsaturated hydrocarbons overestimate the binding enthalpies by 3–5 kcal/mol compared to the experimental data, leading to an increased MAD of 2.2 kcal/mol for the average over six cases. This over binding of the unsaturated adsorbates is consistent with the short Fe–C bond distances in the opt12 structures for these cases, which was already discussed.

Table 2.1 Binding energies and enthalpies (kcal/mol) calculated for the adsorption of a guest molecule at the central iron ion of the 88-atom model for the 222 spin state.

		calculated		**experimental**
Guest	ΔE	$\Delta H_{298.15}$	ΔH_{318}	ΔH_{318}
(Fe3opt0-guest).				
methane	7.8	6.8	6.7	4.8
ethane	8.8	7.6	7.5	6.0
ethylene	12.3	11.0	10.9	10.8
acetylene	12.3	11.8	11.8	11.2
propane	9.9	8.6	8.6	7.9
propylene	14.3	13.0	13.0	10.5
(Fe3opt1-guest).				
methane	6.7	5.6	5.6	4.8
ethane	8.3	7.1	7.0	6.0
ethylene	11.9	10.8	10.7	10.8
acetylene	12.7	12.4	12.4	11.2
propane	9.8	8.6	8.5	7.9
propylene	14.2	13.0	12.9	10.5
(Fe3opt12-guest).				

methane	6.6	5.5	5.4	4.8
ethane	8.5	7.3	7.3	6.0
ethylene	15.1	14.0	14.0	10.8
acetylene	14.5	14.3	14.2	11.2
propane	9.0	7.6	7.6	7.9
propylene	16.5	15.4	15.3	10.5

Table 2.2 compares the binding energies of ethane and ethylene in the 88-atom (Fe_3 system) and 106-atom (Fe_5 system) models. The difference averages 1.8 kcal/mol, which is surprisingly large. The structures for Fe5opt1 complexes are shown in Figure 2.8; comparison to Figure 2.3(b) and 2.4(b) shows very good agreement.

Table 2.2 Comparison of binding energies (kcal/mol) of Fe_3 (222 spin state) and Fe_5 (22222 spin state) model systems bound to ethane and ethylene. All calculations were done by M06-L/def2-TZVP.

Fe_5 systems	**ΔE**	**Fe_3 systems**	**ΔE**
Fe5opt0-ethane	10.2	Fe3opt0-ethane	8.8
Fe5opt1-ethane	9.6	Fe3opt1-ethane	8.3
Fe5opt0-ethylene	13.0	Fe3opt0-ethylene	12.3
Fe5opt1-ethylene	15.5	Fe3opt1-ethylene	11.9

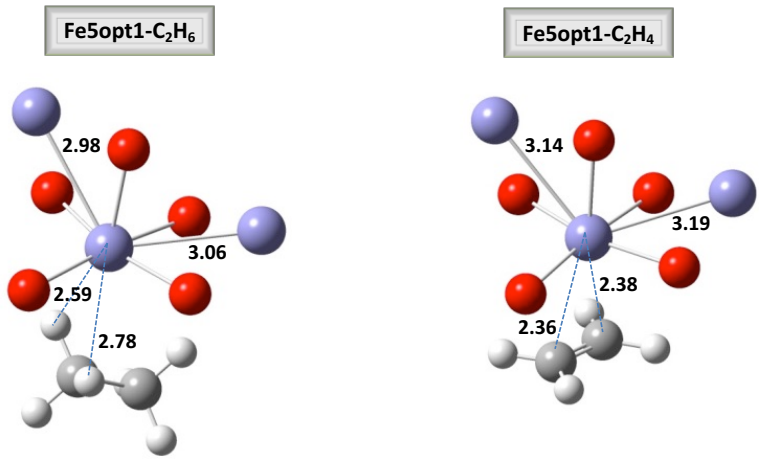

Figure 2.8 Structures of Fe5opt1-C_2H_6 and Fe5opt1-C_2H_4.
(*left*) Fe5opt1-C_2H_6 and (*right*) Fe5opt1-C_2H_4. Some distances are given in Å. [Color code: Violet = iron, Red = oxygen, Gray = carbon, White = hydrogen]

Dispersion energy. There is considerable current interest in the role of dispersion-like interactions in the chemistry of materials. The partition of molecular interactions into dispersion, induction (polarization), and permanent-moment

electrostatics is unique in the long-range, zero-overlap limit; however, for van der Waals and shorter distances it becomes clouded due to overlap that damps the long-range force laws and due to exchange repulsion, charge transfer, partial or full covalency, and other mean-field and correlation contributions to interaction energies. For example, we evaluated the D3 damped dispersion formula that has been parameterized to add dispersion-like corrections to density functional theory,[80] and we found for ethylene dimer values of the D3 "dispersion" ranging from 4.2 kcal/mol to 0.1 kcal/mol using various density functionals because this formula not only accounts for damped dispersion but also includes other systematic corrections to available approximate density functionals. The M06-L approximate density functional used here is one of the methods that yield 0.1 kcal/mol, which indicates that its medium-range correlation energy already includes damped dispersion for ethylene dimer, so we do not need to add a molecular mechanics term to the present calculations.

To gain insight into the contribution of dispersion-like interactions in binding between the guest molecule and the cluster model, we proceeded as follows. Probably the most successful attempt to sort out the damped dispersion contribution is symmetry-adapted perturbation theory (SAPT),[81] and the damped dispersion contribution to the interaction energy in ethylene dimer was calculated to be 2.6 kcal/mol by Podeszwa *et al*.[82] using SAPT. Examining the various dispersion parameter sets of Grimme,[83] we found that the revPBE38[17,20,84] set (with zero damping[80]) gives 2.5 kcal/mol, and therefore we used these parameters to estimate the damped dispersion contributions to the adsorption energies; for comparison, we also examined the HCTH120[20,21,85] parameters which (again with zero damping) give 1.8 kcal/mol. The results for the opt1 geometries for the 88-atom model are in Table 2.3. It can be seen from this table that ΔE_{disp} calculated by subtracting E_{disp} of the cluster-guest complex from that of the separate cluster and the guest molecule, correlates reasonably well with the binding energy, ΔE, although neither damped dispersion set correlates as well as the full M06-L calculations; the damped dispersion sets have mean absolute deviations from experiment of 3.8 and 2.8 kcal/mol, whereas the M06-L energies have mean absolute deviations from the experimental enthalpies of 2.1 kcal/mol. The values for ΔE are found to be smaller than ΔE_{disp} (for most of the systems in Table 2.3), which is not surprising since one must add other effects such as

exchange repulsion to dispersion-like forces and since the damping of the dispersion in the D3 model is approximate.

In Table 2.3, $\Delta\Delta E_{disp}$ gives, for each hydrocarbon, the difference from ethane of the dispersion contribution to binding, again as evaluated by the D3 term parameterized for revPBE38 or HCTH120. This difference gives us a measure of the extent of dispersion for each hydrocarbon as compared to ethane. This column correlates remarkably well with the $\Delta\Delta H_{318}$ values for alkanes and alkenes but not for acetylene, which indicates that the interaction energy of acetylene is more complicated.

Table 2.3 Binding energies (kcal/mol) and dispersion energies (kcal/mol) calculated using Grimme's DFT-D3 method for revPBE38 and HCTH120 parameters with zero damping for the Fe3opt1-guest systems in the 222 spin state.

Guest				Difference from ethane		
	ΔE	ΔE_{disp}	ΔE_{disp}	$\Delta\Delta E_{disp}$	$\Delta\Delta E_{disp}$	$\Delta\Delta H_{318}$[a]
	M06-L	**revPBE38**	**HCTH120**	**revPBE38**	**HCTH120**	**expt.**
methane	6.7	8.8	7.5	–2.0	–2.8	–1.2
ethane	8.3	10.8	10.3	0.0	0.0	0.0
ethylene	11.9	11.7	12.0	0.9	1.7	4.8
acetylene	12.7	14.0	9.0	3.2	–1.3	5.2
propane	9.8	12.2	10.9	1.4	0.6	1.9
propylene	14.2	16.3	13.9	5.5	3.6	4.5

[a] This column is from experiment;[10] the other columns are theoretical.

In another test to check the presence of dispersion-like interactions between the guest molecule and the cluster model, we performed Hartree–Fock (HF) calculations on Fe3opt1 (222 spin state) systems bound to ethane and ethylene. Since the HF method lacks dynamical electron correlation, it does not include dispersion-like interactions between the guest molecule and the cluster model. Table 2.4 shows a comparison of binding energies at HF level with those from M06-L. We find that HF results show a very small attractive interaction between the guest molecule and the cluster model, which is consistent with most of the attractive interaction energy given by M06-L coming from dispersion-like interactions. Also, the optimized structure at the HF level has the ethane molecule more than 3.9 Å away from the metal center and the ethylene molecule more than 3.3 Å away from the metal center.

Table 2.4 Binding energies (kcal/mol) computed at HF and M06-L levels using def2-TZVP basis set for Fe3opt1 systems (222 spin state) bound to ethane and ethylene.

System	M06-L	HF
Fe3opt1-ethane	8.3	0.9
Fe3opt1-ethylene	11.9	1.5

NBO analysis. NBO analysis has been performed for three species (bare MOF, MOF bound to ethane, and MOF bound to ethylene) to gain insights into the bonding between the guest molecule and the central iron ion with the 88-atom model. Although absolute magnitudes of the partial atomic charges from NBO analysis do not agree with our best estimates, this analysis provides a physical interpretation of the nature of the bonding. Our analysis with Fe3opt0 geometries shows that when the guest is bound to the open site of the iron ion in the MOF, the natural electron configuration of the central iron ion is changed from

[core] 4s(0.20) 3d(6.26) 4p(0.30) 4d(0.02)

for bare MOF to

[core] 4s(0.19) 3d(6.24) 4p(0.34) 4d(0.03)

for MOF bound to ethane and to

[core] 4s(0.19) 3d(6.23) 4p(0.37) 4d(0.04)

for MOF bound to ethylene. These populations show the presence of weak electron donation from the π bonding orbital of ethylene and σ bonding orbital of C–H bond of ethane to the 3*d* and 4*p* orbitals of the central Fe ion. The NBO analysis using the Fe3opt1 geometries, where the central iron ion of the cluster is optimized, not only shows much stronger electron donation from ethylene to the central iron ion, but also notable electron back donation from the 3*d* orbital of the central iron ion to the π antibonding orbital of ethylene. The NBO analysis with the Fe3opt1 geometry indicates that the stronger binding energy of ethylene with MOF compared to ethane is also a result of the π bond interaction between ethylene and iron besides stronger dispersion interaction. The Fe3opt12-C_2H_4 geometry has a shorter Fe–C bond distance and the NBO analysis shows an Fe–C single bond, which is not observed for Fe3opt0-C_2H_4 and Fe3opt1-C_2H_4. This explains the larger binding enthalpies calculated with Fe3opt12 geometries than those calculated with Fe3opt0 and Fe3opt1 geometries for MOF bound to ethylene. The NBO analysis with Fe3opt1-ethane and

Fe3opt12-ethane geometries does not show stronger electron donation from ethane to iron ion than with Fe3opt0-ethane nor any electron back donation.

Orbital energy analysis. Figure 2.9 shows the natural atomic orbital (NAO) energy level splitting of the five degenerate *d* orbitals of Fe^{2+} cation obtained from NBO analysis in two ligand fields: one is in a distorted square pyramidal environment of the five oxygen atoms surrounding the central iron ion, and the other one is in a distorted octahedral environment created by the presence of a guest molecule along with five oxygen atoms. The Fe3opt1 geometries of 88-atom model bound to guest are used here instead of Fe3opt12 geometries because based on our binding enthalpy calculations and NBO analysis, the Fe3opt12 could overestimate the interaction between MOF and ethylene. We can see from Figure 2.9 that in the absence of a guest molecule the central iron ion of the 88-atom model shows the expected splitting of *d* orbitals for a distorted square pyramidal environment around a metal center. The presence of ethane or ethylene in the vacant site of the central iron ion makes the environment around it a distorted octahedron, and the splitting of *d* orbitals occurs as expected with three of the five *d* orbital energies getting closer to one another and having lower energy than the other two. The stronger interaction of ethylene with the MOF causes a remarkable change in the orbital energy levels of the *d* orbitals of Fe ion, as compared to ethane. The splitting of the *d* orbitals of the MOF bound to ethylene is more similar to the splitting of *d* orbitals in an octahedral ligand field.

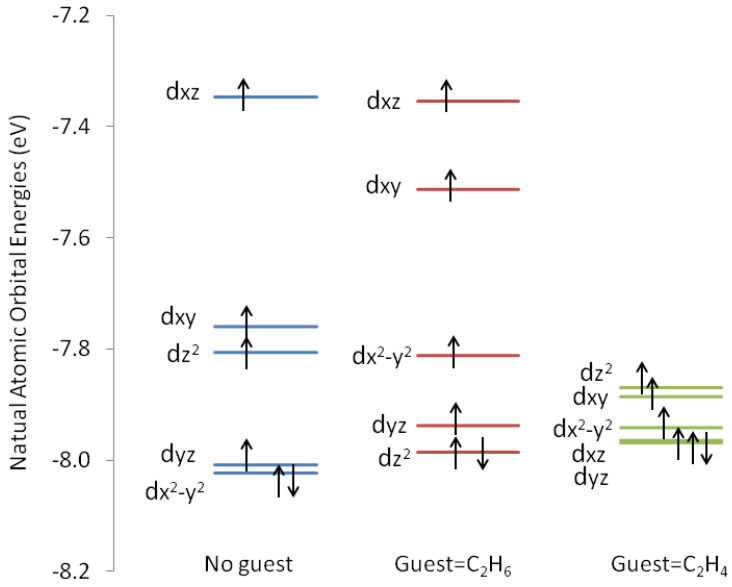

Figure 2.9 Splitting of 3*d* orbitals of the central iron atom of the 88-atom model. The Fe3opt1 geometries are shown in the absence and presence of the guest molecules, ethane and ethylene. The energy levels shown in the figure are the NAO

energies of the α spin orbitals, although we show both α and β spin orbital occupancies. (The β spin orbitals, most of which are unoccupied, have different energies in the unrestricted open-shell treatment employed here, but showing them would complicate the plot too much, and the energies for the majority α spin are more relevant.)

2.4.2 O_2/N_2 Separation

Calculations on two available experimental MOF structures were carried out by partially relaxing their cluster models. First, we consider binding a single adsorbate to the bare MOF structure labeled as B, then we consider binding more than one adsorbate to B, and finally, we consider binding to a distorted MOF structure that was observed experimentally (labeled as structure L in Table 2.5).

Table 2.5 Internuclear distances (in Å) in bare (B) MOF and low-temperature (L) MOF(O_2).

Abbreviation	System	Experiment[a]		
		Fe–Fe	**O–O**	**Fe–O**
B	Bare MOF	3.00	NA[b]	NA[b]
L	Low-temperature MOF(O_2)	3.17	1.25	2.08, 2.10

[a]The experimental structures are taken from Ref. 12. The O–O and Fe–O distances refer to the adsorbed O_2.

[b]NA = not applicable.

Binding a single adsorbate to the bare MOF structure. For the initial spin configurations shown in Table 2.6, partial geometry optimizations were performed using the M06 functional by freezing the entire 88-atom cluster and optimizing only the N_2 or O_2 guest molecules (//B-opt0 calculations). Here, we compare energies of various spin states shown in Table 2.6 and Figure 2.10, where the complexes were obtained by adding adsorbate to structure B in Table 2.5. These energies are computed with respect to the ground spin states of the isolated fragments. The calculated ground spin states of the isolated fragments were found to have N_2 in the singlet state, O_2 in the triplet state, and the bare 88-atom cluster in the high-spin state corresponding to ferromagnetically coupled local quintets. Figure 2.10 shows separated species on the left and the complexes on the right; the numbers in parentheses indicate the final spins on the metal centers or the adsorbate, which were determined based on Hirshfeld spin densities given in Table 2.6.

Table 2.6 Initial charges, initial M_S values, computed CM5 charges, Hirshfeld spin densities, and S values of the iron atoms and the adsorbed guest molecules of the complexes (All quantities are in atomic units except energies of binding, which are in kcal/mol with respect to the separated reactants in their ground spin state).

Initial guess					**Final values**[a]					
MOF(N_2) (3 Fe)		**Adsorbed N_2**		**MOF(N_2)**	**MOF(N_2) (3 Fe)**		**Adsorbed N_2**		**MOF(N_2)**	**MOF(N_2)**
Charge	M_S	Charge	M_S	M_S	charge	Spin density	charge	Spin density	S	Energy
2, 2, 2	2, 2, 2	0	0	6	0.64, 0.66, 0.64	3.66, 3.69, 3.69	0.08	0.02	6.01	–8.5
2, 2, 2	2, 1, 2	0	0	5	0.64, 0.59, 0.64	3.67, 1.94, 3.69	0.09	0.03	5.01	25.8
2, 2, 2	2, 0, 2	0	0	4	0.64, 0.64, 0.65	3.67, 0.02, 3.68	–0.03	0.00	4.03	34.1
MOF(O_2) (3 Fe)		Adsorbed O_2		MOF(O_2)	MOF(O_2) (3 Fe)		Adsorbed O_2		MOF(O_2)	MOF(O_2)
Charge	M_S	Charge	M_S	M_S	charge	Spin density	charge	Spin density	S	Energy
2, 3, 2	2, 2.5, 2	–1	0.5	7	0.64, 0.76, 0.64	3.67, 3.93, 3.69	–0.13	1.65	7.01	–8.7
2, 2, 2	2, 2, 2	0	1	7	0.64, 0.76, 0.64	3.67, 3.93, 3.69	–0.13	1.65	7.01	–8.7
2, 4, 2	2, 2, 2	–2	0	6	0.64, 0.81, 0.65	3.68, 3.92, 3.70	–0.24	–0.33	6.07	–1.9[b]
2, 3, 2	2, 2.5, 2	–1	–0.5	6	0.64, 0.81, 0.65	3.68, 3.92, 3.70	–0.24	–0.33	6.07	–1.9[b]
2, 2, 2	2, 2, 2	0	0	6	0.64, 0.81, 0.65	3.68, 3.92, 3.70	–0.24	–0.34	6.07	–2.0
2, 2, 2	2, 1, 2	0	1	6	0.65, 0.83, 0.66	3.69, 3.96, 3.71	–0.27	–0.44	6.07	–1.3[b]
2, 2, 2	2, 2, 2	0	–1	5	0.64, 0.63, 0.64	3.67, 3.62, 3.69	0.08	–1.88	5.18	–8.3
2, 2, 2	2, 1, 2	0	0	5	0.64, 0.63, 0.64	3.67, 3.61, 3.69	0.08	–1.87	5.18	–8.2[c]
2, 2, 2	2, 0, 2	0	1	5	0.64, 0.61, 0.65	3.67, 0.34, 3.69	–0.07	1.62	5.10	high[d]
2, 2, 2	2, 1, 2	0	–1	4	0.64, 0.58, 0.64	3.67, 1.79, 3.69	0.06	–1.84	4.27	high[d]
2, 2, 2	2, 0, 2	0	0	4	0.64, 0.56, 0.65	3.66, –1.80, 3.69	0.06	1.83	4.22	high[d]

[a]The values in this table correspond to //B-opt0 and //B–X_2-opt0 calculations (X = N or O).

[b]Within convergence tolerance and rounding, this is assumed to be the same state as in the line ending as –2.0.

[c]Within convergence tolerance and rounding, this is assumed to be the same state as in the line ending as –8.3.

[d]Values marked as high are at least 34 kcal/mol above the quintet ground state.

For MOF(N_2), three possibilities were considered by changing the spin state only of the central iron atom (Table 2.6). On the left of Figure 2.10(a) one can see that when no N_2 is bound to the iron center, the two cases that have triplet and singlet iron centers are 35.4 and 49.0 kcal/mol higher in energy than the quintet ground state. The adsorption of N_2 on the central metal atom (shown on the right of Figure 2.10(a)) causes the energy level of each state to drop and makes the N_2 bound cluster more stable compared to the free cluster in each case.

For MOF(O_2), a number of interesting features can be observed from Figure 2.10(b). The eleven initial guesses described in Table 2.6 for MOF(O_2) systems were tried, and they converged to the various structures shown in Table 2.6. In Table 2.6 for any state with energy > –2.0 kcal/mol, we just mark these states as high in energy rather than giving a number because of the difficulty of converging the high-energy states quantitatively. We did not find any state with the central iron having a spin of one with an energy less than 34 kcal/mol above the quintet ground state, and we did not find any state with the central iron having a spin of zero with an energy less than 48 kcal/mol above the quintet ground state. Figure 2.10(b) reports the three lowest energy structures from Table 2.6. Similar to the N_2 case, we also observe here that the adsorption of O_2 causes the energy levels of the various spin states of the cluster to drop. The triplet-singlet splitting of the free O_2 molecule is high (~37 kcal/mol) when it is not bound to the iron center, but when adsorbed on Fe_2(dobdc), this splitting reduces to ~7 kcal/mol. The complexes that have triplet O_2 either ferromagnetically or antiferromagnetically coupled to the quintet iron center have similar energies, *i.e.*, O_2 is weakly coupled to the Fe^{II} center (in terms of isotropic magnetic coupling). For both the MOF(N_2) and MOF(O_2) complexes, it can be seen that when the central Fe does not converge to a quintet state (which can be seen from Hirshfeld spin populations given in Table 2.6 under “final values”), it results in high-energy structures with energies larger than the ground-state one by ~34 kcal/mol or more.

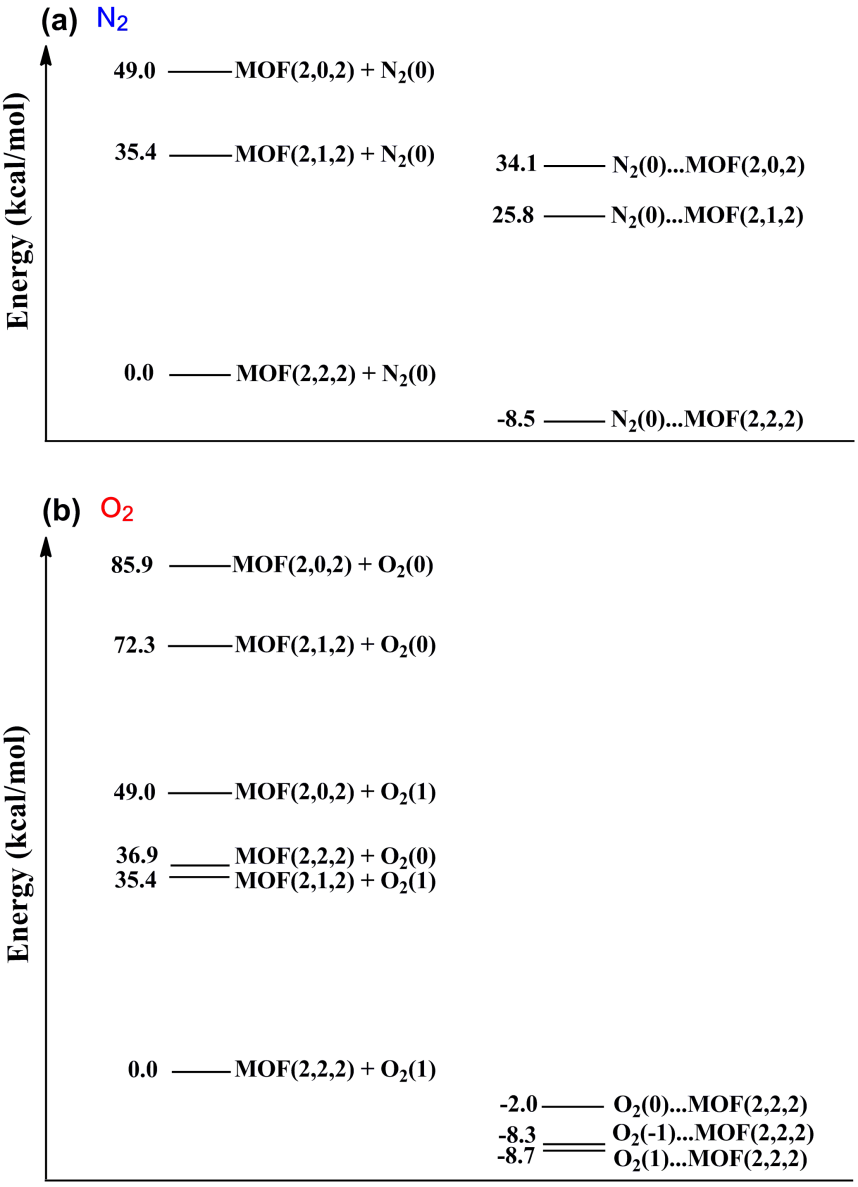

Figure 2.10 Energies of free O_2, bare MOF, MOF(N_2), and MOF(O_2). The left side of the figure has separated fragments, and the right side of the figure has the associated complexes. The final spins of the atoms in each system are indicated in parentheses with the three numbers for the cluster representing its three iron centers. All calculations in this figure are //B-opt0 calculations. (a) On the right are the energy levels of MOF(N_2), computed with respect to the energy levels of separated diamagnetic N_2 and ferromagnetically coupled quintet iron spins of bare MOF, referred to as MOF(2,2,2) + N_2(0) in the figure. (b) On the right are the energy levels of MOF(O_2), computed with respect to the energy levels of separated triplet O_2 and ferromagnetically coupled quintet iron spins of bare MOF, referred to as MOF(2,2,2) + O_2(1) in the figure.

Selected spin configurations (which corresponds to most stable MOF(N_2) and three lowest energy MOF(O_2) complexes) from Figure 2.10 were then chosen to

compute enthalpies of binding at 201 and 298.15 K by considering three levels of optimization, //B-opt0, //B-opt1, and //B-opt6, as shown in Table 2.7. Gibbs free energies were computed for //B-opt1 and //B-opt6 complexes. The selected spin states are—the ground spin state of MOF(N_2) (quintet spins on every iron center with ferromagnetic coupling between them) and the ground spin state of MOF(O_2) (quintet spins on every iron center with ferromagnetic coupling between them and also with the triplet O_2 molecule) plus two other spin states which have singlet O_2 bound to the quintet spin central iron and triplet O_2 antiferromagnetically coupled to this center.

The original experimental values for the isosteric heat of adsorption of N_2 and O_2 are respectively –8.4 kcal/mol and –9.8 kcal/mol;[12] however, a possibly more accurate experimental value of –5.5 kcal/mol for N_2 (under different experimental conditions) was reported in a recent work.[42] Note that a negative sign means that adsorption of the guest molecule is exoergic or exothermic. Table 2.7 shows that the increase in level of optimization does not significantly change the energies and enthalpies of binding for N_2 adsorption and for O_2 adsorption that has triplet O_2 antiferromagnetically coupled to quintet iron, but for O_2 adsorption in the other two cases slight overbinding is observed with //B-opt1 and //B-opt6 structures when compared to the //B-opt0 structure. This overbinding in the Fe–O_2 system with increasing level of optimization could be due to the fact that the Fe–O distances in the //B-opt1 and the //B-opt6 structures are shorter compared to the //B-opt0 structure and also could be due to the fact that the O_2 unit is more prone to charge transfer compared to N_2, as discussed in the CM5 charge analyses section. Nevertheless, the final (i.e., //opt6) energies of adsorption at 201 K agree with experiment within 0.7 or 2.2 kcal/mol for N_2 (depending on which experiment we compare to) and within 1.9 kcal/mol for O_2. The difference between binding enthalpies of N_2 and O_2 with increasing level of optimization is similar to the C_2H_6 and C_2H_4 case discussed in our earlier work.[31] In comparison, the energies of binding reported in Ref. 58 for N_2 and O_2 with Fe_2(dobdc) are respectively –1.7 kcal/mol and –21.0 kcal/mol, in much greater disagreement with experiment than the present values. It can also be seen from

Table 2.7 that for any level of optimization, the difference between ΔE and ΔH is not more than 1 kcal/mol.

As expected, adsorption of the guest is accompanied by a decrease in entropy. Table 2.7 also shows the Gibbs free energy of adsorption, ΔG, which takes into account the entropy change upon adsorption. By comparing the enthalpy and free energy values at 298 K, we see from Table 2.7 that entropy decreases more for O_2 adsorption than for N_2 adsorption. Thus, in the most complete calculations (i.e., the //B-opt6 ones), the O_2 enthalpy of adsorption is 4.0 kcal/mol more favorable than that of N_2, but the free energy of adsorption is only 1.6 kcal/mol more favorable than that of N_2. This is a classic case of enthalpy–entropy compensation. The stronger binding of O_2 compared to N_2 leads to higher frequencies for most of the vibrations in the adduct and therefore a more negative entropy change, which (in the free energy) cancels part of the favorable binding energy. It is interesting that the differences of ΔH and ΔG from ΔE do not change greatly upon improving the calculation from //B-opt1 to //B-opt6; that gives us some confidence that the vibrational contributions are reasonably well converged. The free energy of adsorption is found to be negative for the O_2 and positive for N_2; a positive standard-state free energy change implies that formation of the complex is not a spontaneous process under standard-state conditions at room temperature.

As one goes from //B-opt0 to //B-opt1 to //B-opt6, the binding energies do not change significantly, and hence we use the computationally less expensive //opt0 structures for rest of the analysis in this work.

Table 2.7 Standard-state energies,[a] enthalpies,[b] and Gibbs free energies[c] of binding (in kcal/mol) of O_2 and N_2 with the 88-atom cluster model of Fe_2(dobdc) Computed using three levels of optimization by M06/def2-TZVP.

System	M_S (3 Fe, X_2)	//B-opt0			//B-opt1				//B-opt6			
		ΔE	ΔH_{201}	ΔH_{298}	ΔE	ΔH_{201}	ΔH_{298}	ΔG_{298}	ΔE	ΔH_{201}	ΔH_{298}	ΔG_{298}
Fe–N_2	222, 0	–8.5	–7.8	–7.5	–7.8	–7.0	–6.8	1.2	–8.5	–7.7	–7.5	0.5
Fe–O_2	222, 1	–8.7	–8.4	–8.2	–9.3	–8.9	–8.7	1.7	–12.0	–11.7	–11.5	–1.1
	222, 0	–2.0	–1.7	–1.5	–2.5	–2.1	–1.9	8.3	–4.2	–3.8	–3.7	6.6
	222, –1	–8.3	–7.6	–7.4	–7.5	–6.8	–6.6	2.8	–8.1	–7.4	–7.2	2.3

[a]The energies of binding were computed with respect to the energies of the separated reactants: $\Delta E = E$(host–guest) – E(host) – E(guest), where the host is the bare 88-atom

cluster and the guest is either N_2 or O_2. A negative sign means that adsorption of the guest molecule is exoergic.

[b]The enthalpies of binding were computed using eq 1 of Ref. 31. A negative sign means that adsorption of the guest molecule is exothermic.

[c]The Gibbs free energies of binding were computed with respect to the Gibbs free energies of separated reactants: $\Delta G = G(\text{host–guest}) - G(\text{host}) - G(\text{guest})$

Binding more than one adsorbate to the bare MOF structure. Both Figure 2.10 and Table 2.7 present results for the guest molecule bound only to the central iron atom of the 88-atom cluster of structure B. The three iron centers of the cluster open into different hexagonal channels of the MOF. It is interesting to see whether or not the binding of a guest molecule in one of the channels affects binding in other channels. Hence, we optimized additional guest molecules at peripheral iron sites of the cluster and calculated their energies and enthalpies of binding. The calculations were performed for the ground spin states (that were determined from Figure 2.10) by having one, two, or three guest molecules bound to either the peripheral iron atom or the central iron atom (Fe_a or Fe_b in Figure 1.2(a)), a peripheral iron atom and a central iron atom (Fe_a and Fe_b in Figure 1.2(a)), and all three iron centers (Fe_a, Fe_b, and Fe_c in Figure 1.2(a)), respectively. We refer to these structures as MOF(X_2), MOF(X_2)$_2$, and MOF(X_2)$_3$. While optimizing one or two guest molecules, we consider the centers *a* or/and *b* instead of *c* as these have more accurate environment(s) than *c* when compared to the experimental structure.

For MOF(N_2), we find that the energies and enthalpies of binding of an N_2 molecule at iron sites *a* or *b* are almost identical; the difference between the two binding sites is merely 0.1 kcal/mol (Table 2.8). For the MOF(N_2)$_2$ complex, the binding strength of two N_2 molecules at both iron sites *a* and *b* almost equals the sum of the binding at the two sites separately. The MOF(N_2)$_3$ complex that involves the binding of an N_2 molecule at every iron site of the cluster has binding energies and enthalpies that are three times that of either the MOF(N_2) (Fe_a) or the MOF(N_2) (Fe_b) complex. In MOF(O_2), the binding of a single O_2 molecule at iron sites *a* or *b* are almost identical to each other, which is similar to what was observed for the N_2 case (Table 2.8). Also, the binding enthalpies of two O_2 molecules simultaneously in

$MOF(O_2)_2$ (Fe_a, Fe_b) complex almost equals the sum of the binding enthalpies in $MOF(O_2)$ (Fe_a) and $MOF(O_2)$ (Fe_b) complexes, while the binding enthalpy of three O_2 molecules in $MOF(O_2)_2$ complex deviates from three times the binding enthalpy of a single O_2 molecule of either $MOF(O_2)$ (Fe_a) or $MOF(O_2)$ (Fe_b). This is due to the fact that the third metal site (Fe_c) deviates more from the experimental structure than the sites *a* or *b*, and the adsorbed O_2 unit on this site has one of the Fe–O distances significantly different from the other two sites. Hence, we can conclude that, as expected, the binding of guest molecules N_2 or O_2 on a given metal site has no significant effect on the binding of another guest molecule at a different metal site.

Since we found no significant cooperative effect at the //B-opt0 level, it is unnecessary to carry out more extensive optimization since if there is no effect at the //B-opt0 level, there is unlikely to be an important effect at higher levels of optimization.

Table 2.8 Energies[a] and enthalpies[b] of binding (in kcal/mol) of O_2 and N_2 with the 88-atom cluster model of Fe_2(dobdc) computed by M06/def2-TZVP.

System	site	ΔE	ΔH_{201}	$\Delta H_{298.15}$
$MOF(N_2)$	*a*	–8.4	–7.7	–7.4
$MOF(N_2)$	*b*	–8.5	–7.8	–7.5
$MOF(N_2)_2$	*a* and *b*	–16.8	–15.4	–14.9
$MOF(N_2)_3$	*a*, *b,* and *c*	–25.3	–23.2	–22.4
$MOF(O_2)$	*a*	–8.9	–8.6	–8.4
$MOF(O_2)$	*b*	–8.7	–8.4	–8.2
$MOF(O_2)_2$	*a* and *b*	–17.5	–16.8	–16.3
$MOF(O_2)_3$	*a*, *b,* and *c*	–24.2	–23.1	–22.3

[a]This table is based on //B-opt0 geometries. The energies of binding were computed with respect to the energies of the separated reactants: $\Delta E = E(MOF(X_2)_n - E(MOF) - nE(X_2)$.

[b]The enthalpies of binding were computed using eq 1 of Ref. 31.

Binding of O_2 to the distorted MOF structures. Next, the energies and enthalpies of binding for the low-temperature $MOF(O_2)$ complexes (structure L in Table 2.5) were analyzed. When O_2 is adsorbed on the MOF, various possible

scenarios may be imagined, including the four listed in Table 2.9; we will use the classification of Table 2.9 in the following discussion of the results.

Table 2.9 Possible scenarios for oxygen adsorbed on the MOF.

Case	Description
(a)	O_2 binds to every iron site with little or no charge transfer – resulting in an Fe(II)–O_2 complex.
(b)	O_2 binds to every iron site with an electron transfer to O_2 from the Fe(II) center – resulting in an Fe(III)–O_2^- complex.
(c)	O_2 binds to every other iron site with the transfer of two electrons from two Fe(II) centers (one from each) – resulting in Fe(III)–O_2^- complex at half the sites and Fe(III) at the other half (the high-temperature dosing scenario in Ref. 12).
(d)	O_2 binds to every iron site with the transfer of two electrons from each Fe(II) – resulting in an Fe(IV)–O_2^{2-} complex.

With the low-temperature MOF(O_2) structure as the starting structure, we performed //L-opt0–O_2 calculations for scenarios (a), (b), and (d) in the high-spin state. The initial spins for the three Fe and O_2 are (2,2,2; 1) for (a), (2,2.5,2; 0.5) for (b), and (2,2,2; 0) for (d), which correspond respectively to triplet O_2, doublet O_2^-, and singlet O_2^{2-} bound to the central Fe of the cluster. The results are in

Table 2.10. The (2,2,2; 1) and (2,2.5,2; 0.5) cases converged to the same solution. This also happens for the //B-opt0–O_2 cluster as shown in Table 2.6 (the first two rows under the MOF(O_2) section).

Table 2.10 shows that the binding enthalpy for this case turns out to be 24 kcal/mol, and the binding enthalpy for the (2,2,2; 0) case is 17 kcal/mol. Therefore, the predicted ground state is the (2,2,2; 1) structure. The (2,2,2; 1) case shows stronger binding than the (2,2,2; 0) case, even though greater amount of charge transfer occurs for the (2,2,2; 0) case (Table 2.11). This could potentially be due to the O_2 unit being farther from the iron center in the former case. The Fe–O_A, Fe–O_B, and O_A–O_B distances are respectively 2.10, 2.10, 1.28 Å for the (a/b) case and 2.07, 2.10, and 1.29 Å for case (d), both in excellent agreement with the low-temperature experimental values (Table 2.5), although the binding enthalpies for the two calculations show

significant deviation. Unlike the //L-opt0–O_2 calculations here, the binding enthalpies of //B-opt0–O_2 calculation (Table 2.7) give excellent agreement with experiments for the (2,2,2; 1) spin. Further analysis is provided in later paragraphs.

Table 2.10 Energies[a] and enthalpies[b] of binding (in kcal/mol) of MOF(O_2) complexes computed by M06/def2-TZVP.

Structure	Initial guess (Fe_a,Fe_b,Fe_c; O_2)		//opt0		
	Formal Charge	Spin	ΔE	ΔH_{201}	ΔH_{298}
L: Low-temperature MOF(O_2)	2, 2, 2; 0	2, 2, 2; 1	–24.5	–24.1	–24.0
	2, 4, 2; –2	2, 2, 2; 0	–17.5	–17.2	–17.0

[a]The energies of binding were computed with respect to the energies of the separated reactants: $\Delta E = E$(host–guest) – E(host) – E(guest), where host is the 88-atom cluster obtained after removal of O_2 and the guest is free O_2. A negative sign means that adsorption of the guest molecule is exoergic.

[b]The enthalpies of binding were computed using eq 1 of Ref. 31. A negative sign means that adsorption of the guest molecule is exothermic.

Comparing the Ground-State Structures to Experiment. Here we discuss only the ground-state structures of MOF(N_2) and a few low-energy structures of MOF(O_2). The experimental Fe–N and N–N bond distances at 100 K were reported to be 2.30 and 1.13 Å, respectively.[12] Our calculated values in //B-opt0 calculations are 2.41 and 1.09 Å, in only fair agreement with experiment. The Fe–N distances for the //B-opt1 and //B-opt6 structures were found to be 2.41 Å and 2.36 Å, respectively, with the latter showing significantly improved agreement with experiment and demonstrating that relaxing atoms of the MOF framework is necessary to get accurate metal–adsorbate distances. The N–N distances for these //B-opt1 and //B-opt6 calculations remain unchanged compared to the //B-opt0 calculation. The calculated Fe–N–N angle is 171 deg (//B-opt0), 172 deg (//B-opt1), or 170 deg (//B-opt6).

The converged S value (obtained by equating $S(S+1)$ to the expectation value of S^2 for the Slater determinant) is 6.01 (same for //opt0, opt1, and //opt6), which corresponds to an almost pure spin state, which is often the case for KS-DFT calculations on high-spin states.

The periodic calculations performed using PBE-D2 in Table 2.10 by Parkes *et al.*,[58] yielded an Fe–N–N angle of 169°, an N–N bond distance of 1.13 Å, and the

smallest Fe–N distance to be 1.99 Å. The Fe–N–N angle and the N–N bond distance of Ref. 58 agree well with the cluster calculations performed in this study for the ground spin state, but their Fe–N distance is much smaller than either our calculated value or the experimental value.

MOF(O_2) with the experimental bare MOF structure. Next, consider //B-opt0 calculations for MOF(O_2). The eleven initial guesses described in Table 2.6 for MOF(O_2) systems were tried, and they converged to the various structures shown in Table 2.6 and in Figure 2.10. The lowest-energy structure (the one with energy –8.7 kcal/mol) has high-spin Fe ferromagnetically coupled to triplet O_2 in a side-on but nonsymmetrical fashion, and the two Fe–O distances are 2.21 and 2.42 Å. In comparison, the experimental structure is more symmetrical, and the Fe–O distances are smaller, 2.10 and 2.09 Å. Optimization of atoms of the MOF framework decreases the two Fe–O distances, and for both //B-opt1 and //B-opt6 structures, one gets 2.09 and 2.17 Å, in fairly good agreement with the experimental values (the //B-opt6 value differs from the experiment by only 0.00–0.08 Å). The calculated O–O distance of 1.24 Å agrees with the experimental O–O distance of 1.25 Å within the experimental error bar. The O–O distances for the //B-opt1 and //B-opt6 structures were both found to be 1.27 Å, which also agree with the experimental value quite well.

The two equal Fe–O distances and the O–O distance reported in Table 2.7 of Parkes *et al*.[58] are 1.89 and 1.39 Å, respectively, which deviate quite significantly from the cluster calculations of the current study and from experiments.

The final calculated <*S*> values for the ground state of the MOF(O_2) complex are 7.01 (//B-opt0 and //B-opt1) or 7.00 (//B-opt6), again an almost pure spin state.

MOF(O_2) with the experimental low-temperature MOF(O_2) structure. The experimental low-temperature MOF(O_2) structure that has an Fe–Fe distance of 3.17 Å, an O–O distance of 1.25 Å, and Fe distances to the oxygen atoms of O_2 equal to 2.08 and 2.10 Å is proposed to fall in case (a) or case (b) described in Table 2.9. The Fe–O_A, Fe–O_B, and O_A–O_B distances are respectively 2.10, 2.10, and 1.28 Å for the lowest-energy structure obtained from (a) and (b) initial guesses. We note that the distances (in the same order) are 2.07, 2.10, and 1.29 Å for the second-lowest-energy

structure, which was obtained with a case (d) initial guess, and these are also in good agreement with experiment.

Nature of the Fe–Guest Interactions, Spin Populations, Charges, Vibrational Frequencies, and Bond Order Analyses. Next, we looked at the Hirshfeld spin densities, CM5 charges, vibrational frequencies of the guest molecules, and Mayer bond orders to gain insight into the nature of bonding between the guest molecules N_2 and O_2 and central metal of the MOF. The geometries used are: ground state //B-opt0, //B-opt0–N_2 in the three spin states shown in Figure 2.10(a), //B-opt0–O_2 for the ground spin state and two other higher-energy spin states shown in Figure 2.10(b), and //L-opt0, //L-opt0–O_2 for the two spin states shown in Table 2.10.

The Hirshfeld spin densities in Table 2.11 tell the number of unpaired electrons on the iron center and the adsorbed guest molecule. It can be seen that the iron center has approximately four unpaired electrons in the ground spin states of the bare cluster and of MOF(N_2) and MOF(O_2). The natural atomic orbital occupancies obtained from a natural bond order analysis of the //B-opt0, //B-opt0–N_2, and //B-opt0–O_2 systems gave the difference in occupancies of α and β spin orbitals as 3.65, 3.56, and 3.70 for the central iron atom, which is consistent with the Hirshfeld spin density calculations. The guest molecules N_2 and O_2 in these complexes were found to be singlet and triplet, respectively, from both the analyses.

Partial atomic charge calculations using CM5 show that the adsorption of N_2 on the central metal atom decreases the positive charge on iron and simultaneously increases the positive charge on N_2 indicating a transfer of electron density from N_2 to the MOF fragment. For the ground spin state and the next higher energy spin state of the two types of MOF(O_2) structures considered, an opposite trend is observed. The O_2 unit gains negative charge from the MOF fragment and at the same time causes the positive charge on the iron center to increase. The magnitude of the charge transfer involved in the O_2 case is larger than the N_2 case and this is a factor that could contribute to the higher binding strength of O_2 as compared to N_2; however, for the two MOF(O_2)//L complexes in Table 2.11, a higher binding energy is not associated with higher charge transfer. An interesting result in Table 2.6 (which list

all the spin states of //B-opt0-O_2) is that the converged electronic structures all have essentially neutral O_2. The partial atomic charge on the molecule is between +0.06 and –0.24 a.u. for a very high-energy structure, with the lowest-energy structure having a partial charge on O_2 of only –0.13 a.u.

The charge transfers we calculate in O_2 may be compared with the calculation of Maximoff and Smit.[59] We observe a transfer of 0.13 electrons to O_2, for the ground-state //L-opt0–O_2 and //H-opt0–O_2 complexes, with 0.08 coming from Fe and 0.05 from the rest of the MOF. Using a different density functional (with no Hartree–Fock exchange but with empirical changes in the Coulomb and exchange integrals), a different scheme for charge analysis, and optimizing the Fe–Fe distance (whereas we fix it), they obtain a charge transfer of 0.44 electrons to O_2, with 0.27 from Fe and 0.17 from the rest of the MOF. Local density functionals tend to overestimate charge transfer,[86] and the higher charge transfer in the previous calculation could be due to that factor.

The larger partial charge transfer in the case of O_2 relative to that in N_2 is consistent with the change in vibrational frequencies, which are also shown in Table 2.11. The calculated vibrational frequency of free N_2 is 2360 cm^{-1}, while that of the adsorbed N_2 in MOF(N_2) (ground spin state) is 2356 cm^{-1}, which is a reduction of only 4 cm^{-1}. On the other hand, the calculated vibrational frequency of free O_2 is 1636 cm^{-1}, while that of the adsorbed O_2 in //B-opt0–O_2 (ground spin state) is 1343 cm^{-1}, which is a reduction of 293 cm^{-1}. This indicates that upon adsorption the double bond of O_2 weakens more than the triple bond of N_2 due to a gain of antibonding electrons by O_2. The ground state //L-opt0–O_2 structure also shows a considerable drop in vibrational frequency of the O_2 unit. This is further illustrated by comparing the calculated bond orders for these complexes in Table 2.12.

The infrared spectrum reported in the experimental work[12] on oxygenated Fe_2(dobdc) shows bands at 1129, 541, and 511 cm^{-1} which were assigned to O–O, Fe–O_2, and Fe–O_{linker} stretches, respectively. The MOF(O_2) //opt6 calculations predict that the O–O band is at 1286 cm^{-1}, and the Fe–O_{linker} band is around 500 cm^{-1}, but the Fe–O_2 band is at less than 350 cm^{-1}. Unlike the interpretation of the

experiments, our calculations predict that the Fe–O_{linker} and the Fe–O_2 bands are quite different. This could be expected based on the fact that the natures of the Fe–O_{linker} and Fe–O_2 bonds are quite different.

If we compare the spin populations, charges, and vibrational frequencies of MOF(O_2)//B MOF(O_2)//L complexes, we find that quite different values for these quantities are obtained. This difference is also reflected in the binding enthalpies.

Table 2.11 Hirshfeld spin densities (in atomic units), CM5 atomic charges (in atomic units), and vibrational frequencies (cm^{-1}) for the MOF(N_2) and MOF(O_2) complexes computed by M06/def2-TZVP.

System	M_S	Energy (kcal/mol)	Spin density		Charge		Vibrational frequency
			Fe_b	X1 + X2[a]	Fe_b	X1 + X2[a]	X_2
separated N_2	0	0.0	NA	0.00	NA	0.00	2360
separated O_2	1	0.0	NA	0.00	NA	0.00	1636
experimental bare MOF structure							
bare MOF	6	0.0[b]	3.69	NA	0.68	NA	NA
MOF(N_2)	6	–8.5[b]	3.69	0.02	0.66	0.08	2356
	5	25.8	1.94	0.03	0.59	0.09	2358
	4	34.1	0.02	–0.001	0.64	–0.03	2301
MOF(O_2)	7	–8.7[b]	3.93	1.65	0.76	–0.13	1343
	6	–8.3	3.92	–0.34	0.81	–0.24	1231
	5	–2.0	3.62	–1.88	0.63	0.08	1585
experimental low-temperature-dosing MOF(O_2) structure							
bare MOF	6	0.0[b]	3.67	NA	0.70	NA	NA
MOF(O_2)	7	–24.5[b]	4.08	1.43	0.88	–0.27	1264
	6	–17.5	4.11	–0.59	0.91	–0.32	1256

[a]X = O or N, and X1 and X2 are the two atoms of the X_2 molecule. NA denotes not applicable.

[b]GS denotes the ground state.

In Table 2.12, Mayer bond orders for the MOF(N_2) and MOF(O_2) complexes were calculated for the same spin states that were discussed in the CM5 charge analyses. In these complexes, N1 and O1 are those atoms of the guest molecules N_2 and O_2 that are closer to the iron center than the atoms labeled N2 and O2. We can see that the Fe–N1 bond order of MOF(N_2) is weaker than the Fe–O1 bond orders of the MOF(O_2) structures in their ground spin states. The Fe–N2 bond order being close to zero for M_S = 6 and 5 indicates that the interaction with the distant N atom has no

covalent component. Furthermore, the bond order of the N_2 molecule decreases only slightly, in particular from 3.03 in free N_2 to 3.00 or 2.91 when bound to the cluster. This indicates that N_2 is hardly perturbed upon adsorption. On the other hand, the bond order of the O_2 molecule decreases from 2.03 in free O_2 to 1.69 and 1.53 for the ground spin state of //B-opt0–O_2 and //L-opt0–O_2 clusters, indicating that the O_2 unit is destabilized upon adsorption.

Table 2.12 Mayer bond order computed using M06/def2-TZVP (X = O or N, where X1 is closer to the metal center than X2).

X	M_S		MOF(X_2)			Free X_2[a]
			Fe_b–X1	Fe_b–X2	X1–X2	X1–X2
experimental bare MOF structure						
N	6	GS[b]	0.26	0.03	3.00	3.03
	5		0.28	0.03	3.00	
	4		0.63	0.13	2.91	
O	7	GS[b]	0.40	0.34	1.69	2.03
	6		0.72	0.25	1.55	
	5		0.23	0.06	1.96	
experimental low-temperature-dosing MOF(O_2) structure						
	7	GS[b]	0.49	0.48	1.53	
	6		0.47	0.49	1.53	

[a]The bond orders are calculated by NBO analysis for singlet N_2 and triplet O_2.

[b]GS denotes the ground state.

For comparison with MOF(O_2), we carried out calculations on dioxygen anion and potassium superoxide. The calculated bond order and bond distance of free O_2^- were found to be 1.54 and 1.33 Å, respectively, and for the O_2 unit in KO_2 they were found to be 1.47 and 1.30 Å, respectively. This shows that the O_2 unit in KO_2 is very similar to free O_2^-. The CM5 charge of O_2 unit of KO_2 is –0.90 a.u. Since KO_2 is reasonably interpreted as an ionic linking of K^+ and O_2^-, a calculated CM5 charge of approximately –0.90 a.u. on O_2 in MOF(O_2) would suggest that an essentially complete transfer of an electron from the Fe(II) center to O_2 has occurred, leading to an Fe(III)–O_2^- complex.

Table 2.13 Comparison of bond distances, Mayer bond orders, and CM5 charges on the dioxygen units.

Structure	Source	O–O distance (Å)	Bond order (unitless)	charge (a.u.)
free O_2	present[a]	1.19	2.03	0.00
O_2^-	present[a]	1.33	1.54	–1.00
KO_2	present[a]	1.30	1.47	–0.90
MOF(O_2)//B	present[a]	1.27	1.69	–0.13
MOF(O_2)//L	present[a]	1.28	1.53	–0.27
	Experiment[b]	1.25		

[a]M06/def2-TZVP.

[b]The experimental value is taken from Ref. 12.

Table 2.13 summarizes various findings discussed above regarding the state of the oxygen molecule. We find that the O_2 unit bound to the MOF has a bond order and bond distance that lie between free O_2 and free O_2^- (or, equivalently, between free O_2 and the O_2^- unit of KO_2), and this indicates that less than an electron is transferred from the iron center to adsorbed O_2. This is corroborated by a CM5 charge of –0.13 a.u. on O_2 in the ground state MOF(O_2) structures, which is much less than –0.90 a.u. Curiously, although both quantities in the MOF are intermediate between free O_2 and O_2^-, the bond order is closer to that of O_2^-, whereas the CM5 charge is closer to that of free O_2. The experiments were interpreted as involving some oxidation of Fe to Fe(III) by transfer of an electron to O_2. We, therefore, emphasize here that, even though we started the SCF iterations with charge transferred states (see Table 2.6), we found no evidence for a state with full O_2^- character (see Table 2.11).

Next, we analyzed the orbital energies of the //B-opt0, //B-opt0–N_2, and //B-opt0–O_2 structures. First, we compared the canonical orbital energies (in eV) of highest occupied molecular orbitals (HOMOs) and lowest unoccupied molecular orbitals (LUMOs). All the three systems were found to have an α-HOMO and a β-LUMO. The (α-HOMO, β-LUMO) energies of bare MOF, MOF(N_2), and MOF(O_2) are (–4.91, –2.32), (–4.90, –2.29), and (–4.95, –3.31), respectively. This shows that the adsorption of O_2 on the MOF changes the α-HOMO energy by only a small

amount but causes a more significant change in the β-LUMO energy, while the adsorption of N_2 causes a negligible change in both the α-HOMO and β-LUMO energies. Second, we considered the natural atomic orbital energies of the *d* orbitals of the central iron atom (to which the guest molecule binds), and we find that they show larger fluctuations with the adsorption of O_2 than with N_2. Both these analyses show that O_2 perturbs the orbital energies more than N_2 does, and this indicates that it interacts more strongly with iron.

2.4.3 N_2/CH_4 Separation

A molecular orbital picture can be used to predict selective adsorption of N_2 over CH_4 with V-MOF-74. The model exploits the square-pyramidal coordination geometry of the metal in desolvated M-MOF-74 (Figure 2.11d). A key consideration is the d^3 electronic configuration of V(II). In the case of N_2 binding, our DFT calculations show that a three-center bond is formed between the framework oxo ligand *trans* to dinitrogen, the metal, and N_2 (Figure 2.11d). Given an end-on coordination geometry, a pair of nonbonding electrons on N_2 and its respective *trans* framework atom interact with the V(II) d_z^2 orbital, and the net result is a three-center bond with two electrons each in a bonding and nonbonding orbital. In addition to the resulting σ bond, the unoccupied π^* orbitals of N_2 can accept back bonding electrons from the metal $d\pi$ orbitals. This back bonding is *not* present for methane, due to the lack of low-energy π^* orbitals on the hydrocarbon. The Fe(II), in contrast, has a high-spin d^6 electronic configuration with a singly occupied d_z^2 orbital. In this case, the two doubly occupied lone pairs provide four electrons to the three-center bond and the occupation of the metal d_z^2 orbital provides one electron, for a total of five electrons in the three-center bond; so, one electron is in the antibonding orbital. As the N_2 approaches the metal site, it thus experiences unfavorable σ anti-bonding plus additional exchange-repulsion from the occupied nonbonding orbital. Consequently, N_2 cannot approach the Fe(II) center close enough to experience π^* back-bonding stabilization as favorable as is present in the V(II)–N_2 system.

Next, we confirm the differential stabilization effect with DFT calculations, confirming our molecular orbital prediction that as-yet-unsynthesized V-MOF-74 could be used to separate N_2 from CH_4. We also reinforce our DFT results with

correlated wave function calculations to rule out the possibility of artificial back-bonding owing to the possible underestimation of the energy gap and the delocalization of *d* electrons in the DFT models. Finally, we analyze single-determinant Kohn-Sham reference functions to confirm the above explanation of the effect.

N_2 and CH_4 adsorption in V-MOF-74 and Fe-MOF-74. The key quantity we calculated is the differential adsorption energy defined by

$$\Delta E_{\text{ads}} = E_{\text{ads}}\left(\text{N}_2\right) - E_{\text{ads}}\left(\text{CH}_4\right)$$

where E_{ads} is the energy of adsorption (here defined as a positive number to denote that desorption is endoergic); thus ΔE_{ads} is more positive when N_2 binds more strongly. The results are in Table 2.14. Across all levels of theory and all models, CH_4 binding is comparable between the two metals, but N_2 is predicted to bind significantly more strongly than CH_4 to the coordinatively unsaturated metal site when the metal is V rather than Fe.

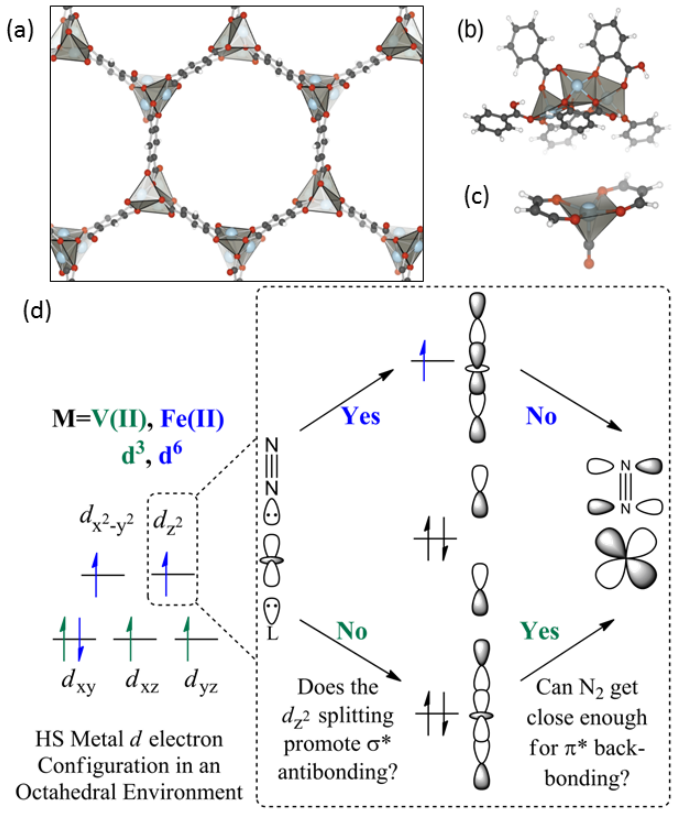

Figure 2.11 (a, b, and c) Structural models used in this work.
(a) Optimized periodic framework model, based on the symmetry of the experimental primitive cell. (b) 88-atom cluster. (c) Small model. Light blue, red, dark gray, and

white spheres represent vanadium, oxygen, carbon and hydrogen atoms, respectively. (d) Three-center bonding diagram between framework O atoms, the metal, and a guest. On the left we show the *d* subshell occupancy of Fe(II) in both blue and green; V(II) would have only three electrons (green alone) in the *d* subshell, and the metal d_z^2 orbital would be empty. On the right, the middle section shows how the d_z^2 orbital splits upon interacting with the four lone pair electrons of two axial Lewis bases; the occupancies shown are for Fe(II) – only four electrons would be present for V(II) because the d_z^2 orbital of V(II) is unoccupied. The right-most orbital diagram shows the nature of the interaction of the ligand unoccupied π* orbitals with the occupied *d*π orbitals of the metal; when the anti-bonding orbital is occupied, the ligand cannot approach the metal as closely, and this interaction is substantially weaker.

We noted above the consistent trend observed for calculated ΔE_{ads} values; the trends in calculated E_{ads} values are also consistent across the methods. Absolute adsorption energies for the 88-atom cluster and the periodic model are compared in Table 2.15. We see remarkable agreement between the adsorption energies calculated with the 88-atom cluster and with the periodic model and further remarkable agreement between the absolute binding energies calculated by DFT with different functionals and by WFT; the good agreement of results obtained with several methods that incorporate the physics in different ways adds confidence to the predictions. Inspection of Table 2.15 shows relatively large differences in the absolute binding energies between the large and small clusters. The enhanced attraction in the 88-atom cluster model can partially be attributed to greater medium-range correlation effects. One should also consider that the two models have different ligand coordination environments, and this too has an influence on the absolute binding energies.

Table 2.14 N_2/CH_4 adsorption energy differences (ΔE_{ads}) in kcal/mol.

Level of Theory	Small Model		Large Models[a]	
	V	Fe	V	Fe
DFT, vdW-DF2+U			6.0	0.4
DFT, vdW-DF2+U	4.9	0.4	5.8	0.3
DFT, M06-L	4.3	0.0	10.1	0.9
DFT, M06	4.5	0.1	6.9	0.4
DFT, M11-L	4.2	-0.8	5.9	-1.7
DFT, LPNO-CCSD/CBS	4.8	0.7	*b*	*b*
WFT, CASPT2 CP	3.8	0.3	2.1	0.3

[a]The first row is for the periodic model and the other large-model calculations are for the 88-atom cluster.

[b]Impractically computationally intensive.

Table 2.15 Absolute binding energies in kcal/mol.

	V–N_2	**Fe–N_2**	**V–CH_4**	**Fe–CH_4**
Periodic Model				
vdW-DF2+U	13.4	6.6	7.4	6.3
88-atom Cluster				
vdW-DF2+U	12.0	4.5	6.2	4.2
M06-L	19.9	7.8	9.8	6.9
M06	17.5	8.1	10.6	7.7
M11-L	13.4	4.4	7.5	6.1
CASPT2 CP	7.4	3.3	5.3	3.0
Small Model				
vdW-DF2+U	8.5	3.2	3.6	2.9
M06-L	9.1	4.3	4.8	4.3
LPNO-CCSD/CBS	9.6	4.2	4.8	3.6
CASPT2 CP	6.5	3.3	2.7	3.0

To further verify the validity of these predictions, isosteric heats of CH_4 and N_2 adsorption in Fe_2(dobdc) were obtained experimentally from adsorption isotherms at 175 K. As seen in Figure 2.12, the uptake of N_2 in Fe-MOF-74 is relatively steep and approaches one N_2 molecule per iron cation site at 1 bar and 175 K. Methane uptake, while similar at low pressure, reaches a higher value of approximately 1.5 CH_4 molecules per iron at 1 bar. These plots yield isosteric heats of adsorption for methane and dinitrogen that are both relatively low and quite similar; in particular, they are 5.3±0.2 and 5.5±0.2 kcal/mol, respectively, which yields an experimental difference of 0.2±0.3 kcal/mol. These results differ from the previously reported values of 4.8 kcal/mol for CH_4[10] and 8.4 kcal/mol for N_2[12] both because of the lower temperature and because of the change in experimental procedure; the present results should be more accurate for the difference because they were done with isotherms at the same temperature on the exact same batch of sample. An attempt to obtain the same information for V-MOF-74 was not successful.

Experimental *enthalpies* of adsorption should not be compared directly to the *energies* of adsorption in Table 2.15. For the 88-atom cluster, however, we computed the enthalpies of adsorption at 175 K by a formula given previously.[31] The M06-L, M06, and M11-L levels of theory give predicted differences in adsorption enthalpy of 1.1, 0.5, and -1.6 kcal/mol, respectively. The average difference in predicted

adsorption enthalpy of 0.0 kcal/mol is in good agreement with the 0.2 kcal/mol difference observed experimentally.

Structural parameters, vibrational frequencies, and charges. Table 2.16 shows that the M–N distance is shorter in V-MOF-74 than in Fe-MOF-74, as anticipated above; there is also a smaller difference in the M–C distances for CH_4. Neutron powder diffraction experiments on Fe-MOF-74 at 10 K indicate excellent agreement between the calculated and experimentally observed structures of methane bound to Fe^{2+}. Specifically, the Fe–C distance of 2.98(1) Å is very close to the distance of 2.96 Å calculated for the 88-atom cluster. Differences in M–N distances are consistent with the energetic results presented above.

The potential energy curves (given in Figure 2.13) provide further evidence for qualitatively different kinds of interaction; we give just one example, the interaction of N_2 with M in the small model, calculated by M06-L. Single-point energies were calculated by modifying the M–N_2 distance, but keeping all other geometrical parameters unchanged from the geometric minima. Interestingly, the predicted interaction energy at 2.8 Å is nearly equivalent for N_2 with the Fe and V small models. At an M–N distance of 2.8 Å, the interaction energy is ~–4 kcal/mol for both V and Fe. As N_2 approaches more closely, the potential energy reaches a minimum of –4.3 kcal/mol at 2.73 Å for Fe, but it goes to a much deeper well at –9.1 kcal/mol at 2.21 Å for V. (This further reinforces the conclusion that the binding interaction to vanadium is quite different from that of other metals studied.) For comparison, the Fe–N distance was determined to be 2.30 Å for N_2 adsorbed within Fe-MOF-74 by neutron diffraction experiments at 9 K.[87] The predicted Fe–N distance for the 88-atom cluster compares favorably with the measured value of 2.30 Å.

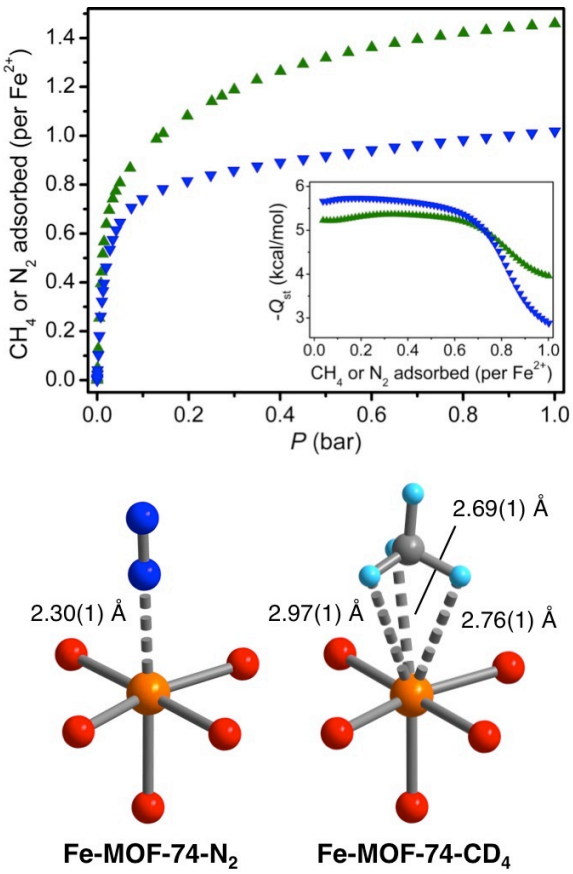

Figure 2.12 Adsorption of methane and dinitrogen in Fe_2(dobdc).
(Upper) Adsorption of methane (green) and dinitrogen (blue) in Fe_2(dobdc) at 175 K. (Upper Inset) Isosteric heats of adsorption. (Lower) The first coordination spheres for the iron centers in the solid-state structures obtained upon dosing Fe-MOF-74 with dinitrogen or methane; orange, red, blue, gray, and light blue represent iron, oxygen, nitrogen, carbon, and deuterium, respectively.

The N–N stretching frequency is a probe of back bonding, because these shifts result from weakening the bond by $d\pi \rightarrow \pi^*$ back donation. The periodic vdW-DF2+U calculations show that, as compared to the isolated gas-phase diatomic vibrational frequency (2415 cm^{-1}), N_2 bound to V experiences a significant shift in the N–N stretch (–102 cm^{-1}), whereas N_2 bound to Fe shows a negligible change (–6 cm^{-1}). In contrast, the vibrational frequency shifts for C–H modes in CH_4, where no back bonding is predicted, are negligible. For the 88-atom cluster, M06 calculations for N_2 bound to MOF show similar trends—a 103 cm^{-1} shift for V and a 4 cm^{-1} shift for Fe; M11-L also shows similar shifts: 101 and 5, respectively. Table 2.16 shows a more

complete set of results for M06-L; and these too are consistent with our analysis

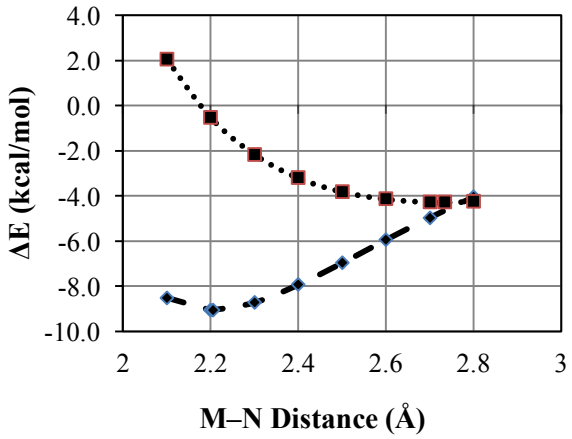

Figure 2.13 Potential energy curve as a function of M–N_2 distance.
The curve is for the small model calculated with the M06-L exchange–correlation functional. The curve for M = V(II) is shown as a dashed line with diamond points indicating single-point energies. The curve for M = Fe(II) is shown as a dotted line with square points indicating single-point energies.

Next, we examine in more detail the amount of charge transfer between the metal and the N_2 guest. Key charges in atomic units are given in Table 2.16.

Table 2.16 M06-L bond distances, adsorbate frequencies, and partial atomic charges.

	Gas phase	**Small model**		**88-atom cluster**	
		V	**Fe**	**V**	**Fe**
		Structural descriptors: binding N_2			
M-N (Å)	-	2.21	2.73	2.08	2.34
ν_{N-N} (cm^{-1})	2424	2357	2430	2252	2360
		Structural descriptors: binding CH_4			
M-C (Å)	-	3.00	3.15	2.77	2.96
ν_{C-H} (cm^{-1})	3057	3037	3043	3017	3031
		Partial atomic charges: bare MOF			
M	-	0.90	0.69	0.81	0.69
		Partial atomic charges: binding N_2			
M	-	0.89	0.66	0.88	0.70
N_2	0.00	0.01	0.07	-0.09	0.09
		Partial atomic charges: binding CH_4			
M	-	0.85	0.66	0.74	0.66
CH_4	0.00	0.06	0.03	0.05	0.08

The total charge on the guest molecule is computed by summing the partial charges of the individual atoms of the guest molecule; this indicates the magnitude and direction of charge transfer between the MOF and the guest. For each of the three

functionals, CM5 partial atomic charges for the 88-atom cluster indicate donation of negative charge from the central metal ion to the nitrogen molecule and an opposite direction of transfer for methane. This is also reflected in the charge on the metal ion being increased for N_2 adsorption and decreased for CH_4 adsorption when compared to the bare MOF. The increase or decrease in the positive charge of the central metal ion with N_2/CH_4 adsorption does not exactly equal the total charge on the guest molecule. This reflects charge change within the rest of the MOF framework.

We find that the direction of electron transfer from the metal center to the guest molecule for the Fe–N_2 system is *opposite* to what is observed for V–N_2. Specifically, the partial atomic charge on Fe is 0.66 in the presence of either N_2 or CH_4; these values are the same as the value of 0.66 for the bare Fe-MOF-74. The partial atomic charge on the V ions in V-MOF-74 is significantly higher in all structures, and it is not very sensitive to the adsorbates in the small model, but in the 88-atom cluster the partial atomic charge on the V increases by 0.07 upon adsorption of N_2 and decreases by 0.07 upon adsorption of CH_4. Overall these changes are consistent with our interpretation of increased back bonding in the V–N_2 case.

2.5 Concluding Remarks

An 88-atom model and a 106-atom model of a well-known MOF, Fe-MOF-74, were introduced based on its experimental crystal structure. These two models were used to investigate the properties of Fe-MOF-74 and its binding to C1–C3 hydrocarbons with the M06-L density functional. The four high-spin states (222, $22\overline{2}$, $2\overline{2}2$, and $\overline{2}22$) of 88-atom model with three irons and one spin state (22222) of 106-atom model with five ions, in which each iron is in a local quintet state, were considered.

This study shows that magnitude of binding enthalpies for unsaturated hydrocarbons is higher than those for saturated hydrocarbons, which agrees with the experimental results. These binding enthalpies for a given hydrocarbon have similar values for the four spin states of 88-atom model considered in this study. NBO analysis showed that there exists weak electron donation from π-bonding orbital of ethylene and σ-bonding orbital of C–H bond of ethane to the 3*d* and 4*p* orbitals of the central Fe ion. The filled *d*-orbitals on the d^6 metal-center can share electrons with unsaturated hydrocarbons and hence contribute to stronger binding. However, the

bonding trends in all cases except acetylene also correlate with differences in estimates of the damped dispersion contribution, which is included implicitly in the M06-L functional.

The Fe_2(dobdc)–N_2 and Fe_2(dobdc)–O_2 complexes were investigated using cluster models carved from their corresponding experimental structures. The calculated ground spin states of the Fe–N_2 and Fe–O_2 interacting systems were found to have ferromagnetically coupled quintet Fe(II) sites bound to singlet N_2 or ferromagnetically bound to triplet O_2. The Fe–N and Fe–O distances optimized by density functional theory are in reasonably good agreement with experiments, being long by 0.06 Å for the former and by 0.00–0.08 Å for the latter. The density functional enthalpies of binding agree with experiment within about 2 kcal/mol for the ground spin states, and they are consistent with the experiment in that they predict that O_2 binds more strongly than N_2 to Fe_2(dobdc). For the Fe_2(dobdc)–O_2 complex, binding enthalpies were computed using two experimental structures, and it was found that calculations with the bare MOF structure gave good agreement with experiments. In the most complete calculations (i.e., the //opt6 ones in which we optimized the coordinates of the adsorbate, the Fe to which it is bound, and the first coordination shell oxygen atoms of the iron ion), the O_2 free energy of adsorption was found to be 1.6 kcal/mol more favorable than that of N_2. The free energy difference between N_2 and O_2 is much less than the enthalpy difference due to enthalpy–entropy compensation. Binding of more than one guest molecule was studied for the Fe–N_2 and Fe–O_2 interacting systems, and it was found (for their ground spin states) that binding at one metal site does not significantly affect binding at the other metal site.

Our calculated vibrational spectrum shows that the Fe–O_{linker} band is around 500 cm^{-1}, but the Fe–O_2 band is at less than 350 cm^{-1}, whereas the experiments were interpreted as having an Fe–O_2 band at 541 cm^{-1}, which is not compatible with our theoretical prediction.

The difference in the enthalpies of binding of the two guest molecules was rationalized in terms of charge transfer, bond order, vibrational frequencies, and orbital energies. It is especially noteworthy that whereas binding of N_2 involves charge transfer of 0.08 electrons from N_2 to the MOF (0.02 to Fe and 0.06 to the rest

of the MOF) and lowers the vibrational frequency of the adsorbate by only 4 cm^{-1}, adsorption of O_2 involves transfer of 0.13 electrons from the MOF to O_2 (0.08 from Fe and 0.05 from the rest of the MOF) and lowers the vibrational frequency of the adsorbate by 293 cm^{-1}. Experimentally[88] the O_2 frequency is observed to drop even more, 426 cm^{-1} from 1555 down to 1129 cm^{-1}. The partial charge transfer in the O_2 case is also demonstrated by calculating Mayer bond orders for the two complexes; we find that the decrease in N–N bond order of N_2 upon adsorption is negligible compared to the decrease in O–O bond order of O_2 upon adsorption. The canonical orbital energies of α-HOMO and β-LUMO of the bare MOF were found to be affected more upon adsorption of O_2 than N_2. However, none of our calculations show evidence for the superoxide structure inferred experimentally.

The binding of N_2/CH_4 was investigated on V-MOF-74 and Fe-MOF-74, and we predict that nitrogen separation from methane can be effected by the as-yet-unsynthesized V-MOF-74, because the vanadium ions in this MOF have their interaction energies significantly increased by π back bonding with N_2, but not with CH_4. This provides a new M-MOF-74 target as a challenge to synthesis. Our qualitative analysis is placed on a quantitative footing by a variety of density functionals and wave function calculations of relative binding energies, using models validated against experimental binding energies for the analogous Fe-MOF-74.

3 Catalysis

3.1 Synopsis

The catalytic properties of the metal–organic framework Fe_2(dobdc), containing open Fe(II) sites, include hydroxylation of phenol by pure Fe_2(dobdc) and hydroxylation of ethane by its magnesium-diluted analogue, $Fe_{0.1}Mg_{1.9}$(dobdc). The latter reaction has been proposed to occur through a redox mechanism involving the generation of an iron(IV)–oxo species, which is an intermediate that is also observed or postulated (depending on the case) in some heme and non-heme enzymes and their model complexes. Here, we present a detailed mechanism by which the catalytic material, $Fe_{0.1}Mg_{1.9}$(dobdc), activates the strong C–H bonds of ethane. Kohn–Sham density functional calculations have been performed to characterize the electronic structure of key species. We show that the catalytic non-heme-Fe hydroxylation of the strong C–H bond of ethane proceeds by a quintet pathway after the formation of highly reactive iron–oxo intermediate. The mechanistic pathway involves three key transition states, with the highest activation barrier for the transfer of oxygen from N_2O to the Fe(II) center. The uncatalyzed reaction, where nitrous oxide directly oxidizes ethane to ethanol is found to have an activation energy of 280 kJ/mol, in contrast to 82 kJ/mol for the slowest step in the iron(IV)–oxo catalytic mechanism. The energetics of the C–H bond activation steps of ethane and methane are also compared. Dehydrogenation and dissociation pathways that can compete with the formation of ethanol were shown to involve higher barriers than the hydroxylation pathway.

3.2 Introduction

The rich chemistry and biology exhibited by high-valent iron–oxo intermediates of heme and non-heme enzymes[89,90,91,92] have generated considerable interest. The ability of enzymatic catalysts to oxidize methane to methanol under mild conditions without subsequent further oxidation to CO_2 has inspired a host of synthetic biomimetic catalysts. Much of the synthetic effort has been dedicated toward characterization of synthetic non-heme iron(IV)–oxo intermediates that can activate strong C–H bonds of alkanes and efficiently convert them to useful compounds such as hydroxylated alkanes or alkenes. However, the synthesized mononuclear

complexes[93,94,95,96,97,98,99] tend to have an $S = 1$ intermediate spin (IS)[100,101,102,103] iron(IV)–oxo unit, which is in contrast to the enzymatic catalysts, which exhibit a high-spin (HS) ground state ($S = 2$) iron(IV)–oxo[104,105,123] unit. Kohn-Sham density functional calculations and simulations[102,106,107,108,109,110,111,112] are consistent with most non-heme Fe(IV)–oxo complexes possessing an $S = 1$ spin state, but with catalysis proceeding on the excited quintet surface that involves a smaller barrier. This has generated interest in designing synthetic materials that have a quintet ground spin state with catalysis proceeding entirely on the quintet surface with an activation barrier that makes the reaction feasible. Two approaches have been used to target such high-spin species, namely: (i) the use of weak-field ligands in an octahedral environment, and (ii) the utilization of ligands that enforce trigonal bipyramidal geometry. An example of the first approach is the compound $[Fe^{IV}O(H_2O)_5]^{2+}$,[95] which has an $S = 2$ ground spin state and a half-life of only 7 s at 25 °C.[113] Theoretical analysis of this complex indicated that substitution of some of these water molecules by a strong-field ligand can lead to a triplet spin state.[114] This confirms that, as usual, the electron donor properties of ligands surrounding the metal center play an important role in determining the ground spin state. In addition to the ligand donor properties, the geometry of the compound also plays a significant role in determining its spin state. For example, the trigonal bipyramidal iron–oxo complex $[Fe^{IV}(O)(TMG_3tren)]^{2+}$ (TMG_3tren = tris(2-(tetramethylguanidino)ethyl)amine) also has a quintet spin state, as indicated by Mössbauer spectroscopy.[115] However, this complex exhibited reactivity similar to $S = 1$ iron(IV)–oxo complexes, perhaps owing to the steric bulk of the TMG_3tren ligand that diminishes access to the iron(IV)–oxo unit for oxidation reactions.[116,117]

Metal–organic frameworks (MOFs) with coordinatively-unsaturated iron centers surrounded by weak-field oxygen-based ligands are promising scaffolds for accessing high-spin non-heme iron(IV)–oxo intermediates. Here, the porosity of the structure, along with the constraints on the ligand environment imparted by the extended framework, prevent steric hindrance at the iron(IV)–oxo units and provide easy access for reactivity. Recently, it has been shown that oxidation of an MOF with open iron(II) sites by nitrous oxide generates an intermediate, proposed to be a high-spin non-heme iron(IV)–oxo, which can activate the strong C–H bonds of ethane.[26]

Previous theoretical mechanistic studies[108,109] on the reactivity of non-heme iron(IV)–oxo intermediates have shown that all three spin states (S = 0, 1, 2) of the intermediate participate in C–H bond activation. Even if the S = 2 state of the iron(IV)–oxo species is energetically less favorable than the S = 1 state, the S = 2 transition state for C–H bond activation may have a lower energy than the S = 1 transition state. Iron(IV)–oxo complexes exhibiting this behavior can be described as S = 1 reactants with a highly reactive S = 2 spin state.[99] This has been observed for hydroxylation reactions for a series of non-heme model complexes.[108,118] Kohn-Sham studies predict a spin-crossover between the S = 1 and S = 2 states, and the concept of two-state reactivity (TSR) has been used for understanding the mechanism of the reaction;[108,118,119,120,121] if the triplet-quintet energy gap of reactants is very small, the triplet ground state may pre-equilibrate with the higher-energy quintet state, and the reaction may proceed on the quintet surface. But if the triplet-quintet gap is larger, the spin-crossover and H-abstraction steps may occur in a concerted fashion. If one makes synthetic materials with weak ligand fields, the quintet state may be lower at both the reactant and the transition-state geometry, and the reaction may occur with single-state reactivity (SSR) on the quintet surface, thereby avoiding the complexity of needing spin inversion.

Once the C–H bond is activated and forms a radical of the substrate, competitive mechanistic pathways can be followed that lead to different products. For example, the hydroxylated product can be formed by an oxygen rebound mechanism, the desaturated product may be formed after another hydrogen atom abstraction, and other possible outcomes can occur due to dissociation of the radical.[122,123,124,125,126,127] The relative propensity for hydroxylation and desaturation processes is based on two mechanistic scenarios that can be followed after the first hydrogen atom transfer (HAT), which is accompanied by the formation of an Fe(III)–OH intermediate. Rearrangement of the radical-bound Fe(III)–OH intermediate leads to hydroxylation,[91] whereas abstraction of the second hydrogen atom from the substrate radical leads to desaturation.[128] The selection of the preferable pathway is based on electronic and steric inhibition of the rebound of the OH radical,[129] and under controlled conditions, desaturation leading to an olefin can compete with the hydroxylation of an aliphatic C–H bond.[130] It would be interesting to observe the possibility of such a competition in MOFs with Fe(IV)=O units. Hence, we also

investigate the three competitive pathways—hydroxylation, desaturation, and dissociation—that have been reported in various cases in the literature, although experimentally only hydroxylation has been observed[26] for the MOF studied here.

Because the intermediates involved in catalytic reactions can be difficult to observe, theory can and has played an important role in elucidating the atomic-level mechanisms of catalytic reactions.[131,132,133,134] Since the instability of synthetic Fe(IV)=O intermediates very often hinders their isolation and crystallographic characterization, Kohn-Sham calculations have played a prominent role in characterizing them, unraveling their properties, and shedding light on their mechanistic details. A lot of activity in this area has led to theoretical concepts that have been shown to be successful in rationalizing the Fe(IV)=O chemistry.[135] The chemistry has been explained within the framework of the following key concepts: (1) SSR vs. TSR, which delineates whether a spin change is required to access a surface with a lower activation barrier, (2) the exchange-enhanced reactivity (EER) principle,[136,137] which explains how exchange enhancement[138] of a high-spin pathway promotes its chemical reactivity, while the low-spin pathway will be less favorable due to exchange depletion, and (3) orbital-selection rules, which suggests the preferred geometry adopted by the key transition state for a favorable orbital overlap.

We use electronic structure calculations by employing Kohn-Sham density functional theory[35] to study the mechanism of a non-heme iron species that operates as a single-site catalyst supported by a MOF, in particular $Fe_{0.1}Mg_{1.9}$(dobdc), where $dobdc^{4-}$ denotes 2,5-dioxido-1,4-benzenedicarboxylate. This catalyst may also be described as a variant of Mg_2(dobdc) (also known as Mg-MOF-74) in which 5% of the Mg atoms are substituted by Fe. Previous experimental work[26] has shown that, using nitrous oxide (N_2O) as the oxidant, this system can catalyze ethane oxidation with the primary products being ethanol and acetaldehyde. Concomitant theoretical work indicated that the reaction is likely to proceed through a high–spin (quintet) iron(IV)–oxo intermediate. This work extends the iron(IV)–oxo chemistry, that was previously limited mainly to biological systems and their model complexes, to MOFs. Here we elucidate the full mechanism, compare the catalytic cycles for oxidation of ethane and methane, investigate competitive pathways that can compete with the formation of ethanol, and examine the uncatalyzed oxidation of ethane (Scheme 1).

Scheme 1. The three reactions investigated in this work. The complete catalytic cycle is studied for reaction (1), the C–H bond activation step is studied for reaction (2) and compared with the same step in reaction (1), and the direct uncatalyzed reaction (3) is also studied and compared to the catalyzed reaction (1).

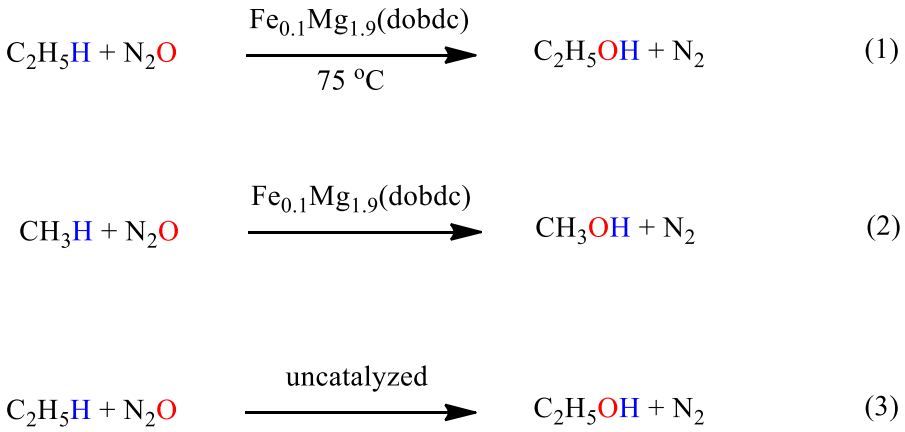

3.3 Methodology

The computational details of both periodic DFT and cluster calculations used in elucidating the mechanism of conversion of ethane to ethanol are described next.

Periodic calculations. A comparison of cell parameters, cell volume, and surface areas for Fe_2(dobdc), Mg_2(dobdc), and $Fe_{0.1}Mg_{1.9}$(dobdc), reported in Ref. 26 (see Supplementary Table 10 of Ref. 26), indicates that the catalytic material $Fe_{0.1}Mg_{1.9}$(dobdc) is closer to Mg_2(dobdc) (shown in Figure 3.1) than to Fe_2(dobdc). Hence, we used the experimetal structure of Mg_2(dobdc) as our starting point to perform periodic Kohn-Sham calculations and model the reaction of interest using a cluster model carved from this periodic structure.

Mg_2(dobdc)[139] (shown in Figure 3.1) was optimized using periodic boundary conditions with the PBE[60] exchange–correlation functional as implemented in the *VASP* software package.[76,77] Projector-augmented wave potentials were used to describe the interaction between core and valence electrons. A 2x2x2 *k*-point integration grid was used with a plane-wave kinetic energy cutoff of 520 eV. Ionic positions were relaxed with energy and force convergence criteria of 10^{-5} eV and 0.05 eV/Å, respectively.

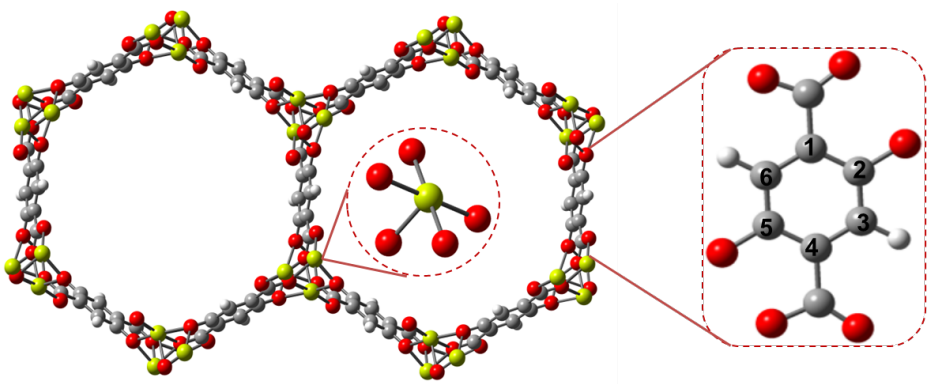

Figure 3.1. The extended structure of Mg_2(dobdc).
In the insets are the building blocks—pentacoordinate Mg(II) ion and the organic linker, $dobdc^{4-}$ ($dobdc^{4-}$ = 2,5–dioxido-1,4–benzenedicarboxylate). [Color code: light green = Mg, red = O, gray = C, and white = H]

Cluster Calculations. Because the catalytic reaction under study was observed in a MOF in which Fe is highly diluted by Mg, we assume that catalysis occurs at a single Fe site and does not require Fe–Fe interactions. Therefore, we model $Fe_{0.1}Mg_{1.9}$(dobdc) by a mixed-metal cluster in which the central metal site is Fe(II) and the other two metal sites are Mg(II); see Figure 3.2. An 88-atom neutral molecular cluster (with hydrogen atoms included to cap dangling valences and to make the cluster neutral) was carved from the periodic Kohn-Sham optimized structure of Mg_2(dobdc). This cluster has three Mg(II) ions and six organic linkers as shown at the top right of Figure 3.2, and the central Mg(II) ion was replaced by an Fe(II) ion as shown at the bottom of Figure 3.2. This mixed-metal cluster was used as the starting structure to determine the reaction intermediates and transition structures. Details of the design of the 88-atom cluster as a model for M_2(dobdc) (also known as M-MOF-74) and its validation have been addressed in previous studies.[26,31]

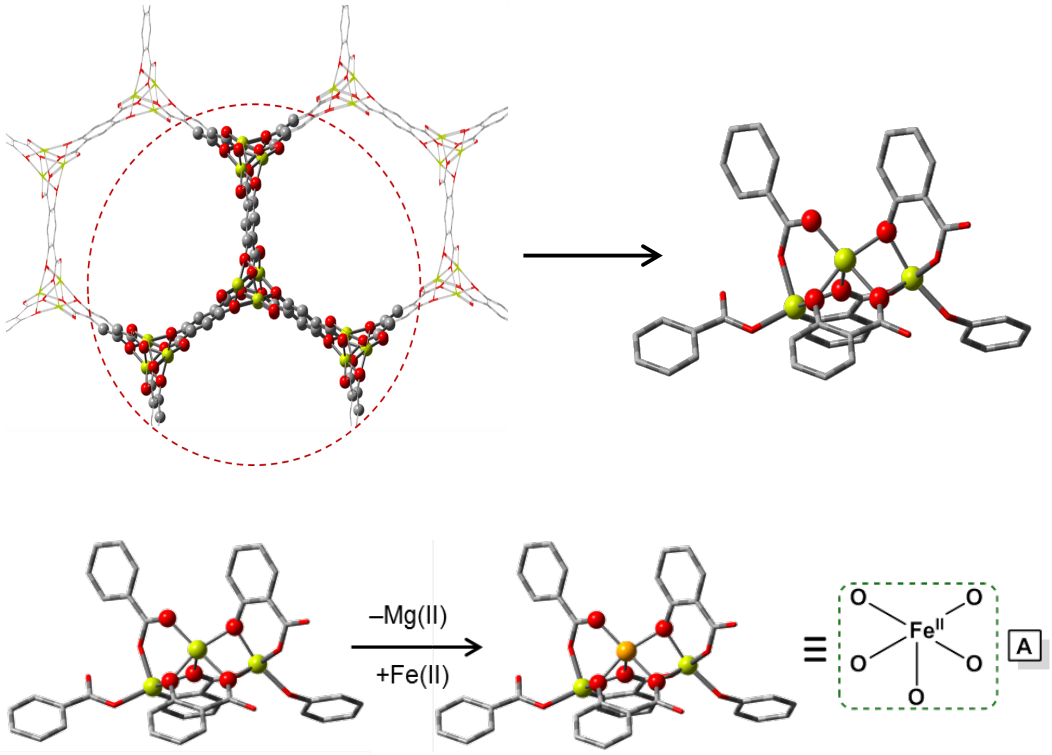

Figure 3.2 Cluster model of $Fe_{0.1}Mg_{1.9}$(dobdc).
Top: The cluster model of Mg_2(dobdc) carved from its extended structure. The atoms within the dotted circle of the extended structure on the left were truncated to obtain the molecular cluster shown on the right. This cluster has 88 atoms including three Mg(II) ions and six organic linkers. Bottom: The modification of the 88-atom cluster model of Mg_2(dobdc) (*left*) with three Mg(II) sites to obtain the mixed-metal cluster (*center*) that is representative of $Fe_{0.1}Mg_{1.9}$(dobdc) and is used for performing quantum mechanical calculations in this work. The first coordination sphere of this cluster is shown on the *right*. [Color code: orange = Fe, light green = Mg, red = O, and gray = C]. H atoms are omitted for clarity.

All Kohn-Sham cluster calculations were performed with the M06-L[140] exchange–correlation functional using the def2-TZVP[141] all-electron basis set. The *Gaussian 09* suite of quantum mechanical programs[75] was used for all Kohn-Sham cluster calculations. The density-fitting algorithm was used. The Kohn-Sham determinant was tested for stability and was relaxed to a stable solution using the *Stable = Opt* keyword of *Gaussian*. Geometry optimizations were constrained such that all atoms of the MOF portion of the cluster were kept fixed except for the iron atom and the five oxygen atoms composing its first coordination sphere. The atoms of the guest molecules (N_2O, C_2H_6, and their fragments) bound to or reacting with the iron atom of the cluster were always optimized without any constraints. Force constants were determined analytically in the optimized degrees of freedom, and

zero–point vibrational energy contributions were added to all energies to produce 0 K enthalpies. The enthalpies at 298.15 K were computed by M06-L/def2-TZVP by adding the zero–point energy and the thermal vibrational-rotaional entropy of the lowest-energy conformer in the quasiharmonic approximation, which corresponds to the harmonic oscillator-rigid rotator approximation with frequencies scaled by a factor of 0.976.[142] The transition structures were characterized by the presence of a single imaginary frequency along the reaction coordinate; all optimized intermediate structures were confirmed to have only real frequencies.

Spin densities were calculated from partial atomic charges determined by Charge Model 5 (CM5)[72] using the *CM5PAC*[73] package with a Hirshfeld population analysis[74] as input.

3.4 Results and Discussion

Catalytic Cycle for the Oxidation of Ethane. The proposed mechanism for the oxidation of ethane to ethanol is shown in Scheme 2. It involves four key steps with four transition state structures and seven intermediates. The four steps are (a) formation of an iron(IV)–oxo intermediate, (b) C–H bond activation of ethane by the iron(IV)–oxo intermediate, (c) the radical rebound to form ethanol, and (d) the release of ethanol. For every intermediate and transition structure, only the first coordination sphere around the Fe center and the guest molecule bound/reacting with it are shown in Scheme 2. The bare 88-atom mixed-metal cluster is labeled as species **A**. The enthalpy profile of the catalytic cycle is shown in Figure 3.3. In this profile, the numbers under each energy level correspond to $\Delta H_{298.15}$ (in kJ/mol) calculated with respect to the separated reactants (sum of the energies of bare cluster **A**, N_2O, and C_2H_6). These values are reported for the ground-state geometries of the ground spin state. The calculated ground spin state for the Fe(II) center is a quintet, for the Fe(III) center it is a sextet, and for the Fe(IV) center it is a quintet, although, the entire complex (intermediate or transition state (TS)) is always found to be a quintet state owing to the ethyl radical being anti-ferromagnetically coupled to the Fe(III) center.

It has been very often found in literature that the non-heme Fe(IV)=O model complexes have a triplet ground state, and during C–H bond activation catalyzed reaction the triplet surface crosses the quintet surface.[108,118,119] This crossing occurs in

those studies before the rate-determining step (which is usually the C–H bond activation step). It should be emphasized here that, in this work, the rate-determining step is the one that leads to the formation of the Fe(IV)=O intermediate and not the one that involves C–H bond activation (see Figure 3.3). Our calculations show that the triplet surface is much higher in energy than the quintet surface and crossing of the two spin surfaces does not occur at any point throughout the whole catalytic cycle. The reaction evolves entirely on the quintet (or the high-spin) surface. This high-spin state is relatively more stable in the present case than in the non-heme model complexes because the iron centers in the MOF are ligated by the oxygen donor atoms of weak-field ligands. Thus, the catalysis in the present case occurs on a single spin surface, i.e., the present catalyst exhibits single-state reactivity.

Scheme 2. The proposed mechanism for the oxidation of ethane to ethanol in $Fe_{0.1}Mg_{1.9}$(dobdc). The first coordination sphere of the 88-atom cluster is shown along with the guest species bound to it.

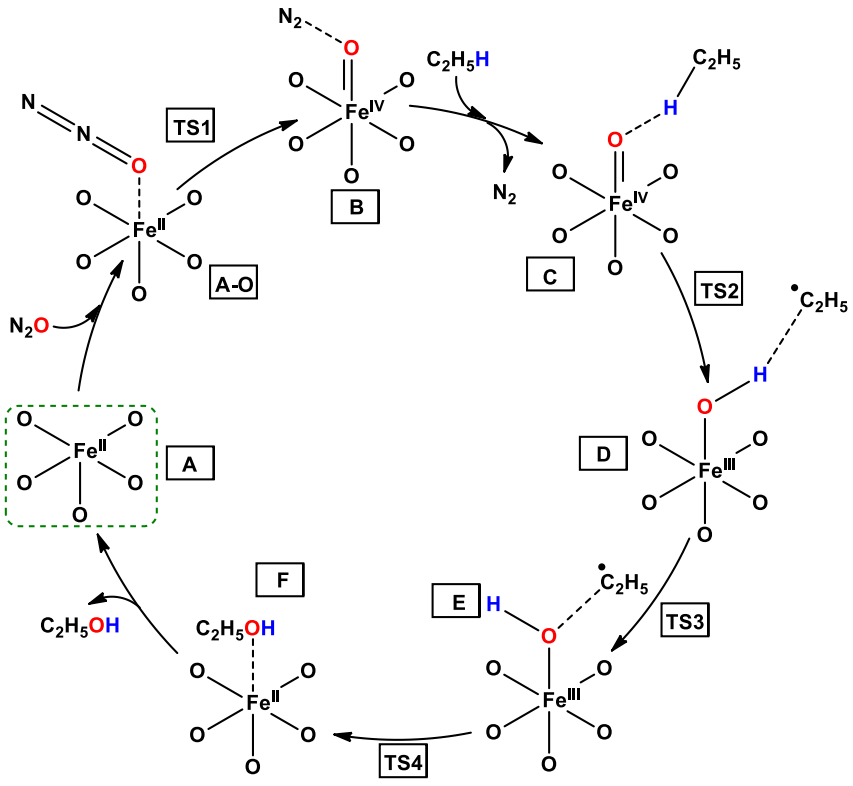

(a) ***Iron(IV)–oxo formation.*** The first step of the catalytic oxidation reaction is the adsorption of an N_2O molecule on the uncoordinated Fe(II) site (Scheme 2) of $Fe_{0.1}Mg_{1.9}$(dobdc) (represented by cluster **A**). Structure **A** possesses a high-spin (S =

2) Fe(II) center, with an open site in its first coordination sphere. The $S = 2$ spin state for Fe_2(dobdc) was verified by magnetic susceptibility measurements performed on the activated framework[10] and by theoretical calculations[27] and has been confirmed for the mixed Fe/Mg MOF in the current work.

Experimentally it has been found that N_2O binds to **A** yielding two connectivity isomers resulting in the η^1-O (represented by **A–O** in Scheme 2) and the η^1-N (not shown in Scheme 2) coordination modes. [26] A bent Fe–O–N angle in the case of **A–O** and a bent Fe–N–N angle in the case of **A–N**, in both cases ~120°, are observed from powder neutron diffraction, which was also supported by M06-L and M06[140] calculations in the same work.[26] Both neutron diffraction experiments and Kohn-Sham calculations predict the two binding modes to have similar stabilities. Neutron diffraction experiments predicted the η^1-O coordination to be favored (60%) over the η^1-N coordination (40%),[26] while M06-L calculations of this work predict the η^1-N coordination to be 7 kJ/mol lower in energy than the η^1-O coordination mode.

In the proposed mechanism, the adsorption of N_2O *via* the η^1-O coordination mode (forming species **A–O**) is followed by the formation of an iron(IV)–oxo intermediate (**B**), which occurs through the cleavage of the N–O bond of N_2O and the subsequent release of N_2 molecule. The transition structure for the release of N_2 to form **B** (**TS1**) has an O–N–N angle of 136° that strongly deviates from the linearity (180°) observed in gaseous N_2O (Figure 3.3). The activated O–N bond is elongated from 1.18 Å in free N_2O to 1.49 Å in **TS1**.

In the complete enthalpy profile is shown in Figure 3.3, **TS1** is the highest-energy stationary point, and it is associated with the rate-determining step of the reaction; it is found to have an enthalpy of activation of 82 kJ/mol. When this barrier is surpassed, intermediate **B** is reached. This step, that corresponds to the formation of iron(IV)–oxo intermediate, is highly exothermic (ΔH for **A** $\rightarrow$ **B** is = –108 kJ/mol).

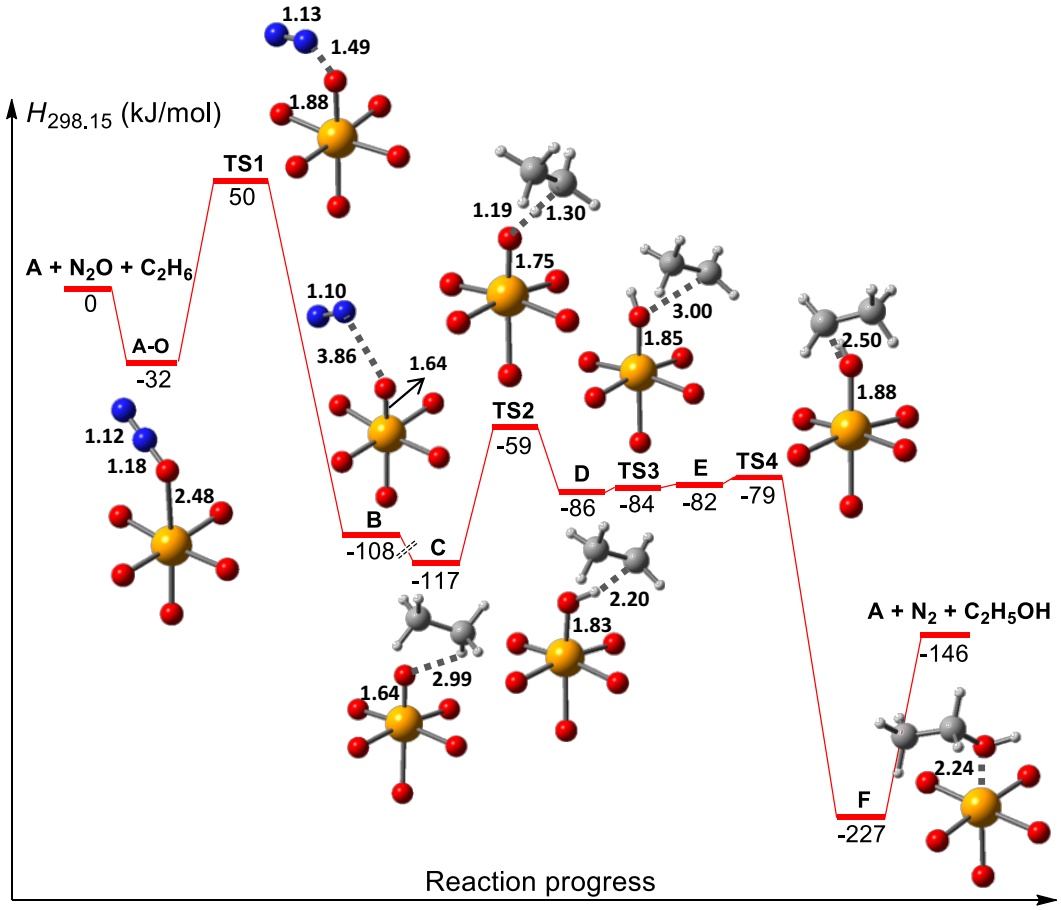

Figure 3.3 Enthalpy profile of the catalyzed reaction.
$H_{298.15}$ (kJ/mol) is calculated relative to the reactants (**A** + N_2O + C_2H_6). The first coordination sphere and key bond distances (in Å) obtained by M06-L/def2-TZVP are shown for the intermediates and TSs of the catalytic cycle. [Color code: orange = Fe, red = O, blue = N, gray = C, and white = H]

The high-valent iron(IV)–oxo (**B**) is the key intermediate for the activation of the aliphatic C–H bond of ethane. Typically, a weak ligand field or a five-coordinated trigonal bipyramidal ligand field results in a high-spin electron configuration for the iron center,[90] while stronger field N-donor ligands (e.g., in Fe(II)–porphyrins) favor an intermediate-spin electronic configuration for iron.[143] The high-spin behavior is observed mainly in nature's non-heme cases,[124,100,144] while most of the synthesized non-heme molecular complexes exhibit intermediate-spin ground state configurations. The coordination sphere around iron in structures **A–O** through **TS4** of Figure 3.3 (six bonds, five of which are to carboxylate and oxido oxygen atoms of the linker of the MOF) forms a weak-field ligand which allows **B** to be in a quintet state, while, in general, a ligand set of five nitrogen atom bonds and one oxygen atom bond favors an

intermediate-spin Fe(IV) configuration.[100] Despite the strong-field ligand character of the oxo unit, the presence of five oxygen atoms that come from the carboxylate and aryloxide groups of the $dobdc^{4-}$ linker enforces a weak ligand field at the Fe center, resulting in **B** being a quintet. The high-spin state is also favored in a series of spectroscopically characterized non-heme iron(IV)–oxo enzymes.[122] In Ref. 26, CASPT2[145] and M06[140] calculations predicted the energy gap between the high-spin ground state and the intermediate-spin state to be around 130 kJ/mol.

The calculated Fe–O bond length of 1.64 Å is characteristic of the oxo–ferryl species, indicating a double bond between Fe and O, and is in agreement with EXAFS and X-ray diffraction studies on iron(IV)–oxo heme[146] and non-heme enzymes (1.64–1.68 Å).[122] The computed Fe–O stretching frequency of 830 cm^{-1} is within the range of the experimentally observed iron(IV)–oxo frequencies (776–843 cm^{-1}).

(b) *C–H bond activation*. The highly reactive oxo–ferryl group in species **B** interacts with the ethane molecule to form intermediate **C** (shown in Scheme 2). The formation of this intermediate is followed by cleavage of the aliphatic C–H bond of ethane.[108,109] The abstraction of the H-atom from ethane (in species **C**) by the iron(IV)–oxo yields a formal iron(III)–hydroxo species with a nearby ethyl radical (referred to as intermediate **D**). This step is accomplished *via* **TS2**, which has a geometry between the structures of **C** (the reacting ethane bound to iron(IV)–oxo species) and **D**. The Fe–O bond distance is elongated from 1.64 Å in both **B** and **C** to 1.75 Å in **TS2** (Figure 3.3), while the C–H aliphatic bond is elongated from 1.09 Å to 1.30 Å. The enthalpy of activation for **TS2** is 58 kJ/mol, and its imaginary frequency of 1859i cm^{-1} corresponds to a hydrogen atom transfer. **TS2** has a high-spin Fe(III) center ($S_{Fe} = 5/2$) antiferromagnetically coupled to an unpaired electron of the •O–H–CH_2- group ($S_{C–H–O} = 1/2$, $M_S = -1/2$).

(c) *Formation of ethanol*. This step involves the reaction of the iron(III)–hydroxo complex with the ethyl radical to form ethanol. Intermediate **D** undergoes conformational change via **TS3** to give intermediate **E**. The ethyl radical in intermediate **E** abstracts the hydroxyl group bound to the Fe(III) site to form ethanol. This step is usually called the rebound mechanism in the literature, and it involves **TS4**, which has a significantly lower enthalpy of activation (3 kJ/mol) than **TS1** (82 kJ/mol) and **TS2** (58 kJ/mol). For **TS4**, the (alkyl)C···O(hydroxyl) distance is 2.50 Å (Figure 3.3), in agreement with similar Fe(OH)···CH_2–R transition states (2.33–2.82

Å) reported in literature.[108] We carried out a natural bond order analysis, which shows that **TS4** has a high-spin Fe(III) center ($S_{Fe} = 5/2$) antiferromagnetically coupled to the ethyl radical ($S_C = 1/2$, $M_S = -1/2$) through the hydroxyl group. The five α electrons of Fe(III) are coupled with the antiparallel electron of the ethyl radical via the doubly occupied oxygen 2*p* orbital of the hydroxyl group. The presence of a β electron on the carbon of the ethyl radical has also been verified by Hirshfeld population analysis.

The formation of **TS4** is preceded by (1) a rotation of hydrogen atom of the hydroxo group along the Fe(III)–O axis in intermediate **D** that leads to intermediate **E** via **TS3** and (2) a shift of the ethyl radical toward the Fe(III)–OH center. The first circumvents the stereochemical hindrance from the hydrogen atom of the hydroxyl group. The second allows the ethyl radical to approach the hydroxyl group in such a manner that the C–O bond formation (that ultimately results in the generation of ethanol) is favored. In **TS2**, the O–H–C–C torsional angle in the complex (where H–C–C comes from the ethyl radical) is about 180° (Figure 3.3), while the same torsional angle for **TS4** is about 105°. This favorable angle enables the formation of ethanol from **TS4** and recovery of the Fe(II) active site (intermediate **F**). As has been suggested by Usharani *et al.*[147] and Ye *et al.*[148], a σ-mechanism for hydrogen abstraction is followed by a π-rebound mechanism, *i.e.* an electron transfer from the singly occupied MO of the ethyl radical to the $3d_{xz/yz}$ orbital of Fe(III). Similarly, a π-mechanism for hydrogen abstraction will be followed by a σ-rebound mechanism (electron transfer from the ethyl radical to the $3d_{x^2-y^2}$ orbital of Fe(III)). These mixed σ/π and π/σ pathways are based on the overlap of the electron-donating and electron-accepting orbitals. Thus, since the σ-rebound mechanism is calculated here to be energetically more favorable, an electron transfer from the 2*p* orbital of the oxygen to the $3d_{xz/yz}$ orbital of Fe(III) is expected. An electron de-excitation from the $3d_{xz/yz}$ to the $3d_{xy}$ orbital forms the Fe(II) center of intermediate **F**. Simultaneously, in intermediate **E**, the singly occupied 2*p* orbital of the oxygen can overlap with the 2*p* of the carbon from the ethyl radical and form the C–O bond of ethanol.

Figure 3.3 summarized the reaction steps of the oxidation of ethane to ethanol. The complete reaction profile with the first coordination sphere of Fe for each intermediate and transition state are included. The overall reaction is exothermic by 146 kJ/mol.

Table 3.1 CM5 charges (in atomic units), Hirshfeld spin densities, and distances (in Å) computed for various species.

Species	**A**	**A–O**	**TS1**	**B**	**C**	**TS2**	**D**	**TS3**	**E**	**TS4**	**F**
Oxidation state	II	II	III	IV	IV	III	III	III	III	III	II
Fe spin density	3.65	3.64	3.89	3.33	3.33	3.86	4.04	4.04	4.04	3.99	3.65
O6 spin density	NA[a]	0.01	–0.06	0.51	0.51	0.13	0.31	0.33	0.33	0.26	0.03
Charge on Fe	0.71	0.67	0.85	0.87	0.88	0.88	0.88	0.87	0.87	0.85	0.67
Charge on O6	NA[a]	–0.04	–0.29	–0.47	–0.45	–0.53	–0.63	–0.62	–0.62	–0.60	–0.42
<Charge on O1–5>[b]	–0.41	–0.41	–0.41	–0.40	–0.40	–0.40	–0.40	–0.40	–0.40	–0.40	–0.41
Fe–O6 distance[c]	NA[b]	2.48	1.88	1.64	1.64	1.75	1.83	1.85	1.85	1.88	2.24
<Fe–O distance>[d]	2.08	2.08	2.10	2.12	2.12	2.13	2.13	2.12	2.12	2.13	2.10

[a] Intermediate **A** is the bare cluster and does not have an oxygen bound at its sixth site

[b] Average charge on the five MOF oxygen atoms in the first coordination shell of Fe

[c] O6 is the oxygen atom transferred from N_2O to the iron center

[d] Average Fe–O distance for the five MOF oxygen atoms in the first coordination shell of Fe

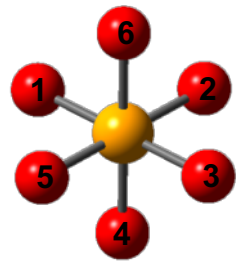

Figure 3.4 The first coordination sphere around Fe for all the species except A. Atoms O1–O5 are the five MOF oxygen atoms around the Fe center, and O6 is the oxygen atom transferred from N_2O to the iron center. [Color code: Orange = Fe and red = O]

Table 3.1 includes selected parameters monitored for the electronic structures of the intermediates and **TS**s along this reaction path for the Fe center and the six oxygen atoms around it (shown in Figure 3.4). The Hirshfeld spin density on the iron center for various intermediates and **TS**s lies between 3.33 and 4.04. The CM5 charge on the iron center of the bare cluster (**A**) is 0.71 atomic units and of **A–O** is 0.67 atomic units, indicating that the adsorption of N_2O is accompanied by the transfer of positive charge from iron to the rest of the atoms of the complex. These charges are smaller than that of the iron center of most of the species (**TS1**, **B**, **C**, **TS2**, **D**, **TS3**, **E**,

and **TS4**). This can be attributed to the O6 atom (that was initially part of N_2O) being closer to the iron center in these species than in intermediates **A**, **A–O**, and **F**. The increase in positive charge of the iron center as one goes from **A–O** to **TS4** is also reflected in the increase in negative charge of O6 as the reaction progresses. However, the average charge on the five oxygen atoms (O1–O5) coordinated to Fe remains almost unchanged during the catalytic cycle, indicating no incipient oxidation of the oxygen atoms ligated to the iron center.

Similarly, the average Fe–O*n* (*n* = 1–5) bond distances show negligible variation as one goes along the reaction path and as the nature of the catalytic site varies. After surmounting the energy barrier of **TS1**, the iron(II) center of intermediate **A–O** shifts to oxidation state IV of the highly reactive oxy–ferryl. In parallel, the spin density on Fe is reduced from 3.64 (**A–O**) to 3.33 (**B** & **C**). This is also accompanied by an increase in spin density on O from 0.01 to 0.51. The formation of the iron(III)–hydroxo group (in **D**, **E**, and **TS3**) increases the spin density of Fe, before returning to the initial coordinatively-unsaturated species (**A**). The evolution of the bond distance from Fe to the reactive oxygen (O6) is shown in Table 3.1. The Fe–O6 distance varies from 2.48 Å in **A–O** (when N_2O is adsorbed), reaches a minimum of 1.64 Å for species **B** and **C** (for the iron(IV)–oxo species), and finally increases to 2.24 Å (**F**) before the release of the ethanol product.

Comparison of the C–H Bond Activation Step for Methane and Ethane. In contrast to the hydroxylation of ethane, the oxidation of methane by N_2O on the coordinatively-unsaturated Fe sites of $Fe_{0.1}Mg_{1.9}$(dobdc) has not yet been found to occur under similar reaction conditions.[26] The goal here is to understand why the reaction for ethane is feasible on the surface of $Fe_{0.1}Mg_{1.9}$(dobdc), while that for methane is much more difficult. The conventional starting point for such a discussion is to compare bond energies; the experimental bond dissociation enthalpies at 298 K are 439 kJ/mol for methane and 423 kJ/mol for ethane,[149] indicating that the C–H bond of methane is stronger than that of ethane by 16 kJ/mol. For comparison, we note that M06-L (with scaled frequencies) gives 432, 409, and 23 kJ/mol for these quantities, in good agreement with experiment. With this background, we studied the energetics of the C–H bond activation step of reactions 1 and 2 (Scheme 1).

Figure 3.5 shows the reaction profiles for the hydrogen abstraction step of methane (red) and ethane (black). This step involves intermediates **C** and **D** and **TS2**.

The enthalpies for both the reactions are reported under the energy levels. We find that the formation of **D** is more exothermic for ethane than for methane, hence the methyl radical intermediate **D** is energetically less favorable than the ethyl radical intermediate **D**. The difference is 29 kJ/mol, similar to 23 kJ/mol calculated bond enthalpy difference mentioned in the previous paragraph. The enthalpy of activation from **C** to **TS2** for ethane is 58 kJ/mol, while for methane it is 69 kJ/mol, a difference of 11 kJ/mol. Thus, the calculations predict that 38% of the 29 kJ/mol reaction energy difference shows up in the enthalpy of activation, and consequently activation by iron(IV)–oxo is more facile for ethane than for methane. The 11 kJ/mol difference is smaller than the reliability of the theoretical methods for absolute barrier energies, but we believe it is well within the reliability of the method we used for relative energy differences of two similar processes. This can be illustrated by an example. The mean unsigned error in the M06-L values for the electronic binding energies (including nuclear repulsion but excluding vibrational contributions) of H and CH_3 to C_2H_5 is 14.5 kJ/mol, but M06-L reproduces the difference of these energies within 0.2 kJ/mol (predicting 54.3 kJ/mol vs. an accurate value of 54.5 kJ/mol); this illustrates how relative energies are often more accurate than absolute energies.

Figure 3.3 and 3.5 also show key bond distances for ethane and methane, respectively. For both the cycles, the Fe–O distances (here O is the terminal oxygen atom that is transferred from N_2O) of **C** and **D** and **TS2** remain the same to within 0.01 Å, but there are larger differences in bond distances of the partial bonds to the transferred H. In particular, we find a shorter O–H distance (1.14 Å) of the **TS2** optimized geometry of methane catalytic cycle compared to ethane catalytic cycle (1.19 Å), and simultaneously the distance between the activated hydrogen atom and the methyl radical is 1.37 Å, which is 0.07 Å longer than the hydrogen–ethyl radical distance. These two trends suggest that the **TS2** structure for methane has more product-like iron(III)–hydroxo character than the **TS2** structure for ethane, which is consistent with the Hammond postulate[150] since the methane reaction is endothermic with a higher barrier. The methyl radical of intermediate **D** lies 2.29 Å away from the hydroxyl group, which is 0.09 Å longer compared to that of the ethyl radical of **D** (2.20 Å). Therefore, for both **TS2** and **D**, the methyl radical is farther away from the evolving –OH group and it destabilizes the C–H activation mechanism in comparison to the C–H activation of ethane.

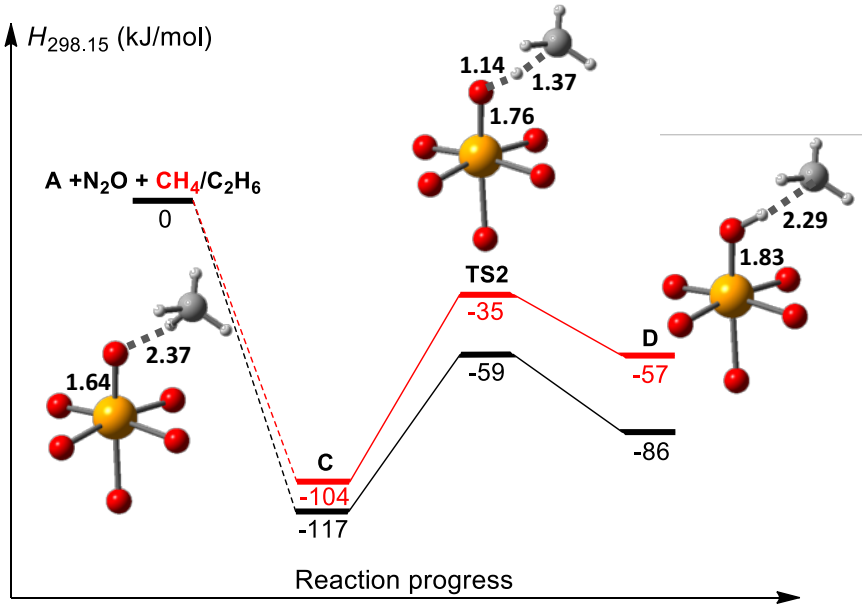

Figure 3.5 Enthalpies of C–H bond activation of CH_4 (red) and C_2H_6 (black). The first coordination sphere of Fe for the intermediates **C** and **D** and **TS2** of the CH_4 cycle are shown. The dotted lines in the enthalpy profile indicate that the reaction does not go directly from the reactants (**A** + N_2O + CH_4/C_2H_6) to intermediate **C**. [Color code: orange = Fe, red = O, gray = C, and white = H]

The step from **C** to **TS2** has an activation enthalpy of 69 kJ/mol for methane, as compared to 58 kJ/mol for ethane, which – other things being equal – would make this step slower for methane by a factor of 85 at 298 K.

Competitive Pathways After the Formation of Intermediate D. Since various pathways can be followed after an alkyl radical is formed from an alkane, we computed two competitive pathways, namely desaturation and dissociation, that can in principle compete with the hydroxylated product that is usually formed upon C–H bond activation by non-heme model complexes after the formation of intermediate **D**, as shown in Scheme 3. Desaturation would involve the abstraction of H atom from ethyl radical to form ethylene and water, and dissociation would involve the departure of ethyl radical without undergoing rebound. The departed ethyl radical can react with other reagents in its vicinity and give rise to secondary products. A comparison of enthalpies of activation associated with hydroxylation and desaturation pathways is shown in Figure 3.6. It can be seen from Figure 3.6 that hydroxylation and desaturation pathways have enthalpies of activation of 7 and 27 kJ/mol, respectively, indicating that hydroxylation is more facile than desaturation by 20 kJ/mol. The dissociation of the ethyl radical from intermediate **D** required 21 kJ/mol, which is

again three times more than the enthalpy of activation for hydroxylation. The dissociation of the methyl radical from the corresponding intermediate **D** (shown in Figure 3.5) required 14 kJ/mol. Since this is smaller than for the ethyl radical dissociation, the rebound to produce methanol is less likely to occur than the rebound that produces ethanol.

The energy diagram of Figure 3.6 shows that the desaturation process is unfavorable. The Fe(III)–OH group of intermediate **D** is directed toward the inside of the pore of the material, and it can be approached without steric hindrance by both the carbon and the hydrogen atoms of the ethyl radical, which can lead to hydroxylated and desaturated products, respectively. Usharani *et al.*[147] have shown that the probability of the desaturation reaction depends on the energy gap between the doubly occupied $\sigma_{C\text{-}H}$ orbital and the singly occupied φ_C orbital of the alkyl radical. For the ethyl radical, they calculated this gap to be ~560 kJ/mol, which was relatively large in comparison to other substrate radicals (377-427 kJ/mol) formed from cyclic hydrocarbons investigated in the same work; the largeness of this value explained why the hydroxylation pathway is preferred. A similar analysis for the free ethyl radical in the present work, using M06-L, gives ~542 kJ/mol for the same orbital energy gap, again indicating that hydroxylation is the preferred pathway.

Scheme 3. The competitive pathways that can follow after the formation of the ethyl radical in intermediate **D**.

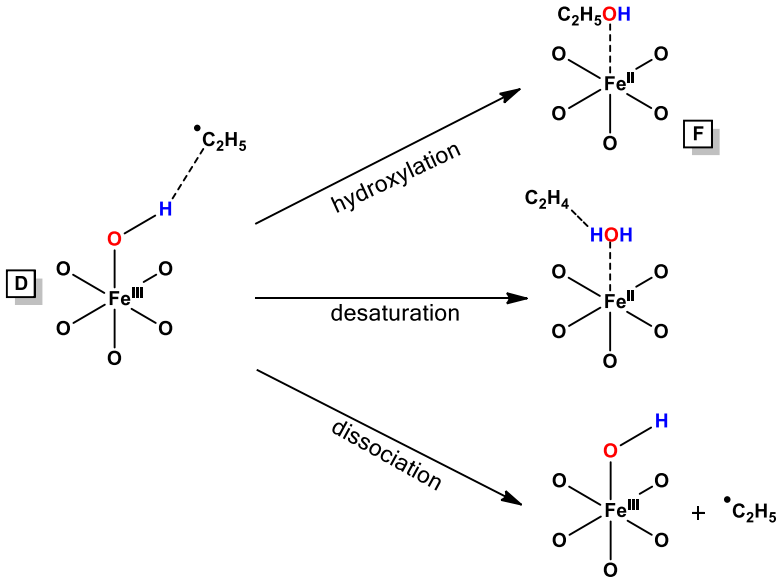

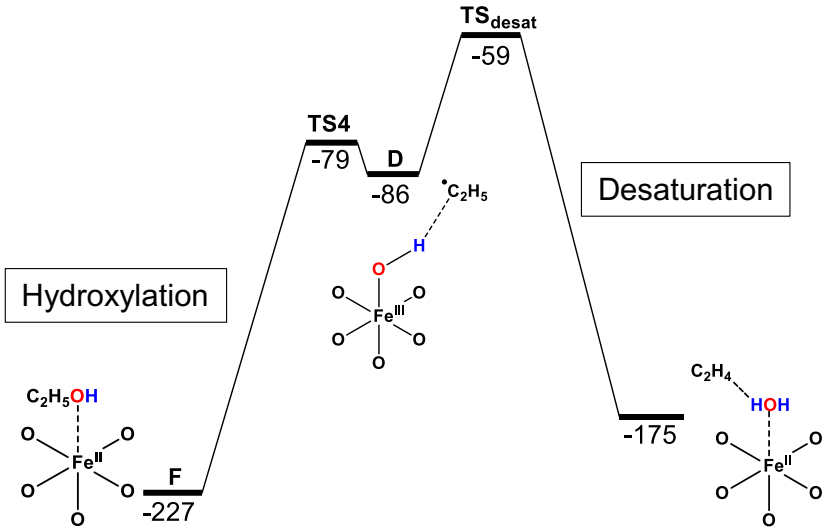

Figure 3.6 Enthalpy profiles of hydroxylation and desaturation.
$H_{298.15}$ (kJ/mol) is computed with respect to the separated reactants (cluster **A** + N_2O + C_2H_6) using M06-L/def2-TZVP.

Comparison of Catalyzed and Uncatalyzed Reactions. Finally, the reaction between ethane and nitrous oxide in the absence of any catalytic material was examined. This gives us an estimate of the reduction in energy barrier that is achieved due to the catalyst. To investigate this, the direct hydroxylation of ethane by nitrous oxide was studied, where the reaction is not facilitated by an iron(IV)–oxo intermediate supported by the catalytic material (eq (3), Scheme 1). Figure 3.7 shows the enthalpy associated with the uncatalyzed reaction process. The enthalpy of activation for this direct step is considerably higher (280 kJ/mol) than the highest enthalpy of activation of the catalyzed reaction (82 kJ/mol), indicating that the direct pathway is highly unfavorable. We find that this direct pathway occurs without the formation of an ethyl radical, which differs from what is observed for the catalyzed reaction. This is confirmed by following the minimum energy path[151,152,153,154,155] from the saddle point; this path leads to the reactant and product (**A** and **B**, respectively) shown in Figure 3.7. Unlike the catalyzed reaction, this one-step reaction involves the simultaneous cleavage of the C–H and N–O bonds and the rearrangement of the –OH group to give ethanol directly without proceeding via the formation of an intermediate containing ethyl radical. The transition state of Figure 3.7 explains this mechanism; both C–H and N–O bonds are activated before the insertion of oxygen in the developing ethyl radical.

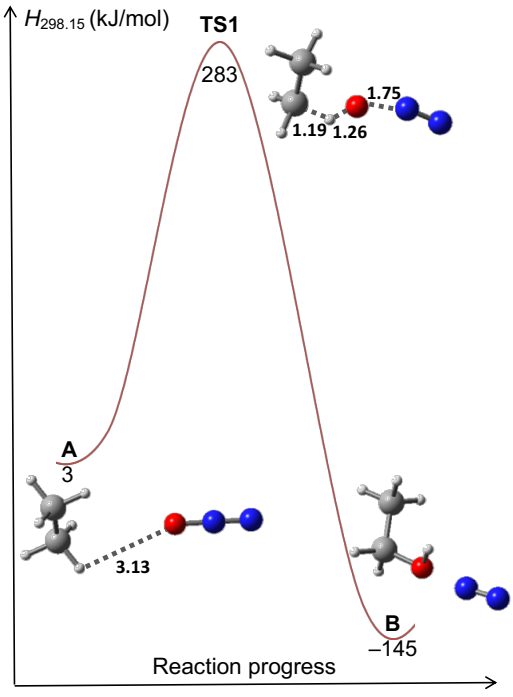

Figure 3.7 Enthalpy profile of the uncatalyzed reaction (eq 3, Scheme 1).
The profile was calculated relative to reactants using M06-L/def2-TZVP. [Color code: red = O, blue = N, gray = C, and white = H]

3.5 Concluding Remarks

The ability of the magnesium-diluted MOF, $Fe_{0.1}Mg_{1.9}$(dobdc), to catalyze the oxidation reaction in the presence of N_2O has been studied. This reaction was originally suggested[26] to proceed via the formation of a high-spin $S = 2$ iron(IV)–oxo intermediate, and here the full mechanism is elucidated. An 88-atom model cluster carved from a periodic Kohn-Sham optimized geometry of Mg_2(dobdc) was used for the Kohn-Sham calculations to locate the stationary points. We showed that the metal–organic framework catalyzed hydroxylation of ethane proceeds by an $S = 2$ single-state pathway. Four transition structures were found. The first transition state involves the cleavage of the N–O bond of N_2O to create the iron(IV)–oxo species. The high energy barrier dictates that this step is the rate-determining step of the reaction. Intermediate **B** possesses the iron(IV)–oxo double bond (1.64 Å) with an electronic structure very similar to that found in other non-heme model complexes. Ethanol is formed after the reaction passes from the low-energy barrier of the fourth transition state. The reaction follows a single-state mechanism, as it is dictated from the large energy gaps between the high-spin and intermediate-spin states of all intermediates and **TS**s. The reaction is highly exothermic with an enthalpy of reaction equal to –146 kJ/mol.

Comparison of the energy barrier of the C–H activation step for methane and ethane shows, as expected, that cleaving a C–H bond of ethane is more facile than cleaving a C–H bond of methane. This explains why the MOF, $Fe_{0.1}Mg_{1.9}$(dobdc), catalyzes the hydroxylation of ethane but methane hydroxylation has not yet been observed. The uncatalyzed reaction is investigated and is found to have an energy barrier of 280 kJ/mol, which clearly implies that the direct reaction between nitrous oxide and ethane is not observable, and iron(IV)–oxo is essential for hydroxylating ethane to ethanol. Finally, competing pathways were explored, which suggested that hydroxylation is more likely to occur than desaturation and dissociation.

4 Magnetism

4.1 Synopsis

Magnetic properties together with their structural dependencies are reported for the metal–organic framework Fe_2(dobdc) (dobdc^{4-} = 2,5-dioxido-1,4-benzenedicarboxylate), its physisorbed species (Fe_2(dobdc)-2C_2H_6 and Fe_2(dobdc)-2C_2H_4), and its derivatives, $Fe_2(O)_2$(dobdc) and $Fe_2(OH)_2$(dobdc)—species arising in the previously proposed mechanism for the oxidation of ethane to ethanol using N_2O as an oxidant. Magnetic susceptibility measurements reported for Fe_2(dobdc) and the physisorbed species in an earlier study and reported in the current study for $Fe^{II}_{0.26}[Fe^{III}(OH)]_{1.74}$(dobdc)$(DMF)_{0.15}(THF)_{0.22}$, which is more simply referred to as $Fe_2(OH)_2$(dobdc), were used to confirm the computational results. Structural and magnetic properties were computed by using Kohn-Sham density functional theory both with periodic boundary conditions and with cluster models. In addition, we studied the effects of different treatments of the exchange interactions on the magnetic coupling parameters by comparing several approaches to the exchange-correlation functional: generalized gradient approximation (GGA), GGA with empirical Coulomb and exchange integrals for 3*d* electrons (the GGA+U method), nonseparable gradient approximation with empirical Coulomb and exchange integrals for 3*d* electrons (GAM+U), hybrid GGA, meta-GGA, and hybrid meta-GGA. We found the coupling between the metal centers to be ferromagnetic in the case of Fe_2(dobdc), (Fe_2(dobdc)—2C_2H_6, and Fe_2(dobdc)—2C_2H_4) and antiferromagnetic in the cases of $Fe_2(O)_2$(dobdc) and $Fe_2(OH)_2$(dobdc). The shift in magnetic coupling behavior correlates with the changing electronic structure of the framework, which derives from both structural and electronic changes that occur upon metal oxidation and addition of the charge-balancing oxo and hydroxo ligands.

4.2 Introduction

MOFs with unpaired electrons or those that can potentially have unpaired electrons after physisorption or chemisorption have the potential to behave as bulk magnetic

materials.[156] This can arise due to the presence of open-shell metal atoms or open-shell organic ligands in the MOF, or due to the presence of magnetic adsorbates within the pores of the MOF. Additionally, magnetism can arise after post-synthetic modification of a non-magnetic MOF material. In any scenario, for a MOF to behave as a bulk magnetic material, the existence of exchange magnetic interactions between the magnetic sites is important along with single-ion magnetic anisotropy. The M_2(dobdc) (where M in any open-shell metal ion in the 3*d* series) family of MOFs can be potentially used as a magnetic material as the metal sites are in an environment of weak-field dobdc^{4-} ligand, and hence have localized unpaired electrons.

Experimental and theoretical studies have been reported for the magnetic properties of bare MOF and MOFs with adsorbate molecules.[10,27,30,157,158,159,160,161] Theoretical studies on MOFs can be particularly challenging because the periodic model or the cluster model must be adequately chosen to be large enough to account for all the magnetic interactions in the material. Furthermore, the structure of the MOF may change upon adsorption, and therefore one needs to take into account the high-coverage limit (that has one adsorbate per metal site), where there could be significant changes in the structure.

This work explores magnetic properties of bare,[27] physisorbed (with ethane and ethylene),[28,30] and chemisorbed Fe_2(dobdc) ($Fe_2(O)_2$(dobdc) and $Fe_2(OH)_2$(dobdc)),[29] where in the latter two cases, the structure of the MOF can change thereby allowing us to see how this changes the magnetic property.

4.3 Methodology

The quantum mechanical methods along with the spin configurations considered for calculating isotropic coupling constants are discussed in subsections 4.3.1 and 4.3.2, respectively.

4.3.1 Quantum Mechanical Methods.

The isotropic coupling constants were calculated using 25 exchange–correlation functionals shown in Table 4.1. Functionals from various rungs of the density functional ladder were chosen – nine of them are local functionals,[162,163,164,165,166,167,60,168,169] eleven are global hybrid functionals,[140,170,171,172,173,174,175,166,176,177,178,179,180]

four are range-separated hybrid functionals,[181,182,183,184,185,186] and one is a doubly hybrid functional.[187] The def2-TZVP or def2-QZVP basis sets were used,[141] and all DFT calculations were performed with *Gaussian 09* programs[188,75] or an in-house modified version[189] of *Gaussian 09*. An "UltraFine" pruned grid that has 99 radial nodes and 590 angular points per node was used for numerical integrations with all the exchange–correlation functionals. Stable solutions were obtained by first checking the stability of Kohn–Sham Slater determinants, and if found unstable, by breaking all symmetries using the "*stable=opt*" keyword of *Gaussian 09*.[188] For the partially optimized complexes, frequency calculations were performed in the optimized degrees of freedom, and structures were confirmed to be minimum by the absence of imaginary frequencies.

Table 4.1 The exchange–correlation functionals used for calculating magnetic coupling constants with cluster models.

Functional	X^a
GAM	0
M06-L	0
M11-L	0
MN12-L	0
mPWPW	0
N12	0
PBE	0
RPBE	0
SOGGA	0
B3LYP	20
MPW20	20
HSE06	25–0
MN12-SX	25–0
N12-SX	25–0
mPW1PW	25
PBE0	25
M06[d]	27
M05	28
PW6B95	28
MPW1K	42.8
M11	42.8–100
PWB6K	46
B2PLYP	53

M06-2X	54
M08-SO	56.79

[a] *X* = percentage of HF exchange. When a range for *X* is given, the first value indicates small interelectronic separations and the second value indicates large interelectronic separations.

With two of the local functionals (PBE and GAM), the +U treatment was used, and periodic DFT optimizations were performed with these methods using *VASP*[76,77] or an in-house modified version of *VASP*.[190]

Table 4.2 gives the *U* values chosen in this work. The +U correction was applied only to the valence 3*d* orbitals of iron in the formulation of Dudarev *et al*.[191] (which is specified by LDAUTYPE = 2 in *VASP*) in which the results depend only on the difference (*U* – *J*) of on-site Coulomb (*U*) and exchange (*J*) energies. Because the systems Fe_2(dobdc), $Fe_2(C_2H_6)_2$(dobdc), and $Fe_2(C_2H_4)_2$(dobdc) [the chemisorbed systems are yet to be included here], have open-shell iron centers, the periodic DFT calculations were spin-polarized calculations, where nuclear positions, cell shape, and cell volume were allowed to relax. The isolated adsorbates, C_2H_6 and C_2H_4, involved non-spin-polarized calculations, where only nuclear positions were allowed to relax. All calculations involved PBE PAW potentials[192,193] provided with the *VASP* package, a cut-off energy of 600 eV, a *k*-point mesh of 4×2×2, an SCF energy convergence criterion of 10^{-5} or 10^{-6} eV, and a force convergence criterion of -10^{-3} eV/Å.

Table 4.2 The DFT+U methods used in this work.

Method	+U correction (eV)
GAM+U	0.25
	1.00
	2.00
	4.00
PBE+U	2.00
	4.00

4.3.2 Spin Configurations

For all the models, the isotropic couplings between two iron centers were computed by considering various spin configurations. For the 88-atom cluster model, four spin configurations were calculated (shown in Figure 4.1), for the 106-atom cluster model

16 spin configurations were calculated (shown in Figure 4.2), and for the periodic model three spin configurations were calculated (shown in Figure 4.3).

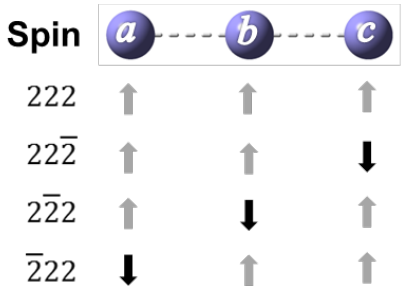

Figure 4.1 Spin configurations of the 88-atom cluster.
The four unpaired electrons of each iron center are shown by arrows, with the direction of the arrow indicating the direction of the four unpaired electrons on a given iron center. In the cluster shown in Figure 1.2a, the iron centers do not lie on a line, but on a helix.

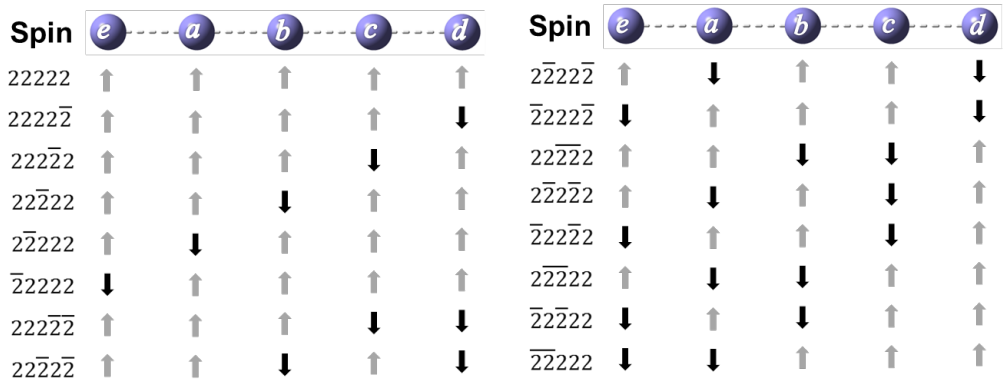

Figure 4.2 Spin configurations of the 106-atom cluster.
The four unpaired electrons of each iron center are shown by arrows, with the direction of the arrow indicating the direction of the four unpaired electrons on a given iron center. In the cluster shown in Figure 1.2b, the iron centers do not lie on a line, but on a helix.

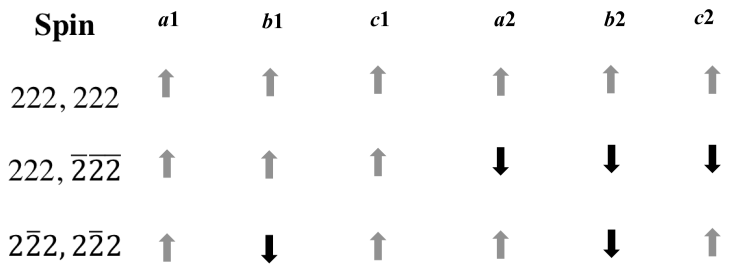

Figure 4.3 Spin configurations of the periodic model.
The four unpaired electrons of each iron center are shown by arrows, with the direction of the arrow indicating the direction of the four unpaired electrons on a given iron center. The first three iron centers (*a*1, *b*1, and *c*1) lie along one helix

(chain 1 of Figure 1.3) and the next three (*a*2, *b*2, and *c*2) along another helix (chain 2 of Figure 1.3).

The Heisenberg-Dirac-van Vleck (HDV) spin Hamiltonian[194,195,196] given by eq 4.1 is used to extract the coupling constants. There is more than one definition of the HDV Hamiltonian, and the one used here is the same as that used in the experimental study to ensure direct comparison of calculated and experimental results.

$$H_{\mathrm{HDV}} = -2\sum_{j>i}\sum_{i} J_{ij}\hat{S}_i \cdot \hat{S}_j \qquad 4.1$$

Here, i and j are labels for iron centers, J_{ij} indicates isotropic coupling between centers i and j, and $\hat{S}_i$ indicates spin vector on iron center i. A positive value of J_{ij} indicates ferromagnetic (FM) coupling and a negative value indicates antiferromagnetic (AFM) coupling. For both the cluster and periodic calculations, energies of the possible spin configurations (shown by Figure 4.1–4.3) obtained from single Slater determinant DFT calculations were equated to the diagonal elements of the H_{HDV} Hamiltonians,[197] which led to simultaneous linear equations, and solving them gave the coupling constants.

Furthermore, the scheme employed here has the advantage that it can be applied in precisely the same way to the periodic calculations and the cluster calculations, whereas more complicated spin-projection techniques would be harder to employ for the periodic calculations. Since in this work, the computed magnetic couplings are weak, and since we want to fairly compare cluster and periodic calculations, we chose to use the weak-coupling computational scheme.

4.4 Results and Discussion

The experimental unit cells of Fe_2(dobdc) and of Fe_2(dobdc) dosed with ethane or ethylene have been used as starting structures for performing periodic DFT calculations or for carving the clusters. The experimental structures of Fe_2(dobdc)–ethane and Fe_2(dobdc)–ethylene complexes were not completely dosed with the adsorbates and hence had vacant metal sites, but for the purpose of our calculations we started with fully dosed unit cells. The nearest-neighbor Fe–Fe distances in the three experimental structures are not all the same. The distances are 3.00, 2.96, and

3.16 Å for the bare MOF, MOF–ethane, and MOF–ethylene structures, respectively. The shortest Fe–Fe interchain distances for these three structures are 7.37, 7.39, and 7.92 Å, respectively.

4.4.1 Isotropic Coupling Constants of Bare MOF

Every Fe(II) center is in a local quintet state ($S = 2$) in both cluster and periodic models. In the high-spin state, all the Fe(II) centers have $|M_S| = 2$, where M_S is the local spin component on an Fe(II) center. Various broken-symmetry configurations (*i.e.*, Slater determinants that are not eigenfunctions of S^2) have been considered by flipping the spins at some of the magnetic centers, and the energies of these states (after they are individually optimized by self-consistent-field calculations) are modeled by the HDV spin Hamiltonian given by eq 4.1. For the 88-atom cluster, flipping one spin generates ${}^3C_1 = 3$ possible configurations (Figure 4.1) and flipping more than one would give rise to another equivalent set of solutions (only differing by the direction of the quantization axis). These along with the ferromagnetically coupled configuration result in four Slater determinants, which are represented by $|M_{S_a} M_{S_b} M_{S_c}\rangle$, and can be used to determine the isotropic coupling constants by solving the following equations:

$$\begin{aligned}
\langle 222 | H_{\mathrm{HDV}} | 222 \rangle &= E_{222} = -8J_{ab} - 8J_{bc} - 8J_{ac} \\
\langle 22\bar{2} | H_{\mathrm{HDV}} | 22\bar{2} \rangle &= E_{22\bar{2}} = -8J_{ab} + 8J_{bc} + 8J_{ac} \\
\langle 2\bar{2}2 | H_{\mathrm{HDV}} | 2\bar{2}2 \rangle &= E_{2\bar{2}2} = +8J_{ab} + 8J_{bc} - 8J_{ac} \\
\langle \bar{2}22 | H_{\mathrm{HDV}} | \bar{2}22 \rangle &= E_{\bar{2}22} = +8J_{ab} - 8J_{bc} + 8J_{ac}
\end{aligned} \qquad 4.2$$

The set of equations represented by eq 4.2 when solved for J_{ab}, J_{bc}, and J_{ac} results in the following expressions leading to all the three J_{ij} values of the 88-atom cluster:

$$J_{ab} = \frac{1}{32}\left[E_{2\bar{2}2} - E_{222} + E_{\bar{2}22} - E_{22\bar{2}}\right]$$

$$J_{bc} = \frac{1}{32}\left[E_{22\bar{2}} - E_{\bar{2}22} + E_{2\bar{2}2} - E_{222}\right]$$

$$J_{ac} = \frac{1}{32}\left[E_{\bar{2}22} + E_{22\bar{2}} - E_{222} - E_{2\bar{2}2}\right]$$

4.3

If the centers *a* and *c* were equivalent, as is the case in the real MOF, then $E_{\bar{2}22} = E_{22\bar{2}}$ which leads to:

$$J_{ab} = J_{bc} = \frac{1}{32}\left[E_{2\bar{2}2} - E_{222}\right]$$

4.4

But $E_{\bar{2}22}$ and $E_{22\bar{2}}$ are not equal on account of the peripheral Fe(II) ions in the 88-atom cluster being non-equivalent. Note that we averaged the values of the two nearest-neighbor couplings, such that $J_{NN} = ½(J_{ab} + J_{bc})$, leading to precisely the same values that are obtained from eq 4.4, which assumes equivalence of centers *a* and *c*.

Table 4.3 gives the NN and NNN coupling values for bare Fe3//opt0 using the 25 density functionals specified in Table 4.1. Most, but not all of the functionals agree with the experimental finding of ferromagnetic couplings along a chain, *i.e.*, positive J_{NN}. The table shows that inclusion of more HF-exchange usually decreases the nearest-neighbor interaction (J_{NN}); this is seen most clearly in the series mPWPW, MPW20, mPW1PW, and MPW1K, which differ only in the percentage *X* of Hartree–Fock exchange. This series also shows that the decrease in the magnetic coupling constant is much great between *X* = 0 and *X* = 20 than between *X* = 20 and *X* = 42.8. Functionals that agree with the experimental J_{NN} within 2 cm^{-1} are in bold; most of these functionals have *X* in the range 20–28. M06 gives the nearest-neighbor interaction closest to experiments (with a deviation of only 0.5 cm^{-1}); the second and third closest being M05 (with a deviation of 1.4 cm^{-1}) and PW6B95 (with a deviation of 1.5 cm^{-1}), respectively. Amongst the local density functionals employed, M06-L agrees best with experiment, amongst the range-separated hybrid functionals, HSE06 gave the best agreement with experiment, and the only doubly hybrid density functional that we tested, B2PLYP, agrees with experiment within 2.2 cm^{-1}.

For most of the exchange–correlation functionals, we find that the magnitude of J_{NNN} is significantly smaller than the magnitude of J_{NN}. All the functionals in bold give J_{NNN} in the range 0.3–0.7 cm^{-1}.

Table 4.3 Magnetic coupling constants (in cm^{-1}) of the bare 88-atom cluster (Fe3//opt0) computed using the def2-TZVP basis set.

Functional	X^a	$J_{NN}{}^b$	$J_{NNN}{}^c$
GAM	0	23.2	1.3
M06-L	0	10.3	2.0
M11-L	0	–3.8	0.3
MN12-L	0	–7.9	0.2
mPWPW	0	12.9	0.9
N12	0	19.7	–0.7
PBE	0	14.5	0.8
RPBE	0	11.3	1.2
SOGGA	0	23.6	0.3
B3LYP	**20**	**2.2**	**0.5**
MPW20	**20**	**2.2**	**0.6**
HSE06	**25–0**	**2.2**	**0.5**
MN12-SX	25–0	–2.0	0.2
N12-SX	25–0	–1.4	0.3
mPW1PW	**25**	**2.1**	**0.5**
PBE0	**25**	**2.2**	**0.5**
M06	**27**	**3.6**	**0.5**
M05	**28**	**5.5**	**0.7**
PW6B95	**28**	**2.6**	**0.5**
MPW1K	42.8	1.9	0.3
M11	42.8–100	0.2	0.1
PWB6K	**46**	**2.3**	**0.3**
B2PLYP	53	1.9	0.2
M06-2X	54	1.6	0.3
M08-SO	56.79	1.4	0.3
Expt.[d]	…	4.1	[e]

[a]Percentage of Hartree–Fock exchange. When a range is indicated, the first value corresponds to small interelectronic separations, and the second value corresponds to large interelectronic separations.

[b]J_{NN} is computed by taking the average of J_{ab} and J_{bc}.

[c]$J_{NNN} = J_{ac}$

[d]The experimental value is reported in Ref. 10.

[e]Not available.

The effect of the basis set size on the computed magnetic coupling constants in Fe3//opt0 was tested with the M06-L, M06, and M05 exchange–correlation functionals by comparing the def2-TZVP results presented in Table 4.3 with the def2-QZVP basis set shown in Table 4.4. The choice of these three functionals for Table 4.4 is based on our observation in Table 4.3 that M06-L is the best local functional and M06 and M05 are the best hybrid functionals among the functionals tested. We find that the nearest-neighbor and the next-nearest-neighbor interactions obtained using M06-L/def2-QZVP are 9.5 and 2.0 cm^{-1}, respectively, while those using M06-L/def2-TZVP are 10.3 and 2.0 cm^{-1}, respectively. This shows that both values change by less than 1.0 cm^{-1}. Furthermore, the M06 calculation remains unchanged to the number of significant digits reported in Table 4.4, while the M05 result changes by only 0.2 cm^{-1} for the nearest-neighbor interaction. This implies that the def2-TZVP basis set already provides nearly converged values with respect to the basis set size, and thus we use the def2-TZVP basis set for almost all of our calculations.

Table 4.4 Magnetic coupling constants (in cm^{-1}) of the bare 88-atom cluster (Fe3//opt0) computed using the M06-L, M06, and M05 density functionals.

Functional	Basis set	J_{NN} [a]	J_{NNN} [b]	Expt. [c]
M06-L	def2-TZVP	10.3	2.0	4.1
	def2-QZVP	9.5	2.0	
M06	def2-TZVP	3.6	0.5	
	def2-QZVP	3.6	0.5	
M05	def2-TZVP	5.5	0.7	
	def2-QZVP	5.3	0.7	

[a] J_{NN} is computed by taking the average of J_{ab} and J_{bc}.

[b] $J_{NNN} = J_{ac}$

[c] The experimental value is reported in Ref. 10.

To test the convergence of results with respect to the cluster size, we investigate a 106-atom cluster (Fe5//opt0) consisting of five Fe(II) centers that have local high-spin component, $M_S = 2$. The 106-atom cluster has the advantage of having the environment of Fe(II) ions *a* and *c* (shown in Figure 1.2(b)) closer to the experimental crystal structure than the Fe(II) ions *a* and *c* of the 88-atom cluster shown in Figure 1.2(a). (Recall that the iron atoms in the larger cluster have been

labeled as *e*, *a*, *b*, *c*, and *d* from left to right so that we can easily compare the *J* values for the three central irons of this cluster with that of the 88-atom cluster; see Figure 2 for the labeling of the iron centers). Since the environments around the three central iron atoms, of the 106-atom cluster are closer to the crystal structure than the three iron atoms of the 88-atom cluster, comparing the two clusters is a test of convergence of calculated magnetic properties with respect to cluster size.

Unlike the 88-atom cluster that allows us to calculate only the nearest-neighbor (J_{ab} and J_{bc}) and the next-nearest-neighbor (J_{ac}) interactions, the 106-atom cluster also allows us to compute magnetic interactions between Fe(II) centers along a chain that are farther apart, for instance J_{ec}, J_{ad}, and J_{ed}. Hence, four nearest-neighbor interactions (J_{ea}, J_{ab}, J_{bc}, and J_{cd}), three next-nearest-neighbor interactions (J_{eb}, J_{ac}, and J_{bd}), and three more interactions that involve Fe(II) centers that are farther apart (J_{ec}, J_{ad}, and J_{ed}) can be computed using the 106-atom cluster. To compute these ten magnetic interactions, eleven Slater determinants are required which are constructed from various spin configurations obtained from the high-spin configuration by flipping one or more spins on the five Fe(II) centers as shown in Figure 4.2. If only one spin of the five Fe(II) centers is flipped, it generates ${}^5C_1 = 5$ possible configurations and if two spins are flipped then ${}^5C_2 = 10$ configurations are obtained. Flipping more than two spins gives rise to the existing configurations if the direction of the quantization axis is inverted. Thus, a total of 16 configurations can be obtained for Fe5//opt0, one high-spin configuration for which all the spins are ferromagnetically coupled, and 15 for which various ferromagnetic and antiferromagnetic couplings coexist. Out of these 16 configurations, the 11 lowest energy solutions obtained with the M06-L exchange–correlation functional have been chosen to extract the 10 isotropic coupling constants of Fe5//opt0 described above.

The relative energies of all the 16 configurations with respect to the most stable configuration (ferromagnetic coupling along a chain) are given in Figure 4.2 placed in the order of increasing energies as computed by M06-L.

Table 4.5 Relative energies (ΔE in cm^{-1})[a] of various spin configurations of the 106-atom cluster.

Spin Configuration	ΔE (in cm^{-1})	
	M06-L	**M06**
22222	0.0	0.0
222$\bar{2}\bar{2}$	155.2	55.6
2222$\bar{2}$	186.3	89.1
$\bar{2}$2222	189.2	35.0
$\bar{2}\bar{2}$222	220.4	83.6
22$\bar{2}\bar{2}$2	295.7	132.1
22$\bar{2}$22	325.3	131.4
2$\bar{2}$222	343.3	103.9
2$\bar{2}\bar{2}$22	345.7	92.5
$\bar{2}$222$\bar{2}$	375.9	124.2
22$\bar{2}\bar{2}$2	406.2	174.4
$\bar{2}$2$\bar{2}$22	444.6	149.8
22$\bar{2}$2$\bar{2}$	466.7	206.3
$\bar{2}$222$\bar{2}$	486.3	169.0
2$\bar{2}$22$\bar{2}$	529.6	194.8
2$\bar{2}$2$\bar{2}$2	586.7	224.7

[a]Energies are relative to the most stable configuration. These are Fe5//opt0 (bare 106-atom cluster with no atoms optimized) calculations with the def2-TZVP basis set.

The set of equations required to extract all the ten coupling constants in Fe5 is given by eq 4.5. The first four equations correspond to nearest-neighbor interaction; the next three equations correspond to next-nearest-neighbor interaction and the last three correspond to an interaction between Fe(II) centers that are farther apart. The values obtained with M06-L and M06 are given in Table 4.6.

$$J_{ea} = \frac{1}{32}\left[E_{\bar{2}2222} + E_{2\bar{2}222} - E_{\bar{2}\bar{2}222} - E_{22222}\right]$$

$$J_{ab} = \frac{1}{32}\left[E_{2\bar{2}222} + E_{22\bar{2}22} - E_{2\bar{2}\bar{2}22} - E_{22222}\right]$$

$$J_{bc} = \frac{1}{32}\left[E_{22\bar{2}22} + E_{222\bar{2}2} - E_{22\bar{2}\bar{2}2} - E_{22222}\right]$$

$$J_{cd} = \frac{1}{32}\left[E_{222\bar{2}2} + E_{2222\bar{2}} - E_{222\bar{2}\bar{2}} - E_{22222}\right]$$

$$J_{eb} = \frac{1}{32}\left[E_{\bar{2}\bar{2}222} + E_{22\bar{2}\bar{2}2} - E_{2\bar{2}222} - E_{222\bar{2}\bar{2}}\right]$$

$$J_{ac} = \frac{1}{32}\left[E_{2\bar{2}\bar{2}22} + E_{22\bar{2}\bar{2}2} - E_{\bar{2}2222\bar{2}} - E_{22\bar{2}22}\right]$$

$$J_{bd} = \frac{1}{32}\left[E_{22\bar{2}\bar{2}2} + E_{2222\bar{2}\bar{2}} - E_{\bar{2}\bar{2}222} - E_{2222\bar{2}\bar{2}}\right]$$

$$J_{ec} = \frac{1}{32}\left[E_{\bar{2}2222\bar{2}} - E_{2\bar{2}\bar{2}222} - E_{22222\bar{2}} + E_{222\bar{2}\bar{2}2}\right]$$

$$J_{ad} = \frac{1}{32}\left[E_{\bar{2}\bar{2}2222} + E_{\bar{2}2222\bar{2}} - E_{\bar{2}22222} - E_{22\bar{2}\bar{2}22}\right]$$

$$J_{ed} = \frac{1}{32}\left[E_{2222\bar{2}} + E_{\bar{2}22222} - E_{\bar{2}2222\bar{2}} - E_{22222}\right]$$

4.5

Table 4.6 Magnetic coupling constants (in cm^{-1}) computed for the 106-atom cluster.[a]

Type	Parameter	M06-L	M06
NN	J_{ea}	9.8	1.7
	J_{ab}	10.1	4.5
	J_{bc}	6.7	2.8
	J_{cd}	10.2	5.2
	average	9.2	3.5
	"central" average[b]	8.4 (10.3)[c]	3.7 (3.6)[c]
NNN	J_{eb}	2.1	0.5
	J_{ac}	1.6	0.4
	J_{bd}	1.4	0.4
	average	1.7 (2.0)[b]	0.4 (0.5)[b]
NNNN	J_{ec}	–0.029	–0.061
	J_{ad}	0.028	0.054
NNNNN	J_{ed}	–0.011	-7.5×10^{-4}

[a]These are Fe5//opt0 (bare 106-atom cluster with no atoms optimized) calculations with the def2-TZVP basis set.

[b]Here "central" average means the average of J_{ab} and J_{bc}.

[c]Values in parentheses are for Fe3//opt0 (bare 88-atom cluster with no atoms optimized) from Table 4.3.

Table 4.6 also shows values averaged over interactions of the same type, which would be the same in a periodic model. (For NN interactions we also show a value average over just the central three atoms). Although we do obtain significantly

closer values for J_{ab} and J_{bc} in the 106-atom cluster with M06, that is not the case with M06-L. Nevertheless, for both the exchange–correlation functionals, the values obtained with this set of equations lead to interactions of the same type being the same as the average within about two cm^{-1} for NN interactions and within a few tenths of a cm^{-1} for NNN interactions. In contrast, we found that considering some higher-energy configurations than the ones reported in Table 4.5 led in some cases to inconsistent values. We conclude that the set of determinants in Table 4.5 provides a stable extraction scheme, justifying its use in the present work. However, the NNNN and NNNNN couplings are extremely small, and even with this more stable set of equations, our cluster is apparently not large enough to yield reliable values for these constants. These values are so small that they are expected to be less quantitatively accurate than the larger NN and NNN coupling values.

Comparing the average values in Table 4.6 to the values from Table 4.3, we find that the 106-atom cluster provides coupling values in reasonable agreement with the 88-atom cluster, within about two cm^{-1} for NN interactions and within a few tenths of a cm^{-1} for NNN interactions.

The effect of optimizing the coordinates of one or more atoms of the bare 88-atom cluster on the magnetic coupling constants is shown in Table 4.7. These effects were investigated using the M06-L and M06 exchange–correlation functionals. Table 4.7 shows that the //opt1 calculations, which involve optimizing only the central iron atom of the cluster, show negligible change in J values compared to the//opt0 calculations for both the functionals. The "//opt12" calculations, which involve optimizing central iron atom of the cluster and the three carboxylates and the two oxido groups around it, show an increase in J values compared to the //opt0 and //opt1 calculations, and this can be attributed to the central iron atom getting closer to the peripheral iron atoms upon optimization.

Table 4.7 Fe–Fe distances (in Å) and magnetic coupling constants (in cm^{-1})[a] of Fe3//opt0, Fe3//opt1, and Fe3//opt12 clusters[b] computed using the def2-TZVP basis set.

System	M06-L			M06		
	J_{NN}[c]	J_{NNN}[d]	Fe–Fe[e]	J_{NN}[c]	J_{NNN}[d]	Fe–Fe[e]
Fe3//opt0	10.3	2.0	3.00, 3.00	3.6	0.5	3.00, 3.00
Fe3//opt1	10.3	2.0	2.97, 3.06	3.4	0.5	2.96, 3.05
Fe3//opt12	16.1	3.0	2.93, 2.92	5.9	0.6	2.93, 2.94

[a]The experimental value reported in Ref. 10 is 4.1 cm^{-1}.

[b]The Fe3//opt0, Fe3//opt1, and Fe3//opt12 notations imply zero, one, and twelve atoms of the bare cluster were optimized, respectively.

[c]J_{NN} is computed by taking the average of J_{ab} and J_{bc}.

[d]$J_{NNN} = J_{ac}$

[e]The first number is the *ab* distance, and the second is the *bc* distance.

Having now completed the benchmark and validation tests to determine the most accurate density functional, a sufficient basis set size, and a sufficient cluster size, we turn to the effect of hydrocarbon adsorption on magnetic coupling constants.

4.4.2 Isotropic Coupling Constants of Physisorbed MOF

The effect on magnetic coupling constants of adsorbed hydrocarbon molecules is illustrated in Table 4.8 and 4.9. Table 4.8 shows the effect the adsorption of three molecules of methane, ethane, or ethylene on the three iron centers of the 88-atom cluster, with all the atoms of the cluster frozen and the three guests being optimized (referred to as Fe3–3guest//opt0). The adsorption of the two saturated hydrocarbon molecules has a small effect on the nearest-neighbor coupling (J_{NN}) and a negligible effect on the next-nearest-neighbor coupling constant (J_{NNN}) when compared to the case when no guest is adsorbed. Furthermore, with the M06 exchange–correlation functional, the *J* values for these two cases agree with the experimental values within 0.8 cm^{-1}. However, our results for the adsorption of the unsaturated hydrocarbon, ethylene, do not agree with experiment in these //opt0 calculations, and this particular case will, therefore, be investigated in detail later.

Table 4.8 Magnetic coupling constants (J in cm^{-1}) of Fe3–3guest//opt0 cluster[a] computed using the def2-TZVP basis set.

Guest	Expt.[b]	M06-L		M06	
	J_{NN}	J_{NN}[c]	J_{NNN}[d]	J_{NN}[c]	J_{NNN}[d]
None	4.1	10.3	2.0	3.6	0.5
CH_4	3.3	7.8	2.2	2.5	0.5
C_2H_6	3.2	8.7	2.2	2.8	0.5
C_2H_4	–3.9	8.6	2.1	2.2	0.5

[a]The Fe3–3guest//opt0 notation implies the cluster-guest complex where the cluster was frozen and the three guest molecules were optimized.

[b]The experimental values are reported in Ref. 10.

[c]J_{NN} is computed by taking the average of J_{ab} and J_{bc}.

[d]$J_{NNN} = J_{ac}$

Table 4.9 is like Table 4.8 except that some of the atoms of the cluster are allowed to relax along with the guest molecules. It is shown using the M06 exchange–correlation functional. The choice of M06 for Table 4.9 is because it provided the best agreement with the experimental values in earlier tables. The //opt3 calculations in Table 4.9 involve optimizing only the adsorbates and three iron atoms of the cluster, and the //opt14 calculations involve optimizing the adsorbates, the three iron atoms of the cluster, and the first coordination environment around each of them (five oxygens around each iron, but two of these are shared between two of the irons). For methane and ethane, the //opt3 calculations show negligible change in J values compared to the //opt0 calculations, but the //opt14 calculations show an increase in J_{NN}. For ethylene, both //opt3 and //opt14 change the coupling by at least 0.5 cm^{-1}. Even after optimizing a portion of the cluster, good agreement with the experimental value for the ethylene complex could not be achieved. The change in magnetic coupling upon optimization with an adsorbed guest arises as a result of an interplay between the changing Fe–Fe and Fe–C distances and the Fe–O–Fe angles. It is hard to sort out the Fe–Fe and Fe–O–Fe effects because we cannot change the internal coordinates one at a time, but we can change the Fe–C distance with the MOF fixed, and we examine that next.

Table 4.9 Fe–Fe distances (in Å) and magnetic coupling constants (J in cm^{-1}) computed using M06/def2-TZVP.

System[a]	Fe–Fe	J_{NN}[b]	J_{NNN}[c]	Expt. J_{NN}[d]
adsorbate = methane				
Fe3–3CH_4//opt0	3.00, 3.00	2.5	0.5	
Fe3–3CH_4//opt3	3.05, 3.18	2.4	0.2	3.3
Fe3–3CH_4//opt14	2.98, 3.10	4.4	0.1	
adsorbate = ethane				
Fe3–3C_2H_6//opt0	3.00, 3.00	2.8	0.5	
Fe3–3C_2H_6//opt3	3.05, 3.19	2.4	0.2	3.2
Fe3–3C_2H_6//opt14	2.99, 3.11	4.6	0.1	
adsorbate = ethylene				
Fe3–3C_2H_4//opt0	3.00, 3.00	2.2	0.5	
Fe3–3C_2H_4//opt3	3.14, 3.33	–0.1	0.0	–3.9
Fe3–3C_2H_4//opt14	3.03, 3.25	1.7	–0.1	

[a]//opt0, //opt3, and //opt14 implies zero, three, and fourteen atoms of the cluster along with the adsorbates were optimized in the cluster-guest complexes (Fe3-3guest), respectively.

[b]J_{NN} is computed by taking the average of J_{ab} and J_{bc}.

[c]$J_{NNN} = J_{ac}$

[d]The experimental values are reported in Ref. 10.

Table 4.10 and Figure 4.4 show how J_{NN} and J_{NNN} in Fe3–3C_2H_4//opt0 change with Fe–C distance. The first row of Table 4.10 corresponds to the internuclear distance in the //opt0 structure, the second row corresponds to single-point calculations at the experimental internuclear distance, and the remaining rows correspond to single-point calculations where the ethylene molecules have been pulled in closer to the iron centers. The table shows that J_{NNN} remains almost constant with changing Fe–C distance, while J_{NN} becomes negative when the ethylene molecules get closer. A graphical representation of J_{NN} vs Fe–C distance is shown in Figure 4.4. When the Fe–C distance becomes 2.22 Å, J_{NN} starts to become negative, although at the expense of causing the energy of the complex to rise by ~50 kcal/mol (Figure 4.5).

Figure 4.4 also gives results for the M06-2X functional. M06-2X yields a smaller magnetic coupling when ethylene is far away, and one might have wondered

if it would show a transition to negative J_{NN} at a larger Fe–C distance, but the figure shows that this is not the case.

Table 4.10 Magnetic coupling constants (in cm^{-1}) of Fe3–3C_2H_4//opt0 cluster[a] computed using M06/def2-TZVP by varying the Fe–C internuclear distance.

	Expt.[b]	**M06**	
Fe–C (Å)	J	J_{NN}[e]	J_{NNN}[f]
2.79, 2.86[c]		2.2	0.5
2.42[d]	–3.9	1.1	0.5
2.22		–0.2	0.4
2.02		–2.5	0.4
1.92		–4.0	0.4
1.82		–5.8	0.4

[a]The Fe3–3C_2H_4//opt0 notation implies only the adsorbate ethylene was optimized and no atom of the cluster was optimized in this complex.

[b]The experimental value is reported in Ref. 10.

[c]The two Fe–C distances at the central iron in the optimized Fe3–3C_2H_4 //opt0complex are unequal. The remaining four Fe–C distances for the peripheral iron centers are 2.80, 2.80, 2.81, and 2.90 Å.

[d]The Fe–C distance of 2.42 Å is the distance reported for the experimental structure.

[e]J_{NN} is computed by taking the average of J_{ab} and J_{bc}.

[f]$J_{NNN} = J_{ac}$

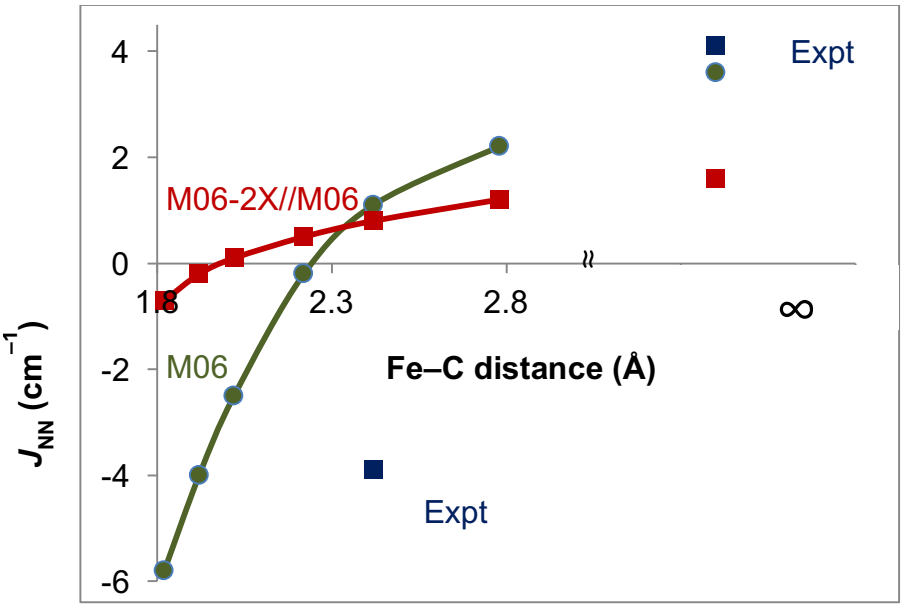

Figure 4.4 J_{NN} (in cm^{-1}) vs Fe–C distance (Å) for Fe3–3C_2H_4//opt0.
The curves were computed using M06/def2-TZVP and M06-2X/def2-TZVP//M06/def2-TZVP. J_{NN} is the average of two nearest-neighbor interactions (J_{ab} and J_{bc}) in the 88-atom cluster model. C_2H_4 molecules were moved rigidly.

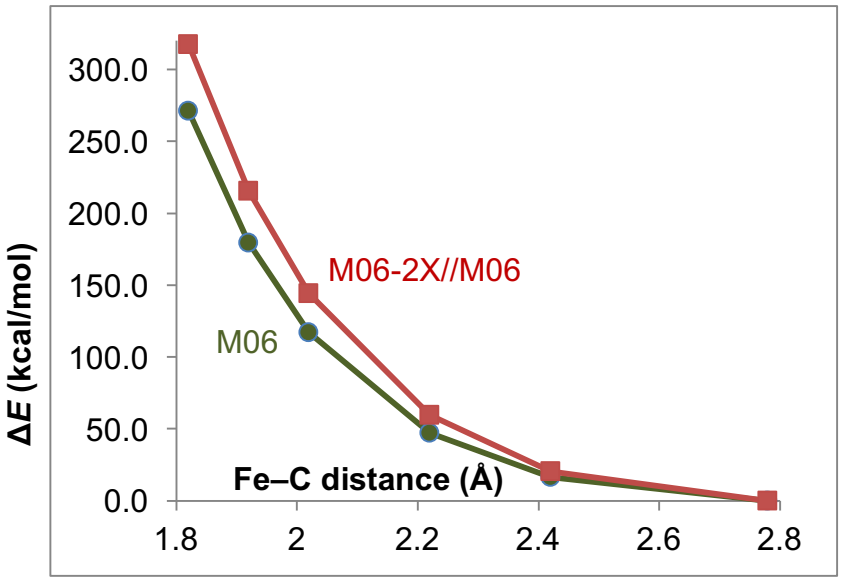

Figure 4.5 ΔE vs Fe–C distance for the Fe3–3C_2H_4//opt0 complex.
The curves were computed using M06/def2-TZVP and M06-2X/def2-TZVP. ΔE is calculated with respect to the energy of the optimized structure in the 222 spin configuration.

Next, we investigated the effect of rotation of the three ethylene molecules in their planes (referred to as horizontal rotation) and perpendicular to their planes

(referred to as vertical rotation). The dihedral angles that were changed are Fe–X–C–H for vertical rotation and O–Fe–X–C for horizontal rotation, where X is a dummy atom placed at the center of the C=C bond, C and H atoms belong to the ethylene molecule, and O is one of the equatorial oxygen atoms. Table 4.11 shows that vertical rotation of the three ethylene molecules causes a small increase in J_{NN}, while the horizontal rotation causes a small decrease in J_{NN}, when compared to the optimized structure. These results show that although the translation of the ethylene molecules toward the iron centers has a moderate effect on J_{NN} and eventually causes flipping of J_{NN} (but only at unrealistically short distances), their rotation has negligible effect.

Table 4.11 Magnetic coupling constants (in cm^{-1})[a] of Fe3–3C_2H_4//opt0 cluster[b] computed using M06/def2-TZVP by rotating the three C_2H_4 molecules.

Angle (°)	J_{NN}[c]	J_{NNN}[d]
Vertical rotation		
Opt	2.2	0.5
120	2.5	0.5
150	2.7	0.6
180	2.7	0.6
Horizontal rotation		
Opt	2.2	0.5
120	2.1	0.6
150	2.0	0.7
180	1.9	0.6

[a]The experimental value reported in Ref. 10 is –3.9 cm^{-1}.

[b]The Fe3–3C_2H_4//opt0 notation implies only the adsorbate ethylene was optimized and no atom of the cluster was optimized in this complex.

[c]J_{NN} is computed by taking the average of J_{ab} and J_{bc}.

[d]$J_{NNN} = J_{ac}$

In Table 4.8–4.11 and Figure 4.4, we find that the calculated J_{NN} value for ethylene does not match the experimental value of –3.9 cm^{-1} for either the partially optimized structures or the ones for which the Fe–C distances have been varied or fixed to the experimental Fe–C distance of 2.42 Å. In Table 4.9, J_{NN} becomes –0.1 cm^{-1} for Fe3–3C_2H_4//opt3, and in Table 4.10, it becomes negative only by bringing

the ethylene molecules as close as 2.22 Å (or even closer than that) to the iron centers. It does become –4.0 cm^{-1} at a distance of 1.92 Å when the ethylene molecules are pulled in sufficiently close to the Fe center, but at the expense of causing the energy to rise by ~180 kcal/mol (Figure 4.5). Therefore, the explanation of the negative value of J_{NN} upon ethylene adsorption must involve further considerations.

On examining the experimental structure of the ethylene complex, one finds that the nearest-neighbor Fe–Fe distance is 3.16 Å, much larger than the 3.00 Å in the bare MOF. To study the effect of this relaxation of the MOF, we carried out periodic DFT calculations not only on the ethylene complex but also the ethane complex and the bare MOF by optimizing with GAM+U and PBE+U for various values of $U–J$ using the experimental lattice constants as initial guesses. The rationale for choosing +U corrected local density functionals is as follows. In Table 4.3 we showed by using cluster calculations that good agreement with experiments could be achieved for magnetic coupling constant by using hybrid density functionals. However, when plane-wave basis sets are used, as in the present calculations, the computation of the HF exchange terms may become very expensive when large supercells are used, as is required for the accurate computation of magnetic couplings. The DFT+U method is a practical alternative in that the +U correction mimics some of the orbital-dependent self-interaction effects that are present in calculations with HF exchange,[198,199,200,201] but at a much lower cost in plane wave calculations than a hybrid functional.

The geometries of the three structures are presented in Table 4.12, and their magnetic couplings are in Table 4.13. For the values of $U–J$ tested in Table 4.12, we find that GAM+U ($U–J$ = 2 eV) has the best agreement with experiments for Fe_2(dobdc) and $Fe_2(C_2H_6)_2$(dobdc), and PBE+U ($U–J$ = 2 eV) has the best agreement with experiments for $Fe_2(C_2H_4)_2$(dobdc). For a small value of the $U–J$ correction (0.25 eV) to GAM, the mean unsigned error (MUE) is quite high for Fe_2(dobdc) and $Fe_2(C_2H_6)_2$(dobdc) and increasing the $U–J$ value reduces the MUE. From both theory and experiment it can be seen that the adsorption of ethylene has more significant effect on the geometry of Fe_2(dobdc) than the adsorption of ethane. The important changes in the geometry are in the Fe–Fe (NN) and Fe–Fe (NNN) distances and in the Fe–O_{oxido}–Fe and in the Fe–$O_{carboxylate}$–Fe angles. Next, we

examine the impact these changes in geometries have on the magnetic coupling values. It is indeed interesting to see if the methods that give good geometries in Table 4.12 can also give accurate coupling values in Table 4.13.

Table 4.12 Key bond distances (in Å) and angles (°) of Fe_2(dobdc), $Fe_2(C_2H_6)_2$(dobdc), and $Fe_2(C_2H_4)_2$(dobdc) periodic structures fully optimized using DFT+U in ground configuration.

Method	**GAM+U**	**GAM+U**	**GAM+U**	**PBE+U**	**Expt.**[b]
***U–J* (eV)**[a]	**0.25**	**1.00**	**2.00**	**2.00**	
		Fe_2(dobdc)			
Fe–Fe (NN)[c]	2.80	2.97	2.98	2.97	3.00
Fe–Fe (NNN)[d]	4.78	4.92	4.94	4.96	4.96
<Fe–O_{eq}>[e]	2.05	2.06	2.06	2.07	2.09
Fe–O_{ax}	2.12	2.15	2.16	2.12	2.13
Fe–O_{oxido}–Fe	85.2	92.0	92.7	91.8	95.1
Fe–$O_{carboxylate}$–Fe	84.7	89.1	89.2	89.7	89.9
MUE[f] (distances)	0.11	0.03	0.02	0.02	0.00
MUE[f] (angles)	7.5	2.0	1.6	1.7	0.0
		$Fe_2(C_2H_6)_2$(dobdc)			
Fe–Fe (NN)[c]	2.82	2.99	3.01	2.98	2.96
Fe–Fe (NNN)[d]	4.79	4.93	4.96	4.96	4.94
<Fe–O_{eq}>[e]	2.05	2.06	2.07	2.07	2.01
Fe–O_{ax}	2.13	2.16	2.17	2.13	2.12
<Fe–H>[g]	3.20	2.88	2.83	3.06	2.59
C–C	1.50	1.50	1.50	1.53	1.47
Fe–O_{oxido}–Fe	86.1	92.9	93.7	92.3	99.4
Fe–$O_{carboxylate}$–Fe	85.4	89.7	89.8	89.9	90.9
MUE[f] (distances)	0.28	0.13	0.12	0.20	0.00
MUE[f] (angles)	9.4	3.9	3.4	4.1	0.0
		$Fe_2(C_2H_4)_2$(dobdc)			
Fe–Fe (NN)[c]	3.22	3.17	3.11	3.20	3.16
Fe–Fe (NNN)[d]	5.19	5.16	5.08	5.21	5.11
<Fe–O_{eq}>[e]	2.10	2.10	2.09	2.11	2.08
Fe–O_{ax}	2.24	2.21	2.20	2.22	2.18
<Fe–C>[h]	2.41	2.54	2.80	2.42	2.43
C–C	1.34	1.33	1.33	1.35	1.28
Fe–O_{oxido}–Fe	103.3	101.3	98.0	101.8	102.3
Fe–$O_{carboxylate}$–Fe	92.7	92.1	91.4	93.0	92.4
MUE[f] (distances)	0.04	0.06	0.16	0.04	0.00
MUE[f] (angles)	0.7	0.6	2.6	0.5	0.0

[a] *U* = Coulomb interaction parameter and *J* = exchange interaction parameter.

[b]The experimental data is taken from Ref. 10.

[c,d]NN = nearest-neighbor and NNN = next-nearest-neighbor.

[e]Average Fe−O distance of the four equatorial oxygen atoms in the first coordination shell of Fe(II).

[f]MUE = mean unsigned error.

[g]Average Fe−H distance of the two closest H atoms of ethane directed toward the Fe^{II} center.

[h]Average Fe−C distance of the two C atoms of ethylene bound to Fe(II) center.

The three periodic models have two chains of Fe atoms and hence both intrachain and interchain (J_{IC}) coupling constants can be calculated. The three Slater determinants that are required to compute the coupling constants are represented by $|M_{S_{a1}}M_{S_{b1}}M_{S_{c1}}, M_{S_{a2}}M_{S_{b2}}M_{S_{c2}}\rangle$ where the M_S values before and after comma are the values for the iron centers in the two chains (Figure 1.3). These determinants are used to determine the isotropic coupling constants, J_{NN} and J_{IC}, by solving the following equations:

$$\langle 222,222 | H_{HDV} | 222,222\rangle = E_{222,222} = -2[6J_{NN}2\cdot 2 + 6J_{IC}2\cdot 2]$$
$$\langle 2\bar{2}2,2\bar{2}2 | H_{HDV} | 2\bar{2}2,2\bar{2}2\rangle = E_{2\bar{2}2,2\bar{2}2} = -2[-2J_{NN}2\cdot 2 + 6J_{IC}2\cdot 2]$$
$$\langle 222,\bar{2}\bar{2}\bar{2} | H_{HDV} | 222,\bar{2}\bar{2}\bar{2}\rangle = E_{222,\bar{2}\bar{2}\bar{2}} = -2[6J_{NN}2\cdot 2 - 6J_{IC}2\cdot 2]$$

4.6

where H_{HDV} is the HDV Hamiltonian represented by eq 4.1, $E_{222,222}$ is the total energy of the ferromagnetic case, and $E_{222,\bar{2}\bar{2}\bar{2}}$ and $E_{2\bar{2}2,2\bar{2}2}$ are the total energies of the two antiferromagnetic cases. Solving eq 4.6 results in

$$J_{IC} = \frac{1}{96}\left[E_{222,\bar{2}\bar{2}\bar{2}} - E_{222,222}\right]$$
$$J_{NN} = \frac{1}{64}\left[E_{2\bar{2}2,2\bar{2}2} - E_{222,222}\right]$$

4.7

The resulting magnetic coupling constants for the methods in Table 4.12 are presented in Table 4.13, where they are compared to the experimental data for Fe_2(dobdc), $Fe_2(C_2H_6)_2$(dobdc), and $Fe_2(C_2H_4)_2$(dobdc). From experiments, we find that adsorption of ethane decreases J_{NN} by less than 1 cm^{-1} and the adsorption of ethylene changes the sign of J_{NN} indicating that antiferromagnetic coupling between the iron centers along a chain is the ground state. Table 4.13 shows that GAM+U with $U - J$ equal to 2 eV agrees quite well with experiments for Fe_2(dobdc) and $Fe_2(C_2H_6)_2$(dobdc), while GAM+U with $U - J$ equal to 1 eV agrees quite well with experiments for $Fe_2(C_2H_4)_2$(dobdc) in terms of both sign and magnitude. Based on the value of J_{NN} it can be said that GAM+U ($U - J$ = 1 eV) also gives reasonable results for Fe_2(dobdc) and $Fe_2(C_2H_6)_2$(dobdc). Hence, GAM+U with a $U - J$ value of 1 eV describes the coupling in the three compounds adequately. This method also gives reasonably good agreement with experiments for geometries (see Table 4.12).

To understand if the decrease in J_{NN} value with ethane adsorption or the switch in sign of J_{NN} from positive in bare MOF to negative upon ethylene adsorption comes from the structural changes associated with adsorption or from the ligand field effect of the adsorbate, we take the following approach to separate the effect of the two contributions, geometrical changes and ligand field effect, on J_{NN}. The optimized structure of bare Fe_2(dobdc) is assumed to go to the optimized structure of the high-coverage Fe_2(dobdc)–adsorbate in two conceptual steps. In the first step, bare Fe_2(dobdc) changes its geometry in the absence of any adsorbate and takes the geometry of the MOF fragment in the high-coverage Fe_2(dobdc)–adsorbate system. This is followed by the second step where the adsorbate now binds to the Fe(II) centers in the same MOF structure as in the high-coverage Fe_2(dobdc)–adsorbate. During the second step, the geometry of the MOF itself does not change.

To compute coupling value at the end of the first step (which gives us the effect of only changing the MOF geometry), we use the structures of $Fe_2(C_2H_6)_2$(dobdc) and $Fe_2(C_2H_4)_2$(dobdc) optimized by using GAM+U (with $U - J$ = 1 eV, in Table 4.12) and remove the adsorbates, ethane and ethylene, from these structures. The spin states of the iron centers do not change upon removal of the

adsorbates. This gives rise to two newly created bare Fe_2(dobdc) structures that differ from the optimized bare Fe_2(dobdc) only in terms of geometry. The J_{NN} values for these newly created bare Fe_2(dobdc) structures were determined by doing single-point calculations using GAM+U (with $U - J = 1$ eV) for the spins described by Figure 4.3. We find that the bare Fe_2(dobdc) structure created from the ethane complex has J_{NN} equal to 5.6 cm^{-1}, which lies between that of optimized bare Fe_2(dobdc) (6.0 cm^{-1}) and $Fe_2(C_2H_6)_2$(dobdc) (5.2 cm^{-1}) (Table 4.13). Hence, the effect of change in geometry is 0.4 cm^{-1} (6.0 – 5.6) and the effect of the ligand field of ethane is 0.4 cm^{-1} (5.6 – 5.2). The bare Fe_2(dobdc) structure created from the ethylene complex has J_{NN} equal to –0.4 cm^{-1}, and this lies between that of optimized bare Fe_2(dobdc) (6.0 cm^{-1}) and $Fe_2(C_2H_4)_2$(dobdc) (–3.1 cm^{-1}) (Table 4.13). Hence, the effect of change in geometry in this case is 6.4 cm^{-1} (6.0 – (–0.4)) and the effect of the ligand field of ethylene is 2.7 cm^{-1} (–0.4 – (–3.1)). This shows that both factors play an important role in determining the magnetic coupling. The effect of change in geometry for the ethane case (0.4 cm^{-1}) is much smaller than the ethylene case (6.4 cm^{-1}), which can be attributed to the fact that ethylene complex undergoes more significant structural changes than does the ethane complex.

Unlike the periodic calculations described in Table 4.12–4.13, the cluster calculations had most of the MOF framework frozen, and the geometry changes occurred only for the optimized atoms, and hence the case of ethylene adsorption that involved a significant change in the geometry of the MOF framework could not be treated properly. For the M06 cluster calculations shown for ethylene adsorption in Figure 4.4 and Table 4.10, we found that J_{NN} takes negative values at Fe–C distances less than or equal to 2.22 Å and with the MOF framework fixed at the geometry of the bare MOF. We found that one needs to go to unphysical Fe–C distance to achieve agreement with the experimental value of magnetic coupling. In contrast to this, Table 4.13 shows that with full optimization by periodic GAM+U (with $U - J = 0.25$ and 1 eV) and PBE+U (with $U - J = 2$ eV) calculations, we can achieve negative J_{NN} values for the optimized structures that have Fe–C distance greater than 2.22 Å (Table 4.12). This shows that not just the Fe–C distance is important in determining the magnetic coupling, but also the geometrical parameters of the MOF framework that

changed more significantly with the high-coverage adsorption of ethylene than with ethane. In the next three paragraphs, we compare our work to that reported in the literature.

In Ref. 157, Canepa *et al.* showed using periodic DFT calculations with PBE and ultrasoft psuedopotentials that the nearest-neighbor magnetic coupling constant of Fe_2(dobdc) is ~28 cm^{-1} when the experimental structure of Fe_2(dobdc) is used. Their work uses the same HDV Hamiltonian as given by eq 4.1 here; hence we can compare the result of Ref. 157 to the PBE result presented in Table 4.3 for cluster calculations done using the experimental structure. In Table 4.3, the nearest-neighbor magnetic coupling constant computed using PBE/def2-TZVP is 14.5 cm^{-1}. The difference of ~14 cm^{-1} between the two results is possibly due to the difference in the basis set used. The prediction of Ref. 157 is consistent with our observation of Table 4.3 that most of the local functionals overestimate the nearest-neighbor magnetic coupling.

In Ref. 158, Park *et al.* studied the guest-induced magnetic transition from FM to AFM in Fe_2(dobdc) due to adsorption of olefins. By performing periodic DFT calculations, they showed that in Fe_2(dobdc) and Fe_2(dobdc)-paraffin complexes, the magnetic ordering is FM, while in Fe_2(dobdc)-olefin complexes, the magnetic ordering is AFM. The olefins that they investigated were acetylene, ethylene, and propylene and the paraffins that they investigated were methane, ethane, and propane. Our periodic DFT calculations reported for the bare MOF and the ethane and ethylene cases in Table 4.13 are consistent with these observations. In Ref. 158, the switch in magnetic ordering with olefin adsorption was attributed mainly due to geometry changes in the MOF framework that occurred upon π-complexation with the olefins, and similarly, we find that change in geometry of the MOF plays an important role in deciding the magnetic coupling and ordering of the ethylene complex. As described in an earlier paragraph, we have shown that the change in geometry of Fe_2(dobdc) caused due to ethylene adsorption results in a decrease in magnetic coupling by 6.4 cm^{-1} and the effect of the presence of ethylene further decrease it by 2.7 cm^{-1}, ultimately resulting in AFM ordering. Hence one can conclude that magnetic coupling and magnetic ordering can be affected by both geometrical changes in the MOF framework as well as the presence of the adsorbate.

In Ref. 161, Han *et al*. studied the magnetic behavior of Fe_2(dobdc) and $Fe_2(C_2H_4)_2$(dobdc) using RPBE-D2+U with an "effective *U* parameter" of 1.0 eV for Fe atoms. The optimizations of both these structures were done using a plane-wave basis set and the PAW potential implemented in *VASP*. The nearest-neighbor magnetic coupling constants were extracted using the same HDV Hamiltonian as used by Ref. 157 and this work (eq 4.1). The magnetic coupling values for Fe_2(dobdc) and $Fe_2(C_2H_4)_2$(dobdc) were found to be 2.1 and –5.4, respectively, which are in good agreement with experiments and with our results presented in Table 4.13 using both PBE+U and GAM+U. The preferred magnetic ordering of Fe_2(dobdc) and $Fe_2(C_2H_4)_2$(dobdc) are ferromagnetic and antiferromagnetic, respectively, which agrees with the work of Ref. 161. The geometrical parameters, Fe–Fe distances and Fe–O–Fe angles, for both the structures reported in Table 4.12 were also found to be in good agreement with experiments and with Ref. 161, Table 4.12.

Table 4.13 Magnetic coupling constants (in cm^{-1})[a] of the three periodic systems computed using DFT+U.

System	atoms in unit cell	Method	*U*–*J* (eV)	J_{NN}	zJ_{IC}[c]
Fe_2(dobdc)	54	GAM+U	0.25	103.0	–6.5
		GAM+U	1.00	6.0	–6.2
		GAM+U	2.00	2.8	–1.6
		PBE+U	2.00	1.4	–4.1
		expt.[b]	-	4.1	–3.4
$Fe_2(C_2H_6)_2$(dobdc)	112	GAM+U	0.25	92.1	–4.7
		GAM+U	1.00	5.2	–6.6
		GAM+U	2.00	2.6	–1.7
		PBE+U	2.00	0.4	–4.9
		expt.[b]	-	3.2	–2.9
$Fe_2(C_2H_4)_2$(dobdc)	90	GAM+U	0.25	–7.1	–3.6
		GAM+U	1.00	–3.1	–3.3
		GAM+U	2.00	0.0	–1.7
		PBE+U	2.00	–7.1	–3.5
		expt.[b]	-	–3.9	–3.3

[a]The coupling constants, J_{NN} and J_{IC}, were computed by relaxing the MOF in the $222, \bar{2}\bar{2}\bar{2}$ spin configuration, followed by single-point calculations on the optimized geometry using 222, 222 and $2\bar{2}2, 2\bar{2}2$ spin configurations. Equations used to compute coupling constants are described by eq 4.7.

[b]The experimental values are taken from Ref. 10.

[c]Here $z = 3$ and is based on the fact that each chain has equal interaction with three nearest-neighbor chains.

4.4.3 Isotropic Coupling Constants of Chemisorbed MOF

The calculated magnetic coupling parameters for Fe_2(dobdc), $Fe_2(O)_2$(dobdc), and $Fe_2(OH)_2$(dobdc) are provided in Table 4.14 and 4.15. The periodic DFT calculations with PBE+U were run with both primitive unit cells (54, 60, or 66 atoms) and doubled cells (108, 120, or 132 atoms) as indicated in the second column of Table 4.14. This table shows that there is no significant difference between the PBE+U calculations with 54 and 108 atoms in the unit cell, which indicates that the primitive cell is adequate for these computations. The same is true for couplings in $Fe_2(O)_2$(dobdc) and $Fe_2(OH)_2$(dobdc).

The PBE nearest-neighbor couplings in Fe_2(dobdc) are two orders of magnitude larger both than the experimental ones and then those computed with the other methods tested in Table 4.14. The PBE values are calculated for the PBE geometry, which has short Fe···Fe distances. The overestimation of magnetic properties by GGA functionals is well established.[202] A previous study[157] of magnetic interactions in Fe_2(dobdc) employed the PBE exchange-correlation functional with experimental geometries and obtained a J_{NN} equal to 28 cm^{-1}, which is smaller but still a significant overestimation. They concluded[157] that there is fairly strong ferromagnetic coupling in Fe_2(dobdc). It now appears that such large calculated J_{NN} values are an artifact of the simple gradient approximation used in the PBE functional. This was first shown in Ref. 27 where a calculation with HF exchange gave 3.6 cm^{-1}, in good agreement with the experimental value of 4.1 cm^{-1}.

Table 4.14 shows that the PBE+U and HSE06 calculated values of J_{NN} are smaller than the PBE value and in more reasonable agreement with experiment. For Fe_2(dobdc) the coupling values obtained by HSE06 and HSE06-D2 are identical to each other and are larger than those predicted by PBE+U, whereas for the $Fe_2(O)_2$(dobdc) and $Fe_2(OH)_2$(dobdc) cases, HSE06 and HSE06-D2 yield magnetic couplings that are smaller than the values computed with PBE+U and PBE. PBE+U and HSE06 predict the same signs of the magnetic couplings.

Table 4.14 shows that the periodic calculations of J_{NNN} using PBE+U yield 0.3 cm^{-1}, –0.1 cm^{-1}, and –0.9 cm^{-1} for $Fe_2(dobdc)$, $Fe_2(OH)_2(dobdc)$, and $Fe_2(O)_2(dobdc)$, respectively. These J_{NNN} values may be compared to the respective J_{IC} coupling values of –0.6 cm^{-1}, –2.1 cm^{-1}, and 0.4 cm^{-1}. The magnitude of the PBE+U J_{IC} coupling values for $Fe_2(dobdc)$ and $Fe_2(O)_2(dobdc)$ are smaller than the J_{NNN} values, while the PBE+U J_{IC} value of $Fe_2(OH)_2(dobdc)$ is larger than the J_{NNN} value. It is worth noting that the J_{IC} coupling values for $Fe_2(OH)_2(dobdc)$ are notably larger than the other two cases with all functionals. This may indicate that separate from the oxidation of the metal centers, an addition of the $(OH)^-$ groups enhance interchain magnetic coupling.

Table 4.14 Periodic DFT exchange and coupling energies (cm^{-1}) of the iron centers.[a]

method	atoms	$E_{AFM1} - E_{FM}$ ($E_{AFM3} - E_{FM}$)	$E_{AFM2} - E_{FM}$	$J_{NN}(J_{NNN})$	J_{IC}
			Fe(II) case: $Fe_2(dobdc)$		
PBE	54	7287.7	–160.0	113.9	–5.0
PBE+U	108	56.6(92.9)	–121.1	0.5(0.3)	–1.9
PBE+U	54	41.6	–60.4	0.7	–1.9
PBE+U-D2	54	31.1	–64.6	0.5	–2.0
HSE06	54	171.6	–32.2	2.7	–1.0
HSE06-D2	54	163.2	–47.5	2.6	–1.5
GAM+U	54	145.4	–52.8	2.3	–1.7
Expt.[b]		-	-	4.1	–1.1
			Fe(III) case: $Fe_2(OH)_2(dobdc)$		
PBE	66	–2308.1	–2042.3	–23.1	–40.8
PBE+U	132	–3216.0(–2259.0)	–630.7	–10.2(–1.1)	–6.3
PBE+U	66	–1129.6	–315.9	–11.3	–6.3
PBE+U-D2	66	–1133.9	–311.7	–11.3	–6.2
HSE06	66	–562.0	–169.8	–5.6	–3.4
HSE06-D2	66	–561.4	–170.3	–5.6	–3.4
GAM+U	66	–691.7	–272.7	–6.9	–5.5
			Fe(IV) case: $Fe_2(O)_2(dobdc)$		
PBE	60	–795.8	–164.1	–12.4	–5.1
PBE+U	120	–205.6(–270.2)	81.1	–1.2(–0.9)	1.3
PBE+U	60	–133.8	40.9	–2.1	1.3
PBE+U-D2	60	–157.6	36.1	–2.5	1.1
HSE06	60	–31.8	17.9	–0.5	0.6
HSE06-D2	60	–43.3	15.8	–0.7	0.5
GAM+U	60	17.5	–42.4	0.3	–1.3

[a]All coupling values were extracted using geometries optimized with the FM spin state. E_{FM} is the electronic energy of the ferromagnetic state, E_{AFM1} is the electronic

energy of antiferromagnetic state 1, and E_{AFM2} is the electronic energy of antiferromagnetic state 2 (see Figure 4.6). E_{AFM3} is the electronic energy of antiferromagnetic state 3 of the supercell. J_{NN}, J_{IC}, and J_{NNN} coupling parameters represent the nearest-neighbor, interchain, and next-nearest-neighbor magnetic couplings, respectively.

[b]Ref. 10.

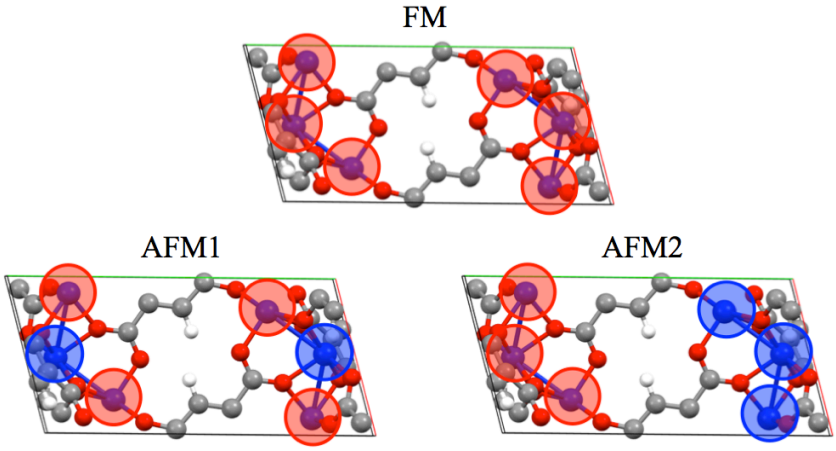

Figure 4.6 A side view of the primitive unit cell of Fe_2(dobdc).
The entirely ferromagnetic (FM), intrachain antiferromagnetic (AFM1), and interchain antiferromagnetic spin states were considered in this work (AFM2). AFM1 is actually ferrimagnetic with this unit cell. Iron is represented by blue, oxygen by red, carbon by gray, and hydrogen by white. Red and blue circles indicate the upward or downward spin of the high-spin iron ions, respectively.

Table 4.15 provides the results of cluster calculations that can be compared to the periodic calculations in Table 4.14. The PBE+U optimized periodic structures were close to the experimental structure, therefore, they used to make the clusters in most cases. The PBE//PBE J_{NN} value is much larger than the PBE//PBE+U value, in part because the periodic PBE metal-metal bond distances are too small for Fe_2(dobdc). The PBE//PBE cluster calculation predicts J_{NN} values for Fe_2(dobdc) that are significantly larger than the experiment. However, the cluster J_{NN} values obtained by HSE06, M06, PBE0, B3LYP, and GAM+U are all quite reasonable when compared to both the periodic and experimental magnetic coupling parameters.

The results for PBE+U structures in Table 4.15 show that HF exchange in HSE06, PBE0, M06, and B3LYP, decreases the predicted intrachain coupling values. If one assumes that the main effect of the U parameter is to mimic HF exchange, this is consistent with the periodic results.

The cluster values of J_{NNN} in Table 4.15 are considerably smaller than the periodic calculations of J_{NNN} in Table 4.14. They do, however, correctly predict the experimentally determined magnetic ordering of Fe_2(dobdc) and $Fe_2(OH)_2$(dobdc). In the case of $Fe_2(O)_2$(dobdc), the magnetic coupling values are likely extremely weak, which is why GAM+U and HSE06//PBE+U predict different magnetic orderings than the other functionals. This demonstrates the difficulty of accurately calculating the small energies of these interactions.

Table 4.15 Isotropic magnetic coupling constants of the iron centers for each studied MOF as obtained by cluster calculations.[a]

Method	J_{NN} (J_{NNN}) (cm^{-1})		
	Fe_2(dobdc)	**$Fe_2(OH)_2$(dobdc)**	**$Fe_2(O)_2$(dobdc)**
PBE//PBE	64.6	–18.2	–9.9
PBE//PBE+U	14.3	–18.7	–9.0
HSE06//PBE+U	2.4 (0.4)	–3.2 (–0.1)	0.3 (–0.2)
M06//PBE+U	4.3	–3.9	–0.5
PBE0//PBE+U	2.5	–3.1	–0.1
B3LYP//PBE+U	2.7	–4.1	–0.5
Expt.[b]	4.1	-	-

[a] X//Y indicates a cluster calculation with method X employing a fragment of a MOF optimized by periodic calculations with method Y. Only nearest- and next-nearest-neighbor intrachain coupling values (J_{NN} and J_{NNN}) were computed, and they may be compared with Table 4.14.

[b] Ref. 10.

It was suggested by Park *et al.*[17] that the changes in magnetism within Fe_2(dobdc) upon guest adsorption are due to structural changes within the MOF. When the intrachain Fe···Fe distances were less than ~3.12 Å, the magnetic interactions were interpreted as being dominated by direct exchange between the metal centers and were ferromagnetic; at longer Fe···Fe separations, the magnetic interactions were interpreted as dominated by superexchange through the bridging oxygen atoms. In our work, $Fe_2(O)_2$(dobdc) has intrachain Fe···Fe distances of ~3.12 Å and the nearest-neighbor AFM coupling is calculated to be very weak (Table 4.14 and 4.15). For comparison, $Fe_2(OH)_2$(dobdc) has intrachain Fe···Fe distances of ~3.22 Å and shows a larger AFM coupling. But the Fe···Fe separation is not the only geometrical parameter that changes. Fe–O_c–Fe bond angles increase from Fe_2(dobdc)

to $Fe_2(O)_2$(dobdc) to $Fe_2(OH)_2$(dobdc). Table 4.14 shows that these structural changes are associated with a switch from positive J_{NN} values to negative J_{NN} values—i.e., a switch from FM to AFM coupling of the nearest-neighbor metal centers. However, many factors besides geometry may contribute to the changes in magnetic coupling. These factors include electronic effects resulting from (1) the presence of the $(OH)^-$ and O^{2-} ligands, (2) the change in oxidation state to Fe(III) for $(OH)^-$ and to Fe(IV) for O^{2-}, and (3) the change in spin state of the metal centers from quintet to sextet resulting from the inclusion of the $(OH)^-$ ligands. The magnetic coupling equations for $Fe_2(OH)_2$(dobdc) take into account the effect of the spin state change (3), but, completely separating all three of these electronic contributions from the geometric contributions required a separate set of calculations.

4.5 Concluding Remarks

Fe_2(dobdc) is a metal–organic framework with localized unpaired electrons on the Fe(II) sites. These Fe(II) ions are susceptible to moderate isotropic coupling between them. The adsorption of hydrocarbons, mainly driven by medium-range correlation effects, in particular dispersion interactions, does not significantly change the electronic structure of the Fe(II) centers, in the sense that the +2 oxidation number remains, and that the effective magnetic interactions do not completely change to a different regime after adsorption.

Prior to studying the role of guest adsorption on the isotropic couplings, we studied the dependence of the computed couplings on (i) the choice of the exchange–correlation functional, (ii) the basis set size, (iii) the cluster size, and (iv) the choice of a cluster model *vs.* a periodic model. It is shown that the hybrid exchange-correlation functionals provide good coupling values with a triple-zeta plus polarization basis set on the 88-atom cluster, and that the results are converged with respect to the basis set and cluster size. Thus, these levels of theory were considered to study the role of the adsorption on the coupling values. It is found that the cluster models give a good agreement with experimental values for Fe_2(dobdc) and Fe_2(dobdc) dosed with saturated hydrocarbons. For the periodic models calculated using DFT+U, good agreement with experiments could be achieved for all the structures by choosing appropriate values of U.

In contrast to Fe_2(dobdc) and the physisorbed species, the derivatives, $Fe_2(O)_2$(dobdc) and $Fe_2(OH)_2$(dobdc), feature AFM coupling down each metal chain. We find here that the effect can also be partially accounted for by the electronic effect of the ligands, the oxidation state of the metal centers, and/or the spin state of the metal centers, even in the absence of geometry changes. This indicates that structural and electronic changes upon framework oxidation likely act in concert to effect magnetic coupling.

The computationally efficient PBE+U and GAM+U approaches predict structural properties that agree quite well with the values obtained using more expensive hybrid functionals. Inclusion of damped dispersion effects by molecular mechanics does alter equilibrium volumes; however, the effect is minor when compared to the inclusion of HF exchange. Thus, rescaling PBE+U or GAM+U unit cells and correcting for the electronic structure with single-point hybrid functional calculations appears to be an efficient approach to calculate magnetic properties of MOFs. Cluster models can be used to compute J_{NN} coupling values quite accurately, and can be used conveniently with a wider array of computational methods at a lower cost. However, capturing both the J_{NN} and J_{IC} magnetic coupling dependency on the MOF structure does require periodic calculations. Overall, theory can correctly describe the magnetic and electronic properties and their structural dependencies for these materials provided one is aware of the strength and limitations of both periodic and cluster-based modeling.

5 Density Functional Development

5.1 Synopsis

Local approximations to exchange–correlation functionals are widely used in Kohn–Sham density functional theory. They are especially attractive owing to their low computational cost combined with the relatively high accuracy for key properties. This work aims at developing improved local functionals, which are trained and validated using a newly extended broad database called Database 2015, which is organized in terms of databases and subdatabases. The key properties considered in Database 2015 are main group bond energies, transition metal bond energies, reaction barrier heights, molecular structures, lattice constants and band gaps of solids, solid-state cohesive energies, etc. A nonseparable gradient approximation (NGA), as first employed in the N12 functional, is optimized using Database 2015 by adding smoothness constraints to the optimization of the functional. The resulting functional called gradient approximation for molecules (GAM) gives better results than any available generalized gradient approximation (GGA) or NGA for most of the properties.

This work also examines the question of how a Hubbard U correction to a local exchange–correlation functional, which leads to the DFT+U method, compares with adding Hartree–Fock exchange to a local functional for both solid-state and molecular properties. We find that a calculation with a Hubbard U correction may or may not mimic a hybrid functional—depending on the atom, the subshell, and the property to which it is applied.

Local functionals usually underestimate band gaps and molecular excitation energies, and therefore, it becomes necessary to use more expensive hybrid functionals or more empirical DFT+U functionals for accurate predictions and modeling of these properties. In addition to GAM, this work presents two more local functionals—a GGA called High Local Exchange 2016 (HLE16) and a meta-GGA called High Local Exchange 2017 (HLE17), and illustrates how they can be useful for obtaining accurate semiconductor band gaps and molecular excitation energies. The HLE functionals provide a strategy for calculating properties that are otherwise difficult to calculate by a local functional, and unlike the conventional way of using

the DFT+U method, one does not need to determine new parameters for every property or system studied.

5.2 Introduction

KS-DFT has been very successfully used for electronic structure calculations in both physics and chemistry.[35] The accuracy of KS calculations depends on the quality of the exchange–correlation functional. The quest for quantum mechanical methods that can be accurately applied to study atomic, molecular, and material properties has resulted in the design of exchange–correlation functionals with a variety of ingredients, costs, and accuracies, where the accuracy may depend strongly on the kind of property that is calculated. Exchange–correlation functionals that depend only on spin-up and spin-down electronic densities (ρ_α and ρ_β) are known as local spin density approximations (LSDAs), and ones that depend on both the spin densities and spin density gradients are called gradient approximations (GAs, in particular, GGAs and NGAs). More complicated functionals include ingredients calculated from the orbitals (which are functionals of the density), in particular, spin-up and spin-down local kinetic energy densities (as in meta-GGAs and meta-NGAs), nonlocal Hartree–Fock exchange (as in hybrid functionals), and/or nonlocal correlation (as in doubly hybrid functionals, which have nonlocal exchange and nonlocal correlation.). (One can also include nonlocal correlation without including nonlocal exchange.) Functionals depending only on local variables, such as spin densities, their gradients, and spin-specific local kinetic energy densities, are often called local (especially in the chemistry literature, while the physics literature often labels them as semilocal if they include density gradients or spin kinetic energy densities).

Even though the meta and nonlocal functionals can give more accurate results than GGAs and LSDAs, the GAs are still of great interest for four reasons. First, GAs are widely implemented in many programs because of their ease of coding. Second, GAs often have better self-consistent field (SCF) convergence and smaller grid requirements than meta functionals. Third, calculations employing GAs are less expensive than calculations involving nonlocal functionals, with the difference being more pronounced for extended and large systems and when geometries are optimized. The fourth reason for special interest in GAs is that local functionals often have better

performance than hybrid functionals, on average, for systems with high multi-reference character. Multi-reference character is the extent to which a wave function is inherently multi-configurational so that a single Slater determinant does not provide a good starting point (reference function) for approximating the complete wave function. Although KS theory does not calculate the wave function of the interacting system, it does use a Slater determinant to represent the density, and calculating the exchange from the Slater determinant, as in Hartree–Fock exchange, can introduce static correlation error, a result of which is that it is often more challenging to obtain good approximations for multi-reference systems when Hartree–Fock exchange is included. (The unknown exact exchange–correlation energy functional includes nonlocal exchange effects and does not have static correlation error, but the problem just mentioned is not completely solved by currently available functionals). Multi-reference systems are sometimes called strongly correlated. Many open-shell systems and transition-metal systems have multi-reference character, and hence the ability to treat multi-reference systems is critical to the ability to treat many catalytic reaction mechanisms. Systems without high multi-reference character are called single-reference systems.

Most GAs have a form that separately approximates exchange and correlation, as first introduced by Langreth and Mehl[203] and usually called a generalized gradient approximation[204] (GGA); however, it has been shown that a nonseparable gradient approximation[167] (which has more flexibility at the cost of satisfying less exact constraints) is capable of performing well for a broader set of properties. The original NGA, called N12,[167] was designed to give good predictions both of solid-state lattice constants and of cohesive energies and molecular atomization energies; it also gave good predictions of molecular bond lengths. Here we show that we can get improved performance for barrier heights (which are important for studies of both uncatalyzed and catalyzed reactions) by relaxing the accuracy for lattice constants, which are not needed for molecular (as opposed to solid-state) processes. By diminishing the emphasis on obtaining good lattice constants we can obtain an exchange–correlation functional that may be more useful for treating many large and complex homogeneous and enzymatic catalysts that do not require the calculations on solid-state material.

A second goal of this work is to obtain improved results for compounds containing metal atoms, including transition metal compounds with high multi-

reference character, by incorporating a greater amount of representative data for metal-ligand bond energies in the training set of a density functional. A third goal of the present work is to obtain a very smooth exchange–correlation functional by enforcing an unsmoothness penalty as part of the optimization process.

Combining these three goals, we have designed a new exchange–correlation functional called gradient approximation for molecules, or GAM,[163] and this new functional is presented here. The GAM functional is an NGA, and so it depends only on spin densities and spin density gradients. The parameters of the GAM functional are optimized against a broad set of molecular and solid-state data in a new database called Database 2015, which is also presented here. We will show that the resulting GAM functional yields good results for main group bond energies, chemical reaction barrier heights, transition-metal bond energies, weak interaction energies between noble gas atoms, and bond lengths of diatomic molecules.

We also test the DFT+U method (where U is a Hubbard correction) on various databases and compare its performance to PBE, GAM, PBE+U, GAM+U, and HSE06, for various values of U.

The local exchange–correlation functionals are known to delocalize electrons, underestimate excitation energies, and underestimate band gaps, and this limitation of local functionals is usually overcome by using the DFT+U method or hybrid density functionals, where in the case of latter a fraction of local exchange is replaced by HF exchange (also called nonlocal exchange). This work discusses the design of two high local exchange functionals (HLE16 and HLE17)[205,206] that overcome the limitations of local functionals, do not depend on an empirical parameter like DFT+U, and are not as computationally expensive as hybrid functionals.

This chapter is organized as follows. Section 5.3 describes subdatabases in Database 2015, whose complete information is provided in the electronic supplementary information of Ref. 163. Section 5.4 describes the optimization of the GAM functional and a comparison of its performance with available functionals, Section 5.5 compares DFT+U with hybrid DFT, Section 5.6 discusses the design of HLE functionals, and Section 5.7 summarizes the main conclusions.

5.3 Databases

One important aspect of developing exchange–correlation functionals is to test their performance on diverse databases for which accurate experimental data is known, or if not known, for which the reference values can be calculated from high-level quantum mechanical methods. As part of our continued efforts to diversify our databases, we have recently included transition-metal containing systems[163] that are mainly multi-reference, to test how well functionals that use the single-reference formalism do for systems that cannot be represented by a single Slater determinant. This database is called Database 2015 whose subdatabases are shown in Table 5.1 along with other databases that were included as part of our work after Database 2015 was developed. It was obtained by expanding an earlier version of our database called Common Database 2.0,[207] and can be broadly divided into solid-state and molecular databases depending on the property being investigated. An exchange–correlation functional can be optimized to obtain across-the-board performance on the databases or to accurately predict specific properties on a database. In this work, we adopt both approaches for optimizing functionals.

Table 5.1 The databases used for optimization and validation of functionals.

Databases	Description
Solid-state properties	
SBG31	Semiconductor Band Gaps
SSCE8	Solid-State Cohesive Energies
TMOBG4	Transition-Metal Oxide Band Gaps
LC17	Lattice constants
MGLC4	Main Group Lattice Constants
ILC5	Ionic Lattice Constants
TMLC4	Transition Metal Lattice Constants
SLC34	Semiconductor Lattice Constants
Molecular properties	
SR-MGM-BE9	Single-reference main-group metal bond energy
SR-MGN-BE107	Single-reference main-group non-metal bond energies
SR-TM-BE17	Single-reference TM[a] bond energies
MR-MGM-BE4	Multi-reference main-group metal bond energies
MR-MGN-BE17	Multi-reference main-group non-metal bond energies
MR-TM-BE13	Multi-reference TM bond energies
MR-TMD-BE2	Multi-reference TM dimer bond energies (Cr_2 and V_2)
AE6	Atomization Energies (of main-group molecules)
TMABE10	Transition-Metal Average Bond Energies
AE17	Atomic energies
HC7/11	Hydrocarbon chemistry

DC9/12	Difficult cases
NGDWI21	Noble gas dimer weak interaction
IsoL6/11	Isomerization energies of large molecules
πTC13	Thermochemistry of π systems
DBH24	Diverse Barrier Heights
DBH18[b]	Diverse Barrier Heights of Neutrals
HTBH38/08	Hydrogen transfer barrier heights
NHTBH38/08	Non-hydrogen transfer barrier heights
PA3	Proton Affinities
EA13	Electron Affinities
IP21	Ionization Potentials
NCCE31	Noncovalent Complexation Energies
2pIsoE4	2p Isomerization Energies
4pIsoE4	4p Isomerization Energies
3dAEE7	3d transition metal atomic excitation energies
4dAEE5	4d transition metal atomic excitation energies
pEE5	p-block excitation energies
EE23	Excitation Energies (of molecules)
EEA11	Excitation Energies of Atoms
DM20	Dipole Moments
MGHBL9	Main-Group Hydrogenic Bond Lengths
MGNHBL11	Main-Group Non-Hydrogenic Bond Lengths
DGL6	Diatomic geometries of light-atom molecules
DGH4	Bond lengths for diatomic molecules (geometries) with one or more heavy atoms

[a]TM = transition metal

[b]DBH24 has 24 barrier heights, 18 of which involve only neutral species, and 6 of which involve ions; DBH18 is the subset of 18 barrier heights for the neutral reactions.

5.4 The GAM Functional

The general functional form of GAM is the same as N12, which has the flexibility to approximate both exchange and correlation effects in terms of spin density ρ_σ and reduced spin density gradient x_σ. In order to design a good functional, we use a broad molecular and solid-state database to optimize the parameters of the functional, and we also add smoothness constraints to our optimization. The functional form, optimization of the functional, and the performance of the functional in comparison to the other well-known functionals is discussed in the next few subsections.

5.4.1 Functional Form

The exchange–correlation energy E_{xc} of the GAM functional is the sum of nonseparable exchange-correlation component $E_{\mathrm{nxc}}^{\mathrm{NSGA}}$ and an additional term that is

nominally treated as a correlation energy E_{c}. Typically, one writes the first component as E_{x}, however, we label it as $E_{\mathrm{nxc}}^{\mathrm{NSGA}}$ to show that it is a nonseparable approximation involving both exchange and correlation. Since we optimize the functional empirically and do not enforce the factorizable form on the first term, the first term also represents part of correlation energy, and similarly, the second term is not purely correlation. Both terms must also include an empirical contribution required to account for the difference of the exact electronic kinetic energy from that computed from the orbitals of the Kohn-Sham determinant. The philosophy used in designing the functional form is consistent with the statement of Tozer and Handy that "The functionals represent exchange and correlation effects in a combined manner. Individual exchange and correlation terms cannot be isolated."[208] Our total exchange-correlation functional is

$$E_{\mathrm{xc}} = E_{\mathrm{nxc}}^{\mathrm{NSGA}} + E_{\mathrm{c}} \tag{5.1}$$

where

$$E_{\mathrm{nxc}}^{\mathrm{NSGA}} = \sum_{\sigma=\alpha}^{\beta} \int dr\, \Gamma_{\mathrm{nxc}\sigma}^{\mathrm{NSGA}}(\rho_\sigma, x_\sigma) \tag{5.2}$$

$$E_c = E_{c\alpha\beta} + \sum_{\sigma=\alpha}^{\beta} E_{c\sigma\sigma} \tag{5.3}$$

Nonseparable exchange-correlation terms. In eq 5.2 the nonseparable energy density is written as

$$\Gamma_{\mathrm{nxc}\sigma}^{\mathrm{NSGA}} = \varepsilon_{\mathrm{x}\sigma}^{\mathrm{UEG}}(\rho_\sigma) F_{\mathrm{x}}(\rho_\sigma, x_\sigma) \tag{5.4}$$

where F_{x} is the exchange enhancement factor, which in the present work is defined as

$$F_{\mathrm{x}} = \sum_{i=0}^{m} \sum_{j=0}^{m'} a_{ij} u_{\mathrm{x}\sigma}^{i} v_{\mathrm{x}\sigma}^{j} \tag{5.5}$$

where ρ_σ stands for the spin density, $u_{\mathrm{x}\sigma}$ and $v_{x\sigma}$ are finite variables defined by

$$u_{\mathrm{x}\sigma} = \gamma_{x\sigma} x_\sigma^2 / (1 + \gamma_{x\sigma} x_\sigma^2) \tag{5.6}$$

$$v_{x\sigma} = \omega_{\mathrm{x}\sigma} \rho_\sigma^{1/3} (1 + \omega_{\mathrm{x}\sigma} \rho_\sigma^{1/3}) \tag{5.7}$$

x_σ stands for reduced spin density gradient, for which we use the definition of Becke:[170]

$$x_\sigma = \frac{|\nabla \rho_\sigma|}{\rho_\sigma^{4/3}} \tag{5.8}$$

$\varepsilon_{x\sigma}^{UEG}$ stands for the uniform electron gas energy, which is calculated by[32,209]

$$\varepsilon_{x\sigma}^{UEG} = -\frac{3}{2}\left(\frac{3}{4\pi}\right)^{1/3}\rho_\sigma^{4/3} \tag{5.9}$$

$\gamma_{x\sigma}$, and $\omega_{x\sigma}$ are unitless parameters taken to have the same values as the ones in N12, namely $\gamma_{x\sigma} = 0.004$ and $\omega_{x\sigma} = 2.5$, and a_{ij}, are unitless parameters to be determined. Since both ρ_σ and x_σ range over $[0, \infty)$, the dependent variables $u_{x\sigma}$ and $v_{x\sigma}$ range over $[0, 1]$.

A GGA exchange functional can be written like eq 5.4 but where the enhancement factor F_x depends only on the reduced spin density gradient x_σ. For an NGA, we allow the enhancement factor to depend also on the spin density ρ_σ.

Correlation terms. In eq 5.3, the correlation functional has two parts. One is the contribution $E_{c\alpha\beta}$ from opposite spins, and the other is the contribution $E_{c\sigma\sigma}$ from same spins. These two contributions are defined by

$$E_{c\alpha\beta} = \int dr\, \varepsilon_{c\alpha\beta}^{UEG}\{\sum_{i=0}^{n} b_i u_{c\alpha\beta}^i\} \tag{5.10}$$

$$E_{c\sigma\sigma} = \int dr\, \varepsilon_{c\sigma\sigma}^{UEG}\{\sum_{i=0}^{n'} c_i u_{c\sigma\sigma}^i\} \tag{5.11}$$

where b_i and c_i are unitless parameters to be determined,

$$u_{c\alpha\beta} = \frac{\gamma_{c\alpha\beta} x_{avg}^2}{1+\gamma_{c\alpha\beta} x_{avg}^2} \tag{5.12}$$

$$u_{c\sigma\sigma} = \frac{\gamma_{c\sigma\sigma} x_\sigma^2}{1+\gamma_{c\sigma\sigma} x_\sigma^2} \tag{5.13}$$

$\gamma_{c\alpha\beta}$ and $\gamma_{c\sigma\sigma}$ are unitless parameters given the same values as in N12, namely, $\gamma_{c\alpha\beta} = 0.006$ and $\gamma_{c\sigma\sigma} = 0.2$, x_{avg}^2 is defined as the average of x_α^2 and x_β^2, and $\varepsilon_{c\alpha\beta}^{UEG}$ and $\varepsilon_{c\sigma\sigma}^{UEG}$ represent the correlation energy of the uniform electron gas. The uniform-

gas functions are taken from the Perdew-Wang parameterization[210] and the ansatz of Stoll, which is used to separate the correlation energy into same-spin and the opposite-spin contributions.[211,212]

5.4.2 Optimization of the Functional

In eqs 5.5, 5.10, and 5.11 above, we see that a_{ij}, b_i, and c_i are linear parameters of the functionals, which will be optimized. We do not force the uniform-electron-gas limit to hold when we optimize the functional. In order to make our functional smooth, smoothness constraints are added to the optimization, which will be explained in detail in the last paragraph of this section. The values of *m, m´, n*, and *n´* are chosen as 3, 3, 4, and 4 respectively. We found that the performance of the functional is not significantly improved by increasing these values, which shows that one cannot obtain improved functionals simply by adding more parameters. Therefore, in order to design good density functionals we must pay more attention to the mathematical form of the functional and the diversity of the database we are optimizing against, instead of concentrating on the number of parameters.

We optimize the GAM functional against 27 primary databases (shown later) self-consistently by minimizing the following unfitnesss function:

$$U = \sum_{n=1}^{27} R_n/I_n + \lambda(a + b + c) \tag{5.14}$$

where R_n is the root mean squared error of database *n*, I_n is the inverse weight of database *n*, and the product of λ and $(a + b + c)$ is the smoothness constraint, which is explained by

$$a = \sum_{i=0}^{3}\sum_{j=0}^{2}(a_{i,j} - a_{i+1,j})^2 + (a_{03} - a_{10})^2 + (a_{13} - a_{20})^2 + (a_{23} - a_{30})^2 \tag{5.15}$$

$$b = \sum_{i=0}^{3}(b_i - b_{i+1})^2 \tag{5.16}$$

$$c = \sum_{i=0}^{3}(c_i - c_{i+1})^2 \tag{5.17}$$

The purpose of this constraint is to ensure that the density functional is a reasonably smooth function of the spin densities and their gradients. We varied the value of λ from 0.001 to 0.1, where the range is selected such that $\lambda(\mathrm{a} + \mathrm{b} + \mathrm{c})$ has about the

same magnitude as $\sum_{n=1}^{27} R_n / I_n$. We made fits with various values of λ, and we monitored the smoothness of the resulting exchange-correlation functionals by plotting them, by examining the magnitudes of the linear coefficients of the exchange-correlation functional (they should not be too large in magnitude or have severely oscillating signs), and by checking whether there is any difficulty in achieving self-consistent-field convergence on difficult cases (we had made a list of cases where previous functionals sometimes showed SCF convergence difficulties). After balancing the performance of the functional and the smoothness of the enhancement factor (as judged by the three criteria just mentioned), we finally chose λ to be 0.001, which gives what we judged to be the best combination of overall accuracy, convergence, and smoothness of the exchange-correlation functional.

To design a good across-the-board performance functional, we include various molecular and solid-state properties in our training set, such as main-group bond energies, transition metal bond energies, transition metal atomic excitation energies, barrier heights, ionization potentials, proton affinities, electron affinities, and lattice constants, etc. In Table 5.2, the inverse weight of each primary database that was used in the optimization of the functional is given. The smaller the inverse weight is, the more emphasis we put on that primary database. The inverse weights were chosen as follows: First, we calculated the mean unsigned errors (MUEs) of 80 exchange-correlation functionals (previously published functionals developed in many different groups) for all the molecular subdatabases in Database 2015; this shows how well previous exchange-correlation functionals typically perform for each kind of data. The average of these MUEs for a given subdatabase was used as our initial inverse weights. Then we modified the inverse weights iteratively to improve performance on the various subdatabases where we wished to reduce the error. Our goal in this process was to obtain good across the board performance for as many subdatabases as possible, not to simply reduce the overall mean unsigned error.

Table 5.2 Databases[a,b] used in the optimization of GAM functional.

n	**Database**	**Description**	I_n [c]
ME417			
1	SR-MGM-BE9	Single-reference main-group metal bond energy	2.00
2	SR-MGN-BE107	Single-reference main-group non-metal bond energies	0.20
3	SR-TM-BE17	Single-reference TM[d] bond energies	3.15

4	MR-MGM-BE4	Multi-reference main-group metal bond energies	4.95
5	MR-MGN-BE17	Multi-reference main-group non-metal bond energies	1.25
6	MR-TM-BE13	Multi-reference TM bond energies	0.76
7	MR-TMD-BE2	Multi-reference TM dimer bond energies (Cr_2 and V_2)	10.00
8	IP23	Ionization potentials	5.45
9	NCCE30	Noncovalent complexation energies	0.10
10	NGDWI21	Noble gas dimer weak interaction	0.01
11	3dAEE7	3d TM atomic excitation energies	0.40
12	4dAEE5	4d TM atomic excitation energies	6.90
13	pEE5	p-block excitation energies	1.74
14	4pIsoE4	4p isomerization energies	8.00
15	2pIsoE4	2p isomerization energies	7.81
16	IsoL6/11	Isomerization energies of large molecules	2.00
17	EA13/03	Electron affinities	2.96
18	PA8	Proton affinities	2.23
19	πTC13	Thermochemistry of π systems	5.75
20	HTBH38/08	Hydrogen transfer barrier heights	0.25
21	NHTBH38/08	Non-hydrogen transfer barrier heights	0.80
22	AE17	Atomic energies	10.22
23	HC7/11	Hydrocarbon chemistry	6.48
24	DC9/12	Difficult cases	10.00
MS10			
25	DGL6	Diatomic geometries of light-atom molecules	0.01
26	DGH4	Diatomic geometries of heavy-atom molecules: ZnS, HBr, NaBr	0.01
		Diatomic geometry of Ag_2	0.0013
SS17			
27	LC17	Lattice constants	0.013

[a]Databases 1-27 were used with various inverse weights (I_n) in training.

[b]In the name of a database, the number at the end of the name or before the solidus is the number of data. For example, ME417, SR-MGM-BE9, IsoL6/11, and DGH4 contain 417, 9, 6, and 4 data, respectively.

[c]Inverse weights with units of kcal/mol per bond for databases 1–7, kcal/mol for databases 8–24, and Å for databases 25–27.

[d]TM denotes transition metal.

Whereas the N12 functional involved 20 optimized linear coefficients and the constraint that it reduced to PBEsol at low density, the new GAM functional involves optimizing 26 linear coefficients in eqs 5.5, 5.10, and 5.11 with no constraints. We use the same values as N12 for the nonlinear parameters $\omega_{\mathrm{x}\sigma}$, $\gamma_{x\sigma}$, $\gamma_{\mathrm{c}\alpha\beta}$, and $\gamma_{\mathrm{c}\sigma\sigma}$. Table 5.3 lists the values for the optimized parameters of the GAM functional. A key element in the optimization is the choice of weights. We do not choose them to

minimize the overall error but rather to try to get small errors across the board, *i.e.*, relatively small errors for each database, to the greatest extent possible. The final choice of weights was determined after considerable trial and error and is a subjective decision that cannot be justified by any numerical argument.

Table 5.3 Optimized and inherited parameters of the GAM functional.

	Exchange		**Correlation**
Optimized parameters			
a_{00}	1.32730	b_0	0.860548
a_{01}	0.886102	b_1	-2.94135
a_{02}	-5.73833	b_2	15.4176
a_{03}	8.60197	b_3	-5.99825
a_{10}	-0.786018	b_4	-23.4119
a_{11}	-4.78787	c_0	0.231765
a_{12}	3.90989	c_1	0.575592
a_{13}	-2.11611	c_2	-3.43391
a_{20}	0.802575	c_3	-5.77281
a_{21}	14.4363	c_4	9.52448
a_{22}	8.42735		
a_{23}	-6.21552		
a_{30}	-0.142331		
a_{31}	-13.4598		
a_{32}	1.52355		
a_{33}	-10.0530		
Inherited parameters			
$\omega_{x\sigma}$	2.5	$\gamma_{c\alpha\beta}$	0.006
$\gamma_{x\sigma}$	0.004	$\gamma_{c\sigma\sigma}$	0.2

5.4.3 Methodology

The optimization of GAM and the testing of all the functionals were performed using a locally modified version[213] of the *Gaussian 09* program.[188] The UltraFine grid ("99,590") that has 99 radial nodes and 590 angular points per node is used. The "stable=opt" keyword in *Gaussian 09*[188] is used to find a stationary solution to the Kohn-Sham equations by allowing symmetry breaking in the wave function if the symmetry-constrained solution is unstable. The periodic boundary condition (PBC) algorithm[214] in *Gaussian 09*[188] is used to calculate the lattice constants, cohesive energies, and semiconductor band gaps.

Besides testing the new functional on the subdatabases of Database 2015, we made several tests outside the training set:

(1) We tested the new functional on subdatabases SBG31 and SSCE8, which are in Database 2015, but outside the training set.

(2) We also tested our functional against other data that is not in the training set. This data includes a recently published database WCCR for transition metal coordination reactions[215] (renamed here as WCCR10 for consistency with our general naming scheme). We use the same basis set (def2-QZVPP) and geometries as used in the original paper;[215] these geometries were optimized by BP86 functional[170,216] are provided by the supporting information of Ref. 215.

(3) The enthalpies of binding of O_2 and N_2 to the metal organic framework Fe-MOF-74 were calculated. We used the 88-atom cluster model containing three iron centers, which was carved from the experimental structure of Fe-MOF-74.[10,12] The details of this cluster are described in Section 1.3.1. The cluster has three iron atoms, and here we studied binding at the central iron, which best represents, the immediate environment around iron in the actual MOF. During optimization, the cluster of the MOF was frozen and the guest molecules (O_2 or N_2) were allowed to relax. The binding enthalpies were calculated using the formula given in eq 1 of Ref. 31.

(4) The binding energy of the $Pd(PH_3)_2C_2H_4$ complex was computed using four basis sets. In all four basis sets, Pd atom has 18 active electrons and 28 core electrons that are replaced by effective core potential. Basis set BS1 denotes Stuttgart-Dresden-Dunning (SDD) basis set for Pd [217] and the cc-pVTZ basis set for P,[218] C, and H.[219] Basis set BS2 denotes the def2-TZVP basis set[141] for Pd and the cc-pVTZ basis set for P, C, and H. Basis set BS3 denotes the def2-TZVP basis set for Pd, the cc-pV(T+d)Z basis set for P[220,221] and the cc-pVTZ basis set for C and H. Basis set BS4 denotes the def2-TZVP basis set for Pd, the maug-cc-pV(T+d)Z basis set for P,[222] the maug-cc-pVTZ basis set for C[222,223] and the cc-pVTZ basis set for H.

(5) The Ar_2 potential energy curve was calculated. Two basis sets were used for Ar dimer, namely the aug-cc-pVQZ[218,219] and aug-cc-pV6Z[224] basis sets.

5.4.4 Functionals Used for Comparison

We compare our results to 22 previously available exchange–correlation functionals. Since GAM depends only on spin densities and spin density gradients, we compare our results mainly to GAs, in particular to 14 GGAs and the one previously available NGA. In a practical sense, three of the GGAs are corrected to second order in the density gradient expansion for exchange, and the other 11 are not. Altogether we compare to 20 local functionals of four types and to two hybrid functionals. The local functionals are an LSDA, namely GKSVWN5;[32,209,225] 14 GGAs, namely SOGGA,[169] PBEsol,[226] PBE,[60] BP86,[216,170] PW91,[227] BLYP[170,171] mPWPW,[166] revPBE,[228] BPW91, [170,227] RPBE,[168] HCTH407,[229] SOGGA11,[230] OLYP[171,174] and OreLYP;[171,174,231] an NGA, namely N12;[167] and four meta-GGAs, namely TPSS,[232] revTPSS,[233] M06-L,[162] and M11-L.[164] For context we also compare to two popular hybrid functionals, namely a global-hybrid GGA, B3LYP;[174,173,172] and a range-separated hybrid GGA, HSE06.[181,182,183,184] All these functionals are listed in Table 5.4 with the type, the percentage of HF exchange, the year, and the original reference.

Table 5.4 The exchange–correlation functionals used for comparison with GAM.

Category	X^a	Type	Year	Method	Ref.
local	0	LSDA	1980	GKSVWN5[b]	35, 209, 225
	0	GGA - correct to 2nd order in exchange	2008	SOGGA	169
	0		2008	PBEsol	226
	0		2011	SOGGA11	230
	0	GGA - other	1988	BP86	216, 170
	0		1988	BLYP	170, 171
	0		1991	PW91[c]	227
	0		1991	BPW91	170, 227
	0		1996	PBE	60
	0		1997	mPWPW	166
	0		1997	revPBE	228
	0		1999	RPBE	168
	0		2000	HCTH407	229
	0		2001	OLYP	171, 167
	0		2009	OreLYP	171, 174, 231
	0	NGA	2012	N12	167
	0		2015	GAM	163
	0	meta-GGA	2003	TPSS	232
	0		2006	M06-L	162

	0		2009	revTPSS	233
	0		2011	M11-L	164
nonlocal	20	global hybrid GGA	1994	B3LYP	173, 167
	0-25	range-separated hybrid GGA	2009	HSE06	181, 182, 183, 184

[a] X is the percentage of HF exchange. When a range is given, the first value is for small interelectronic distances, and the second value is for large interelectronic distances.

[b] GVWN5 denotes the Gáspár approximation for exchange and the VWN5 fit to the correlation energy; this is an example of the local spin density approximation (LSDA), and it has the keyword SVWN5 in the *Gaussian 09* program. Note that Kohn-Sham exchange is the same as Gáspár exchange, but Slater exchange (not tested here) is greater by a factor of 1.5.

[c] PW91 formally satisfies the gradient expansion for exchange to second order but only at such small values of the gradient that for practical purposes it should be grouped with functionals that do not satisfy the gradient expansion to second order.

5.4.5 Results and Discussion

Table 5.5 and 5.6 compare the performance of the new functional, GAM, to that of 22 existing functionals for molecular energetic data. Table 5.5 and 5.6 show that the GAM functional gives especially good results for main group bond energies, transition metal bond energies, reaction barrier heights, molecular structures, and noble gas weak interactions. Furthermore, the GAM functional provides reasonably good results for the test sets including semiconductor band gaps, solid-state cohesive energies, and transition metal coordination reactions.

Table 5.5 shows that among LSDA, all the GGAs, and the previous NGA, the new functional GAM gives the smallest overall mean unsigned error for the entire molecular energy database ME417; the mean unsigned error is only 4.51 kcal/mol. In Table 5.5 and 5.6 we calculate the average error for each of these four categories by averaging the errors from each subdatabase. Among LSDA and all GGAs and NGAs, the GAM functional ranked the best for the MGBE137, TMBE32, and BH76 subdatabases. If we consider all the functionals in Table 5.5 and 5.6, the GAM functional ranks the second best for TMBE32 subdatabase, for which M06-L is the best with an error 0.48 kcal/mol smaller than the GAM; the GAM functional ranks the second best for the MGBE137 subdatabase, for which M06-L is the best with an error 0.28 kcal/mol smaller than the GAM; and the GAM functional ranks the fifth best for

BH76 subdatabase, for which M11-L is the best followed by M06-L, B3LYP, and HSE06. We note that M06-L is a meta functional, and therefore it should be better than a simpler gradient approximation, but we gave several reasons for optimizing a gradient approximation in the introduction.

In addition to the databases mentioned above, the GAM functional also provides good results for 3*d* transition metal atomic excitation energies, which are very hard for most available density functionals, but which we have recently shown[234] can be very important for understanding metal–metal bonding. The GAM functional ranks the fifth best for the 3dAEE7 subdatabase, behind M06-L, B3LYP, PBE, and RPBE.

Next, we consider noble-gas weak interactions. From Table 5.5 and 5.6 we can see that all the functionals tested except GAM give a mean unsigned error larger than 0.081 kcal/mol for the NGDWI21 subdatabase, for which GAM only gives 0.019 kcal/mol. The average value of noble gas weak interaction energies in our database is 0.160 kcal/mol, which means that most functionals give an average error that is larger than 50% of the average of the reference values. The GAM functional gives the best results for the NCCE30 subdatabase as compared to all tested GGAs and N12.

The GAM functional also provides the second-best results for MR-TMD-BE2 (Cr_2 and V_2, which are known to be very hard cases for density functional theory) among all functionals tested.

Table 5.5 MUE (kcal/mol) for the Molecular Energy Database and its subdatabases: GAM compared to LSDA and other gradient approximations.

Type	**LSDA**	**GGA**	**GGA**	**GGA**	**GGA**	**GGA**	**GGA**	**GGA**	**GGA**	**GGA**	**GGA**	**GGA**	**GGA**	**GGA**	**GGA**	**NGA**	**NGA**
Functional	GKSVWN5	SOGGA	PBEsol	PBE	BP86	PW91	BLYP	mPWPW	revPBE	BPW91	RPBE	HCTH407	SOGGA11	OLYP	OreLYP	N12	**GAM**
SR-MGM-BE9	11.64	4.43	4.47	2.72	3.10	2.57	5.07	2.87	4.26	3.20	4.57	3.52	8.79	4.67	4.06	5.92	**2.00**
SR-MGN-BE107	16.21	7.27	7.28	3.40	4.06	3.51	2.78	2.80	2.99	2.49	3.35	2.55	2.77	2.32	2.56	2.38	**2.27**
SR-TM-BE17	20.89	11.59	11.33	7.20	7.39	8.76	6.52	6.73	6.22	7.34	6.24	8.36	11.44	9.32	7.15	8.31	**6.31**
MR-MGM-BE4	24.56	14.48	15.81	9.31	9.49	10.26	8.75	9.02	6.24	8.03	6.43	10.11	7.44	8.39	8.35	9.10	**7.76**
MR-MGN-BE17	36.89	21.29	23.16	14.80	13.87	14.80	6.67	12.45	5.94	10.74	5.51	5.24	8.57	5.15	4.25	6.93	**4.22**
MR-TM-BE13	34.07	22.03	21.24	12.73	12.11	13.25	10.64	11.67	8.55	10.81	7.73	19.70	18.79	5.77	5.10	12.54	**4.94**
IsoL6/11	2.05	1.89	1.55	1.98	2.28	1.92	3.73	2.16	2.82	2.38	2.99	3.02	1.73	3.44	3.39	1.73	**1.96**
IP23	9.59	4.84	5.82	6.19	8.44	7.29	6.52	6.85	5.00	6.30	4.92	6.81	5.92	3.12	3.03	4.36	**4.53**
EA13/03	5.70	2.70	2.16	2.27	4.21	2.60	2.68	2.31	2.40	2.26	2.37	3.70	5.23	3.60	2.32	4.12	**4.49**
PA8	5.07	2.33	2.10	1.34	1.41	1.30	1.58	1.52	2.00	1.88	1.98	2.84	2.11	2.40	1.70	1.35	**3.84**
πTC13	4.80	4.06	4.20	5.59	5.85	5.73	6.07	6.41	7.15	7.08	7.20	8.23	7.41	8.26	7.27	8.61	**8.59**
HTBH38/08	17.56	12.88	12.69	9.31	9.16	9.60	7.52	8.43	6.58	7.38	6.43	5.48	6.57	5.63	6.28	6.94	**5.35**
NHTBH38/08	12.42	9.68	9.86	8.42	8.72	8.80	8.53	8.03	6.82	7.26	6.82	6.29	4.32	5.25	5.57	6.86	**5.15**
NCCE30	3.61	2.12	2.07	1.46	1.53	1.60	1.64	1.42	1.71	1.74	1.61	1.32	1.48	2.52	2.68	1.38	**1.29**
AE17	421.13	283.06	245.90	47.24	16.92	4.63	8.68	12.55	10.88	11.95	9.39	16.80	10.06	10.13	2.37	14.21	**10.18**
HC7/11	21.45	17.88	13.31	3.97	9.95	4.55	27.39	8.08	13.65	10.77	14.96	14.97	6.26	17.01	16.34	4.27	**6.24**
3dAEE7	11.86	10.87	10.77	9.80	10.36	10.47	10.27	10.63	10.05	10.84	9.78	12.00	12.50	11.56	10.98	18.51	**9.82**
4dAEE5	14.10	4.77	8.48	4.70	5.07	4.73	5.73	4.89	4.49	5.03	4.27	7.75	7.60	5.94	6.42	10.24	**5.23**
pEE5	4.36	6.30	5.15	3.96	3.46	4.14	5.10	5.22	4.37	6.33	3.51	4.27	5.01	2.09	3.25	14.86	**2.99**
DC9/12	17.35	14.61	13.34	14.99	15.11	13.94	17.88	14.76	20.35	16.21	21.48	19.74	16.65	21.71	22.57	10.20	**23.07**
2pIsoE4	2.05	1.44	1.71	2.73	3.21	2.87	5.45	3.20	3.59	3.43	3.70	4.59	1.72	3.95	3.72	3.41	**5.02**
4pIsoE4	3.05	2.29	2.28	2.43	2.87	2.58	4.00	2.50	2.16	2.41	2.16	3.29	3.27	2.15	2.22	1.73	**3.57**
NGDWI21	0.212	0.082	0.081	0.102	0.528	0.165	0.385	0.220	0.282	0.587	0.179	0.246	0.650	0.323	0.389	0.387	**0.019**
MR-TMD-BE2	51.28	33.08	30.87	28.10	24.40	27.97	42.70	29.43	28.40	30.96	26.79	20.09	35.20	25.18	12.74	27.97	**10.67**
MGBE137[a]	18.72	9.04	9.31	4.94	5.38	5.05	3.58	4.18	3.54	3.73	3.79	3.17	4.02	3.00	3.04	3.37	**2.65**

TMBE32[b]	28.14	17.18	16.58	10.75	10.37	11.79	10.45	10.15	8.55	10.22	8.13	13.70	15.91	8.87	6.66	11.26	**6.03**
BH76[c]	14.99	11.28	11.27	8.87	8.94	9.20	8.02	8.23	6.70	7.32	6.62	5.88	5.44	5.44	5.92	6.90	**5.25**
ME417[d]	30.67	19.55	18.04	7.45	6.68	5.98	5.89	5.80	5.27	5.60	5.26	5.90	5.74	5.01	4.56	5.57	**4.51**
ME400xAE[d]	14.07	8.36	8.36	5.76	6.25	6.03	5.77	5.51	5.03	5.33	5.09	5.44	5.56	4.79	4.66	5.20	**4.27**

[a] The MGBE137 database consists of SR-MGM-BE9, SR-MGN-BE107, MR-MGM-BE4, and MR-MGN-BE17.

[b] The TMBE32 database consists of SR-TM-BE17, MR-TM-BE13, and MR-TMD-BE2.

[c] The BH76 database consists of HTBH38/08 and NHTBH38/08.

[d] The ME417 database consists all the 24 subdatabases above and the ME400xAE consists all the subdatabases except AE17. The functionals are listed in this table in order of decreasing ME400xAE.

Table 5.6 MUE (kcal/mol) for the Molecular Energy Database and its subdatabases: GAM compared to meta and hybrid functionals.

Type	**NGA**	**meta**	**meta**	**meta**	**meta**	**hybrid**	**hybrid**
Functional	**GAM**	TPSS	revTPSS	M06-L	M11-L	B3LYP	HSE06
SR-MGM-BE9	**2.00**	2.55	2.91	3.40	7.24	4.58	3.47
SR-MGN-BE107	**2.27**	2.43	2.24	2.03	1.76	2.45	2.08
SR-TM-BE17	**6.31**	6.11	6.13	6.24	5.73	5.48	4.96
MR-MGM-BE4	**7.76**	6.69	5.98	6.15	13.50	7.76	8.52
MR-MGN-BE17	**4.22**	4.25	4.62	3.11	4.02	5.09	5.30
MR-TM-BE13	**4.94**	8.87	6.81	4.40	4.44	5.33	4.87
IsoL6/11	**1.96**	3.66	3.96	2.76	1.57	2.61	1.25
IP23	**4.53**	4.29	4.07	3.91	4.77	5.51	4.06
EA13/03	**4.49**	2.35	2.59	3.83	5.54	2.33	2.77
PA8	**3.84**	2.66	2.79	1.88	2.17	1.02	1.10
πTC13	**8.59**	8.12	7.85	6.69	5.14	6.03	6.20
HTBH38/08	**5.35**	7.71	6.96	4.15	1.44	4.23	4.23
NHTBH38/08	**5.15**	8.91	9.07	3.81	2.86	4.55	3.73
NCCE30	**1.29**	1.34	1.33	0.90	0.81	1.09	0.95
AE17	**10.18**	18.04	23.81	7.04	21.81	18.29	32.82
HC7/11	**6.24**	10.48	6.42	3.35	2.42	16.80	7.34
3dAEE7	**9.82**	10.78	10.47	7.84	14.03	8.47	10.62
4dAEE5	**5.23**	5.19	5.11	6.58	11.04	5.67	5.07
pEE5	**2.99**	2.25	2.31	7.50	10.39	2.87	5.70
DC9/12	**23.07**	14.20	14.94	10.67	5.90	12.02	9.08
2pIsoE4	**5.02**	3.54	2.53	3.16	3.32	4.69	2.44
4pIsoE4	**3.57**	2.60	3.27	2.88	5.03	4.24	2.64
NGDWI21	**0.019**	0.171	0.174	0.125	0.568	0.276	0.102
MR-TMD-BE2	**10.67**	26.21	26.59	7.22	22.18	31.21	45.13
MGBE137[a]	**2.65**	2.79	2.69	2.37	2.74	3.07	2.76
TMBE32	**6.03**	8.49	7.68	5.55	6.24	7.03	7.43
BH76	**5.25**	8.31	8.01	3.98	2.15	4.39	3.98
ME417	**4.51**	5.40	5.42	3.55	4.15	4.68	4.83
ME400xAE	**4.27**	4.86	4.64	3.41	3.40	4.10	3.64

[a] The MGBE137, TMBE32, BH76, ME417, and ME400xAE notations are explained in footnotes to Table 5.5.

Table 5.7 compares GAM with 22 other functionals for molecular bond distances, and we find that the relative performance of GAM for molecular structures is not quite as good as for energies. The GAM functional ranks the 13th for MS10 subdatabase with an MUE of 0.018Å, which is 0.002 Å larger than the average MUE of all functionals tested in Table 5.7. Next, we turn to data not used for training.

Table 5.7 MUE (kcal/mol) for the Molecular Structure Database and its subdatabases.

Functional	Type	DGL6	DGH4	MS10[a]
GKSVWN5	LSDA	0.011	0.031	0.019
SOGGA	GGA	0.009	0.013	0.010
PBEsol	GGA	0.010	0.007	0.009
PBE	GGA	0.013	0.020	0.016
BP86	GGA	0.015	0.021	0.018
PW91	GGA	0.012	0.019	0.015
BLYP	GGA	0.019	0.037	0.026
mPWPW	GGA	0.012	0.021	0.016
revPBE	GGA	0.015	0.034	0.023
BPW91	GGA	0.013	0.022	0.017
RPBE	GGA	0.016	0.038	0.025
HCTH407	GGA	0.004	0.033	0.015
SOGGA11	GGA	0.008	0.053	0.026
OLYP	GGA	0.009	0.036	0.020
OreLYP	GGA	0.011	0.034	0.020
N12	NGA	0.008	0.007	0.008
GAM	**NGA**	**0.007**	**0.034**	**0.018**
TPSS	meta	0.010	0.015	0.012
revTPSS	meta	0.011	0.009	0.010
M06-L	meta	0.006	0.018	0.011
M11-L	meta	0.012	0.033	0.021
B3LYP	hybrid	0.009	0.027	0.016
HSE06	hybrid	0.003	0.015	0.008

[a]The MS10 database consists of DGL6 and DGH4 subdatabases. The functionals are listed in the same order as in Table 5.5 and 5.6.

Table 5.8 gives the performance for solid-state databases, but since B3LYP calculations with periodic boundary conditions are very expensive, we only compare 21 density functionals for the solid-state lattice constant and energetic data of Table 5.8. Table 5.8 shows that the GAM functional also shows reasonably good results for the solid-state energies databases. Among the 17 LSDA, GGAs, and NGAs, the GAM functional ranks the sixth best for the SGB31 database and fifth best for the SSCE8 database. These databases were not used for training.

Table 5.8 Mean unsigned errors for lattice constants and nearest neighbor distances (NNDs) in Å, band gaps in eV, and cohesive energies in eV/atom.

Functional[a]	Type	LC17	NND[b]	SBG31	SSCE8
GKSVWN5	LSDA	0.069	0.032	1.14	0.70
SOGGA	GGA	0.022	0.010	1.14	0.31
PBEsol	GGA	0.023	0.011	1.14	0.27
PBE	GGA	0.068	0.031	0.98	0.11

BP86	GGA	0.073	0.034	1.12	0.12
PW91	GGA	0.065	0.030	1.11	0.50
BLYP	GGA	0.111	0.052	1.14	0.37
mPWPW	GGA	0.075	0.035	1.11	0.10
revPBE	GGA	0.110	0.051	1.08	1.12
BPW91	GGA	0.083	0.038	1.10	0.20
RPBE	GGA	0.119	0.055	1.07	0.61
HCTH407	GGA	0.120	0.056	0.89	0.30
SOGGA11	GGA	0.125	0.058	0.89	0.07
OLYP	GGA	0.118	0.055	0.90	0.36
OreLYP	GGA	0.113	0.053	0.92	0.20
N12	NGA	0.027	0.012	0.99	0.13
GAM	**NGA**	**0.092**	**0.046**	**0.99**	**0.13**
TPSS	meta	0.055	0.025	0.85	0.22
revTPSS	meta	0.039	0.018	1.00	0.13
M06-L	meta	0.080	0.037	0.73	0.17
M11-L	meta	0.073	0.034	0.54	0.24
HSE06	hybrid	0.041	0.019	0.26	0.11

[a]The functionals are listed in the same order as in Table 5.5 and 5.6.

[b]The values in this column are obtained by dividing the previous column by 2.15 (a standard factor determined in previous work – see text) so that the results may be compared more physically to errors in molecular bond lengths.

Table 5.9 compares the performance of GAM to that of eight density functionals for the WCCR10 database. The GAM functional ranks the second best among all functionals tested, where the functionals tested are those chosen by the previous[215] authors. The WCCR10 database includes ten transition metal coordination reactions. The molecules involved in these reactions are very large and very different from the training sets in Database 2015. The performance against these large molecules is slightly worse than that for the transition metal molecules in our training set but within a reasonable range.

Table 5.9 Mean unsigned errors for the WCCR10 database in kcal/mol.[a]

Functional	**Type**	**WCCR10**
PBE0	hybrid	6.40
GAM	NGA	**6.60**
PBE	GGA	7.58
TPSSh	hybrid	7.62
TPSS	GGA	7.84
B97-D-D2	GGA	8.59

B3LYP	hybrid	9.30
BP86	GGA	9.42
BP86-D3	GGA	10.62

[a]The GAM results are from the present calculations, but all other results in this table are from Ref. 215.

Table 5.10 is a test for the binding of dioxygen and dinitrogen to Fe-MOF-74, where we compare to experiments of Bloch *et al*.[12] We find that GAM gives good results when compared to experiments for the separation of O_2 and N_2 on Fe-MOF-74, with a deviation from experimental adsorption enthalpies of 1.0 kcal/mol for O_2 and 1.6 kcal/mol for N_2. It should be noted here that our training set has no data on MOFs or any other type of nanoporous materials. This average deviation from the latest experimental values is under 3 kcal/mol and is within experimental error. This indicates that the GAM functional shows good agreement with experimental data not used for training.

Table 5.10 Binding enthalpies (kcal/mol) of O_2 and N_2 bound to the 88-atom cluster model of Fe-MOF-74 calculated using GAM.[a]

		ΔH^b	
	M_S(Fe, X_2)[c]	GAM[d]	Expt.[e]
Fe–N_2	2, 0	**3.9**	5.5
Fe–O_2	2, 1	**10.8**	9.8
	2, 0	**7.8**	NA[f]
	2, –1	**5.0**	NA

[a]The basis set is def2-TZVP.

[b]The binding enthalpy (a positive value indicates exothermic binding)

[c]This column has the M_S values for the central Fe and the guest molecule in the initial iteration of self-consistent field calculations. The two peripheral Fe centers where no guest is bound were taken to have $M_S = 2$ for all the calculations.

[d]This column is calculated by eq 1 of Ref. 31.

[e]The most recent experimental value is shown, as discuss in the text.

[f]NA denotes not applicable.

Table 5.11 presents results for the binding of ethylene to $Pd(PH_3)_2$, where we compare the results of GAM to the best estimate computed using BCCD(T)[235] in our earlier work.[236] This datum is outside of the training set. This is a difficult case for functionals; for example, BLYP gives a binding energy of 10.2 kcal/mol as compared to the best estimate of 17.6 kcal/mol. Table 5.11 shows good stability with respect to changes in the basis set and that the GAM functional deviates from the best estimate by 6.5 kcal/mol with the largest basis set used. This is comparable to the 6.3 kcal/mol mean unsigned error for single-reference transition metal bond energies of molecules in the training set, and therefore it is an example where we obtain comparable performance inside and outside of the training set.

Table 5.11 Binding energies (kcal/mol) of C_2H_4 bound to $Pd(PH_3)_2$ calculated using GAM and various basis sets.

Basis set[a]	GAM	Best estimate[b]
BS1	**11.0**	17.6
BS2	**11.1**	
BS3	**11.1**	
BS4	**11.1**	

[a]The various basis sets used are:

BS1 = SDD (Pd), cc-pVTZ (P, C, H);

BS2 = def2-TZVP (Pd), cc-pVTZ (P, C, H);

BS3 = def2-TZVP (Pd), cc-pV(T+d)Z (P), cc-pVTZ (C, H);

BS4 = def2-TZVP (Pd), maug-cc-pV(T+d)Z (P), maug-cc-pVTZ (C), cc-pVTZ (H).

[b]The best estimate was calculated in an earlier work using BCCD(T) and is described in Ref. 236.

Table 5.12 presents results for the bond distance of homonuclear transition metal dimer, where we compare the results of GAM and N12 with five functionals in a recent paper.[237] A very recent paper, which we considered only after our training set weights were final, reported bond distance for eight transition metal dimers, only one of which (Ag_2) is in our training set. We therefore use the bond distances of the seven others as a test against data quite different from that used for training. These seven dimers, Cu_2, Au_2, Ni_2, Pd_2, Pt_2, Ir_2, and Os_2, include two 3d metals, one 4d metals, and four 5d metals. (No 5d data were used for training.) The GAM functional gives the

third best results all the functionals tested in Table 5.12, with an MUE of 0.05 Å; the only functionals that do better are LSDA, which is much better for bond lengths than for molecular energies, and N12, the only previous NGA. This is very encouraging performance well outside the training set.

Table 5.12 Homonuclear transition metal dimers: equilibrium bond lengths (Å) and mean unsigned errors as compared to experiment.

	Cu_2	Au_2	Ni_2	Pd_2	Pt_2	Ir_2	Os_2	MUE
LSDA	2.215	2.495	2.118	2.373	2.353	2.271	2.354	0.038
PBE	2.278	2.552	2.135	2.397	2.391	2.302	2.384	0.062
B3LYP	2.292	2.577	2.099	2.411	2.392	2.301	2.387	0.071
B3PW91	2.288	2.552	2.095	2.367	2.375	2.287	2.373	0.068
mPWPW	2.293	2.549	2.088	2.359	2.369	2.282	2.369	0.068
N12	2.224	2.543	2.110	2.501	2.366	2.262	2.282	0.026
GAM	**2.306**	**2.543**	**2.189**	**2.536**	**2.408**	**2.283**	**2.292**	**0.050**
Exp.[a]	2.219	2.472	2.155	2.480	2.333	2.270	2.280	0.000

[a]The experimental bond length is taken from Ref. 237.

We also tested our new functional against the experimental bond dissociation energies of Ag_2 and FeC, which are 38.0 kcal/mol and 88.32 kcal/mol respectively.[238,239] The GAM functional predicts these bond dissociation energies to be 39.21 kcal/mol and 86.49 kcal/mol. Li et al.[239] have tested the bond dissociation energy of FeC with various functionals, and in Table 5.13 we add our new result to their comparison. The results in Table 5.13 show that the GAM functional is the second best among all 18 functionals being tested, and that many of the previous functionals have large errors for this difficult case.

Table 5.13 Errors for bond dissociation energy (kcal/mol) of FeC.

	M11-L	**SOGGA11**	**τ-HCTHhyb**	**M06-L**	**BLYP**	**B3LYP**	**M05**	**M0**
FeC	-4.60	10.81	-7.13	-7.36	12.88	-1.38	5.75	-20.9
	ωB97	**ωB97X**	**ωB97X-D**	**M08-SO**	**M08-HX**	**M11**	**SOGGA11-X**	**GAM**
FeC	-38.87	-20.01	21.39	-26.68	-35.65	-37.03	-67.16	1.8

Recent studies pointed out that some density functionals give unstable results for large basis sets.[240] Figure 5.1 shows the potential curve of Ar_2 with the GAM functional and the aug-cc-pVQZ and aug-cc-pV6Z basis sets. Figure 5.1 shows that our results are very close to the reference values[241] and there is no slow convergence

issue with respect to the basis sets. Moreover, the excellent agreement with the reference plot shows that the GAM functional provides good results for noble gas weak interaction. This is consistent with Table 5.5 and 5.6 showing that the GAM functional is the best for NGDWI21 among all the functionals tested in this work.

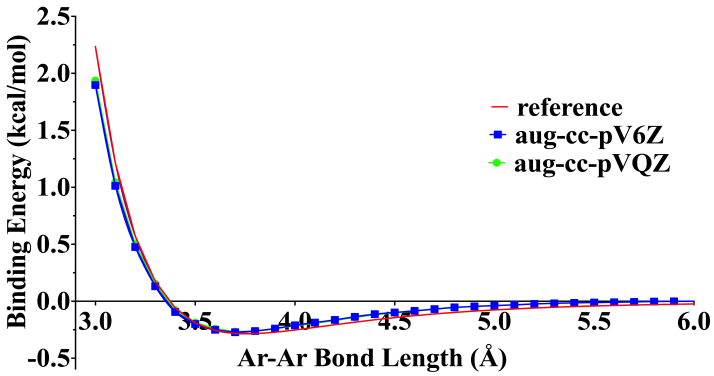

Figure 5.1 Ar-Ar potential energy curve.
The bonding energies are calculated with GAM/aug-cc-pVQZ and GAM/aug-cc-pV6Z level of theory. The reference is from the Tang-Toennies model.

5.5 DFT+U

Hybrid density functionals, which include a fraction of HF exchange, are often necessary to get certain properties such as charge transfer, band gaps, and excitation energies right. However, unlike molecular calculations, applying hybrid density functionals for solid-state calculations with plane-wave basis sets can be enormously expensive or even impractical. Therefore, an alternative to hybrid density functionals is required, where one could get properties similar to hybrid functionals and at a much lower computational cost. One such alternative is the DFT+U method, with a local functional for the DFT part; this is widely used for solid-state calculations with plane-wave basis set because it has a low computational cost similar to local-functional DFT. The parameter *U* can be tuned according to the system, the property, and the DFT method being tested.[28,29,242] There is more than one formulation for applying the +U correction and the two formulations that have been used in this work are: (1) exchange (*U*) and Coulomb (*J*) terms are chosen separately for the valence subshells and (2) the difference *U*–*J* is chosen and applied to the valence subshells also known as the formulation of Dudarev *et al.*

Here we discuss whether the determination of a general value of *U* is possible and how well DFT+U mimics hybrid DFT.[242]

5.5.1 Methodology

All calculations were performed using *Gaussian 09*,[188] a locally modified version (*MN-GFM*) of *Gaussian 09*,[243] *VASP*,[76,77] and a locally modified version (*MN-VFM*)[190] of *VASP*.

Gaussian 09 and MN-GFM calculations with Gaussian basis sets. The calculations with the *Gaussian 09* and *MN-GFM* software were performed using the GAM,[163] PBE,[60] and HSE06[181,182,183,184] exchange–correlation functionals. Both GAM and PBE are local functionals, where PBE is simpler and less well optimized than GAM, and HSE06 is a range-separated hybrid functional that reduces to PBE for large interelectronic separation, but has 25% of PBE's local exchange replaced by Hartree–Fock exchange at small interelectronic separation.

The solid-state calculations on SBG14 were done using the periodic boundary conditions (PBC) code[214] of *Gaussian 09* and involved optimization of nuclear positions and cell parameters. These calculations used the modified 6-311G* basis set, which is also referred to as *m*-6-311G*,[182] for light atoms—C, N, O, Mg, Al, Si, P, and S; they used a small-core relativistic effective core potential with a polarized double zeta valence basis set denoted by *m*-cc-pVDZ-PP[182] for Ga, Se, In, and Te; and they used the *m*-Stuttgard-RSC-1997[182] basis set for Zn and Cd. The TMOBG4 database was not analyzed using *Gaussian 09*.

The molecular calculations on the AE6, TMABE10, and DBH18 databases were single-point calculations at fixed geometries using the reference geometries that are listed in the supporting information of Ref. 163. An ultrafine integration grid (with 99 radial shells and 590 angular points per shell) was used for all the calculations. The stability of a single Slater determinant for open-shell atoms and molecules was tested, and the self-consistent field (SCF) iterations were allowed to converge to the most stable solution using the "Stable=Opt" keyword of *Gaussian 09*. The MG3S[244] basis set was used for the AE6 and DBH24 databases, and the def2-TZVP[141] (metals and H atom) and ma-TZVP[245] (nonmetals) basis sets were used for the TMABE10 database. The calculations on these three databases with the three functionals are without spin-orbit coupling. (Spin-orbit coupling is not included in either the calculated or the experimental values.) We calculated the AE6 database with the jun-cc-pV(Q+d)Z basis set[246] as well.

The TMABE10 database was further analyzed by calculating Charge Model 5 (CM5)[72] partial atomic charges and Hirshfeld[74] spin densities. The CM5 partial atomic charges were calculated using the *CM5PAC* package.[73]

VASP and MN-VFM calculations with plane-wave basis sets. The calculations with *VASP* and *MN-VFM* were done using PBE, GAM, PBE+U, and GAM+U for various value of the Hubbard U correction. The Hubbard U correction to both PBE and GAM was applied in the formulation of Dudarev *et al*.[191] (specified using "LDAUTYPE = 2" in *VASP*), where the results depend only on the difference of the Coulomb (U) and exchange (J) parameters, $U–J$. This difference will be denoted by "U" or "U correction" for simplicity. The plane-wave basis set and the projector-augmented-wave (PAW) potentials[192,193] provided with the *VASP* package were used. The Gaussian smearing method or the tetrahedron method with Blöchl corrections was used to converge the SCF iterations.

A k-point mesh of 11×11×11, an energy cut-off of 500 eV, an SCF energy convergence criterion of 10^{-6} eV or even tighter, and a force convergence criterion of -10^{-3} or -10^{-4} eV/Å were used for the SBG14 and TMOBG4 databases. The optimizations involved three protocols. In protocol 1, only the nuclear positions were allowed to relax for various values of the lattice constant, and a plot of energy vs lattice constant gave the optimum structure, which was used to compute band gap. In protocol 2, the nuclear positions and cell shape were allowed to relax for various values of the cell volume, and a plot of energy vs cell volume gave the optimum structure, which was used to compute band gap. In protocol 3, the nuclear positions, cell shape, and cell volume were allowed to relax at the same time before calculating the band gap. Most of the discussion here is based on protocol 2, which is recommended.

A k-point mesh of 1×1×1, a cell size of 10×11×12 Å^3, an energy cut-off of 1000 eV, an SCF energy convergence criterion of 10^{-7} eV or even tighter, and a force convergence criterion of -10^{-3} eV/Å were used for the AE6, TMABE10, and DBH18 databases. Unlike the solid-state databases (that involved either partial optimization or complete optimization), all molecular calculations were single-point calculations using the reference geometries listed in the supporting information of Ref. 163.

The TMABE10 database was further analyzed by calculating CM5 partial atomic charges and magnetizations. The CM5 partial atomic charges were calculated

by first determining the Hirshfeld charges using the *Chargemol* program[247] followed by CM5 charge calculation using the *CM5PAC* package.[73] Magnetization is defined as the difference between the number of alpha and beta electrons on an atom, and it is determined from an SCF calculation in *VASP*.

5.5.2 Results and Discussion

In the discussions and tables that follow, the U correction has been applied to the valence *s* orbitals for groups 1–2 (except H, which has no U correction), to the valence *d* orbitals for groups 4–12, and to the valence *p* orbitals for groups 15–17. Atoms in groups 13–14 were treated in more than one way, as specified in each case; in particular, we tried U corrections for either valence *p* or *d* orbitals, and we also tried no Hubbard U correction for these groups. There are no atoms from groups 3 or 18 in the compounds that we investigate here. The tables report MUEs, which are calculated as the average of the absolute difference between the calculated and the reference values, where the reference is from experiment or high-level calculations, as specified above.

Band gaps. The band gap is a widely studied quantity in solid-state physics. For the present work, we approximate the band gap as the energy difference between the bottom of the conduction band and the top of the valence band. Local density functionals tend to underestimate band gaps; therefore Hubbard-corrected functionals or hybrid functionals such as B3LYP and HSE06 (or HSE03) are often used to correct this systematic error to obtain band gaps (and possibly some other properties as well) that agree better with experiments.[248,249,250,251,252,253,254,255,256,257,258] The use of B3LYP and HSE06 in periodic codes with plane-wave basis sets is computationally very demanding, and hence Hubbard-corrected functionals are often preferred over hybrid functionals for efficiency reasons. In Table 5.14–5.16 we present band gaps for the TMOBG4 database that contains open-shell transition metals. Table 5.14 uses protocol 1 and is done with PBE, PBE+U, while Table 5.15 and 5.16 use protocol 2, and are done with PBE, PBE+U and GAM, GAM+U, respectively. Table 5.17 contains literature values of band gaps for these four compounds as obtained using LSDA,[259] PBE, HSE03, and B3LYP. Table 5.18 gives band gaps of main-group semiconductors as obtained using GAM and GAM+U, Table 5.19 reports band gaps of Zn and Cd containing semiconductors as obtained using GAM and GAM+U, and

Table 5.20 reports band gaps of semiconductors presented in both Table 5.18 and 5.19, but performed with *Gaussian 09* using GAM, PBE, and HSE06. These tables allow us to test how well the band gaps obtained with a Hubbard-corrected functional mimic those obtained with a hybrid functional.

Table 5.14 and 5.15 are both obtained using PBE and PBE+U, but they differ in the protocols used for optimization. It is interesting to note that the two protocols yield very similar band gaps for the values of *U* common to both the tables (0, 4, and 8 eV), and the only exception to this is CoO with *U* = 4 eV. MnO and NiO give nonzero band gaps with PBE, and increasing the U value increases their band gaps, but FeO in both the tables gives ~0 eV band gap for every U value tested. This unique metallic behavior of FeO with PBE+U has been attributed to the fact that symmetry breaking is required by the inclusion of a spin-orbit coupling term,[260] which is beyond the scope of the present work. Examination of the MUEs shows that in both the tables the highest values of *U* yield the minimum MUE. For Table 5.15, we also applied *U* = 4 eV on all the elements, which means for both the transition metal and the oxygen atom for FeO and CoO. The band gap for FeO was 0.0 eV and for CoO it was 2.0 eV. Comparing these numbers to PBE+U (*U* = 4.0 eV on TM) values in Table 5.15, we see that the FeO value didn't change, and the CoO value decreased by 0.2 eV making it farther from the experimental value. Hence, we finally applied U correction only on the transition metal. As explained later with other examples, applying U correction to all the elements doesn't always yield the most accurate results.

Table 5.14 Band gaps (eV) of transition metal oxides calculated using PBE and PBE+U and plane-wave basis sets with protocol 1.[a]

solid	**PBE**	**PBE+U**	**PBE+U**		
U (eV)	-	4.0	8.0	expt.[c]	type[d]
U correction on[b]	-	TM	TM		
MnO	0.7	1.5	2.1	3.9	I
FeO	0.0	0.1	0.0	2.4	I
CoO	0.0	0.0	2.9	2.5	I
NiO	0.7	2.5	3.3	4.2	I
MUE (without FeO)	3.0	2.2	1.0		

MUE (all)	2.9	2.2	1.4

[a]For details of protocol 1, see Section 5.5.1.

[b]U correction is applied to the valence *d* subshells of transition metals (TMs).

[c]The experimental values are from Ref. 261.

[d]I = indirect band gap

Table 5.15 Band gaps (eV) of transition metal oxides calculated using PBE and PBE+U and plane-wave basis sets with protocol 2.[a]

solid	**PBE**	**PBE+U**	**PBE+U**	**PBE+U**		
U (eV)	-	4.0	8.0	12.0	expt.[c]	type[d]
U correction on[b]	-	TM	TM	TM		
MnO	0.7	1.5	2.1	2.5	3.9	I
FeO	0.0	0.0	0.0	0.0	2.4	I
CoO	0.0	2.2	2.9	3.3	2.5	I
NiO	0.7	2.6	3.3	4.2	4.2	I
MUE (without FeO)	3.0	1.4	1.0	0.8		
MUE (all)	2.9	1.7	1.4	1.2		

[a]For details of protocol 2, see Section 5.5.1.

[b]U correction is applied to the valence *d* subshells of transition metals (TMs).

[c]The experimental values are from Ref. 261.

[d]I = indirect band gap

In Table 5.16, we test another gradient approximation density functionals, GAM. Band gaps using GAM and GAM+U with protocol 2 are reported, and we see that, similarly to PBE, GAM gives zero band gaps for both FeO and CoO. For MnO and NiO, the band gaps are 1.5 eV and 0.9 eV, respectively, which are larger than that predicted by PBE. Adding U correction to GAM increases band gap for every compound except FeO. A U value of 7.6 eV was predicted by doing quadratic fit to the MUEs of U = 0.0, 4.0, and 8.0 eV, and it was found to be the one that minimized the error. Running the four compounds with this U value didn't improve the results compared to U = 8.0 eV.

Table 5.16 Band gaps (eV) of transition metal oxides calculated using GAM and GAM+U and plane-wave basis sets with protocol 2.[a]

solid	**GAM**	**GAM+U**	**GAM+U**	**GAM+U**		
U (eV)	-	4.0	7.6	8.0	expt.[c]	type[d]
U correction on[b]	-	TM	TM	TM		
MnO	1.5	1.9	2.2	2.2	3.9	I
FeO	0.0	0.0	0.0	0.0	2.4	I
CoO	0.0	2.2	2.8	2.8	2.5	I
NiO	0.9	2.5	3.5	3.5	4.2	I
MUE (without FeO)	2.7	1.3	0.9	0.9		
MUE (all)	2.6	1.6	1.3	1.3		

[a]For details of protocol 2, see Section 5.5.1.

[b]U correction is applied to the valence *d* subshells of transition metals (TMs).

[c]The experimental values are from Ref. 261.

[d]I = indirect band gap

Table 5.17 gives literature values[261] of band gaps of the four compounds as calculated with LSDA, PBE, HSE03, and B3LYP. Both LSDA and PBE predict a zero band gap for FeO and CoO and a nonzero band gap for MnO and NiO. This is also what we predict with PBE in Table 5.14 and 5.15 and GAM in Table 5.16. Adding screened exchange to PBE leads to the screened hybrid functional HSE03, which improves the band gaps of the four compounds significantly. Also, a global hybrid functional, B3LYP leads to a drastic improvement compared to the local functionals, LSDA and PBE.

The second last rows of Table 5.15, 5.16, and 5.17 give MUEs calculated without considering the special case of FeO, and by comparing these we find that the MUEs for PBE+U (0.8 eV) and GAM+U (0.9 eV) are comparable with that of HSE03 (0.7 eV). Therefore, the DFT+U method improves the band gap significantly compared to DFT, and it does mimic the effect of adding HF exchange to a local functional. B3LYP gives an improvement over HSE03, but being a global hybrid functional it is a more expensive calculation than the screened hybrid functional, HSE03. HSE03 gives a small improvement compared to PBE+U and GAM+U, but is

much costlier than PBE+U and GAM+U, and is not always a practical method for large unit cells. Hence if we consider both cost and accuracy, the PBE+U and GAM+U methods are quite competitive with HSE06, even when we use a general value of *U* rather than a specific value for each material. (Note that HSE03 has two general parameters, namely the short-range value of *X* and the range parameter that determines the range over which exchange is switched between local exchange and nonlocal exchange, whereas PBE+U and GAM+U each have only the one U parameter.) The MUEs with GAM+U and PBE+U can be reduced even further if U values are chosen separately for each compound as has been done by Anisimov et al.,[262] Pickett et al.,[263] and Jiang et al.[264] using constrained density functional theory. An alternative to using hybrid functionals is to use the GW method for accurate band gaps, but, just as for hybrid functionals, this is not as cost-effective as DFT+U. Note that the U correction required for PBE is larger than that required for GAM by more than 4 eV. The smaller empirical correction needed by GAM+U as compared to PBE+U could be considered an advantage. Next, we look at band gaps of solids that do not have open-shell atoms.

Table 5.17 Literature values of band gaps (in eV) of transition metal oxides calculated using LSDA, PBE, HSE03, and B3LYP.

solid	**LSDA**	**PBE**[a]	**HSE03**	**B3LYP**	**Expt**[b]
MnO	0.4	0.9	2.8	3.9	3.9
FeO	0.0	0.0	2.2	3.7	2.4
CoO	0.0	0.0	3.4	3.6	2.5
NiO	0.4	0.9	4.2	4.1	4.2
MUE (without FeO)	3.3	2.9	0.7	0.4	
MUE (all)	3.0	2.8	0.6	0.6	

[a]The PBE values are from Ref. 261 and the remaining functionals are from Ref. 265.

[b]The experimental values are from Ref. 261 and references therein.

In Table 5.18, the GAM+U ($U = 2.0$ eV) results for main-group semiconductors show that adding a Hubbard U correction to the valence orbital does

not necessarily increase the band gap compared to GAM. The GaN and InN cases each have two rows, where a Hubbard U correction was applied to either the valence *p* orbitals or the *d* orbitals, and neither strategy gives improved band gaps. These calculations are relevant to the question of which orbitals can profit from a Hubbard U correction in addition to the question of the optimum value for that correction. For the orbitals and the values of *U* tested in Table 5.18, the MUE doesn't improve with a Hubbard U correction. For most of the compounds, adding Hubbard U correction leads to a decrease in band gap and therefore greater disagreement with experiments compared to uncorrected GAM, which suggests that a U correction for this database does not help, and hence we did not test any other value of *U*.

Table 5.18 Band gap (in eV) of main-group semiconductors calculated using GAM and GAM+U with plane-wave basis sets.

solid	GAM	U correction on	GAM+U[a]	expt.[b]	type[c]
AlP	2.34	*p* of Al	2.37	2.51	I
C	4.40	*p* of C	4.13	5.48	I
GaN	2.15	*p* of Ga	1.73	3.50	D
GaN	2.15	*d* of Ga	1.78	3.50	D
InN	0.38	*p* of In	0.27	0.69	D
InN	0.38	*d* of In	0.43	0.69	D
MgS	3.79	*s* of Mg	3.85	5.40	D
Si	0.94	*p* of Si	0.81	1.17	I
SiC	2.06	*p* of Si	2.04	2.42	I
MUE	0.75		0.88		

[a] U = 2.0 eV for the valence orbitals of the elements specified in column 3 and is set to zero for the rest of the elements.

[b] The experimental values are taken from Ref. 266.

[c] I = indirect band gap and D = direct band gap

In Table 5.19, a Hubbard U correction of 2.0 or 8.0 eV was first applied only to the valence *d* orbitals of Zn and Cd atoms, while setting it to zero for group 16 elements—O, S, Se, and Te. A value of *U* equal to 2.0 eV increased the band gap and improved it by a small amount, and a value of 8.0 eV improved it further, but it still differs from experiments by a large amount. We next added a Hubbard U correction of 8.0 eV to all the elements to see if the results improved any further. If we compare GAM+U with U = 8.0 eV applied to Zn and Cd only to GAM+U with U = 8.0 eV

applied to all the elements, we find that only for ZnO did the "all" protocol improve the results, while for the rest of the semiconductors, the band gap decreased. This means that adding a Hubbard U correction only to the valence *d* orbitals of the metals, Zn and Cd, increases the band gap more than when it is applied to both the valence *d* orbitals of the metal and the valence *p* orbitals of the nonmetal (with ZnO being an exception). Unlike the solids of Table 5.18, in Table 5.19 band gap increases for every solid when Hubbard U correction is applied only to Zn and Cd atoms. A very high value of U correction (= 12 eV) was applied and it improves the results significantly, but such a high value of U may not have a physical meaning for these systems. We note that the Hubbard U correction was originally proposed for systems with partially filled *d* subshells, which we tested above (Table 5.14– 5.17), whereas we are using it here (Table 5.19) for Zn and Cd, which have filled *d* subshells. (Table 5.18 also involves only closed-shell systems.)

Table 5.19 Band gap (in eV) of group 12 semiconductors calculated using GAM and GAM+U with plane-wave basis sets.

solid	**GAM**	**GAM+U**	**GAM+U**	**GAM+U**	**GAM+U**		
U (eV)	-	2.0	8.0	12.0	8.0	expt.[b]	type[c]
U correction on[a]	-	Cd, Zn	Cd, Zn	Cd, Zn	all		
CdS	1.14	1.24	1.64	2.40	1.34	2.55	D
CdSe	0.60	0.69	1.04	1.59	0.73	1.90	D
CdTe	0.51	0.58	0.85	1.28	0.25	1.92	D
ZnO	1.13	1.37	2.29	3.47	2.80	3.40	D
ZnS	2.33	2.49	3.13	3.83	2.78	3.66	D
ZnSe	1.44	1.58	2.09	2.62	1.75	2.70	D
ZnTe	1.11	1.20	1.55	1.86	0.78	2.38	D
MUE	1.46	1.34	0.85	0.28	1.15		

[a]U correction was applied to the valence *d* subshells of Cd and Zn for columns 3 and 4, and also to the valence *p* subshells of O, S, Se, and Te for column 5.

[b]The experimental values are taken from Ref. 266 except for ZnO, which is from Ref. 267.

[c]D = direct band gap

We next examine the use of a hybrid functional, HSE06, on band gaps. Table 5.20 presents a comparison of GAM, PBE, and HSE06 done using *Gaussian 09*. Band gaps predicted by HSE06 are higher than those predicted by PBE for every datum in

Table 5.20. This is unlike Table 5.18 and 5.19 where adding a Hubbard U correction to GAM does not always increase the band gap. In Table 5.18, we did not try additional values for U correction because we found that when we use $U = 2$ eV, for some systems the band gap increases while for others it decreases, which is in contrast to what is obtained by adding HF exchange to a local functional. The latter case always increases band gap.

Table 5.20 Band gap (in eV) of semiconductors[a] calculated using Gaussian basis sets.

solid	GAM	PBE	HSE06	Expt.[b]	Type[c]
AlP	2.28	1.78	2.51	2.51	I
C	4.44	4.24	5.49	5.48	I
CdS	1.28	1.26	2.25	2.55	D
CdSe	0.40	0.63	1.51	1.90	D
CdTe	0.41	0.81	1.67	1.92	D
GaN	1.57	2.22	3.53	3.50	D
InN	0.00	0.00	0.76	0.69	D
MgS	3.75	3.65	4.75	5.40	D
Si	0.91	0.72	1.28	1.17	I
SiC	1.91	1.46	2.40	2.42	I
ZnO	1.16	0.88	2.90	3.40	D
ZnS	2.43	2.30	3.49	3.66	D
ZnSe	1.12	1.37	2.42	2.70	D
ZnTe	0.87	1.39	2.36	2.38	D
MUE	1.19	1.17	0.19	0.00	

[a]The GAM results were calculated as part of our work in Ref. 163 and the PBE and HSE06 results were published in Ref. 268.

[b]The experimental values are taken from Ref. 266 except for ZnO which is from Ref. 267.

[c]I = indirect band gap and D = direct band gap

Main-group bond energies. Table 5.21 presents the average bond energies of molecules containing only main-group elements. We first applied a Hubbard U correction of 2.0 or 4.0 eV on all elements except H (referred to as "all-exH" in the table). We find that addition of a Hubbard U correction decreases the average bond energy of all six molecules. The mean unsigned errors (MUEs) (5.9 and 12.3 kcal/mol) are larger than those of GAM (2.3 kcal/mol). Next, we applied a Hubbard U correction only to O and S atoms, and we find again that the average bond energies decrease. These cases gave improved results compared to the "all-exH" protocol, but

the results are still not better than uncorrected GAM. Next, we did a quadratic fit to the MUEs of GAM, GAM+U (U = 2.0 eV on O and S), and GAM+U (U = 4.0 eV on O and S) and found that the value of U that would lead to minimum MUE is 0.8 eV. But running the database with this value of U gives an MUE of 2.4 kcal/mol, which again is not an improvement compared to GAM.

Table 5.21 Main-group average bond energies (kcal/mol) calculated using plane-wave basis sets.

AE6	**GAM**	**GAM+U**	**GAM+U**	**GAM+U**	**GAM+U**	**GAM+U**	
U (eV)	-	0.8	2.0	4.0	2.0	4.0	**Ref.**[a]
U correction on	-	only O, S	only O, S	only O, S	all-exH	all-exH	
C_3H_4 (propyne)	117.1	117.1	117.1	117.1	112.2	107.4	117.5
C_4H_8 (cyclobutane)	95.1	95.1	95.1	95.1	92.0	88.9	95.8
$H_2C_2O_2$ (glyoxal)	130.3	128.7	126.3	122.4	122.7	115.3	126.8
S_2	109.8	107.5	104.1	98.8	104.1	98.8	104.3
SiH_4	77.9	77.9	77.9	77.9	75.2	72.8	81.2
SiO	192.5	188.4	182.3	172.2	177.0	162.0	193.1
MUE	2.3	2.4	2.6	5.9	5.9	12.3	

[a]The reference values are taken from Ref. 269.

Table 5.22 is similar to Table 5.21 except that PBE is used instead of GAM. Here we see that PBE+U (U = 2.0 eV on O and S) does give an improvement in MUE of 0.5 kcal/mol compared to PBE. Doing a quadratic fit to the MUEs of PBE, PBE+U (U = 2.0 eV on O and S), and PBE+U (U = 4.0 eV on O and S) gave the optimum value of U as 1.7 eV and the predicted MUE corresponding to it as 3.5 kcal/mol. This MUE is what we already have with PBE+U (U = 2.0 eV on O and S); hence running the database with U value of 1.7 eV on O and S will not significantly improve the results.

Table 5.22 Main-group average bond energies (kcal/mol) calculated using plane-wave basis sets.

AE6	**PBE**	**PBE+U**	**PBE+U**	**PBE+U**	**PBE+U**	
U (eV)	-	2.0	4.0	2.0	4.0	**Ref.**[a]
U correction on	-	only O, S	only O, S	all-exH	all-exH	
C_3H_4 (propyne)	119.9	119.9	119.9	114.9	109.9	117.5
C_4H_8 (cyclobutane)	97.1	97.1	97.1	93.8	90.5	95.8
$H_2C_2O_2$ (glyoxal)	131.9	128.1	124.4	124.4	117.0	126.8
S_2	115.0	109.3	103.9	109.3	103.9	104.3
SiH_4	78.2	78.2	78.2	75.6	73.1	81.2
SiO	194.9	185.2	175.5	179.5	164.6	193.1
MUE	4.0	3.5	4.5	5.2	9.9	

[a]The reference values are taken from Ref. 269.

Table 5.23 presents Gaussian-basis-set results for the AE6 database using GAM, PBE, and HSE06. We find that addition of screened Hartree–Fock exchange in HSE06 decreases the MUE compared to the local functional PBE, and this decrease in error (1.9 kcal/mol) is more than what could be achieved with PBE+U (for which the decrease in MUE compared to PBE is 0.5 kcal/mol). Note that both PBE and GAM give very similar results in the two computer programs for some of the molecules, but there are also differences. The differences for PBE are all less than 1.5 kcal/mol, while for GAM with the largest basis set used, jun-cc-pV(Q+d)Z,[246] the three molecules with the biggest difference between the two software are $H_2C_2O_2$ (2.4 kcal/mol), S_2 (2.6 kcal/mol), and SiO (9.6 kcal/mol). These differences might be due to the different methodologies adopted by the two software packages. For example, *VASP* calculations for the GAM functional are done using PAW potentials with plane-wave basis sets (because no PAW potential optimized for GAM is available, we used the PBE PAW potential, which should be applicable), and the *Gaussian 09* calculations were done using all-electron Gaussian basis sets, MG3S[244] or jun-cc-pV(Q+d)Z.[246] It is possible that using a PAW potential optimized for GAM, if it existed, would lead to a better agreement between the two software packages, just like PBE. It has been shown by Paier et al.[270] that for the PBE functional, *VASP* and the *Gaussian* software could be made to agree very well with each other for atomization energies if one used a very high cut-off energy (1000 eV) in *VASP* and a large basis set such as aug-cc-pV5Z[218,271] in Gaussian-orbital calculations. Since we already use

high cut-off energy (1000 eV) in *VASP*, that would not seem to be the source of the disagreement. Although neither of the Gaussian basis sets we used is as large as aug-cc-pV5Z, the calculations using the larger basis set, jun-cc-pV(Q+d)Z are in worse agreement with the *VASP* calculations than MG3S. But, independent of these technical issues, the key result is that Hubbard U corrections do not lead to an improvement over GAM for main-group bond energies, but Hartree–Fock exchange can lead to such an improvement. The Hubbard U correction to PBE does improve results by a small amount (0.5 kcal/mol), but PBE doesn't not perform as well as GAM in either of the software packages, and also the best Hubbard-corrected method, PBE+U (U = 2.0 eV on O and S) in Table 5.22 does not perform as well as the GAM result reported in Table 5.21.

Table 5.23 Main-group average bond energies (kcal/mol) calculated using Gaussian basis sets.

AE6	GAM/MG3S	GAM/jun-cc-pV(Q+d)Z	PBE/MG3S	HSE06/MG3S	Ref.[a]
C_3H_4 (propyne)	118.5	118.6	120.2	117.6	117.5
C_4H_8 (cyclobutane)	96.2	96.4	97.3	96.0	95.8
$H_2C_2O_2$ (glyoxal)	127.9	127.9	132.7	126.7	126.8
S_2	110.7	112.4	114.7	106.2	104.3
SiH_4	78.0	78.1	78.4	78.7	81.2
SiO	183.8	182.9	196.3	182.8	193.1
MUE	3.6	4.0	4.4	2.5	

[a]The reference values are taken from Ref. 269.

Transition-metal−ligand bond energies. Table 5.24 presents average bond energies for the TMABE10 database. As we did for AE6, we began by applying a Hubbard U correction of 2.0 or 4.0 eV to all elements except H atom, and we did not find a significant improvement of the results. Next, we applied a Hubbard U correction of 2.0 or 4.0 eV only to the transition metals (TMs). Applying a Hubbard U correction to only the transition metal in each compound improved the results compared to the "all-exH" protocol. Carrying out a quadratic fit to the MUEs of GAM, GAM+U (U = 2.0 eV on TM), and GAM+U (U = 4.0 eV on TM), we find that the optimum value of U that would lead to a minimum MUE is 2.4 eV. However, the predicted value of minimum MUE for U = 2.4 eV on TMs is 5.8 kcal/mol, which is the same as what GAM+U (U = 2.0 eV on TMs) gives, and therefore we decided not to run this database with U = 2.4 eV, as this would not reduce the error significantly.

Hence for this database, we conclude (based on MUEs) that GAM+U can improve results by a maximum of 1.3 kcal/mol.

Table 5.24 Transition-metal−ligand average bond energies (kcal/mol) calculated using plane-wave basis sets.

TMABE10	**GAM**	**GAM+U**	**GAM+U**	**GAM+U**	**GAM+U**	**Ref.**[b]
U (eV)	-	2.0	4.0	2.0	4.0	
U correction on	-	only TM[a]	only TM[a]	all-exH	all-exH	
AgH	50.1	49.6	49.4	49.6	49.4	54.0
$CoCl_2$	90.9	89.0	91.9	85.8	84.8	93.5
CoH	55.4	56.4	63.9	56.4	63.9	45.2
CrCl	95.8	92.5	89.9	88.2	81.4	91.0
$CrCl_2$	88.2	84.7	79.9	80.5	71.1	91.4
$FeCl_2$	98.1	97.9	95.1	93.5	86.4	96.6
FeH	51.6	52.4	46.4	52.4	46.4	36.8
MnF_2	126.7	123.3	120.6	116.1	106.2	116.5
TiCl	113.8	108.2	100.1	103.9	91.4	102.3
VF_5	121.5	113.6	105.7	106.4	91.3	113.4
MUE	7.1	5.8	6.3	6.5	12.5	

[a]TM = transition metal

[b]The reference values are taken from Ref. 163.

Table 5.25 presents Gaussian-basis-set results carried out using GAM, PBE, and HSE06 for the TMABE10 database. We find that a hybrid functional, HSE06 decreases the MUE by 2.7 kcal/mol compared to its corresponding local functional, PBE. In contrast, we saw in Table 5.24 that adding the Hubbard U correction to the valence *d* orbitals of the transition metal gave a maximum improvement of 1.3 kcal/mol in the MUE. This example shows that adding Hartree–Fock exchange to a local functional improves the results more than adding a Hubbard U correction to a local functional. However, we must be cautious here because GAM is a better optimized functional than PBE.

Since Table 5.24 and 5.25 report GAM results on the same database, we can see how well the two software packages – *VASP* and *Gaussian 09* – agree for this database. The molecules that give more than 2 kcal/mol difference with GAM in the two software packages are $FeCl_2$ (2.9 kcal/mol), FeH (3.0 kcal/mol), MnF_2 (7.2 kcal/mol), TiCl (6.3 kcal/mol), and VF_5 (4.0 kcal/mol). As discussed earlier, this

difference could possibly be due to the use of the PBE PAW potential with GAM in *VASP*.

Table 5.25 Transition-metal−ligand average bond energies (kcal/mol) calculated using Gaussian basis sets.

TMABE10	GAM	PBE	HSE06	Ref.[a]
AgH	52.0	55.9	51.8	54.0
$CoCl_2$	88.9	94.0	90.0	93.5
CoH	54.4	61.2	56.9	45.2
CrCl	94.8	89.8	85.6	91.0
$CrCl_2$	87.8	88.7	84.5	91.4
$FeCl_2$	95.2	99.5	97.4	96.6
FeH	48.6	56.0	50.7	36.8
MnF_2	119.5	127.6	117.3	116.5
TiCl	107.5	116.6	110.6	102.3
VF_5	117.5	126.5	110.5	113.4
MUE	4.9	8.3	5.6	

[a]The reference values are taken from Ref. 163.

Table 5.26 presents CM5 partial atomic charges calculated for atoms of the TMABE10 database using PBE and HSE06 with Gaussian basis sets and GAM and using GAM+U (U = 2.0 eV on TMs) with plane-wave basis sets. We selected GAM+U (U = 2.0 eV on TMs) for this analysis because it gave the best results in Table 5.24. The goal is to see whether or not the effect of adding HF exchange to a local functional is the same for partial atomic charges as the effect of adding Hubbard U correction to a local functional. We find that for all atoms, the magnitude of charge computed using HSE06 is higher than that computed using PBE. The magnitude of charge computed using GAM+U is also higher than that computed using GAM, except for the atoms of CoH and FeH. Hence, it appears that the Hubbard U correction approximately mimics the effect of HF exchange for partial atoms charges on atoms with transition metal–ligand bonds.

Table 5.26 CM5 partial atomic charges (in atomic units)[a] on the atoms of TMABE10 database.

TMABE10	Atoms	Gaussian basis sets		Plane-wave basis sets	
		PBE	HSE06	GAM	GAM+U[b]
AgH	Ag	0.03	0.05	0.09	0.10
	H	–0.03	–0.05	–0.09	–0.10
$CoCl_2$	Co	0.47	0.60	0.51	0.63
	either Cl	–0.23	–0.30	–0.26	–0.31
CoH	Co	0.11	0.14	0.10	0.10
	H	–0.11	–0.14	–0.10	–0.10
CrCl	Cr	0.42	0.47	0.40	0.41
	Cl	–0.42	–0.47	–0.40	–0.41
$CrCl_2$	Cr	0.67	0.78	0.62	0.65
	either Cl	–0.34	–0.39	–0.31	–0.33
$FeCl_2$	Fe	0.59	0.69	0.61	0.65
	either Cl	–0.30	–0.35	–0.31	–0.32
FeH	Fe	0.13	0.15	0.11	0.11
	H	–0.13	–0.15	–0.11	–0.11
MnF_2	Mn	0.78	0.89	0.81	0.83
	either F	–0.39	–0.44	–0.40	–0.41
TiCl	Ti	0.36	0.41	0.35	0.37
	Cl	–0.36	–0.41	–0.35	–0.37
VF_5[c]	V	1.36	1.51	1.48	1.50
	F eq	–0.26	–0.29	–0.29	–0.29
	F ax	–0.29	–0.32	–0.31	–0.32

[a]In some cases the partial atomic charges on atoms of a molecule do not add to zero due to rounding to two decimal places.

[b]U = 2.0 eV only for valence *d* subshells on transition metals is used because it gave the best results in Table 5.24.

[c]Note that the charges on the five F atoms of VF_5 are not the same because it has a trigonal bipyramid structure with the three equatorial (eq) V–F bond distances being shorter than the two axial (ax) ones.

In Table 5.27, Hirshfeld spin densities calculated using Gaussian basis sets and magnetizations calculated using plane-wave basis sets are presented. Both spin density and magnetization provide a measure of the difference between the number of α and β electrons. For some molecules (AgH and VF_5), Hirshfeld spin densities and magnetizations are zero because they are closed-shell molecules. For molecules with non-zero values in Table 5.27, we find that adding HF exchange or adding a Hubbard U correction usually increases the values of spin densities and magnetizations on the transition metal, which is the expected result.

Table 5.27 Hirshfeld spin densities (in atomic units) calculated using Gaussian basis sets and magnetizations calculated using plane-wave basis sets for the atoms of the TMABE10 database.[a]

TMABE10	Atoms	Gaussian basis sets		Plane-wave basis sets	
		PBE	HSE06	GAM	GAM+U[b]
AgH	Ag	0.00	0.00	0.00	0.00
	H	0.00	0.00	0.00	0.00
$CoCl_2$	Co	2.46	2.63	2.55	2.62
	either Cl	0.27	0.18	0.11	0.04
CoH	Co	2.00	2.00	1.82	2.08
	H	0.00	0.00	–0.03	–0.02
CrCl	Cr	4.93	4.95	4.39	4.48
	Cl	0.07	0.05	–0.02	–0.03
$CrCl_2$	Cr	4.02	4.00	3.92	3.98
	either Cl	–0.01	0.00	–0.10	–0.10
$FeCl_2$	Fe	3.55	3.71	3.51	3.63
	either Cl	0.22	0.14	0.05	0.03
FeH	Fe	3.00	3.00	3.15	3.18
	H	0.00	0.00	–0.04	–0.04
MnF_2	Mn	4.72	4.81	4.45	4.55
	either F	0.14	0.10	0.04	0.02
TiCl	Ti	3.00	2.99	2.35	2.37
	Cl	0.00	0.01	–0.02	–0.01
VF_5	V	0.00	0.00	0.00	0.00
	any F	0.00	0.00	0.00	0.00

[a]Hirshfeld spin densities are with hydrogens summed into heavy atoms and give the difference between the number of alpha and beta electrons i.e. the number of unpaired electrons. Magnetization is a similar quantity calculated in *VASP*.

[b]U = 2.0 eV only for valence *d* subshells on transition metals is used as it gave the best results in Table 5.24.

Barrier heights. Table 5.28 shows the 18 barrier heights (9 forward and 9 reverse) of nine reactions in the DBH18 database. Since AE6 and TMABE10 databases (Table 5.21 and 5.24, respectively) do not show significantly improved results when a Hubbard U correction is applied to all elements except H, we applied a Hubbard U correction only to N, O, F, S, and Cl for this database. We find that the MUE for this database can improve by a kcal/mol when a Hubbard U correction is applied to GAM. We did a quadratic fit to the three methods reported in Table 5.28 to find the optimum value of U that gives the minimum MUE. The estimated values of U and MUE from the quadratic fit were found to be 4.5 eV and 5.1 kcal/mol,

respectively, which indicates that optimizing a generic *U* will not significantly improve the results compared to the ones already in Table 5.28.

Table 5.28 Forward and reverse barrier heights for small molecules (kcal/mol) calculated using plane-wave basis sets.

barrier height ***U* (eV)** **U correction on**[a]	**GAM** **-** **-**	**GAM+U** **2.0** **N, O, F, S, Cl**	**GAM+U** **4.0** **N, O, F, S, Cl**	**Ref.**[b]
$OH + CH_4 \rightarrow H_2O + CH_3$	–4.4	–1.3	1.7	6.5
reverse	15.1	13.2	11.1	19.6
$H + HO \rightarrow H_2 + O$	5.0	3.1	1.1	10.5
reverse	3.9	7.3	10.7	12.9
$H + H_2S \rightarrow H_2 + HS$	1.9	1.4	0.8	3.5
reverse	13.3	15.1	16.7	16.8
$H + N_2O \rightarrow OH + N_2$	16.7	15.8	14.8	17.1
reverse	51.0	56.8	62.6	82.3
$H + ClH \rightarrow HCl + H$	15.8	15.2	14.6	18.0
reverse	15.8	15.2	14.6	18.0
$CH_3 + FCl \rightarrow CH_3F + Cl$	–4.7	–4.2	–3.7	6.8
reverse	42.4	43.9	45.4	59.2
$H + N_2 \rightarrow HN_2$	9.5	9.2	8.9	14.4
reverse	10.1	10.6	11.2	10.6
$H + C_2H_4 \rightarrow CH_3CH_2$	1.4	1.4	1.4	1.7
reverse	42.6	42.6	42.6	41.8
$HCN \rightarrow HNC$	49.7	49.1	48.5	48.1
reverse	34.9	32.0	29.0	32.8
MUE	6.1	5.4	5.1	

[a]The Hubbard U correction for C and H atoms was set to zero.

[b]The reference values are taken from Ref. 272.

Table 5.29 reports barrier heights calculated using GAM, PBE, and HSE06 in *Gaussian 09*. The PBE functional, which has no Hartree–Fock exchange, gives an MUE of 8.6 kcal/mol, and the hybrid HSE06, which has 25% Hartree–Fock exchange at short interelectronic distances and no Hartree–Fock exchange at long interelectronic distances, gives an MUE of 4.2 kcal/mol, which is a significant improvement over PBE. In contrast, Table 5.28 showed that GAM+U gave an improvement of no more than a kcal/mol over GAM. For every datum in Table 5.29, HSE06 gives a higher barrier height than PBE, while this is not true when one compares GAM+U with GAM results in Table 5.28. For some reactions, GAM+U increased the barrier height, while for others it decreased the barrier heights. This

shows that DFT+U does not always mimic a hybrid functional. Additionally, if we compare GAM in *VASP* (Table 5.28) to GAM in *Gaussian 09* (Table 5.29), we find that they don't agree for all cases, which we expect could be due to the use of the PBE PAW potential with GAM in *VASP*.

Table 5.29 Forward and reverse barrier heights for small molecules (kcal/mol) calculated using Gaussian basis sets.

barrier height	GAM	PBE	HSE06	Ref.[a]
$OH + CH_4 \rightarrow H_2O + CH_3$	–0.5	–5.2	2.1	6.5
reverse	12.2	8.8	13.8	19.6
$H + HO \rightarrow H_2 + O$	4.3	3.6	6.9	10.5
reverse	6.6	–1.3	6.1	12.9
$H + H_2S \rightarrow H_2 + HS$	1.9	–1.1	1.1	3.5
reverse	13.4	9.5	12.5	16.8
$H + N_2O \rightarrow OH + N_2$	16.2	10.5	14.3	17.1
reverse	57.5	52.8	69.2	82.3
$H + ClH \rightarrow HCl + H$	15.9	10.4	14.1	18.0
reverse	15.9	10.4	14.1	18.0
$CH_3 + FCl \rightarrow CH_3F + Cl$	–5.6	–6.4	0.1	6.8
reverse	45.2	42.0	52.8	59.2
$H + N_2 \rightarrow HN_2$	9.2	5.6	8.9	14.4
reverse	11.5	9.2	11.6	10.6
$H + C_2H_4 \rightarrow CH_3CH_2$	1.5	0.0	0.7	1.7
reverse	42.5	40.4	44.0	41.8
$HCN \rightarrow HNC$	48.5	46.0	47.0	48.1
reverse	32.8	31.0	33.2	32.8
MUE	5.3	8.6	4.2	

[a]The reference values are taken from Ref. 272.

5.6 HLE functionals

Although the DFT+U method can be applied efficiently, it suffers from the limitation of determination of the empirical parameter *U* before it can be used, and in the absence of experimental data or high-level quantum mechanical reference values, tuning *U* for a given property/system is not possible. There exist *ab initio* ways to determine U, but these cannot be conveniently used. Therefore, it becomes important to find an alternative to the DFT+U approach. Again, this alternative approach cannot be a hybrid functional due to computational cost, and one has to stick to functionals at the GA level or lower. Generally speaking, with the DFT+U method one could obtain values for properties one is interested in by appropriately choosing the value of *U*.

With hybrid functionals one usually gets band gaps and excitation energies larger than that of a local functional thereby correcting the local functional. However, the shortcoming of the DFT+U method is that the *U* value needs to be adjusted not only for the system, not only for the property but also for the DFT method one is interested in calculating. The shortcoming of hybrid functionals is that they can be computationally very expensive for large systems and one may not be able to afford to them for a practical calculation.

Keeping in mind the aforementioned limitations, the high local exchange (HLE) functionals[205,206] were designed with the aim of having computational cost similar to a local functional and properties comparable to hybrid functionals. The two HLE functionals, namely HLE16[205] and HLE17,[206] are based on the idea of increasing the coefficients of local exchange terms and decreasing the coefficients of local correlation terms in a GGA and meta-GGA, respectively. The HLE16 functional is based on the GGA, HCTH/407 and the HLE17 functional is based on the meta-GGA, TPSS. The enhanced local exchange in both these functionals significantly improves band gaps and excitation energies without significantly deteriorating ground-state molecular energies. However, these functionals have not been found to be good for bond lengths of molecules, lattice constants of solids, ionization potentials and electron affinities. The advantage of computationally more expensive HLE17 over HLE16 is that it improves solid-state lattice constants to some extent and in general gives smaller errors for most of the databases that have been tested with both the functionals. These new functionals are not general-purpose functionals, but they provide a strategy for designing better general-purpose functionals, which will be able to predict properties that cannot be obtained with a local functional.

5.6.1 Functional Form

After a preliminary investigation of the effect of various calibrations, we decided to accept the same calibration factors for HLE16 and HLE17. The HLE16 functional was obtained from HCTH/407 by multiplying the exchange functional by 5/4 and the correlation functional by ½, and HLE17 was obtained by using the same factors for TPSS.

To run the HLE16 functional, the keywords in *Gaussian 09* are:

```
HCTH407/def2TZVP IOp(3/76=1250000000) IOp(3/77=1000010000)
IOp(3/78=0500005000)
```

To run the HLE17 functional, the keywords in *Gaussian 09* are:

```
TPSSTPSS/def2TZVP IOp(3/76=1250000000) IOp(3/77=1000010000)
IOp(3/78=0500005000)
```

These functional can also be added in a straightforward way to programs other than *Gaussian*.

5.6.2 Methodology

All databases were calculated using *Gaussian 09*[188] suite of quantum mechanical programs or a locally modified version[273] of *Gaussian 09*, and some were also calculated using *VASP.5.3.5*.[76,77] Both *Gaussian* and *VASP* were used for performing both molecular and solid-state calculations. All *VASP* calculations used periodic boundary conditions; the *Gaussian 09* calculations used Gaussian basis sets for molecules and periodic boundary condition methods[214] for calculations on solids. As usual, band gaps for solids were computed as the difference between the lowest unoccupied crystal orbital and the highest occupied crystal orbital,[274] and excitation energies of molecules were computed by linear-response time-dependent DFT[275] (LR-TDDFT) starting from closed-shell ground state. For molecular triplet states, we also calculated the excitation energy by the ΔSCF method,[276,277] in which one performs separate SCF calculations on the singlet and the triplet.

Gaussian 09 calculations. Because this work aims at improving a local density functional for properties such as band gaps and excitation energies, we chose for comparison with the new density functional some of the most popular local

functionals and one of the most widely used hybrid functionals for solid-state properties. Altogether nine density functionals were tested using *Gaussian 09*; they are shown in Table 5.30.

The basis sets used with each database are given in the SI of Ref. 206. The UltraFine grid, which has 99 radial shells and 590 angular points per shell, was used for both molecular and solid-state calculations. The "stable = opt" keyword was used for open-shell atoms or molecules in order to reoptimize the Slater determinant to a stable solution if it was found unstable. Scalar relativistic effects were not included in our calculations.

To understand some of the trends in some of the results for molecules, we computed B_1 diagnostics[278] of multireference character. A "multireference" molecule is an intrinsically multiconfigurational one (sometimes called strongly correlated). A B_1 diagnostic value below 10 kcal/mol indicates that a molecule or bond is classified as a single-reference molecule or bond, and a value above 10 kcal/mol usually indicates that the molecule or bond is multireference.[278]

VASP calculations. The databases that do not involve charged species (PA3, EA13, and IP21), TDDFT calculations (EE23 and EEA11), or dipole moments (DM20) were calculated using PBE+U in *VASP*. In addition to these databases being left out for PBE+U, six reactions of DBH24 database were also left out as they involved charged species, resulting in the DBH18 database.

The +U correction was applied to valence subshells of atoms following the Dudarev *et al*. approach,[191] where only the difference $U - J$ matters (specified with LDAUTYPE = 2), and where U and J are on-site Coulomb and exchange energies, respectively. The difference $U - J$ will henceforth be denoted by U. In Ref. 242 for some of the databases (AE6, TMABE10, DBH18, a subset of SBG31 (SBG14), and TMOBG4), we had tried to find an optimum value of U, and the results showed that the optimum value could vary significantly with the database. However, here, instead of optimizing a value of U for each database, we will obtain a single value of U from the literature. To see how well DFT+U can do with a single U, we looked at ten highly cited articles in the literature[279,248,280,281,282,283,198,284,201,285] that use PBE+U and averaged the U value they used or recommended. This yields a value around 4 eV. Therefore, we will test PBE+U with a U value of 4 eV. The reason for using a single

value of *U* is to provide a comparison to HLE17, which uses the same parameters for all calculations.

Following the language sometimes used in the literature, the +U correction will be called the Hubbard correction.[286,287,288] For cases where there is a transition metal, we applied the Hubbard correction only to the transition metal. For solids without a transition metal, the Hubbard correction was applied only to the more electropositive element (or to the only element if it is unary). For molecules that do not have a transition metal, the Hubbard correction was applied only to the electronegative element (in particular, N, O, F, S, Cl, and Br). We never apply the Hubbard correction to a C atom or an H atom or inert gases. Although it is possible that in some cases the Hubbard correction would work better when applied to all the elements in a molecule or solid, these choices on selective application of the correction are based on tests done with GAM+U (and PBE+U in a few cases) made in Ref. 242.

For running calculations, the same settings were not applied to all the databases. The projector-augmented-wave (PAW) potentials,[192,193] energy cut-offs, *k*-points, SCF energy and force convergence criteria that were used are provided in Table 5.31–5.33. For most of the cases we used the PAW potentials recommended on the *VASP* website, and in some cases (mainly for molecules) we used a harder PAW potential.

Table 5.30 The exchange–correlation functionals tested in this work.

Type	Method
GGA	PBE
GGA	PBE+U
GGA	BLYP
GGA	PBEsol
NGA	GAM
GGA	HCTH/407
GGA	HLE16
meta-GGA	TPSS
meta-GGA	HLE17
hybrid-GGA	HSE06

Table 5.31 PAW potentials for SBG31, SLC34, ILC5, MGLC4, TMLC4, and SSCE8 databases.

Element	PAW potential used

Li	Li_sv
B	B
C	C
N	N
O	O
F	F
Na	Na_pv
Mg	Mg
Al	Al
Si	Si
P	P
S	S
Cl	Cl
K	K_sv
Cu	Cu
Zn	Zn
Ga	Ga
Ge	Ge
As	As
Se	Se
Rh	Rh_pv
Pd	Pd
Ag	Ag
Cd	Cd
In	In
Sb	Sb
Te	Te
Ba	Ba_sv

Table 5.32 PAW potentials for TMOBG4, AE6, DBH18, TMABE10, NCCE31, DGH4, MGHBL9, and MGNHBL11 databases.[a]

Element	**PAW potential used**
H	H_h
He	He
C	C_h
N	N_h
O	O_h
F	F_h
Ne	Ne
Na	Na_pv
Mg	Mg
Si	Si
S	S_h
Cl	Cl_h
Ar	Ar
Ti	Ti
V	V

Cr	Cr
Mn	Mn
Fe	Fe
Co	Co
Ni	Ni
Zn	Zn
Br	Br
Ag	Ag

[a]Only for HCN molecule in MGHBL9 and MGNHBL11 databases, the PAW potentials used were H, C, and N.

Table 5.33 Cut-off energies (eV), *k*-points, SCF energy (eV) and force (eV/Å) convergence criteria used for various databases.

Database	Cut-off energy	k-points	SCF energy convergence criteria	Force convergence criteria
SBG31	500	11×11×11	10^{-6}	-10^{-3}
SLC34	500	11×11×11	10^{-6}	-10^{-3}
ILC5	500	11×11×11	10^{-6}	-10^{-3}
MGLC4	500	11×11×11	10^{-6}	-10^{-3}
TMLC4	500	11×11×11	10^{-6}	-10^{-3}
SSCE8	500	11×11×11	10^{-6}	-10^{-3}
TMOBG4	500	11×11×11	10^{-8}	-10^{-4}
AE6	1000	1×1×1	10^{-7}	-10^{-3}
DBH18	1000	1×1×1	10^{-7}	-10^{-3}
TMABE10	1000	1×1×1	10^{-7}	-10^{-3}
NCCE31	1000	1×1×1	10^{-7}	-10^{-3}
DGH4	1000	1×1×1	10^{-7}	-10^{-3}
MGBL20	1000	1×1×1	10^{-7}	-10^{-3}

5.6.3 Results and Discussion

Table 5.34 presents mean unsigned errors (MUEs) for the new functionals, HLE16 and HLE17, for the PBE+U (U = 4.0 eV) method, and for well-known functionals. The local functionals have a tendency to underestimate band gaps,[289,290,291] and functionals that depend only on the density and the gradient of the density do underestimate band gaps compared to the experimental values. However, with HLE16 and HLE17, one obtains an MUE of ~0.3 eV on SBG31 database. This is comparable to the performance of the computationally more expensive hybrid GGA, HSE06 (MUE = 0.31 eV). The band gaps calculated by PBE+U, with a universal value of 4 eV for U does not give a good prediction of band gaps (the MUE is greater than 1

eV). Of course, it might be possible to obtain good band gaps by adjusting *U* for each solid, but that is not the goal of the present work.

Although HLE17 does not have an advantage over HLE16 for SBG31, we see that HLE17 is better for the prediction of lattice constants than HLE16 for the same compounds (SLC34 database). The SLC34 database has the same semiconductors as the SBG31 database, but for three of the solids (GaN, InN, and ZnO), there are two independent lattice parameters, and this raises the data count to 34. The PBEsol functional, which was specifically parametrized to predict accurate solid-state lattice constants, is the best performing functional (MUE = 0.031 Å), although it does not do well for band gaps. The hybrid GGA, HSE06, was the second best performing functional (MUE = 0.052 Å) for this database. The HLE17 functional is the third best performing functional with an MUE of 0.077 Å, and it gives a significant improvement over HLE16, which gives an MUE of 0.157 Å. Besides the SLC34 database, lattice constants were calculated for three other databases (MGLC4, ILC5, and TMLC4). For three of the four lattice constant databases (SLC34, ILC5, and TMLC4), HLE17 gives significant improvement over HLE16 as shown in Table 5.34, and it gives performance similar to HLE16 for MGLC4. While most of the functionals in overestimate lattice constants, HLE16 and HLE17 tend to underestimate lattice constants.

The performance of HLE16 and HLE17 was also tested on the EE23 database in which we look at vertical excitation energies. The EE23 database consists of (1) 18 valence excitations of 14 organic molecules – for four of these molecules (benzene, naphthalene, furan, and hexatriene) excitations for the triplet state are also considered; (2) two Rydberg excitations of water molecule for singlet and triplet states; and (3) three charge transfer (CT) excitations – two intramolecular (para-nitroaniline (PNA) and dimethylaminobenzonitrile (DMABN)) and one intermolecular (benzene–tetracyanoethylene complex (B-TCNE)).

The LR-TDDFT approach is used to calculate excitation energies of all the states. Both HLE16 and HLE17 do reasonably well compared to other local functionals for valence and Rydberg excitations. However, the performance for CT excitations is not improved over other local functionals. To understand why the HLE functionals perform well for valence and Rydberg excitations we looked at the

HOMO and LUMO energies of the molecules in the EE23 database with TPSS and HLE17; the results of this examination are given in Table 5.35. Both the HOMO and the LUMO are more strongly bound with HLE17 than with TPSS, but the key point for the calculation of excitation energies is that the LUMO–HOMO difference tends to be greater for HLE17 for most of the cases. We also compared LUMO–HOMO differences to LR-TDDFT results; the "diff." columns in Table 5.35 are obtained by taking an unsigned difference between the LUMO–HOMO and the LR-TDDFT columns. Upon averaging the "diff." columns we see that TPSS gives a small value compared to HLE17 indicating that the LUMO–HOMO gaps in TPSS are closer to the LR-TDDFT results than with HLE17. We conclude that the HLE strategy does not succeed mainly by improving the orbital energies.

The last two rows of Table 5.35 show the mean errors one would get if one computed excitation energies simply from the HOMO–LUMO gaps; we see that the linear response treatment gives more accurate results than the orbital energy gaps, as expected.

Next, if we consider the excitation energies of atoms (EEA11 database). We find that the increased excitation energies seen for the case of molecules with HLE16 and HLE17 functionals in Table 5.34 are also found for singlet and doublet main-group atoms. We limit this examination to systems with closed subshells or with at most one open-shell electron. The valence excitations of Li, Be, Na, Mg, and K were considered and Rydberg excitations of H, He, B, Ne, Al, and Ar were considered. The "MUE valence" value shows that all functionals perform well for valence excitations with HLE17 being the best performing functional with an MUE of 0.10 eV. The "MUE Rydberg" value shows that none of the functionals perform well for Rydberg excitations with the hybrid functional, HSE06, having the smallest MUE of 0.68 eV. Encouragingly, HLE17 has the lowest MUE of any local functional with an MUE of 0.77 eV, and lags behind HSE06 by only 0.09 eV.

Table 5.34 shows that HLE17 performs reasonably well for atomization energies of main-group molecules (AE6 database), forward and reverse barriers heights of 12 reactions (DBH24 database), and noncovalent complexation energies (NCCE31 database), and it is better than HLE16 for these databases. The performance of HLE17 for barrier heights is particularly noteworthy. Whereas PBE+U hardly

improves the barrier heights with respect to PBE, HLE17 greatly improves them as compared to similar functionals with lower local exchange and even with respect to HSE06. However, the performance of HLE17 on proton affinity (PA3 database), electron affinity (EA13 database), and ionization potential (IP21 database), all of which involve charged species, is not good. Also for molecular bond lengths, HLE17 is not as good as most of the local functionals but is slightly better than HLE16.

Finally, we look at molecular densities, as judged by dipole moments. The dipole moment is a leading indicator of the quality of the density because it is the first nonzero moment of the charge distribution for neutral molecules. The DM20 database contains dipole moments of 20 molecules (of which 11 molecules contain transition metals and the remainder contain only main-group elements); the overall MUEs for HLE16 and HLE17 are larger on this database than those for other functionals. To understand this source of error in HLE16 and HLE17, we calculated MUEs for the transition-metal-containing molecules and main-group elements containing molecules separately. We find that the MUEs for the main-group containing molecules are close to each other for all the functionals studied than are those for transition-metal-containing molecules, and they are reasonably small (~ 0.1 D); in contrast, the errors in dipole moments are large for the transition-metal-containing molecules. One possible reason for this could be multireference nature of these molecules; to estimate the extent of their multireference character we calculated the B_1 diagnostic[278] and only two molecules have a B_1 diagnostic value less than 10 kcal/mol, and the rest are highly multireference cases. It is well known[33,292] that KS-DFT with currently available functionals does more poorly for multireference cases than for single-reference ones.

Because the MUEs of dipole moments of molecules with transition metals are higher for HLE16 and HLE17 than other functionals for molecules, we conclude that increasing local exchange can give poor performance for multireference systems. The TMABE10 database considered in Table 5.34 contains open-shell molecules, which often have multireference character, and we look at the spin densities for these molecules using TPSS, HLE17, and HSE06. A hybrid functional with nonlocal exchange is known to localize electron density more than a local functional, and it would be interesting to see if the newly developed functional, HLE17, with an

enhanced local exchange, shows a similar trend. Table 5.36 gives Hirshfeld spin densities on transition metals of the molecules in the TMABE10 database, and we see that HLE17 shows the same trend as HSE06 in that for most of the cases the spin densities increase as one goes from TPSS to HLE17 or to HSE06.

Table 5.34 MUEs for all molecular and solid-state databases.

Database[a]	PBE	PBE+U[b]	BLYP	PBEsol	GAM	HCTH/407	HLE16	TPSS	HLE17	HSE06
Molecular properties										
AE6	4.6	4.5	1.8	9.7	4.1	2.3	4.3	2.3	3.4	2.6
TMABE10	8.3	6.1	7.8	12.7	4.9	6.4	11.0	8.1	10.6	5.6
DBH24	8.2	-	7.7	10.3	5.0	4.7	4.9	8.2	3.7	3.8
DBH18[c]	8.6	8.2	7.8	11.3	5.4	5.3	5.0	8.3	3.5	4.2
NCCE31	1.2	1.1	1.5	1.8	1.0	1.1	2.1	1.2	1.0	0.7
PA3	1.0	-	2.0	2.1	2.6	2.1	16.8	1.8	15.4	0.8
EA13	2.3	-	2.7	2.2	4.5	3.6	18.1	2.4	19.3	2.8
IP21	6.2	-	6.6	5.7	4.1	6.4	32.0	4.1	33.1	3.7
EE23 – valence	0.36	-	0.34	0.35	0.33	0.35	0.35	0.29	0.47	0.30
EE23 – Rydberg	1.01	-	1.14	0.95	0.78	0.84	0.32	0.80	0.37	0.27
EE23 – CT	1.07	-	1.10	1.07	1.05	1.07	1.20	0.98	1.10	0.66
EEA11	0.77	-	0.86	0.78	0.64	0.77	0.58	0.59	0.47	0.42
DM20	0.294	-	0.305	0.305	0.268	0.262	0.486	0.262	0.462	0.275
MGHBL9	0.011	0.014	0.010	0.014	0.004	0.003	0.053	0.007	0.050	0.002
MGNHBL11	0.009	0.016	0.016	0.006	0.007	0.005	0.072	0.007	0.052	0.009
DGH4	0.021	0.021	0.039	0.012	0.037	0.033	0.055	0.015	0.039	0.015
Solid-state properties										
SSCE8	0.11	0.49	0.30	0.33	0.10	0.23	0.27	0.14	0.22	0.10
TMOBG4	2.9	2.2	2.9	3.1	2.8	2.8	2.1	2.7	1.5	0.6[d]
SBG31	1.11	1.19	1.15	1.13	0.99	0.89	0.30	0.96	0.32	0.31
MGLC4	0.037	0.076	0.069	0.023	0.037	0.110	0.140	0.051	0.145	0.045
ILC5	0.078	0.081	0.121	0.020	0.110	0.219	0.142	0.062	0.083	0.023
TMLC4	0.065	0.038	0.139	0.019	0.106	0.072	0.113	0.029	0.028	0.050
SLC34	0.095	0.184	0.180	0.031	0.158	0.155	0.157	0.080	0.077	0.052

[a]The units for various databases are: AE6, TMABE10, DBH24, DBH18, NCCE31, PA3, EA13, and IP21 are in kcal/mol; MGHBL9, MGNHBL11, DGH4, ILC5, MGLC4, TMLC4, and SLC34 are in Å; EE23, EEA11, SSCE8, TMOBG4, and SBG31 are in eV; and DM20 is in D.

[b]The PBE+U (U = 4.0 eV) values were computed using *VASP* and the rest of the table is calculated using *Gaussian 09*.

[c]A subset DBH18 of DBH24 database that contains only reactions of neutral species.

[d]The TMOBG4 database uses HSE03 and the values are from Ref. 265.

Table 5.35 HOMO, LUMO, LUMO – HOMO, and LR-TDDFT energies (in eV) of the EE23 database.

		TPSS					HLE17				
Molecule	**Transition**	**HOMO**	**LUMO**	**LUMO–HOMO**	**LR-TDDFT**	**diff.[a]**	**HOMO**	**LUMO**	**LUMO–HOMO**	**LR-TDDFT**	**diff.[a]**
acetaldehyde	$^1A''$ n → π*	-6.05	-1.88	4.17	4.29	0.12	-7.90	-3.27	4.62	4.61	0.02
acetone	$^1A_2$ n → π*	-5.75	-1.52	4.23	4.36	0.13	-7.56	-2.94	4.63	4.62	0.01
formaldehyde	$^1A_2$ n → π*	-6.39	-2.50	3.89	4.01	0.13	-8.30	-3.84	4.46	4.43	0.03
pyrazine	$^1B_{3u}$ n → π*	-6.03	-2.53	3.50	3.72	0.21	-7.87	-3.90	3.98	4.09	0.12
pyridazine	$^1B_1$ n → π*	-5.57	-2.47	3.10	3.34	0.24	-7.45	-3.84	3.61	3.77	0.16
pyridine	$^1B_1$ n → π*	-6.06	-1.74	4.33	4.53	0.21	-7.83	-3.01	4.82	4.94	0.12
pyrimidine	$^1B_1$ n → π*	-6.08	-2.24	3.84	3.96	0.12	-7.84	-3.56	4.28	4.33	0.05
s-tetrazine	$^1B_{3u}$ n → π*	-5.95	-4.13	1.82	2.04	0.22	-7.95	-5.70	2.25	2.38	0.13
ethylene	$^1B_{1u}$ π → π*	-6.71	-0.90	5.82	7.42	1.60	-7.92	-1.95	5.97	7.69	1.72
butadiene	^1B_u π → π*	-5.79	-1.74	4.06	5.50	1.44	-7.03	-2.88	4.14	5.64	1.49
benzene	$^1B_{2u}$, π → π*	-6.27	-1.09	5.18	5.23	0.05	-7.50	-2.28	5.21	5.20	0.02
”	$^3B_{1u}$, π → π*	-6.27	-1.09	5.18	3.75	1.43	-7.50	-2.28	5.21	4.23	0.98
naphthalene	$^1B_{3u}$, π → π*	-5.45	-1.95	3.51	4.10	0.60	-6.71	-3.16	3.54	4.11	0.57
”	$^3B_{2u}$, π → π*	-5.45	-1.95	3.51	2.70	0.80	-6.71	-3.16	3.54	1.66	1.88
furan	$^1B_2$, π → π*	-5.64	-0.73	4.91	5.95	1.04	-6.97	-2.07	4.91	6.05	1.14
”	$^3B_2$, π → π*	-5.64	-0.73	4.91	3.78	1.13	-6.97	-2.07	4.91	2.63	2.28
hexatriene	^1B_u, π → π*	-5.36	-2.19	3.17	4.50	1.33	-6.61	-3.37	3.24	4.57	1.33
”	^3B_u, π → π*	-5.36	-2.19	3.17	2.14	1.02	-6.61	-3.37	3.24	0.73	2.51
water	Singlet, $2p_x \rightarrow 3s$	-7.31	-0.81	6.51	6.56	0.05	-9.11	-1.32	7.79	7.82	0.03
”	Triplet, $2p_x \rightarrow 3s$	-7.31	-0.81	6.51	6.24	0.26	-9.11	-1.32	7.79	7.31	0.48
pNA	Intramolecular CT, $^1A_1$, π → π*	-5.88	-2.89	2.99	3.64	0.65	-7.43	-4.56	2.86	3.52	0.66
DMABN	Intramolecular CT, $^1A_1$, π → π*	-5.08	-1.47	3.61	4.46	0.84	-6.54	-2.83	3.72	4.54	0.82
B-TCNE	Intermolecular CT, ^1A, π → π*	-6.77	-5.37	1.40	1.41	0.01	-8.02	-6.94	1.08	1.09	0.01

Average		0.59			0.72
MSE (singlet valence and Rydberg)	-0.73	-0.23		-0.39	0.09
MUE (singlet valence and Rydberg)	0.77	0.29		0.62	0.25

[a]The diff. columns give the absolute value of the difference between the LR-TDDFT and LUMO–HOMO columns.

Table 5.36 Hirshfeld spin densities (atomic units) on transition metal ions of molecules in TMABE10 database.

Molecule	TPSS	HLE17	HSE06
AgH	0.00	0.00	0.00
$CoCl_2$	2.52	2.68	2.78
CoH	2.00	2.00	2.00
CrCl	4.93	4.97	4.95
$CrCl_2$	4.01	3.91	4.00
$FeCl_2$	3.58	3.63	3.71
FeH	3.00	3.00	3.00
MnF_2	4.74	4.80	4.81
TiCl	2.95	2.99	2.95
VF_5	0.00	0.00	0.00

5.7 Concluding Remarks

This chapter discusses various ways in which one could improve the existing density functionals to obtain improved excitation energies, charge transfer, and solid-state properties without raising the computational cost.

The recently developed GAM functional has the following advantages over current GGAs and N12.

1. The GAM functional gives the smallest mean unsigned error for main group bond energies (MGBE137), transition metal bond energies (TMBE32), and reaction barrier heights (BH76).
2. The GAM functional gives the smallest mean unsigned error of 0.019 kcal/mol for the noble gas dimer weak interaction energies (NGDWI21), with all the other functionals tested here giving a mean unsigned error larger than 0.081 kcal/mol, which is about 50% of the reference value.
3. GAM is best of any LSDA, GGA, or NGA for both the overall mean unsigned error for molecular energies, either including total atomic energies (ME417) or excluding them (ME400xAE). OreLYP (which has not previously been widely tested) and OLYP are the second and the third best.
4. The GAM functional gives an MUE of 0.018Å for the molecular structure subdatabase (MS10), which is reasonable, although not outstanding.

5. Besides the training sets tested here, we also test the performance of the GAM functional against band gaps (SBG31), solid-state cohesive energies (SSCE8), transition metal coordination reactions (WCCR10), the bond energies of Ag_2 and FeC, adsorption enthalpies of gases on MOFs, the binding of C_2H_4 to $Pd(PH_3)_2$, and the bond distances of homonuclear transition metal dimers (HTMD7). The last-named test includes four 5d transition metals, although no 5d transition metal data was used for training. The GAM functional does acceptably well in these tests. We conclude that the GAM functional we designed is transferable to molecular problems outside our training sets.
6. The linear coefficients optimized for GAM are in a narrow range of magnitude so there is no excessive cancellation between terms. The self-consistent-field convergence of the GAM functional has been tested against more than one thousand data; only one of them shows some convergence problems. The enhancement factor plot of the GAM functional is reasonably smooth.

With all these advantages over the GGAs and the previous NGA, with the advantage of an NGA requiring smaller grids than meta-GGAs or meta-NGAs, and with the advantage of an NGA requiring considerably less computation time for extended systems than hybrid functionals, we expect the GAM functional to be very useful for molecular catalysis and a wide variety of other applications to large and complex molecular systems.

The effect of a Hubbard U correction on both solid-state and molecular properties was shown. The solid-state property that was considered is band gap, and the molecular properties that were considered are main-group average bond energies, transition-metal−ligand bond energies, and barrier heights. We find that adding a Hubbard U correction to a local functional sometimes improves results and sometimes deteriorates it, causing no significant effect on the MUE of the molecular properties, while a hybrid functional always improves the results. For band gaps of main-group containing semiconductors, we find that a hybrid functional always improves results compared to a local functional, while the addition of a Hubbard U correction to a local functional does not always improve results. The Zn and Cd containing semiconductors showed improvement in band gap when a Hubbard U correction was applied to the valence *d* orbitals of the metal, but when a Hubbard U correction was applied to both the metal and the nonmetal the improvement was less than when it

was applied to only the metal. The bad gaps of open-shell transition metal oxides (except FeO) could be improved by using a Hubbard U correction to a local functional, and this improvement is comparable to what could be achieved with a more expensive hybrid functional.

Two new density functionals, HLE16 and HLE17, were calibrated and validated against a diverse set of data that includes ground-state and excited-state properties for both molecules and solids. They have the advantage of giving band gaps and excitation energies comparable in accuracy to hybrid GGAs at a lower computational cost. However, prediction of molecular bond lengths, proton affinities, electron affinities, and ionization potentials is not good with both the HLE funtionals. We also compared HLE17 with PBE+U (with a fixed value of *U* equal to 4 eV), and we find that PBE+U does better than HLE17 on only 3 out of 14 databases for which this comparison is made. We anticipate that HLE17 will be especially useful for solid-state calculations on non-oxide semiconductors, where it provides greatly enhanced performance compared to other functionals with comparable cost and even provides performance comparable to the hybrid HSE06 functional for our largest semiconductor band gap database. In addition to its practical utility, the success of HLE functionals expose a new strategic direction for making more useful exchange-correlation functionals for Kohn-Sham theory.

6 Molecular Mechanics Development

6.1 Synopsis

Damped dispersion can be a significant component of the interaction energy in many physical and chemical processes, for example, physisorption and noncovalent complexation. For physically interpreting and modeling such processes, it is convenient to have an analytic method to calculate damped dispersion that is readily applicable across the entire periodic table. Of the available methods to calculate damped dispersion energy for interacting systems with overlapping charge distributions, we select symmetry-adapted perturbation theory (SAPT) as providing a reasonable definition, and of the possible analytic forms, we choose the D3(BJ) method. However, the available parameterizations of D3(BJ) include not only damped dispersion energy but also corrections for errors in specific exchange-correlation functionals. Here we present a parameterization that provides a physical measure of damped dispersion without such density functional corrections. The method generalizes an earlier method of Pernal and coworkers to all elements from hydrogen to plutonium.

6.2 Introduction

Molecular mechanics (MM) force fields are widely used in simulations;[293] a conventional molecular mechanics force field is the gradient of a potential energy function with four kinds of terms: valence terms (bond stretches, bond-angle bends, and torsions), electrostatics, short-range repulsion, and long-range dispersion. The latter two are often combined and represented by a Lennard-Jones function. The terms in an MM force field have many parameters that are usually fit to experimental data, to quantum mechanical internal energies and interaction energies, or to both. With few exceptions, the individual terms do not have a well-defined meaning; only the sum of the terms has meaning as a potential energy function. Thus, the MM force field does not decompose the internal energy or interaction energy into well-defined physical components, like static-subsystem electrostatics, electric polarization, exchange repulsion, and charge transfer. For example, intermolecular electrostatic interactions are often represented by unscreened Coulomb forces between subsystem

partial atomic charges, although unscreened are technically valid only for long-range interactions when the charge clouds of the interacting partners do not overlap. Since overlap is appreciable even at van der Waals distances, such functional forms do not represent true electrostatics, and they can give correct interaction energies only by a cancellation of errors with other terms in the potential or by using incorrect charge distributions. There has been recent progress in developing functional forms for screened electrostatics that corresponds more closely to the true situation,[294,295,296,297,298,299,300] and such efforts are part of a broader effort to develop physically motivated force fields in which all terms have a physical meaning.

The present work is concerned with a related issue, namely, the representation of damped dispersion interactions between atoms, molecules, or nonbonded fragments of a molecule where the interacting subsystems have overlapping charge distributions. At large distances where charge clouds do not overlap, one can use second-order quantum mechanical perturbation theory to expand dispersion interactions in inverse powers of R, where R is the distance between the subsystems, with the leading term being the well-known R^{-6} term corresponding to the interaction of two induced dipoles. Since an R^{-6} term blows up catastrophically at small R, the functional form must be damped. Physically this occurs due to the breakdown of the multipole expansion when two charge clouds overlap. There is an instructive history of considering the effect of this overlap to make models,[301,302,241] but general rigorous theories of damped dispersion interactions are not available. Instead, most molecular mechanics force fields ignore the damping and simply let the repulsive forces due to exchange-repulsion and nuclear repulsion dominate the undamped dispersion terms. This makes both the dispersion terms and the repulsion terms unphysical.

One important development in recent years[303,304,80,305] is the parameterization of damped dispersion terms to add to Kohn-Sham density functional calculations. With exchange–correlation functionals that do not include nonlocal correlation terms, Kohn-Sham theory does not predict accurate dispersion forces in the nonoverlapping (long-range) region, although they can in principle (and – for some functionals – in practice) represent dispersion-like interactions in regions of charge cloud overlap where dispersion is damped (such regions include van der Waals distances and are sometimes called the medium range). The molecular mechanics terms used to make up for inaccurate treatments of dispersion are parameterized to fit accurate interaction

energies, and therefore they include not only the portion of damped dispersion that was not present in the given exchange–correlation functional but also corrections for other sources of error in the exchange–correlation functionals. Thus, the corrections are different for each density functional and do not simply represent the damped dispersion.

Actually, damped dispersion is not uniquely defined. At large intersystem separation, one can identify sets of paired excitations in the individual subsystems that contribute to each term in the multipole expansion of the dispersion interaction. For example, the R^{-6} term in the interaction of subsystems A and B comes from a double excitation consisting of dipole-allowed single excitations on each center. As R gets smaller, additional contributions to the interaction energy become significant, but when the charge clouds of the fragments interact significantly, classifying these contributions as intermolecular or intramolecular or as dispersion or charge transfer is not unique. Nevertheless, there are methods that attempt to do this, and the one that is usually recognized as most reasonable is symmetry-adapted perturbation theory[81,306] (SAPT). Here we use SAPT, in particular, SAPT based on a density functional theory description of monomers, which is called SAPT(DFT),[307,308] to define the damped dispersion, but one should keep in mind that this choice, although very reasonable, is not unique.

As part of a project to develop a dispersionless density functional (dlDF), Pernal and coworkers[309] used SAPT(DFT) to calculate damped dispersion energies for the interactions of a large number of noncovalently interacting partners and then fit these to a damped dispersion function (labeled as D_{as} in Ref. 309) with four parameters for each of H, He, C, N, O, F, Ne, S, Cl, and Ar. The goal of the present work is to extend this kind of general treatment of damped dispersion to all elements up to $Z = 94$. (Although we have motivated the present treatment of damped dispersion for use in physical-terms molecular mechanics, it could also be used in conjunction with dispersion-free density functionals such as dlDF[309] or APF (Austin-Petersson-Frisch).[310]

6.3 Complexes Studied

In a previous study,[31] we calculated the damped dispersion contribution to the binding energy of ethylene dimer and found that the D3(0) damped dispersion optimized for the revPBE38 functional agrees well with damped dispersion contribution calculated by SAPT(DFT). Here we extend that kind of comparison to the whole NCCE31/05 database[178,311] of 31 noncovalent complexation energies, the S22 database of 22 interaction energies of hydrogen-bonded and dispersion-bonded complexes that are representative of biomolecules,[312] a subset of the training set of dlDF (H_2O–H_2O, NH_3–NH_3, Ar–HF, N_2–HF, CH_4–CH_4, C_2H_2–ClF, NH_3–ClF, and C_2H_4–C_2H_4) that uses three intermonomer distances for each complex,[309] and a subset of the training set of the damping function in the work of Pernal and coworkers that uses 10 intermonomer distances for each of these five complexes (Ne–Ne, Ar–Ar, C_2H_4–Ar, H_2S–H_2S, and C_6H_6–C_6H_6).[309] The reference geometries of the complexes for single-point calculations were taken from the references just cited. The reference values of damped dispersion energies, based on which we calculate the mean unsigned errors (MUEs) of various models for dispersion, are SAPT(DFT) values from the Supporting Information (SI) of Ref. 309, with only the second-order terms (dispersion and exchange-dispersion); the higher-order dispersion terms were not taken into account due to their small contribution. The NCCE31/05 database in Ref. 309 is reported in terms of its subsets: HB6, CT7, DI6, WI7, and PPS5, and in this work, we use the merged form (NCCE31/05) for calculating MUE.

6.4 Methodology

All damped dispersion calculations were done using the DFT-D3 package (version 3.2, rev 0) of Grimme and coworkers[313] by applying either zero damping[303] or Becke-Johnson (BJ) damping[305] to determine the D3 component of a given functional. This D3 component is the sum of E_6 and E_8 terms, which we call the damped dispersion energy:

$$E_{\mathrm{dampdisp}} = E_6 + E_8 \qquad 6.1$$

In D3(0), the terms are given by

$$E_n[\mathrm{D3(0)}] = -\frac{1}{2}\sum_{A\neq B} s_n \frac{C_n^{AB}}{r_{AB}^n} f_{\mathrm{damp},n}(r_{AB})$$

6.2

where s_n are the power-n density-functional-dependent global scaling factors, C_n^{AB} are the power-n dispersion coefficients of atoms A and B, and the damping factors are

$$f_{\mathrm{damp},n}(r_{AB}) = \frac{1}{1 + 6\left[\left(s_{r,n}R_0^{AB}\right)/r_{AB}\right]^{\alpha_n}}$$

6.3

where R_0^{AB} is a cutoff radius, and $s_{r,n}$ is the power-n scaling factor. The parameters α_6 and α_8 are 14 and 16, respectively, in the standard D3(0) model. (Note that D3(0) is often labeled just D3 because it is the original D3 method.) The DFT-D3(BJ) model utilizes

$$E_n[\mathrm{D3(BJ)}] = -\frac{1}{2}\sum_{AB} s_n \frac{C_n^{AB}}{r_{AB}^n + f\left(R_0^{AB}\right)^n}$$

6.4

where

$$R_0^{AB} = \sqrt{\frac{C_8^{AB}}{C_6^{AB}}}$$

6.5

and

$$f(R_0^{AB}) = a_1 R_0^{AB} + a_2$$

6.6

where a_1 and a_2 depend on which functional is used.

The dispersion energy of a complex is the sum of both intramolecular and intermolecular dispersion energies of all the atom pairs, and the dispersion energy of a monomer includes only intramolecular dispersion energy. Therefore, we compute the intermolecular dispersion energy for a complex by subtracting dispersion energies of the monomers from the dispersion energy of the complex

$$(\Delta E_{\mathrm{dampdisp}} = E_{\mathrm{dampdisp}}^{\mathrm{complex}} - E_{\mathrm{dampdisp}}^{\mathrm{monomer\_1}} - E_{\mathrm{dampdisp}}^{\mathrm{monomer\_2}}),$$

6.7

where the geometries of the monomers are the same as they are in the complex. This protocol is followed to do a fair comparison with the reference dispersion energies (SAPT(DFT))[309] that were calculated using the same geometry for the monomers as they have in the complex.

6.5 Results and Discussion

Several damped dispersion terms, including those optimized for B3LYP,[171,170,172,173] B97-D,[61] BOP,[314] OLYP,[171,174] OPBE,[60,174] revPBE0,[84] revPBE38,[84] and revSSB,[315] with zero damping or BJ damping or both, were screened on the NCCE31/05 database. The results for $\Delta E_{\mathrm{dampdisp}}$ with some of these DFT-D3 methods are shown in Table 6.1, which also shows results for SAPT(DFT), for the fitted damping functions of Szalewicz and coworkers (D_{as}),[309,82] and for the dispersion method introduced below in this work, which will be called DD3S ("damped dispersion based on D3 and SAPT").

Table 6.1 shows results using two damping functions (D_{as}) of Szalewicz and coworkers, where the damping function used in Ref. 82 is an improved version of the one used in Ref. 309. The D_{as} function is based on the damping function of Tang and Toennies[301] and an additional attractive exponential term to describe the spherical component of dispersion interactions; the relevant equations are given by eqs. (1)–(3) of the SI of Ref. 309. The revised D_{as} model of Ref. 82 was trained on a much larger database than that used in Ref. 309, and it does not contain pure exponential functions. One can see that both of the D_{as} damped dispersion methods agree very well with the SAPT(DFT) data, but most of the D3 dispersion terms (which were intended to be complementary to specific functionals) give much larger mean unsigned deviations. This confirms that the D_{as} damped dispersion would be a good choice for a general damped dispersion expression if it were available for all elements. The drawback of D_{as} is that it has parameters only for H, He, C, N, O, F, Ne, S, Cl, and Ar so if we want to model a system containing elements other than those ten, either new parameters need to be derived or an alternative method needs to be established.

To find an alternative approach that can be broadly applied, we calculated $\Delta E_{\mathrm{dampdisp}}$ with a number of DFT-D3 damped dispersion expressions and found that OLYP-D3(BJ) is the one that gives the best results, with an MUE of 0.84 kcal/mol. Using this as our starting point, we adjusted two parameters, namely, a_2 and s_8, which are defined in eqs 6.4 and 6.6; a_2 is a medium-range correlation parameter, and s_8 mainly affects the repulsive wall. After a number of preliminary tests, these

parameters were set to values 2.2 and 2.0, respectively. The parameter a_1 also takes into account the medium-range correlation effect, and it was not adjusted in this work. The resulting method with these new parameters, i.e., the modified OLYP-D3(BJ) damped dispersion, is now labeled as DD3S. Table 6.1 shows that DD3S is the best performing method (MUE = 0.57 kcal/mol) when compared with the damped dispersion terms of other DFT-D3 methods. We especially note that the dispersion terms of the widely used DFT-D3 methods, B3LYP-D3(0) and B3LYP-D3(BJ), underestimate $\Delta E_{\mathrm{dampdisp}}$ for every complex in the NCCE31/05 database; this is also reflected in their small average values and large MUEs, thereby rendering them unsuitable for physical calculations of intermolecular damped dispersion energies.

To see how well DD3S performs on complexes outside the NCCE31/05 database on which it was calibrated, its performance is tested on additional complexes, as shown in Table 6.2– 6.4. Note that in all these tables we are considering only the damped dispersion energy, not the whole interaction energy. Table 6.2 shows that for the S22 database, DD3S does better than the unmodified OLYP-D3(BJ) as well as the two variants of B3LYP-D3. The MUEs in the latter cases are quite large.

The NCCE31 and S22 databases in Table 6.1 and 6.2 are for complexes fixed at their equilibrium geometries. In Table 6.3 we study eight complexes for which we consider three intermonomer separations: shorter than, close to, and longer than the equilibrium separation. Table 6.3 shows that although DD3S was not calibrated for complexes with distances away from their equilibrium geometries, it performs reasonably well compared to other DFT-D3 methods in the table.

In Table 6.4 we study five complexes for each of which we consider 10 intermonomer separations. Except for the benzene dimer, the MUEs by the two B3LYP-D3 methods are an order of magnitude larger than that of either the DD3S or D_{as} fitting function. The good performance of the D_{as} fitting function on this set is not surprising as it was parametrized on this data, but it is interesting to note that DD3S also shows very good performance, even though it was not calibrated for complexes that have very short or very long intermonomer separations. For the C_2H_4–Ar complex, its performance is even better than the D_{as} fitting function. Note that in a complex when we allow the intermonomer distances to vary, those distances that

correspond to large interaction energies or damped dispersion contributions dominate the error.

Both Table 6.3 and 6.4 sometimes show patterns for B3LYP-D3(0) that are different from what is seen in the other methods. In particular, in Table 6.3, for complexes Ar–HF, C_2H_2–ClF, and NH_3–ClF, the magnitude of $\Delta E_{\text{dampdisp}}$ decreases monotonically as intermonomer separation increases for all the methods except B3LYP-D3(0). The same is true for the Ar–Ar complex in Table 6.4. In these tables, B3LYP-D3(0) is the only method with -D3(0) damping and its unusual pattern can be attributed to the nature of its damping function at small interatomic separations where the dispersion energy is unphysically damped to zero; that is why the D3(BJ) scheme is more physical. For most of the complexes considered, we found that the damped dispersion terms of the widely used B3LYP-D3(0) and B3LYP-D3(BJ) methods differ from those of the benchmark method (Disp + Exch-Disp) much more than the ones calculated by DD3S.

Figure 6.1 shows an example of applications to a system with atoms heavier than those in the parameterization of Pernal and coworkers.[309] It corresponds to the interaction of Br_2 with Kr in two orientations – parallel and perpendicular. In the parallel orientation, the Kr atom was moved along the line of the Br–Br bond, and in the perpendicular orientation, the Kr atom was moved perpendicular to the line of Br–Br bond such that it was equidistant from the two Br atoms. In the figure, interaction energies were calculated with CCSD(T)[316] to show the shape of a realistic potential curve, and the damped dispersion energies were calculated with the DD3S method and SAPT(DFT). The CCSD(T) calculations were carried out with the def2-QZVP[141] basis set and the *Gaussian 09*[188] program, and the same protocol as described above for the damped dispersion contribution was applied for interaction energy calculations, i.e. the geometries of the monomers were kept the same as they are in the complex. The SAPT(DFT) calculations were carried out using PBE0[176] as the exchange-correlation functional and aug-cc-pVTZ[317] (plus mid-bond basis) basis set in *Molpro*;[318] this is the same basis set as was used in Ref. 309. For the Br_2–Kr parallel complex, the mid-bond functions were placed at the midpoint of Kr and Br that is close to Kr and for the Br_2–Kr perpendicular complex, the mid-bond functions were place at the midpoint of Kr and the center of mass of Br_2.

In Figure 6.1, the comparison of the interaction potentials using CCSD(T) to the damped dispersion contributions allows us to see that as the intermonomer distance decreases the damped dispersion continues to increase even as the potential curve turns up. Figure 6.1 shows that for short intermonomer separations (≤ 2.75 Å) in Figure 6.1(a), the DD3S method slightly underestimates damped dispersion as compared to SAPT(DFT), while for larger separations the agreement between the two methods is very good. Notice that the minimum of the potential curve for this orientation is around 3.75 Å; therefore, good agreement of the DD3S and SAPT(DFT) curves in to 2.75 Å is more than adequate. A similar pattern is seen in Figure 6.1(b), although at 2.75 Å there is an excellent agreement between SAPT(DFT) and DD3S in comparison to Figure 6.1(a). These comparisons confirm that the new DD3S method is working well.

Table 6.1 Damped dispersion contributions ($\Delta E_{\text{dampdisp}}$ in kcal/mol)[a] to the interaction energies for the NCCE31/05 database.

Complex	SAPT(DFT) Disp + Exch-Disp[b]	D_{as}[b]	D_{as}[c]	DD3S	OLYP -D3(BJ)	OPBE -D3(BJ)	B3LYP -D3(BJ)	revPBE38 -D3(0)	B3LYP -D3(0)
$(NH_3)_2$	–2.11	–1.84	–1.65	–2.05	–1.73	–1.77	–0.77	–0.87	–0.78
$(HF)_2$	–1.66	–1.63	–1.71	–1.77	–1.17	–1.12	–0.36	–0.50	–0.46
$(H_2O)_2$	–2.30	–2.14	–2.27	–2.30	–1.69	–1.66	–0.62	–0.77	–0.72
$NH_3…H_2O$	–3.03	–2.78	–2.68	–2.85	–2.13	–2.11	–0.80	–0.96	–0.86
$(HCONH_2)_2$	–7.41	–7.27	–7.02	–7.26	–5.71	–5.78	–2.50	–2.72	–2.53
$(HCOOH)_2$	–8.78	–8.76	–9.03	–8.02	–6.00	–5.97	–2.39	–2.49	–2.31
$C_2H_4…F_2$	–1.63	–1.60	–1.51	–1.19	–1.16	–1.24	–0.62	–0.81	–0.79
$NH_3…F_2$	–1.80	–1.55	–0.89	–0.98	–0.88	–0.90	–0.40	–0.55	–0.56
$C_2H_2…ClF$	–5.01	–5.10	–4.98	–5.29	–4.28	–4.23	–1.84	–1.18	–1.22
HCN…ClF	–4.18	–4.37	–4.76	–3.53	–2.68	–2.61	–1.13	–0.61	–0.62
$NH_3…Cl_2$	–4.70	–4.13	–4.35	–3.55	–2.94	–2.96	–1.30	–1.14	–1.08
$H_2O…ClF$	–4.05	–3.35	–4.67	–3.28	–2.54	–2.49	–1.00	–0.86	–0.82
$NH_3…ClF$	–9.16	–9.26	–9.41	–5.88	–4.21	–4.03	–1.51	–1.27	–1.26
$(H_2S)_2$	–2.05	–1.93	–2.04	–2.28	–2.16	–2.30	–1.20	–1.06	–1.05
$(HCl)_2$	–2.05	–1.91	–1.92	–2.59	–2.22	–2.28	–1.06	–0.98	–0.97
$HCl…H_2S$	–2.96	–2.69	–2.78	–3.40	–2.86	–2.92	–1.36	–1.10	–1.10
$CH_3Cl…HCl$	–3.63	–3.49	–3.52	–4.60	–3.93	–4.03	–1.84	–1.76	–1.72
$HCN…CH_3SH$	–2.69	–2.57	–2.60	–3.72	–3.37	–3.52	–1.72	–1.66	–1.58
$CH_3SH…HCl$	–4.61	–4.48	–4.57	–5.49	–4.65	–4.76	–2.20	–1.98	–1.92
HeNe	–0.08	–0.08	–0.08	–0.08	–0.08	–0.09	–0.05	–0.07	–0.07
HeAr	–0.13	–0.12	–0.12	–0.13	–0.13	–0.15	–0.09	–0.10	–0.10
Ne_2	–0.16	–0.15	–0.16	–0.17	–0.17	–0.18	–0.09	–0.13	–0.12
NeAr	–0.27	–0.26	–0.27	–0.28	–0.29	–0.32	–0.17	–0.20	–0.19
$CH_4…Ne$	–0.33	–0.32	–0.31	–0.36	–0.38	–0.41	–0.23	–0.29	–0.31
$C_6H_6…Ne$	–1.00	–0.97	–1.09	–1.03	–1.09	–1.21	–0.70	–0.80	–0.80
$(CH_4)_2$	–1.26	–1.20	–1.14	–1.58	–1.63	–1.78	–0.98	–1.17	–1.04
$(C_2H_2)_2$	–1.42	–1.26	–1.18	–1.83	–1.85	–2.00	–1.06	–1.16	–1.04
$(C_2H_4)_2$	–2.60	–2.57	–2.47	–3.93	–3.84	–4.11	–2.02	–2.53	–2.12
sandwich $(C_6H_6)_2$	–4.72	–4.55	–4.99	–5.29	–5.78	–6.48	–4.44	–4.00	–4.09

T-shaped $(C_6H_6)_2$	–4.07	–4.19	–3.85	–5.42	–5.47	–5.94	–3.42	–3.53	–3.42
parallel-displaced $(C_6H_6)_2$	–5.82	–5.73	–6.19	–6.71	–7.25	–8.09	–5.26	–4.87	–4.78
Average[d]	–3.09	–2.98	–3.04	–3.12	–2.72	–2.82	–1.39	–1.36	–1.30
MUE[e]	0.00	0.14	0.21	0.57	0.84	0.96	1.69	1.73	1.78

[a] $\Delta E_{\text{dampdisp}}$ is defined by eq 6.7.

[b] Ref. 82.

[c] Ref. 309.

[d] Average for each method is taken over all the 31 complexes.

[e] MUE = mean unsigned error; the methods are arranged in ascending order of MUE.

Table 6.2 Damped dispersion contributions ($\Delta E_{\text{dampdisp}}$ in kcal/mol)[a] to the interaction energies for the S22 database.

Complex	SAPT(DFT) Disp + Exch-Disp[b]	D_{as}[b]	D_{as}[c]	DD3S	OLYP -D3(BJ)	B3LYP -D3(BJ)	B3LYP -D3(0)
stacked adenine–thymine (C_1)	–16.01	–20.09	–20.71	–20.69	–21.27	–13.01	–12.47
Watson-Crick adenine–thymine (C_1)	–9.78	–10.24	–9.55	–10.01	–8.45	–4.28	–4.23
ethane dimer (D_{2d})	–2.58	–2.57	–2.47	–3.92	–3.83	–2.02	–2.12
ethane–ethyne (C_{2v})	–1.41	–1.26	–1.13	–1.84	–1.81	–1.03	–1.06
benzene–methane (C_3)	–2.91	–2.81	–2.44	–3.60	–3.64	–2.19	–2.25
benzene–water (C_s)	–2.82	–3.08	–2.53	–4.25	–4.05	–2.15	–2.33
benzene–HCN (C_s)	–3.60	–4.27	–3.73	–5.85	–5.49	–2.84	–2.74
benzene–ammonia (C_s)	–2.86	–3.07	–2.35	–3.90	–3.85	–2.21	–2.36
benzene dimer (C_{2h})	–8.03	–8.00	–8.58	–9.39	–9.96	–6.70	–6.04
benzene dimer (C_{2v})	–4.63	–4.76	–4.36	–6.19	–6.15	–3.73	–3.70
methane dimer (D_{3d})	–1.06	–1.01	–0.96	–1.31	–1.37	–0.87	–0.92
water dimer (C_s)	–2.44	–2.29	–2.44	–2.46	–1.79	–0.64	–0.74
formamide dimer (C_{2h})	–7.77	–7.68	–7.38	–7.56	–5.92	–2.56	–2.57

formic acid dimer (C_{2h})	–9.51	–9.54	–9.78	–8.43	–6.25	–2.46	–2.33
stacked indole–benzene (C_1)	–11.66	–12.22	–12.91	–13.67	–14.42	–9.49	–8.55
T-shaped indole–benzene (C_1)	–6.32	–7.42	–6.24	–9.15	–8.75	–5.04	–4.93
ammonia dimer (C_{2h})	–2.24	–2.22	–2.09	–2.64	–2.16	–0.89	–0.92
phenol dimer (C_1)	–6.50	–6.66	–6.65	–7.87	–7.32	–4.07	–4.25
pyrazine dimer (C_s)	–8.43	–9.35	–9.41	–10.31	–10.76	–6.82	–6.27
2-pyridoxine–2-aminopyridine (C_1)	–9.68	–9.81	–9.00	–9.67	–8.04	–4.00	–3.91
H-bonded uracil dimer (C_{2h})	–9.16	–9.33	–9.14	–8.80	–7.06	–3.36	–3.33
stacked uracil dimer (C_2)	–11.08	–13.67	–14.70	–14.75	–15.11	–9.26	–9.16
Average[d]	–6.39	–6.88	–6.75	–7.56	–7.16	–4.07	–3.96
Method MUE[e]	0.00	0.55	0.69	1.32	1.76	2.31	2.42

[a] $\Delta E_{dampdisp}$ is defined in eq 6.7.

[b] Ref. 82.

[c] Ref. 309.

[d] Average for each method is taken over all the 22 complexes.

[e] MUE = mean unsigned error; the methods are arranged in ascending order of MUE.

Table 6.3 Damped dispersion contributions to the interaction energies ($\Delta E_{\text{dampdisp}}$ in kcal/mol)[a] of complexes with three intermonomer separations (R in Å).

Complex	R[b]	SAPT(DFT) Disp + Exch-Disp[c]	DD3S	OLYP -D3(BJ)	B3LYP -D3(BJ)	B3LYP -D3(0)
Ar–HF	3.175	–1.43	–2.12	–1.51	–0.53	–0.52
	3.440	–0.83	–1.40	–1.13	–0.45	–0.59
	4.233	–0.19	–0.32	–0.34	–0.21	–0.25
C_2H_2–ClF	2.890	–12.69	–8.86	–5.99	–2.20	–1.06
	3.390	–5.01	–5.29	–4.28	–1.84	–1.22
	3.890	–2.05	–2.43	–2.37	–1.29	–1.29
C_2H_4–C_2H_4	2.200	–3.69	–5.64	–5.21	–2.45	–2.62
	2.600	–1.64	–2.45	–2.52	–1.52	–1.55
	3.400	–0.37	–0.52	–0.57	–0.46	–0.49
CH_4–CH_4	2.700	–6.57	–8.28	–6.19	–2.02	–1.77
	3.410	–1.79	–2.28	–2.28	–1.21	–1.31
	3.810	–0.90	–1.11	–1.17	–0.78	–0.83
H_2O–H_2O	2.500	–5.77	–4.10	–2.64	–0.80	–0.70
	3.100	–1.69	–1.80	–1.40	–0.55	–0.67
	4.000	–0.31	–0.34	–0.35	–0.22	–0.27
N_2–HF	3.175	–3.12	–3.10	–1.99	–0.63	–0.58
	3.551	–1.38	–1.97	–1.39	–0.50	–0.43
	4.233	–0.35	–0.58	–0.56	–0.28	–0.33
NH_3–ClF	2.709	–15.14	–7.67	–5.05	–1.66	–1.10
	2.959	–9.16	–5.88	–4.21	–1.51	–1.26
	3.459	–3.57	–2.94	–2.52	–1.14	–0.98
NH_3–NH_3	3.000	–3.33	–3.76	–2.81	–1.04	–0.92
	3.207	–2.25	–2.68	–2.18	–0.89	–0.91
	4.500	–0.24	–0.27	–0.29	–0.22	–0.23
Average[d]		–3.48	–3.16	–2.46	–1.02	–0.91
Method MUE[e]		0.00	1.09	1.40	2.47	2.58

[a] $\Delta E_{\text{dampdisp}}$ is defined in eq 6.7.

[b] R represents center-of-mass separation between the two monomers.

[c] Ref. 309.

[d] Average for each method is taken over all the 24 complexes.

[e] MUE = mean unsigned error; the methods are arranged in ascending order of MUE.

Table 6.4 Damped dispersion contributions to the interaction energies ($\Delta E_{\text{dampdisp}}$ in kcal/mol)[a] of complexes with 10 intermonomer separations (R in Å).

Complex	R[b]	SAPT(DFT) Disp + Exch-Disp[c]	D_{as}[c]	DD3S	OLYP -D3(BJ)	B3LYP -D3(BJ)	B3LYP -D3(0)
Ne–Ne	2.600	–0.5118	–0.5138	–0.4616	–0.3843	–0.1282	–0.2567
	2.850	–0.2833	–0.2824	–0.2742	–0.2569	–0.1082	–0.1750
	3.091	–0.1648	–0.1642	–0.1665	–0.1670	–0.0865	–0.1247
	3.350	–0.0954	–0.0952	–0.0996	–0.1040	–0.0642	–0.0859
	3.600	–0.0583	–0.0584	–0.0624	–0.0664	–0.0463	–0.0576
	4.200	–0.0205	–0.0206	–0.0228	–0.0245	–0.0201	–0.0219

	5.000	–0.0065	–0.0065	–0.0073	–0.0078	–0.0070	–0.0071
	6.000	–0.0020	–0.0020	–0.0023	–0.0024	–0.0022	–0.0022
	8.000	–0.0003	–0.0003	–0.0004	–0.0004	–0.0004	–0.0004
	10.000	–0.0001	–0.0001	–0.0001	–0.0001	–0.0001	–0.0001
MUE		0.0000	0.0004	0.0073	0.0179	0.0681	0.0416
Ar–Ar	3.000	–2.5314	–2.4990	–2.3623	–1.9304	–0.8187	–0.4941
	3.500	–0.9644	–0.9841	–1.0425	–1.0326	–0.5722	–0.5464
	3.750	–0.6091	–0.6314	–0.6801	–0.7111	–0.4434	–0.4078
	4.000	–0.3917	–0.4118	–0.4478	–0.4837	–0.3312	–0.2993
	4.200	–0.2793	–0.2961	–0.3242	–0.3556	–0.2580	–0.2379
	4.600	–0.1480	–0.1585	–0.1760	–0.1958	–0.1539	–0.1499
	5.000	–0.0829	–0.0888	–0.1002	–0.1118	–0.0923	–0.0915
	6.000	–0.0242	–0.0252	–0.0294	–0.0325	–0.0286	–0.0280
	8.000	–0.0038	–0.0037	–0.0045	–0.0048	–0.0044	–0.0043
	10.000	–0.0009	–0.0009	–0.0011	–0.0011	–0.0011	–0.0010
MUE		0.0000	0.0129	0.0471	0.1026	0.2373	0.2805
C_2H_4–Ar	3.450	–1.6842	–1.4769	–1.6898	–1.7401	–1.0545	–1.1092
	3.700	–1.1064	–0.9720	–1.1136	–1.1875	–0.7967	–0.8004
	3.950	–0.7350	–0.6487	–0.7442	–0.8095	–0.5874	–0.5844
	4.200	–0.4946	–0.4396	–0.5061	–0.5561	–0.4277	–0.4299
	4.450	–0.3378	–0.3027	–0.3506	–0.3868	–0.3106	–0.3143
	5.000	–0.1546	–0.1411	–0.1664	–0.1834	–0.1564	–0.1568
	5.500	–0.0816	–0.0754	–0.0904	–0.0990	–0.0872	–0.0863
	6.000	–0.0458	–0.0427	–0.0519	–0.0564	–0.0508	–0.0498
	8.000	–0.0072	–0.0069	–0.0084	–0.0089	–0.0084	–0.0082
	10.000	–0.0018	–0.0017	–0.0021	–0.0022	–0.0021	–0.0020
MUE		0.0000	0.0541	0.0075	0.0381	0.1195	0.1132
H_2S–H_2S	3.600	–4.6185	–4.9110	–4.6895	–3.8289	–1.8068	–1.2220
	3.850	–2.9968	–3.0590	–3.2672	–2.8852	–1.4746	–1.1553
	4.075	–2.0514	–2.0384	–2.2789	–2.1628	–1.1985	–1.0519
	4.350	–1.3041	–1.2711	–1.4368	–1.4652	–0.9034	–0.8551
	4.600	–0.8741	–0.8473	–0.9479	–1.0089	–0.6822	–0.6441
	5.000	–0.4729	–0.4625	–0.5036	–0.5549	–0.4209	–0.4022
	5.500	–0.2315	–0.2323	–0.2451	–0.2743	–0.2266	–0.2244
	6.000	–0.1210	–0.1246	–0.1281	–0.1444	–0.1251	–0.1241
	8.000	–0.0160	–0.0168	–0.0142	–0.0182	–0.0174	–0.0175
	10.000	–0.0037	–0.0038	–0.0005	–0.0034	–0.0039	–0.0043
MUE		0.0000	0.0443	0.0832	0.1459	0.5842	0.7000
C_6H_6–C_6H_6	3.400	–9.8667	–10.5690	–11.2375	–11.8634	–7.8683	–6.9941
	3.650	–6.7903	–7.2187	–7.6511	–8.2612	–5.9538	–5.3816
	3.900	–4.7207	–4.9864	–5.2933	–5.7818	–4.4375	–4.0929
	4.150	–3.3150	–3.4871	–3.7264	–4.0902	–3.2882	–3.1183
	4.400	–2.3571	–2.4709	–2.6688	–2.9323	–2.4392	–2.3679
	4.800	–1.4020	–1.4652	–1.6176	–1.7727	–1.5316	–1.5108
	5.200	–0.8643	–0.9004	–1.0174	–1.1095	–0.9833	–0.9704
	6.000	–0.3631	–0.3765	–0.4417	–0.4764	–0.4358	–0.4276
	8.000	–0.0651	–0.0672	–0.0813	–0.0858	–0.0816	–0.0800
	10.000	–0.0173	–0.0180	–0.0215	–0.0225	–0.0219	–0.0215
MUE		0.0000	0.1798	0.3995	0.6634	0.3569	0.5415

[a] $\Delta E_{\text{dampdisp}}$ is defined in eq 6.7.

[b] R is the center-of-mass separation between the two monomers.

[c]Ref. 309.

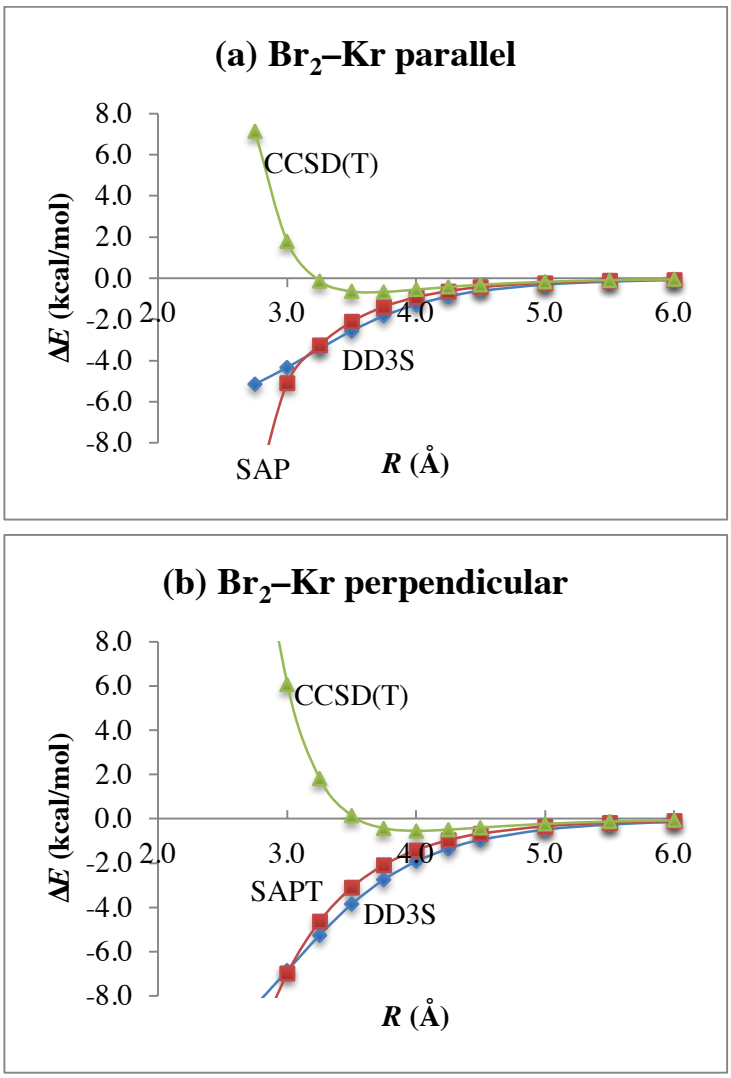

Figure 6.1 Interaction and damped dispersion energy of Br_2 interacting with Kr. Two orientations, (a) parallel and (b) perpendicular, as functions of intermonomer distance, were considered. The interaction energy was calculated by CCSD(T), and the damped dispersion energies were calculated by DD3S and SAPT(DFT), and in SAPT(DFT) only second order terms were included.

6.6 Concluding Remarks

In summary, a method has been proposed called DD3S that can be used to calculate physical damped dispersion energies in noncovalent interactions. This new method is based on DFT-D3(BJ) and SAPT(DFT). Its performance has been tested on a variety of complexes including those that have geometries away from the equilibrium structures.

7 Bibliography

[1] Nanoporous Materials Genome Center. http://www.chem.umn.edu/nmgc/ (accessed Nov 1, 2015).

[2] Rowsell, J. L. C.; Yaghi, O. M. Metal–Organic Frameworks: A New Class of Porous Materials. *Microporous Mesoporous Mater.* **2004**, *73*, 3–14.

[3] Li, J.-R.; Kuppler, R. J.; Zhou, H.-C. Selective Gas Adsorption and Separation in Metal–Organic Frameworks. *Chem. Soc. Rev.* **2009**, *38*, 1477–1504.

[4] Zhou, H.-C.; Kitagawa, S. Metal–Organic Frameworks (MOFs). *Chem. Soc. Rev.* **2014**, *43*, 5415–5418.

[5] Furukawa, H.; Cordova, K. E.; O'Keeffe, M.; Yaghi, O. M. The Chemistry and Applications of Metal-Organic Frameworks. *Science* **2013**, *341*, 1230444.

[6] Czaja, A. U.; Trukhan, N.; Müller, U. Industrial Applications of Metal–Organic Frameworks. *Chem. Soc. Rev.* **2009**, *38*, 1284–1293.

[7] Mueller, U.; Schubert, M.; Teich, F.; Puetter, H.; Schierle-Arndt, K.; Pastré, J. Metal–Organic Frameworks—Prospective Industrial Applications. *J. Mater. Chem.* **2006**, *16*, 626–636.

[8] Li, J.-R.; Ma, Y.; McCarthy, M. C.; Sculleya, J.; Yub, J.; Jeong, H.-K.; Balbuena, P. B.; Zhou, H.-C. Carbon Dioxide Capture-Related Gas Adsorption and Separation in Metal-Organic Frameworks. *Coord. Chem. Rev.* **2011**, *255*, 1791–1823.

[9] Britt, D.; Furukawa, H.; Wang, B.; Glover, T. G.; Yaghi, O. M. Highly Efficient Separation of Carbon Dioxide by a Metal-Organic Framework Replete with Open Metal Sites. *Proc. Natl. Acad. Sci. U.S.A.* **2009**, *106*, 20637–20640.

[10] Bloch, E. D.; Queen, W. L.; Krishna, R.; Zadrozny, J. M.; Brown, C. M.; Long, J. R. Hydrocarbon Separations in a Metal–Organic Framework with Open Iron(II) Coordination Sites. *Science* **2012**, *335*, 1606–1610.

[11] Kishan, M. R.; Tian, J.; Thallapally, P. K.; Fernandez, C. A.; Dalgarno, S. J.; Warren, J. E.; McGraila, B. P.; Atwood, J. L. Flexible Metal–Organic Supramolecular Isomers for Gas Separation. *Chem. Commun.* **2010**, *46*, 538–540.

[12] Bloch, E. D.; Murray, L. J.; Queen, W. L.; Chavan, S.; Maximoff, S. N.; Bigi, J. P.; Krishna, R.; Peterson, V. K.; Grandjean, F.; Long, G. J.; Smit, B.; Bordiga, S.; Brown, C. M.; Long, J. R. Selective Binding of O_2 over N_2 in a Redox-Active Metal-Organic Framework with Open Iron(II) Coordination Sites. *J. Am. Chem. Soc.* **2011**, *133*, 14814–14822.

[13] Corma, A. From Microporous to Mesoporous Molecular Sieve Materials and Their Use in Catalysis. *Chem. Rev.* **1997**, *97*, 2373–2419.

[14] Taguchi, A.; Schüth, F. Ordered Mesoporous Materials in Catalysis. *Microporous Mesoporous Mater.* **2005**, *77*, 1–45.

[15] Shiju, N. R.; Guliants, V. V. Recent Developments in Catalysis Using Nanostructured Materials. *Appl. Catal., A*, **2009**, *356*, 1–17.

[16] Farrusseng, D.; Aguado, S.; Pinel, C. Metal–Organic Frameworks: Opportunities for Catalysis. *Angew. Chem. Int. Ed.* **2009**, *48*, 7502–7513.

[17] Ravon, U.; Domine, M. E.; Gaudillère, C.; Desmartin-Chomel, A.; Farrusseng, D. MOFs as Acid Catalysts with Shape Selectivity Properties. *New J. Chem.* **2008**, *32*, 937–940.

[18] Ramos-Fernandez, E. V.; Garcia-Domingos, M.; Juan-Alcaniz, J.; Gascon, J.; Kapteijn, F. MOFs as Catalysts: Activity, Reusability and Shape-Selectivity of a Pd-Containing MOF. *Appl. Catal., A* **2007**, *250*, 294–298.

[19] Dhakshinamoorthy, A.; Garcia, H. Catalysis by Metal Nanoparticles Embedded on Metal–Organic Frameworks. *Chem. Soc. Rev.* **2012**, *41*, 5262–5284.

[20] Dhakshinamoorthy, A.; Alvaro, M.; Garcia, H. Commercial Metal–Organic Frameworks as Heterogeneous Catalysts. *Chem. Commun.* **2012**, *48*, 11275–11288.

[21] Ma, L.; Abney, C.; Lin, W. Enantioselective Catalysis with Homochiral Metal–Organic Frameworks. *Chem. Soc. Rev.* **2009**, *38*, 1248–1256.

[22] Lee, J.; Farha, O. K.; Roberts, J.; Scheidt, K. A.; Nguyen, S. T.; Hupp, J. T. Metal–Organic Framework Materials as Catalysts. *Chem. Soc. Rev.* **2009**, *38*, 1450–1459.

[23] Ranocchiari, M.; van Bokhoven, J. A. Catalysis by Metal–Organic Frameworks: Fundamentals and Opportunities. *Phys. Chem. Chem. Phys.* **2011**, *13*, 6388–6396.

[24] Valvekens, P.; Vermoortele, F.; De Vos, D. Metal–Organic Frameworks as Catalysts: The Role of Metal Active Sites. *Catal. Sci. Technol.* **2013**, *3*, 1435–1445.

[25] Valvekens, P.; Vandichel, M.; Waroquier, M.; Van Speybroeck, V.; De Vos, D. Metal-Dioxidoterephthalate MOFs of the MOF-74 Type: Microporous Basic Catalysts with Well-Defined Active Sites. *J. Catal.* **2014**, *317*, 1–10.

[26] Xiao, D. J.; Bloch, E. D.; Mason, J. A.; Queen, W. L.; Hudson, M. R.; Planas, N.; Borycz, J.; Dzubak, A. L.; Verma, P.; Lee, K.; Bonino, F.; Crocell, V.; Yano, J.; Bordiga, S.; Truhlar, D. G.; Gagliardi, L.; Brown, C. M.; Long, J. R. Oxidation of Ethane to Ethanol by N_2O in a Metal-Organic Framework with Coordinatively-Unsaturated Iron(II) Sites. *Nat. Chem.* **2014**, *6*, 590–595.

[27] Maurice, R.; Verma, P.; Zadrozny, J. M.; Luo, S.; Borycz, J.; Long, J. R.; Truhlar, D. G.; Gagliardi, L. Single-Ion Magnetic Anisotropy and Isotropic Magnetic Couplings in the Metal–Organic Framework Fe_2(dobdc). *Inorg. Chem.* **2013**, *52*, 9379–9789.

[28] Verma, P.; Maurice, R.; Truhlar, D. G. Adsorbate-Induced Changes in Magnetic Interactions in Fe2(dobdc) with Adsorbed Hydrocarbon Molecules. *J. Phys. Chem. C* **2016**, *120*, 9933–9948.

[29] Borycz, J.; Paier, J.; Verma, P.; Darago, L. E.; Xiao, D. J.; Truhlar, D. G.; Long, J. R.; Gagliardi, L. Structural and Electronic Effects on the Properties of Fe_2(dobdc) upon Oxidation with N_2O. *Inorg. Chem.* **2016**, *55*, 4924–4934.

[30] Verma, P.; Maurice, R.; Truhlar, D. G. Identifying the Interactions That Allow Separation of O_2 from N_2 on the Open Iron Sites of Fe_2(dobdc). *J. Phys. Chem. C* **2015**, *119*, 28499–28511.

[31] Verma, P.; Xu, X.; Truhlar, D. G. Adsorption on Fe-MOF-74 for C1-C3 Hydrocarbon Separation. *J. Phys. Chem. C* **2013**, *117*, 12648–12660.

[32] Kohn, W.; Sham, L. J. Self-Consistent Equations Including Exchange and Correlation Effects. *Phys. Rev.* **1965**, *140*, A1133–A1138.

[33] Cramer, C. J.; Truhlar, D. G. Density Functional Theory for Transition Metals and Transition Metal Chemistry. *Phys. Chem. Chem. Phys.* **2009**, *11*, 10757–10816.

[34] Schrödinger, E. An Undulatory Theory of the Mechanics of Atoms and Molecules. *Phys. Rev.* **1926**, *28*, 1049–1070.

[35] Kohn, W.; Becke, A. D.; Parr, R. G. Density Functional Theory of Electronic Structure. *J. Phys. Chem.* **1996**, *100*, 12974–12980.

[36] Zhao, Y.; Truhlar, D. G. Density Functionals with Broad Applicability in Chemistry. *Acc. Chem. Res.* **2008**, *41*, 157–167.

[37] Bureekaew, S.; Amirjalayer, S.; Tafipolsky, M.; Spickermann, C.; Roy, T. K.; Schmid, R. MOF-FF – A Flexible First-Principles Derived Force Field for Metal-Organic Frameworks. *Phys. Status Solidi B* **2013**, *250*, 1128–1141.

[38] Leclerc, H.; Vimont, A.; Lavelley, J.-C.; Daturi, M.; Wiersum, A. D.; Llellyn, P. L.; Hocajada, P.; Férey, G.; Serre, C. Infrared Study of the Influence of Reducible Iron(III) Metal Sites on the Adsorption of CO, CO_2, Propane, Propene and Propane in the Mesoporous Metal–Organic Framework MIL-100. *Phys. Chem. Chem. Phys.* **2011**, *13*, 11748–11756.

[39] Bae, Y.-S.; Lee, C. Y.; Kim, K. C.; Farha, O. K.; Nickias, P.; Hupp, J. T.; Nguyen, S. T.; Snurr, R. Q. High Propene/Propane Selectivity in Isostructural Metal–Organic Frameworks with High Densities of Open Metal Sites. *Angew. Chem. Int. Ed.* **2012**, *51*, 1857–1860.

[40] Sumida, K.; Rogow, D. L.; Mason, J. A.; McDonald, T. M., Bloch, E. D.; Herm, Z. R.; Bae, T. H.; Long, J. R. Carbon Dioxide Capture in Metal–Organic Frameworks. *Chem. Rev.* **2012**, *112*, 724–781.

[41] Wu, H.; Gong, Q.; Olson, D. H.; Li, J. Commensurate Adsorption of Hydrocarbons and Alcohols in Microporous Metal Organic Frameworks. *Chem. Rev.* **2012**, *112*, 836–868.

[42] Lee, K.; Isley III, W. C.; Dzubak, A. L.; Verma, P.; Stoneburner, S. J.; Lin, L.-C.; Howe, J. D.; Bloch, E. D.; Reed, D. A.; Hudson, M. R.; Brown, C. M.; Long, J. R.; Neaton, J. B.; Smit, B.; Cramer, C. J.; Truhlar, D. G.; Gagliardi, L. Design of a

Metal-Organic Framework with Enhanced Back Bonding for the Separation of N_2 and CH_4. *J. Am. Chem. Soc.* **2014**, *124*, 698–704. In the second last row of Table 1, DFT should be WFT.

[43] Li, B.; Wang, H.; Chen, B. Microporous Metal–Organic Frameworks for Gas Separation. *Chem. Asian J.* **2014**, *9*, 1474–1498.

[44] Lee, K.; Howe, J. D.; Lin, L.-C.; Smit, B.; Neaton, J. B. Small-Molecule Adsorption in Open-Site Metal–Organic Frameworks: A Systematic Density Functional Theory Study for Rational Design. *Chem. Mater.* **2015**, *27*, 668–678.

[45] Lee, J. S.; Vlaisavljevich, B.; Britt, D. K.; Brown, C. M.; Haranczyk, M.; Neaton, J. B.; Smit, B.; Long, J. R.; Queen, W. L. Understanding Small-Molecule Interactions in Metal–Organic Frameworks: Coupling Experiment with Theory. *Adv. Mater.* **2015**, *27*, 5785–5796.

[46] Queen, W. L.; Bloch, E. B.; Brown, C. M.; Hudson, M. R.; Mason, J. A.; Murray, L. J.; Ramirez-Cuesta, A. J.; Peterson, V. K.; Long, J. R. Hydrogen Adsorption in the Metal–Organic Frameworks Fe_2(dobdc) and $Fe_2(O_2)$(dobdc). *Dalton Trans.* **2012**, *41*, 4180–4187.

[47] Zhou, W.; Wu, H.; Yildirim, T. Enhanced H_2 Adsorption in Isostructural Metal–Organic Frameworks with Open Metal Sites: Strong Dependence of the Binding Strength on Metal Ions. *J. Am. Chem. Soc.* **2008**, *130*, 15268–15269.

[48] Wu, H.; Zhou, W.; Yildirim, T. High-Capacity Methane Storage in Metal–Organic Frameworks M_2(dhtp): The Important Role of Open Metal Sites. *J. Am. Chem. Soc.* **2009**, *131*, 4995–5000.

[49] Mason, J. A.; Sumida, K., Herm, Z. R.; Krishna, R.; Long, J. R. Evaluating Metal–Organic Frameworks for Post-Combustion Carbon Dioxide Capture via Temperature Swing Adsorption. *Energy Environ. Sci.* **2011**, *4*, 3030–3040.

[50] Lin, L.-C.; Kim, J.; Kong, X.; Scott, E.; McDonald, T. M.; Long, J. R.; Reimer, J. A.; Smit, B. Understanding CO_2 Dynamics in Metal–Organic Frameworks with Open Metal Sites. *Angew. Chem. Int. Ed.* **2013**, *52*, 4410–4413.

[51] Dietzel, P. D. C.; Besikiotis, V.; Blom, R. Application of Metal–Organic Frameworks with Coordinatively Unsaturated Metal Sites in Storage and Separation of Methane and Carbon Dioxide. *J. Mater. Chem.* **2009**, *19*, 7362–7370.

[52] Wu, X.; Bao, Z.; Yuan, B. Wang, J.; Sun, Y.; Luo, H.; Deng, S. Microwave Synthesis and Characterization of MOF-74 (M = Ni, Mg) for Gas Separation. *Microporous Mesoporous Mater.* **2013**, *180*, 114–122.

[53] Bao, Z.; Alnemrat, S.; Yu, L.; Vasiliev, I.; Ren, Q.; Lu, X.; Deng, S. Adsorption of Ethane, Ethylene, Propane, and Propylene on a Magnesium-Based Metal–Organic Framework. *Langmuir* **2011**, *27*, 13554–13562.

[54] He, Y.; Krishna, R.; Chen, B. Metal-Organic Frameworks with Potential for Energy-Efficient Adsorptive Separation of Light Hydrocarbons. *Energy Environ. Sci.* **2012**, *5*, 9107–9120.

[55] He, Y.; Zhou, W.; Krishna, R.; Chen, B. Microporous Metal–Organic Frameworks for Storage and Separation of Small Hydrocarbons. *Chem. Commun.* **2012**, *48*, 11813–11831.

[56] Herm, Z. R.; Bloch, E. D.; Long, J. R. Hydrocarbon Separation in Metal–Organic Frameworks. *Chem. Mater.* **2014**, *26*, 323–338.

[57] Murray, L. J.; Dinca, M.; Yano, J.; Chavan, S.; Bordiga, S.; Brown, C. M.; Long, J. R. Highly-Selective and Reversible O_2 Binding in Cr_3(1,3,5-benzenetricarboxylate)$_2$. *J. Am. Chem. Soc.* **2010**, *132*, 7856–7857.

[58] Parkes, M. V.; Gallis, D. F. S.; Greathouse, J. A.; Nenoff, T. M. Effect of Metal in $M_3(btc)_2$ and $M_2(dobdc)$ MOFs for O_2/N_2 Separations: A Combined Density Functional Theory and Experimental Study. *J. Phys. Chem. C* **2015**, *119*, 6556–6567.

[59] Maximoff, S. N.; Smit, B. Redox Chemistry and Metal–Insulator Transitions Intertwined in a Nano-porous Material. *Nat. Commun.* **2014**, *5*, 4032.

[60] (a) Perdew, J. P.; Burke, K.; Ernzerhof, M. Generalized Gradient Approximation Made Simple. *Phys. Rev. Lett.* **1996**, *77*, 3865–3868. (b) Perdew, J. P.; Burke, K.; Ernzerhof, M. Errata: Generalized Gradient Approximation Made Simple. *Phys. Rev. Lett.* **1997**, *78*, 1396–1396.

[61] Grimme, S. Semiempirical GGA-Type Density Functional Constructed with a Long-Range Dispersion Correction. *J. Comput. Chem.* **2006**, *27*, 1787–1799.

[62] Valenzano, L.; Civalleri, B.; Chavan, S.; Palomino, G. T.; Arean, C. O.; Bordiga, S. Computational and Experimental Studies on the Adsorption of CO, N_2, and CO_2 on Mg-MOF-74. *J. Phys. Chem. C.* **2010**, *114*, 11185–11191.

[63] Dion, M.; Rydberg, H.; Schroder, E.; Langreth, D. C.; Lundqvist, B. I. Van der Waals Density Functional for General Geometries. *Phys. Rev. Lett.* **2004**, *92*, 246401.

[64] Lee, K.; Murray, E. D.; Kong, L.; Lundqvist, B. I.; Langreth, D. C. Higher-Accuracy van der Waals Density Functional. *Phys. Rev. B.* **2010**, *82*, 081101.

[65] Liechtenstein, A. I.; Anisimov, V. I.; Zaanen, J. Density-Functional Theory and Strong Interactions: Orbital Ordering in Mott-Hubbard Insulators. *Phys. Rev. B.* **1995**, *52*, R5467–R5470.

[66] Zhao, Y.; Truhlar, D. G. Applications and Validations of the Minnesota Density Functionals. *Chem. Phys. Lett.* **2011**, *502*, 1–13.

[67] Becke, A. D. A New Mixing of Hartree-Fock and Local Density-Functional Theories. *J. Chem. Phys.* **1993**, *98*, 1372–1377.

[68] Neese, F.; Hansen, A.; Liakos, D. G. Efficient and Accurate Approximations to the Local Coupled Cluster Singles Doubles Method Using a Truncated Pair Natural Orbital Basis. *J. Chem. Phys.* **2009**, *131*, 064103.

[69] Andersson, K.; Malmqvist, P. A.; Roos, B. O. Second-Order Perturbation Theory with a Complete Active Space Self-Consistent Field Reference Function. *J. Chem. Phys.* **1992**, *96*, 1218–1226.

[70] Fohlmeister, L.; Liu, S.; Schulten, C.; Moubaraki, B.; Stasch, A.; Cashion, J. D.; Murray, K. S.; Gagliardi, L.; Jones, C. Low-Coordinate Iron(I) and Manganese(I) Dimers: Kinetic Stabilization of an Exceptionally Short Fe-Fe Multiple Bond. *Angew. Chem. Int. Ed.* **2012**, *51*, 8294–8298.

[71] LiManni, G.; Dzubak, A. L.; Mulla, A.; Brogden, D. W.; Berry, J. F.; Gagliardi, L. Assessing Metal-Metal Multiple Bonds in Cr-Cr, Mo-Mo, and W-W Compounds and a Hypothetical U-U Compound: A Quantum Chemical Study Comparing DFT and Multireference Methods. *Chem. Eur. J.* **2012**, *18*, 1737–1749.

[72] Marenich, A. V.; Jerome, S. V.; Cramer, C. J.; Truhlar, D. G. Charge Model 5: An Extension of Hirshfeld Population Analysis for the Accurate Description of Molecular Interactions in Gaseous and Condensed Phases. *J. Chem. Theory Comput.* **2012**, *8*, 527–541.

[73] Marenich, A. V.; Cramer, C. J.; Truhlar, D. G. *CM5PAC*, University of Minnesota: Minneapolis, 2011.

[74] Hirshfeld, F. L. Bonded-Atom Fragments for Describing Molecular Charge Densities. *Theor. Chem. Acc.* **1977**, *44*, 129–138.

[75] Frisch, M. J.; Trucks, G. W.; Schlegel, H. B.; Scuseria, G. E.; Robb, M. A.; Cheeseman, J. R.; Scalmani, G.; Barone, V.; Mennucci, B.; Petersson, G. A.; Nakatsuji, H.; Caricato, M.; Li, X.; Hratchian, H. P.; Izmaylov, A. F.; Bloino, J.; Zheng, G.; Sonnenberg, J. L.; Hada, M.; Ehara, M.; Toyota, K.; Fukuda, R.; Hasegawa, J.; Ishida, M.; Nakajima, T.; Honda, Y.; Kitao, O.; Nakai, H.; Vreven, T.; J. A. Montgomery, J.; Peralta, J. E.; Ogliaro, F.; Bearpark, M.; Heyd, J. J.; Brothers, E.; Kudin, K. N.; Staroverov, V. N.; Kobayashi, R.; Normand, J.; Raghavachari, K.; Rendell, A.; Burant, J. C.; Iyengar, S. S.; Tomasi, J.; Cossi, M.; Rega, N.; Millam, J. M.; Klene, M.; Knox, J. E.; Cross, J. B.; Bakken, V.; Adamo, C.; Jaramillo, J.; Gomperts, R.; Stratmann, R. E.; Yazyev, O.; Austin, A. J.; Cammi, R.; Pomelli, C.; Ochterski, J. W.; Martin, R. L.; Morokuma, K.; Zakrzewski, V. G.; Voth, G. A.; Salvador, P.; Dannenberg, J. J.; Dapprich, S.; Daniels, A. D.; Ö. Farkas; Foresman, B.; Ortiz, J. V.; Cioslowski, J.; Fox, D. J. *Gaussian 09, Revision D.01*, Gaussian, Inc.: Wallingford CT, 2009.

[76] Kresse, G.; Furthmüller, J. Efficiency of Ab-Initio Total Energy Calculations for Metals and Semiconductors Using a Plane-Wave Basis Set. *Comput. Mater. Sci.* **1996**, *6*, 15–50.

[77] Kresse, G.; Furthmüller, J. Efficient Iterative Schemes for Abinitio Total-Energy Calculations Using a Plane-Wave Basis Set. *Phys. Rev. B: Condens. Matter Mater. Phys.* **1996**, *54*, 11169–11186.

[78] Neese, F. The ORCA Program System. *WIREs Comput. Mol. Sci.* **2012**, *2*, 73–78.

[79] Aquilante, F.; De Vico, L.; Ferré, N.; Ghigo, G.; Malmqvist, P.-å.; Neogrády, P.; Pedersen, T. B.; Pitoňák, M.; Reiher, M.; Roos, B. O.; Serrano-Andrés, L.; Urban,

M.; Veryazov, V.; Lindh, R. MOLCAS 7: The Next Generation. *J. Comput. Chem.* **2010**, *31*, 224–247.

[80] Grimme, S.; Antony, J.; Ehrlich, S.; Krieg, H. A Consistent and Accurate Ab Initio Parametrization of Density Functional Dispersion Correction (DFT-D) for the 94 Elements H-Pu. *J. Chem. Phys.* **2010**, *132*, 154104/1–19.

[81] Jeziorski, B.; Moszynski, R.; Szalewicz, K. Perturbation Theory Approach to Intermolecular Potential Energy Surfaces of van der Waals Complexes. *Chem. Rev.* **1994**, *94*, 1887–1930.

[82] Podeszwa, R.; Pernal, K.; Patkowski, K.; Szalewicz, K. Extension of the Hartree–Fock Plus Dispersion Method by First-Order Correlation Effects. *J. Phys. Chem. Lett.* **2010**, *1*, 550–555.

[83] The parameters of the D3 damped dispersion terms are available at http://www.thch.uni-bonn.de/tc/downloads/DFT-D3/functionals.html.

[84] Goerigk, L.; Grimme, S. A Thorough Benchmark of Density Functional Methods for General Main Group Thermochemistry, Kinetics, and Noncovalent Interactions. *Phys. Chem. Chem. Phys.* **2011**, *13*, 6670–6688.

[85] Boese, A. D.; Doltsinis, N. L.; Handy, N. C.; Sprik, M. New Generalized Gradient Approximation Functionals. *J. Chem. Phys.* **2000**, *112*, 1670–1678.

[86] Ruiz, E.; Salahub, D. R.; Vela, A. Defining the Domain of Density Functionals: Charge-Transfer Complexes. *J. Am. Chem. Soc.* **1995**, *117*, 1141–1142.

[87] Dietzel, P. D. C.; Morita, Y.; Blom, R.; Fjellvag, H. An In Situ High-Temperature Single-Crystal Investigation of a Dehydrated Metal-Organic Framework Compound and Field-Induced Magnetization of One-Dimensional Metal-Oxygen Chains. *Angew. Chem. Int. Ed.* **2005**, *44*, 6512–6516.

[88] Herzberg, G. *Spectra of Diatomic Molecules;* 2nd ed.; Van Nostrand: Princeton, 1950; pp. 62.

[89] Nam, W. Dioxygen Activation by Metalloenzymes and Models. *Acc. Chem. Res.* **2007**, *40*, 465–465.

[90] Hohenberger, J.; Ray, K.; Meyer, K. The Biology and Chemistry of High-Valent Iron–Oxo and Iron–Nitrido Complexes. *Nat. Commun.* **2012**, *3*, 720.

[91] Groves, J. T. High-Valent Iron in Chemical and Biological Oxidations. *J. Inorg. Biochem.* **2006**, *100*, 434–447.

[92] Ray, K.; Pfaff, F. F.; Wang, B.; Nam, W. Status of Reactive Non-Heme Metal–Oxygen Intermediates in Chemical and Enzymatic Reactions. *J. Am. Chem. Soc.* **2014**, *136*, 13942–13958.

[93] Collins, T. J.; Kostka, K. L.; Münck, E.; Uffelman, E. S. Stabilization of Mononuclear Five-Coordinate Iron(IV). *J. Am. Chem. Soc.* **1990**, *112*, 5637–5639.

[94] MacFaul, P. A.; Ingold, K. U.; Wayner, D. D. M.; Que, L., Jr. A Putative Monooxygenase Mimic which Functions via Well-Disguised Free Radical Chemistry. *J. Am. Chem. Soc.* **1997**, *119*, 10594–10598.

[95] Pestovsky, O.; Stoian, S.; Bominaar, E. L.; Shan, X.; Münck, E.; Que, L., Jr.; Bakac, A. Aqueous FeIV=O: Spectroscopic Identification and Oxo-Group Exchange. *Angew. Chem. Int. Ed.* **2005**, *44*, 6871–6874.

[96] Bukowski, M. R.; Koehntop, K. D.; Stubna, A.; Bominaar, E. L.; Halfen, J. A.; Münck, E.; Nam, W.; Que, L., Jr. A Thiolate-Ligated Nonheme Oxoiron(IV) Complex Relevant to Cytochrome P450. *Science* **2005**, *310*, 1000–1002.

[97] Oliveira, F. T. d.; Chanda, A.; Banerjee, D.; Shan, X.; Mondal, S.; Que, L., Jr.; Bominaar, E. L.; Münck, E.; Collins, T. J. Chemical and Spectroscopic Evidence for an FeV–Oxo Complex. *Science* **2007**, *315*, 835–838.

[98] Lacy, D. C.; Gupta, R.; Stone, K. L.; Greaves, J.; Ziller, J. W.; Hendrich, M. P.; Borovik, A. S. Formation, Structure, and EPR Detection of a High Spin Fe^{IV}—Oxo Species Derived from Either an Fe^{III}—Oxo or Fe^{III}—OH Complex. *J. Am. Chem. Soc.* **2010**, *132*, 12188–12190.

[99] Seo, M. S.; Kim, N. H.; Cho, K.-B.; So, J. E.; Park, S. K.; Clémancey, M.; Garcia-Serres, R.; Latour, J.-M.; Shaik, S.; Nam, W. A Mononuclear Nonheme Iron(IV)–Oxo Complex which is More Reactive than Cytochrome P450 Model Compound I. *Chem. Sci.* **2011**, *2*, 1039–1045.

[100] Que, L., Jr. The Road to Non-Heme Oxoferryls and Beyond. *Acc. Chem. Res.* **2007**, *40*, 493–500.

[101] Nam, W. High-Valent Iron(IV)–Oxo Complexes of Heme and Non-Heme Ligands in Oxygenation Reactions. *Acc. Chem. Res.* **2007**, *40*, 522–531.

[102] Rohde, J.-U.; In, J.-H.; Lim, M. H.; Brennessel, W. W.; Bukowski, M. R.; Stubna, A.; Münck, E.; Nam, W.; Que, L., Jr. Crystallographic and Spectroscopic Characterization of a Nonheme Fe(IV)=O Complex. *Science* **2003**, *299*, 1037–1039.

[103] Lim, M. H.; Rohde, J.-U.; Stubna, A.; Bukowski, M. R.; Costas, M.; Ho, R. Y. N.; Münck, E.; Nam, W.; Que, L., Jr. An FeIV=O Complex of a Tetradentate Tripodal Nonheme Ligand. *Proc. Natl. Acad. Sci. U.S.A.* **2003**, *100*, 3665–3670.

[104] Price, J. C.; Barr, E. W.; Glass, T. E.; Krebs, C.; Bollinger, J. M., Jr. Evidence for Hydrogen Abstraction from C1 of Taurine by the High-Spin Fe(IV) Intermediate Detected During Oxygen Activation by Taurine:α-Ketoglutarate Dioxygenase (TauD). *J. Am. Chem. Soc.* **2003**, *125*, 13008–13009.

[105] Sinnecker, S.; Svensen, N.; Barr, E. W.; Ye, S.; Bollinger, J. M., Jr.; Neese, F.; Krebs, C. Spectroscopic and Computational Evaluation of the Structure of the High-Spin Fe(IV)–Oxo Intermediates in Taurine: α-Ketoglutarate Dioxygenase from *Escherichia coli* and Its His99Ala Ligand Variant. *J. Am. Chem. Soc.* **2007**, *129*, 6168–6179.

[106] Decker, A.; Rohde, J.-U.; Klinker, E. J.; Wong, S. D.; Que, L., Jr.; Solomon, E. I. Spectroscopic and Quantum Chemical Studies on Low-Spin FeIVO Complexes: Fe–O Bonding and Its Contributions to Reactivity. *J. Am. Chem. Soc.* **2007**, *129*, 15983–15996.

[107] Solomon, E. I.; Wong, S. D.; Liu, L. V.; Decker, A.; Chow, M. S. Peroxo and Oxo Intermediates in Mononuclear Nonheme Iron Enzymes and Related Active Sites. *Curr. Opin. Chem. Biol.* **2009**, *13*, 99–113.

[108] Hirao, H.; Kumar, D.; Que, L., Jr.; Shaik, S. Two-State Reactivity in Alkane Hydroxylation by Non-Heme Iron–Oxo Complexes. *J. Am. Chem. Soc.* **2006**, *128*, 8590–8606.

[109] Ye, S.; Neese, F. Nonheme Oxo–iron(IV) Intermediates form an Oxyl Radical upon Approaching the C–H Bond Activation Transition State. *Proc. Natl. Acad. Sci. U.S.A.* **2011**, *108*, 1228–1233.

[110] Grapperhaus, C. A.; Mienert, B.; Bill, E.; Weyhermüller, T.; Wieghardt, K. Mononuclear (Nitrido)iron(V) and (Oxo)iron(IV) Complexes via Photolysis of [(cyclam-acetato)$Fe^{III}(N_3)$]$^+$ and Ozonolysis of [(cyclam-acetato)$Fe^{III}(O_3SCF_3)$]$^+$ in Water/Acetone Mixtures. *Inorg. Chem.* **2000**, *39*, 5306–5317.

[111] Yoon, J.; Wilson, S. A.; Jang, Y. K.; Seo, M. S.; Nehru, K.; Hedman, B.; Hodgson, K. O.; Bill, E.; Solomon, E. I.; Nam, W. Reactive Intermediates in Oxygenation Reactions with Mononuclear Nonheme Iron Catalysts. *Angew. Chem. Int. Ed.* **2009**, *48*, 1257–1260.

[112] Fang, D.; Lord, R. L.; Cisneros, G. A. Ab Initio QM/MM Calculations Show an Intersystem Crossing in the Hydrogen Abstraction Step in Dealkylation Catalyzed by AlkB. *J. Phys. Chem. B* **2013**, *117*, 6410–6420.

[113] Pestovsky, O.; Bakac, A. Reactivity of Aqueous Fe(IV) in Hydride and Hydrogen Atom Transfer Reactions. *J. Am. Chem. Soc.* **2004**, *126*, 13757–13764.

[114] Bernasconi, L.; Louwerse, M. J.; Baerends, E. J. The Role of Equatorial and Axial Ligands in Promoting the Activity of Non-Heme Oxidoiron(IV) Catalysts in Alkane Hydroxylation. *Eur. J. Inorg. Chem.* **2007**, *2007*, 3023–3033.

[115] England, J.; Martinho, M.; Farquhar, E. R.; Frisch, J. R.; Bominaar, E. L.; Münck, E.; Que, L., Jr. A Synthetic High-Spin Oxoiron(IV) Complex: Generation, Spectroscopic Characterization, and Reactivity. *Angew. Chem. Int. Ed.* **2010**, *48*, 3622–3626.

[116] Cho, K.-B.; Shaik, S.; Nam, W. Theoretical Predictions of a Highly Reactive Non-Heme Fe(IV)=O Complex with a High-Spin Ground State. *Chem. Commun.* **2010**, *46*, 4511–4513.

[117] England, J.; Guo, Y.; Van Heuvelen, K. M.; Cranswick, M. A.; Rohde, G. T.; Bominaar, E. L.; Münck, E.; Que, L., Jr. A More Reactive Trigonal-Bipyramidal High-Spin Oxoiron(IV) Complex with a cis-Labile Site *J. Am. Chem. Soc.* **2011**, *133*, 11880–11883.

[118] Dhuri, S. N.; Seo, M. S.; Lee, Y.-M.; Hirao, H.; Wang, Y.; Nam, W.; Shaik, S. Experiment and Theory Reveal the Fundamental Difference Between Two-State and Single-State Reactivity Patterns in Nonheme FeIV=O versus RuIV=O Oxidants. *Angew. Chem. Int. Ed.* **2008**, *47*, 3356–3359.

[119] Hirao, H.; Que, L., Jr.; Nam, W.; Shaik, S. A Two-State Reactivity Rationale for Counterintuitive Axial Ligand Effects on the C–H Activation Reactivity of Nonheme FeIV=O Oxidants. *Chem. Eur. J.* **2008**, *14*, 1740–1756.

[120] Schröder, D.; Shaik, S.; Schwarz, H. Two-State Reactivity as a New Concept in Organometallic Chemistry. *Acc. Chem. Res.* **2000**, *33*, 139–145.

[121] Shaik, S. An Anatomy of the Two-State Reactivity Concept: Personal Reminiscences in Memoriam of Detlef Schröder. *Int. J. Mass spectrom.* **2013**, 354–355, 5–14.

[122] Krebs, C.; Fujimori, D. G.; Walsh, C. T.; Bollinger, J. M. Non-Heme Fe(IV)–Oxo Intermediates. *Acc. Chem. Res.* **2007**, *40*, 484–492.

[123] Price, J. C.; Barr, E. W.; Tirupati, B.; Bollinger, J. M., Jr.; Krebs, C. The First Direct Characterization of a High-Valent Iron Intermediate in the Reaction of an α-Ketoglutarate-Dependent Dioxygenase: A High-Spin Fe(IV) Complex in Taurine/α-Ketoglutarate Dioxygenase (TauD) from *Escherichia coli*. *Biochemistry* **2003**, *42*, 7497–7508.

[124] Hoffart, L. M.; Barr, E. W.; Guyer, R. B.; Bollinger, J. M., Jr.; Krebs, C. Direct Spectroscopic Detection of a C–H-cleaving High-Spin Fe(IV) Complex in a Prolyl-4-hydroxylase. *Proc. Natl. Acad. Sci. U. S. A.* **2006**, *103*, 14738–14743.

[125] Galonić, D. P.; Barr, E. W.; Walsh, C. T.; Bollinger, J. M., Jr; Krebs, C. Two Interconverting Fe(IV) Intermediates in Aliphatic Chlorination by the Halogenase CytC3. *Nat. Chem. Biol.* **2007**, *3*, 113–116.

[126] Eser, B. E.; Barr, E. W.; Frantom, P. A.; Saleh, L.; Bollinger, J. M., Jr.; Krebs, C.; Fitzpatrick, P. F. Direct Spectroscopic Evidence for a High-Spin Fe(IV) Intermediate in Tyrosine Hydroxylase. *J. Am. Chem. Soc.* **2007**, *129*, 11334–11335.

[127] Cho, K.-B.; Wu, X.; Lee, Y.-M.; Kwon, Y.-M.; Shaik, S.; Nam, W. Evidence for an Alternative to the Oxygen Rebound Mechanism in C–H Bond Activation by Non-Heme $Fe^{IV}O$ Complexes. *J. Am. Chem. Soc.* **2012**, *134*, 20222–20225.

[128] Buist, P. H. Fatty Acid Desaturases: Selecting the Dehydrogenation Channel. *Nat. Prod. Rep.* **2004**, *21*, 249–262.

[129] Kumar, D.; de Visser, S. P.; Shaik, S. Oxygen Economy of Cytochrome P450: What is the Origin of the Mixed Functionality as a Dehydrogenase-Oxidase Enzyme Compared with Its Normal Function? *J. Am. Chem. Soc.* **2004**, *126*, 5072–5073.

[130] Bigi, M. A.; Reed, S. A.; White, M. C. Diverting Non-Haem Iron Catalysed Aliphatic C–H Hydroxylations Towards Desaturations. *Nat. Chem.* **2011**, *3*, 216–222.

[131] Hall, M. B.; Margl, P.; Náray-Szabo, G; Schramm, V. I.; Truhlar, D. G.; van Santen, R. A.; Warshel, A.; Whitten, J. L. *ACS Symp. Ser.* **1999**, *721*, 2–17.

[132] Lonsdale, R.; Ranaghan, K. E.; Mulholland, A. J. Computational Enzymology. *Chem. Comm.* **2010**, *46*, 2354–2372.

[133] Cheong P. H.; Legault, C. Y.; Um, J. M.; Çelebi-Ölçüm, N.; Houk, K. N. Quantum Mechanical Investigations of Organocatalysis: Mechanisms, Reactivities, and Selectivities. *Chem. Rev.* **2011**, *111*, 5042–5137.

[134] Bell. A. T., Head-Gordon M. Quantum Mechanical Modeling of Catalytic Processes. *Annu. Rev. Chem. Biomol. Eng.* **2011**, *2*, 453–477.

[135] Usharani, D.; Janardanan, D.; Li, C.; Shaik, S. A Theory for Bioinorganic Chemical Reactivity of Oxometal Complexes and Analogous Oxidants: The Exchange and Orbital-Selection Rules. *Acc. Chem. Res.* **2013**, *46*, 471–482.

[136] Shaik, S.; Chen, H.; Janardanan, D. Exchange-Enhanced Reactivity in Bond Activation by Metal–Oxo Enzymes and Synthetic Reagents. *Nat. Chem.* **2011**, *3*, 19–27.

[137] Janardanan, D.; Wang, Y.; Schyman, P.; Que, L. Jr.; Shaik, S. The Fundamental Role of Exchange-Enhanced Reactivity in C–H Activation by $S = 2$ Oxo Iron(IV) Complexes. *Angew. Chem. Int. Ed.* **2010**, *49*, 3342–3345.

[138] Carter, E. A.; Goddard, W. A. III. Relationships Between Bond Energies in Coordinatively Unsaturated and Coordinatively Saturated Transition-Metal Complexes: A Quantitative Guide for Single, Double, and Triple Bonds. *J. Phys. Chem.* **1988**, *92*, 5679–5683.

[139] Queen, W. L.; Brown, C. M.; Britt, D. K.; Zajdel, P.; Hudson, M. R.; Yaghi, O. M. Site-Specific CO_2 Adsorption and Zero Thermal Expansion in an Anisotropic Pore Network. *J. Phys. Chem. C* **2011**, *115*, 24915–24919.

[140] Zhao, Y.; Truhlar, D. G. The M06 Suite of Density Functionals for Main Group Thermochemistry, Thermochemical Kinetics, Noncovalent Interactions, Excited States, and Transition Elements: Two New Functionals and Systematic Testing of Four M06-Class Functionals and 12 Other Functionals. *Theor. Chem. Acc.* **2008**, *120*, 215–241.

[141] (a) Weigend, F.; Ahlrichs, R. Balanced Basis Sets of Split Valence, Triple Zeta Valence and Quadruple Zeta Valence Quality for H to Rn: Design and Assessment of Accuracy. *Phys. Chem. Chem. Phys.* **2005**, *7*, 3297–3305. (b) Weigend, F. Accurate Coulomb-Fitting Basis Sets for H to Rn. *Phys. Chem. Chem. Phys.* **2006**, *8*, 1057–1065.

[142] Alecu, I. M.; Zheng, J.; Zhao, Y.; Truhlar, D. G. Computational Thermochemistry: Scale Factor Databases and Scale Factors for Vibrational Frequencies Obtained from Electronic Model Chemistries. *J. Chem. Theory Comput.* **2010**, *6*, 2872–2887. See http://comp.chem.umn.edu/freqscale/version3b2.htm

[143] (a) Yamamoto, A. *Organotransition Metal Chemistry*; Wiley: New York, 1986. (b) Crabtree, R. H. *The Organometallic Chemistry of Transition Metals*; Wiley: New York, 1994.

[144] Shu, L.; Nesheim, J. C.; Kauffmann, K.; Münck, E.; Lipscomb, J. D.; Que, L., Jr. An $Fe_2^{IV}O_2$ Diamond Core Structure for the Key Intermediate Q of Methane Monooxygenase. *Science* **1997**, *275*, 515–518.

[145] Andersson, K.; Malmqvist, P.-Å.; Roos, B. O.; Sadlej, A. J.; Wolinski, K. Second Order Perturbation Theory with a CASSCF Reference Function. *J. Phys. Chem.* **1990**, *94*, 5483–5488.

[146] Poulos, T. L. Heme Enzyme Structure and Function. *Chem. Rev.* **2014**, *114*, 3919–3962.

[147] Usharani, D.; Janardanan, D.; Shaik, S. Does the TauD Enzyme Always Hydroxylate Alkanes, While an Analogous Synthetic Non-Heme Reagent Always Desaturates Them? *J. Am. Chem. Soc.* **2011**, *133*, 176–179.

[148] Ye, S.; Geng, C.-Y.; Shaik, S.; Neese, F. Electronic Structure Analysis of Multistate Reactivity in Transition Metal Catalyzed Reactions: The Case of C–H Bond Activation by Non-Heme Iron(IV)–Oxo Cores. *Phys. Chem. Chem. Phys.* **2013**, *15*, 8017–8030.

[149] Blanksby, S. J.; Ellison, G. B. Bond Dissociation Energies of Organic Molecules. *Acc. Chem. Res.* **2003**, *36*, 255–263.

[150] Hammond, G. S. A Correlation of Reaction Rates. *J. Am. Chem. Soc.* **1955**, *77*, 334–338.

[151] Truhlar, D. G.; Kuppermann, A. Exact Tunneling Calculations. *J. Am. Chem. Soc.* **1971**, *93*, 1840–1851.

[152] Fukui, K. The Path of Chemical-Reactions - The IRC Approach. *Acc. Chem. Res.*, **1981**, *14*, 363–368.

[153] Hratchian, H. P.; Schlegel, H. B. Accurate Reaction Paths Using a Hessian Based Predictor-Corrector Integrator. *J. Chem. Phys.* **2004**, *120*, 9918–9924.

[154] Hratchian, H. P.; Schlegel, H. B. *Theory and Applications of Computational Chemistry: The First 40 Years*, Ed. Dykstra, C. E.; Frenking, G.; Kim, K. S.; Scuseria, G. (Elsevier, Amsterdam, 2005) 195–249.

[155] Hratchian, H. P.; Schlegel, H. B. Using Hessian Updating to Increase the Efficiency of a Hessian Based Predictor-Corrector Reaction Path Following Method. *J. Chem. Theory and Comput.* **2005**, *1*, 61–69.

[156] Kurmoo, M. Magnetic Metal–Organic Frameworks. *Chem. Soc. Rev.* **2009**, *38*, 1353–1379.

[157] Canepa, P.; Chabal, Y. J.; Thonhauser, T. When Metal Organic Framework Turn into Linear Magnets. *Phys. Rev. B* **2013**, *87*, 094407.

[158] Park, J.; Kim, H.; Jung, Y. Origin of Selective Guest-Induced Magnetism Transition in Fe/MOF-74. *J. Phys. Chem. Lett.* **2013**, *4*, 2530–2534.

[159] Kim, H.; Park, J.; Jung, Y. The Binding Nature of Light Hydrocarbons on Fe/MOF-74 for Gas Separation. *Phys. Chem. Chem. Phys.* **2013**, *17*, 19644–19650.

[160] Zhang, Q.; Li, B.; Chen, L. First-Principles Study of Microporous Magnets M-MOF-74 (M = Ni, Co, Fe, Mn): The Role of Metal Centers. *Inorg. Chem.* **2013**, *52*, 9356–9362.

[161] Han, S.; Kim, H.; Kim, J.; Jung, Y. Modulating the Magnetic Behavior of Fe(II)–MOF-74 by the High Electron Affinity of the Guest Molecule. *Phys. Chem. Chem. Phys.* **2015**, *17*, 16977–16982.

[162] Zhao, Y.; Truhlar, D. G. A New Local Functional for Main-Group Thermochemistry, Transition Metal Bonding, Thermodynamical Kinetics, and Non Covalent Interactions. *J. Chem. Phys.* **2006**, *125*, 194101.

[163] Yu, H. S.; Zhang, W.; Verma, P.; He, X.; Truhlar, D. G. Nonseparable Exchange–Correlation Functional for Molecules, Including Homogeneous Catalysis Involving Transition Metals. *Phys. Chem. Chem. Phys.* **2015**, *17*, 12146–12160.

[164] Peverati, R.; Truhlar, D. G. M11-L: A Local Density Functional That Provides Improved Accuracy for Electronic Structure Calculations in Chemistry and Physics. *J. Phys. Chem. Lett.* **2012**, *3*, 117–124.

[165] Peverati, R.; Truhlar, D. G. An Improved and Broadly Accurate Local Approximation to the Exchange–Correlation Density Functional: The MN12-L Functional for Electronic Structure Calculations in Chemistry and Physics. *Phys. Chem. Chem. Phys.* **2012**, *10*, 13171–13174.

[166] Adamo, C.; Barone, V. Exchange Functionals with Improved Long-Range Behavior and Adiabatic Connection Methods Without Adjustable Parameters: The mPW and mPW1PW Models. *J. Chem. Phys.* **1998**, *108*, 664–675.

[167] Peverati, R.; Truhlar, D. G. Exchange-Correlation Functional with Good Accuracy for Both Structural and Energetic Properties While Depending Only on the Density and its Gradient. *J. Chem. Theory Comput.* **2012**, *8*, 2310–2319.

[168] Hammer, B.; Hansen, L. B.; Nørskov, J. K. Improved Adsorption Energetics Within Density-Functional Theory Using Revised Perdew-Burke-Ernzerhof Functionals. *Phys. Rev. B* **1999**, *59*, 7413–7421.

[169] Zhao, Y.; Truhlar, D. G. Construction of a Generalized Gradient Approximation by Restoring the Density-Gradient Expansion and Enforcing a Tight Lieb–Oxford Bound. *J. Chem. Phys.* **2008**, *128*, 184109.

[170] Becke, A. D. Density-Functional Exchange-Energy Approximation with Correct Asymptotic Behavior. *Phys. Rev. A* **1988**, *38*, 3098–3100.

[171] Lee, C.; Yang, W.; Parr, R. G. Development of the Colle-Salvetti Correlation-Energy Formula into a Functional of the Electron Density. *Phys. Rev. B* **1988**, *37*, 785–789.

[172] Becke, A. D. Density-Functional Thermochemistry. III. The Role of Exact Exchange. *J. Chem. Phys.* **1993**, *98*, 5648–5652.

[173] Stephens, P. J.; Devlin, F. J.; Chabalowski, C. F.; Frisch, M. J. *Ab Initio* Calculation of Vibrational Absorption and Circular Dichroism Spectra Using Density Functional Force Fields. *J. Phys. Chem.* **1994**, *98*, 11623–11627.

[174] Handy, N.; Cohen, A. Left-Right Correlation Energy. *Mol. Phys.* **2001**, *99*, 403–412.

[175] Thompson, J. D.; Cramer, C. J.; Truhlar, D. G. Density-Functional Theory and Hybrid Density-Functional Theory Continuum Solvation Models for Aqueous and Organic Solvents: Universal SM5.43 and SM5.43R Solvation Models for Any Fraction of Hartree-Fock Exchange. *Theor. Chem. Acc.* **2005**, *113*, 107–131.

[176] Adamo, C.; Barone, V. Toward Reliable Density Functional Methods Without Adjustable Parameters: The PBE0 Model. *J. Chem. Phys.* **1999**, *110*, 6158–6169.

[177] Zhao, Y.; Schultz, N. E.; Truhlar, D. G. Exchange-Correlation Functional with Broad Accuracy for Metallic and Nonmetallic Compounds, Kinetics, and Noncovalent Interactions. *J. Chem. Phys.* **2005**, *123*, 161103.

[178] Zhao, Y.; Truhlar, D. G. Design of Density Functionals That Are Broadly Accurate for Thermochemistry, Thermochemical Kinetics, and Nonbonded Interactions. *J. Phys. Chem. A* **2005**, *109*, 5656–5667.

[179] Lynch, B. J.; Fast, P. L.; Harris, M.; Truhlar, D. G. Adiabatic Connection for Kinetics. *J. Phys. Chem. A* **2000**, *104*, 4811–4815.

[180] Zhao, Y.; Truhlar, D. G. Exploring the Limit of Accuracy of the Global Hybrid Meta Density Functional for Main-Group Thermochemistry, Kinetics, and Noncovalent Interactions. *J. Chem. Theory Comput.* **2008**, *4*, 1849–1868.

[181] Heyd, J.; Scuseria, G. E.; Ernzerhof, M. Hybrid Functionals Based on a Screened Coulomb Potential. *J. Chem. Phys.* **2003**, *118*, 8207–8215.

[182] Heyd, J.; Peralta, J. E.; Scuseria, G. E.; Martin, R. L. Energy Band Gaps and Lattice Parameters Evaluated with the Heyd-Scuseria-Ernzerhof Screened Hybrid Functional. *J. Chem. Phys.* **2005**, *123*, 174101.

[183] Krukau, A. V.; Vydrov, O. A.; Izmaylov, A. F.; Scuseria, G. E. Influence of the Exchange Screening Parameter on the Performance of Screened Hybrid Functionals. *J. Chem. Phys.* **2006**, *125*, 224106.

[184] Henderson, T. M.; Izmaylov, A. F.; Scalmani, G.; Scuseria, G. E. Can Short-Range Hybrids Describe Long-Range-Dependent Properties? *J. Chem. Phys.* **2009**, *131*, 044108.

[185] Peverati, R.; Truhlar, D. G. Screened-Exchange Density Functionals with Broad Accuracy for Chemistry and Solid State Physics. *Phys. Chem. Chem. Phys.* **2012**, *14*, 16187.

[186] Peverati, R.; Truhlar, D. G. Improving the Accuracy of Hybrid Meta-GGA Density Functionals by Range Separation. *J. Phys. Chem. Lett.* **2011**, *2*, 2810–2817.

[187] Grimme, S. Semiempirical Hybrid Density Functional with Perturbative Second-Order Correlation. *J. Chem. Phys.* **2006**, *124*, 034108.

[188] Frisch, M. J.; Trucks, G. W.; Schlegel, H. B.; Scuseria, G. E.; Robb, M. A.; Cheeseman, J. R.; Scalmani, G.; Barone, V.; Mennucci, B.; Petersson, G. A.; Nakatsuji, H.; Caricato, M.; Li, X.; Hratchian, H. P.; Izmaylov, A. F.; Bloino, J.; Zheng, G.; Sonnenberg, J. L.; Hada, M.; Ehara, M.; Toyota, K.; Fukuda, R.; Hasegawa, J.; Ishida, M.; Nakajima, T.; Honda, Y.; Kitao, O.; Nakai, H.; Vreven, T.; Montgomery, J. A.; Jr.; Peralta, J. E.; Ogliaro, F.; Bearpark, M.; Heyd, J. J.; Brothers, E.; Kudin, K. N.; Staroverov, V. N.; Keith, T.; Kobayashi, R.; Normand, J.; Raghavachari, K.; Rendell, A.; Burant, J. C.; Iyengar, S. S.; Tomasi, J.; Cossi, M.; Rega, N.; Millam, J. M.; Klene, M.; Knox, J. E.; Cross, J. B.; Bakken, V.; Adamo, C.; Jaramillo, J.; Gomperts, R.; Stratmann, R. E.; Yazyev, O.; Austin, A. J.; Cammi, R.; Pomelli, C.; Ochterski, J. W.; Martin, R. L.; Morokuma, K.; Zakrzewski, V. G.; Voth, G. A.; Salvador, P.; Dannenberg, J. J.; Dapprich, S.; Daniels, A. D.; Farkas, O.; Foresman, J. B.; Ortiz, J. V.; Cioslowski, J.; Fox, D. J.; *Gaussian 09*, Revision C.01, Gaussian, Inc.: Wallingford CT, 2010.

[189] Zhao, Y.; Peverati, R.; Yang, K. R.; Truhlar, D. G. Minnesota Density Functional Module version 6.2 (*MN-GFM 6.2*), University of Minnesota, Minneapolis, 2012. See http://comp.chem. umn.edu/mn-gfm/ for details.

[190] Duanmu, K.; Luo, S.; Truhlar, D. G. MN-VFM-version 3.0. (http://comp.chem.umn.edu/mn-vfm/)

[191] Dudarev, S. L.; Botton, G. A.; Savroasov, S. Y.; Humphreys, C. J.; Sutton, A. P. Electron-Energy-Loss Spectra and the Structural Stability of Nickel Oxide: An LSDA+U Study. *Phys. Rev. B* **1998**, *57*, 1505–1509.

[192] Blöchl, P. E. Projector Augmented-Wave Method. *Phys. Rev. B: Condens. Matter Mater. Phys.* **1994**, *50*, 17953–17978.

[193] Kresse, G.; Joubert, D. From Ultrasoft Pseudopotentials to the Projector Augmented Wave Method. *Phys. Rev. B: Condens. Matter Mater. Phys.* **1999**, *59*, 1758–1775.

[194] Heisenberg, W. Zur Theorie des Ferromagnetismus. *Z. Phys.* **1928**, *49*, 619–636.

[195] Dirac, P. A. M. Quantum Mechanics of Many-Electron Systems. *Proc. Roy. Soc. Lond. A* **1929**, *123*, 714–733.

[196] van Vleck, J. H. The Coupling of Angular Momentum Vectors in Molecules. *Rev. Mod. Phys.* **1951**, *23*, 213–227.

[197] Moreira, I. P. R.; Illas, F. A Unified View of the Theoretical Description of Magnetic Coupling in Molecular Chemistry and Solid State Physics. *Phys. Chem. Chem. Phys.* **2006**, *8*, 1645–1659.

[198] Franchini, C.; Podloucky, R.; Paier, J.; Marsman, M.; Kresse, G. Ground-State Properties of Multivalent Manganese Oxides: Density Functional and Hybrid Density Functional Calculations. *Phys. Rev. B* **2007**, *75*, 195128.

[199] Sorkin, A.; Iron, M. A.; Truhlar, D. G. Density Functional Theory in Transition-Metal Chemistry: Relative Energies of Low-Lying States of Iron Compounds and the Effect of Spatial Symmetry Breaking. *J. Chem. Theor. Comput.* **2008**, *4*, 307–315.

[200] Mosey, N. J.; Liao, P.; Carter, E. A. Rotationally Invariant Ab Initio Evaluation of Coulomb and Exchange Parameters for DFT+U Calculations. *J. Chem. Phys.* **2008**, *129*, 014103.

[201] Chevrier, V. L.; Ong, S. P.; Armiento, R.; Chan, M. K. Y.; Ceder, G. Hybrid Density Functional Calculations of Redox Potentials and Formation Energies of Transition Metal Compounds. *Phys. Rev. B* **2010**, *82*, 075122.

[202] Martin, R. L.; Illas, F. Antiferromagnetic Exchange Interactions from Hybrid Density Functional Theory. *Phys. Rev. Lett.* **1997,** *79*, 1539–1542.

[203] Langreth, D. C.; Mehl, M. J. Beyond the Local-Density Approximation in Calculations of Ground-State Electronic Properties. *Phys. Rev. B,* **1983**, *28*, 1809–1834.

[204] Perdew, J. P.; Wang, Y. Accurate and Simple Density Functional for the Electronic Exchange Energy: Generalized Gradient. *Phys. Rev. B* **1986**, *33*, 8800–8802.

[205] Verma, P.; Truhlar, D. G. HLE16: A Local Kohn–Sham Gradient Approximation with Good Performance for Semiconductor Band Gaps and Molecular Excitation Energies. *J. Phys. Chem. Lett.* **2017**, *8*, 380–387.

[206] Verma, P.; Truhlar, D. G. HLE17: An Improved Local Exchange-Correlation Functional for Computing Semiconductor Band Gaps and Molecular Excitation Energies. *J. Phys. Chem. C* **2017**, *121*, 7144–7154.

[207] Peverati, R.; Truhlar, D. G. Quest for a Universal Density Functional: The Accuracy of Density Functionals Across a Broad Spectrum of Databases in Chemistry and Physics. *Phil. Trans. R. Soc. A* **2014**, *372*, 20120476.

[208] Tozer, D. J.; Handy, N. C. Development of New Exchange-Correlation Functionals. 2. *J. Phys. Chem. A* **1988**, *102*, 3162–3168.

[209] (a) Gáspár, R. Über eine Approximation des Hartree-Fockschen Potentials Durch eine Universelle Potentialfunktion. *Acta Phys. Hung.* **1954**, *3*, 263-286. (b) Gáspár, R. Statistical Exchange for Electron in Shell and the Xα Method. *Acta Phys. Hung.* **1974**, *35*, 213-218.

[210] Perdew, J. P.; Wang, Y. Accurate and Simple Analytic Representation of the Electron-Gas Correlation Energy. *Phys. Rev. B* **1992**, *45*, 13244–13249.

[211] Stoll, H.; Pavlidou, C. M. E.; Preuß, H. On the Calculation of Correlation Energies in the Spin-Density Functional Formalism. *Theor. Chim. Acta* **1978**, *149*, 143–149.

[212] Stoll, H.; Golka, E.; Preuß, H. Correlation Energies in the Spin-Density Functional Formalism. *Theor. Chim. Acta* **1980**, *55*, 29–41.

[213] Zhao, Y.; Peverati, R.; Yang, K. R.; Luo, S.; Truhlar, D. G., *MN-GFM, version 6.4: Minnesota Gaussian Functional Module*; University of Minnesota: Minneapolis, MN, 2012.

[214] Kudin, K. N.; Scuseria, G. E. Linear-Scaling Density-Functional Theory with Gaussian Orbitals and Periodic Boundary Conditions: Efficient Evaluation of Energy and Forces via the Fast Multipole Method. *Phys. Rev. B* **2000**, *61*, 16440–16453.

[215] Weymuth, T.; Couzijn, E. P. A.; Chen, P.; Reiher, M. New Benchmark Set of Transition-Metal Coordination Reactions for the Assessment of Density Functionals. *J. Chem. Theory Comput.* **2014**, *10*, 3092–3103.

[216] Perdew, J. P. Density-Functional Approximation for the Correlation Energy of the Inhomogeneous Electron Gas. *Phys. Rev. B* **1986**, *33*, 8822–8824.

[217] Andrae, D.; Häussermann, U.; Dolg, M.; Stoll, H.; Preuß, H. Energy-Adjusted Ab Initio Pseudopotentials for the Second and Third Row Transition Elements. *Theor. Chim. Acta* **1990**, *77*, 123–141.

[218] Woon, D. E.; Dunning Jr., T. H. Gaussian Basis Sets for Use in Correlated Molecular Calculations. III. The Atoms Aluminum Through Argon. *J. Chem. Phys.* **1993**, *98*, 1358–1371.

[219] Dunning Jr., T. H. Gaussian Basis Sets for Use in Correlated Molecular Calculations. I. The Atoms Boron Through Neon and Hydrogen. *J. Chem. Phys.* **1989**, *90*, 1007–1023.

[220] Dunning, Jr., T. H.; Peterson, K. A.; Wilson, A. K. Gaussian Basis Sets for Use in Correlated Molecular Calculations. X. The Atoms Aluminum Through Argon Revisited. *J. Chem. Phys.* **2001**, *114*, 9244–9253.

[221] Schuchardt, K. L.; Didier, B. T.; Elsethagen, T.; Sun, L.; Gurumoorthi, V.; Chase, J.; Li, J.; Windus, T. L. Basis Set Exchange: A Community Database for Computational Sciences. *J. Chem. Inf. Model.* **2007**, *47*, 1045–1052.

[222] Papajak, E.; Leverentz, H. R.; Zheng, J.; Truhlar, D. G. Efficient Diffuse Basis Sets: cc-pVxZ+ and maug-cc-pVxZ. *J. Chem. Theory Comput.* **2009**, *5*, 1197–1202.

[223] Papajak, E.; Truhlar, D. G. Efficient Diffuse Basis Sets for Density Functional Theory. *J. Chem. Theory Comput.* **2010**, *6*, 597–601.

[224] van Mourik, T.; Dunning, Jr., T. H. Gaussian Basis Sets for Use in Correlated Molecular Calculations. VIII. Standard and Augmented Sextuple Zeta Correlation Consistent Basis Sets for Aluminum Through Argon. *Int. J. Quantum Chem.* **2000**, *76*, 205–221.

[225] Vosko, S. H.; Wilk, L.; Nusair, M. Accurate Spin-Dependent Electron Liquid Correlation Energies for Local Spin Density Calculations: A Critical Analysis. *Can. J. Phys.* **1980**, *58*, 1200–1211.

[226] Perdew, J. P.; Ruzsinsky, A.; Csonka, G. I.; Vydrov, O. A.; Scuseria, G. E.; Constantin, L. A.; Zhou, X.; Burke, K. Restoring the Density-Gradient Expansion for Exchange in Solids and Surfaces. *Phys. Rev Lett.* **2008**, *100*, 136406.

[227] Perdew, J. P. in *Electronic Structure of Solids '91*; P. Ziesche and H. Eschrig, Eds.; Akademie Verlag: Berlin, 1991; pp. 11–20.

[228] Zhang, Y.; Yang, W. Comment on "Generalized Gradient Approximation Made Simple. *Phys. Rev. Lett.* **1997**, *80*, 890–890.

[229] Boese, A. D.; Handy, N. C. A New Parametrization of Exchange–Correlation Generalized Gradient Approximation Functionals. *J. Chem. Phys.* **2001**, *114*, 5497–5503.

[230] Peverati, R.; Zhao, Y.; Truhlar, D. G. Generalized Gradient Approximation That Recovers the Second-Order Density-Gradient Expansion with Optimized Across-the-Board Performance. *J. Phys. Chem. Lett.* **2011**, *2*, 1991–1997.

[231] Thakkar, A. J.; McCarthy, S. P. Toward Improved Density Functionals for the Correlation Energy. *J. Chem. Phys.* **2009**, *131*, 134109–134120.

[232] Tao, J. M.; Perdew, J. P.; Staroverov, V. N.; Scuseria, G. E. Climbing the Density Functional Ladder: Nonempirical Meta–Generalized Gradient Approximation Designed for Molecules and Solids. *Phys. Rev. Lett.* **2003**, *91*, 146401–146404.

[233] Perdew, J. P.; Ruzsinszky, A.; Csonka, G. I.; Constantin, L. A.; Sun, J. Workhorse Semilocal Density Functional for Condensed Matter Physics and Quantum Chemistry. *Phys. Rev. Lett.* **2009**, *103*, 026403–026406.

[234] Zhang, W.; Truhlar, D. G.; Tang, M. Explanation of the Source of Very Large Errors in Many Exchange–Correlation Functionals for Vanadium Dimer. *J. Chem. Theory Comput.* **2014**, *10*, 2399–2409.

[235] Handy, N. C.; Pople, J. A.; Head-Gordon, M.; Raghavachari, K.; Trucks, G. W. Size-Consistent Brueckner Theory Limited to Double Substitutions. *Chem. Phys. Lett.* **1989**, *164*, 185–192.

[236] Averkiev, B. B; Zhao, Y.; Truhlar, D. G. Binding Energy of d^{10} Transition Metals to Alkenes by Wave Function Theory and Density Functional Theory. *J. Mol. Cata A: Chem.* **2010**, 80–88.

[237] Posada-Borbón, A.; Posada-Amarillas, A. Theoretical DFT Study of Homonuclear and Binary Transition-Metal Dimers. *Chem. Phys. Lett.* **2015**, *618*, 66–71.

[238] Beutel, V.; Krämer, H. G.; Bhale, G. L.; Kuhn, M.; Weyers, K.; Demtröder, W. High-Resolution Isotope Selective Laser Spectroscopy of Ag_2 Molecules. *J. Chem. Phys.* **1993**, *98*, 2699–2708.

[239] Li, R.; Peverati, R.; Isegawa, M.; Truhlar, D. G. Assessment and Validation of Density Functional Approximations for Iron Carbide and Iron Carbide Cation. *J. Phys. Chem. A* **2012**, *117*, 169–173.

[240] Mardirossian, N.; Head-Gordon, M. Characterizing and Understanding the Remarkably Slow Basis Set Convergence of Several Minnesota Density Functionals for Intermolecular Interaction Energies. *J. Chem. Theory Comput.* **2013**, *9*, 4453–4461.

[241] Tang, K. T.; Toennies, J. P. The van der Waals Potentials Between All the Rare Gas Atoms from He to Rn. *J. Chem. Phys.* **2003**, *118*, 4976–4983.

[242] Verma, P.; Truhlar, D. G. Does DFT+U Mimic Hybrid Density Functionals? *Theor. Chem. Acc.* **2016**, *135*, 182–.

[243] Zhao, Y.; Peverati, R.; Luo, S.; Yang, K. R.; He, X.; Yu, H. S.; Truhlar, D. G. Minnesota-Gaussian Functional Module (MN-GFM, version 6.5). See http://comp.chem.umn.edu/mn-gfm/ for details.

[244] Lynch, B. J.; Zhao, Y.; Truhlar, D. G. Effectiveness of Diffuse Basis Functions for Calculating Relative Energies by Density Functional Theory. *J. Phys. Chem. A* **2003**, *107*, 1384–1388.

[245] Zheng, J.; Xu, X.; Truhlar, D. G. Minimally Augmented Karlsruhe Basis Sets. *Theor. Chem. Acc.* **2011**, *128*, 295–305.

[246] Papajak, E.; Truhlar, D. G. Convergent Partially Augmented Basis Sets for Post-Hartree–Fock Calculations of Molecular Properties and Reaction Barrier Heights. *J. Chem. Theory Comput.* **2011**, *7*, 10–18.

[247] Manz, T. A. Chargemol Program for Performing DDEC Analysis, version 2.2 beta, May 25, 2013. ddec.sourceforge.net.

[248] Da Silva, J. L. F.; Ganduglia-Pirovano, M. V.; Sauer, J.; Bayer, V.; Kresse, G. Hybrid Functionals Applied to Rare-Earth Oxides: The Example of Ceria. *Phys. Rev. B* **2007**, *75*, 045121.

[249] Singh, V.; Kosa, M.; Majhi, K.; Major, D. T. Putting DFT to the Test: A First-Principles Study of Electronic, Magnetic, and Optical Properties of Co_3O_4. *J. Chem. Theory Comput.* **2015**, *11*, 64–72.

[250] Bui, V. Q.; Pham, T.-T., Le, D. A.; Thi, C. M.; Le, H. M. A First-Principles Investigation of Various Gas (CO, H_2O, NO, and O_2) Absorptions on a WS_2 Monolayer: Stability and Electronic Properties. *J Phys: Condens Matter* **2015**, 27, 305005.

[251] Xu, Z.; Joshi, Y. V.; Raman, S.; Kitchin, J. R. Accurate Electronic and Chemical Properties of 3d Transition Metal Oxides Using a Calculated Linear Response *U* and a DFT + *U*(V) Method. *J. Chem. Phys.* **2015**, *142*, 144701.

[252] Iwaszuk, A.; Nolan, M. Electronic Structure and Reactivity of Ce- and Zr-Doped TiO_2: Assessing the Reliability of Density Functional Theory Approaches. *J. Phys. Chem. C* **2011**, *115*, 12995–13007.

[253] Zakrzewski, T.; Boguslawski, P. Electronic Structure of Transition Metal Ions in GaN and AlN: Comparing GGA+U with Experiment. *J. Alloys Compd.* **2016**, *664*, 565–579.

[254] Yang, Y.; Sugino, O.; Ohno, T. Band Gap of β-PtO_2 from First-Principles. *AIP Adv.* **2012**, *2*, 022172.

[255] Li, W.; Walther, C. F. J.; Kuc, A.; Heine, T. Density Functional Theory and Beyond for Band-Gap Screening: Performance for Transition-Metal Oxides and Dichalcogenides. *J. Chem. Theory Comput.* **2013**, *9*, 2950–2958.

[256] Chen, J.; Wu, X.; Selloni, A. Electronic Structure and Bonding Properties of Cobalt Oxide in the Spinel Structure. *Phys. Rev. B: Condens. Matter Mater. Phys.* **2011**, *83*, 245204.

[257] Franchini, C.; Bayer, V.; Podloucky, R.; Paier, J.; Kresse, G. Density Functional Theory Study of MnO by a Hybrid Functional Approach. *Phys. Rev. B: Condens. Matter Mater. Phys.* **2005**, *72*, 045132.

[258] Finazzi, E.; Valentin, C. D.; Pacchioni, G.; Selloni, A. Excess Electron States in Reduced Bulk Anatase TiO_2: Comparison of Standard GGA, GGA+U, and Hybrid DFT Calculations. *J. Chem. Phys.* **2008**, *129*, 154113.

[259] Perdew, J. P.; Wang, Y. Accurate and Simple Analytic Representation of the Electron-Gas Correlation Energy. *Phys. Rev. B* **1992**, *45*, 13244–13249.

[260] Essenberger, F.; Sharma, S.; Dewhurst, J. K.; Bersier, C.; Cricchio, F.; Nordström, L.; Gross, E. K. U. Magnon Spectrum of Transition-Metal Oxides: Calculations Including Long-Range Magnetic Interactions Using the LSDA+U Method. *Phys. Rev. B* **2011**, *84*, 174425.

[261] Tran, F.; Blaha, P.; Schwarz, K.; Novák, P. Hybrid Exchange-Correlation Energy Functionals for Strongly Correlated Electrons: Applications to Transition-Metal Monoxides. *Phys. Rev. B* **2006**, *74*, 155108.

[262] Anisimov, V. I.; Zaanen, J.; Andersen, O. K. Band Theory and Mott Insulators: Hubbard *U* Instead of Stoner *I*. *Phys. Rev. B* **1991**, *44*, 943–954.

[263] Pickett, W. E.; Erwin, S. C.; Ethridge, E. C. Reformulation of the LDA + U Method for a Local-Orbital Basis. *Phys. Rev. B* **1998**, *58*, 1201–1209.

[264] Jiang, H.; Gomez-Abal, R. I.; Rinke, P.; Scheffler, M. First-Principles Modeling of Localized *d* States with the GW@LDA + *U* Approach. *Phys. Rev. B* **2010**, *82*, 045108.

[265] Marsman, M.; Paier, J.; Stroppa, A.; Kresse, G. Hybrid Functionals Applied to Extended Systems. *J. Phys. Condens. Matter* **2008**, *20*, 064201.

[266] Heyd, J.; Scuseria, G. E. Assessment and Validation of a Screened Coulomb Hybrid Density Functional. *J. Chem. Phys.* **2003**, *120*, 7274–7280.

[267] Matz, R.; Lüth, H. Ellipsometric Spectroscopy of the ZnO Nonpolar ($1\bar{1}00$) Surface. *Appl. Phys.* **1979**, *18*, 123–130.

[268] Zhao, Y.; Truhlar, D. G. Calculation of Semiconductor Band Gaps with the M06-L Density Functional. *J. Chem. Phys.* **2009**, *130*, 074103.

[269] Lynch, B. J.; Truhlar, D. G. Small Representative Benchmarks for Thermochemical Calculations. *J. Phys. Chem. A* **2003**, *107*, 8996–8999.

[270] Paier, J.; Hirschl, R.; Marsman, M.; Kresse, G. The Perdew–Burke–Ernzerhof Exchange-Correlation Functional Applied to the G2-1 Test Set Using a Plane-Wave Basis Set. *J. Chem. Phys.* **2005**, 122, 234102.

[271] Woon, D. E.; Dunning, Jr., T. H. Gaussian Basis Sets for Use in Correlated Molecular Calculations. IV. Calculation of Static Electrical Response Properties. *J. Chem. Phys.* **1994**, *100*, 2975–2988.

[272] Zheng, J.; Zhao, Y.; Truhlar, D. G. The DBH24/08 Database and Its Use to Assess Electronic Structure Model Chemistries for Chemical Reaction Barrier Heights. *J. Chem. Theory Comput.* **2009**, *5*, 808–821.

[273] Zhao, Y.; Peverati, R.; Luo, S.; Yang, K. R.; He, X.; Yu, H. S.; Truhlar, D. G. *MN-GFM*, version 6.7: Minnesota–Gaussian Functional Module. http://comp.chem.umn.edu/mn-gfm (accessed Jan. 10, 2017).

[274] An, W.; Turner, C. H. Linking Carbon and Boron-Nitride Nanotubes: Heterojunction Energetics and Band Gap Tuning. *J. Phys. Chem. Lett.* **2010**, *1*, 2269–2273.

[275] Casida, M. E. Time-Dependent Density-Functional Response Theory for Molecules. In *Recent Advances in Density Functional Methods, Part I;* Chong, D. P., Ed.; World Scientific: Singapore, 1995; pp. 155–192.

[276] Gutowski M. Favorable Performance of the DFT Methods in Predicting the Minimum-Energy Structure of The Lowest Triplet State of WF_4. *Int. J. Quantum Chem.* **1999**, *73*, 369–375.

[277] Chen, H.; Ikeda-Saito, M.; Shaik S. Nature of the Fe-O_2 Bonding in Oxy-myoglobin: Effect of the Protein. *J. Am. Chem. Soc.* **2008**, *130*, 14778–14790.

[278] Schultz, N. E.; Zhao, Y.; Truhlar, D. G. Density Functionals for Inorganometallic and Organometallic Chemistry. *J. Phys. Chem. A* **2005**, *109*, 11127–11143.

[279] Di Valentin, C.; Pacchioni, G.; Selloni, A. Reduced and n-type Doped TiO_2: Nature of Ti^{3+} Species. *J. Phys. Chem. C* **2009**, *113*, 20543–20552.

[280] Deskins, N. A.; Dupuis, M. Electron Transport via Polaron Hopping in Bulk TiO_2: A Density Functional Theory Characterization. *Phys. Rev. B* **2007**, *75*, 195212.

[281] Rohrbach, A.; Hafner, J.; Kresse, G. Ab Initio Study of the (0001) Surfaces of Hematite and Chromia: Influence of Strong Electronic Correlations. *Phys. Rev. B* **2004**, *70*, 125426.

[282] Huang, M.; Fabris, S. CO Adsorption and Oxidation on Ceria Surfaces from DFT+U Calculations. *J. Phys. Chem. C* **2008**, *112*, 8643–8648.

[283] Dorado, B.; Amadon, B.; Freyss, M.; Bertolus, M. DFT+U Calculations of the Ground State and Metastable States of Uranium Dioxide. *Phys. Rev. B* **2009**, *79*, 235125.

[284] Morgan, B. J.; Watson, G. W. Polaronic Trapping of Electrons and Holes by Native Defects in Anatase TiO_2. *Phys. Rev. B* **2009**, *80*, 233102.

[285] Fabris. S.; De Gironcoli. S.; Baroni. S.; Vicario, G.; Balducci, G. Reply to "Comment on 'Taming Multiple Valency with Density Functionals: A Case Study of Defective Ceria'". *Phys. Rev. B* **2005**, *72*, 237102.

[286] Camellone, M. F.; Kowalski, P. M.; Marx, D. Ideal, Defective, and Gold-Promoted Rutile TiO2(110) Surfaces Interacting with CO, H_2, and H_2O: Structures, Energies, Thermodynamics, and Dynamics from PBE+U. *Phys. Rev. B* **2011**, *84*, 035413.

[287] Nguyen, M.-T.; Camellone, M. F.; Gebauer, R. On the Electronic, Structural, and Thermodynamic Properties of Au Supported on α-Fe_2O_3 Surfaces and Their Interaction with CO. *J. Chem. Phys.* **2015**, *143*, 034704.

[288] Pabisiak, T.; Winiarski, M. J.; Kiejna, A. CO Adsorption on Small Au_n (n = 1-4) Structures Supported on Hematite. II. Adsorption on the O-Rich Termination of α-Fe_2O_3(0001) Surface. *J. Chem. Phys.* **2016**, *144*, 044705.

[289] Perdew, J. P.; Levy, M. Physical Content of the Exact Kohn–Sham Orbital Energies: Band Gaps and Derivative Discontinuities. *Phys. Rev. Lett.* **1983**, *51*, 1884–1887.

[290] Perdew, J. P. Density Functional Theory and the Band Gap Problem. *Int. J. Quantum Chem.* **1985**, 28, 497–523.

[291] Xiao, H.; Tahir-Kheli, J.; Goddard III, W. A. Accurate Band Gaps for Semiconductors from Density Functional Theory. *J. Phys. Chem. Lett.* **2011**, *2*, 212–217.

[292] Yu, H. S.; He, X.; Li, S.; Truhlar, D. G. MN15: A Kohn-Sham Global-Hybrid Exchange-Correlation Density Functional with Broad Accuracy for Multi-Reference and Single-Reference Systems and Noncovalent Interactions. *Chem. Sci.* **2016**, *7*, 5032–5051.

[293] Cisneros, G. A.; Kartunnen, M.; Ren, P.; Sagui, C. Classical Electrostatics for Biomolecular Simulations. *Chem. Rev.* **2014**, *114*, 779–814.

[294] Freitag, M. A.; Gordon, M. S.; Jensen, J. H.; Stevens, W. J. Evaluation of Charge Penetration Between Distributed Multipolar Expansions. *J. Chem. Phys.* **2000**, *112*, 7300–7306.

[295] Cisneros, G. A.; Piquemal, J.-P.; Darden, T. A. Quantum Mechanics/Molecular Mechanics Electrostatic Embedding with Continuous and Discrete Functions. *J. Phys. Chem. B* **2006**, *110*, 13682–13684.

[296] McDaniel, J. G.; Schmidt, J. R. Physically-Motivated Force Fields from Symmetry-Adapted Perturbation Theory. *J. Phys. Chem. A* **2013**, *117*, 2053–2066.

[297] Wang, B.; Truhlar, D. G. Screened Electrostatic Interactions in Molecular Mechanics. *J. Chem. Theory Compt.* **2014**, *10*, 4480–4487.

[298] Wang, Q.; Rackers, J. A.; He, C.; Qi, R.; Narth, C.; Lagardere, L.; Gresh, N.; Ponder, J. W.; Piquemal, J.-P.; Ren, P. General Model for Treating Short-Range Electrostatic Penetration in a Molecular Mechanics Force Field. *J. Chem. Theory Comput.* **2015**, *11*, 2609–2618.

[299] Tafipolsky, M.; Ansorg, K. Toward a Physically Motivated Force Field: Hydrogen Bond Directionality from a Symmetry-Adapted Perturbation Theory Perspective. *J. Chem. Theory Comput.* **2016**, *12*, 1267–1279.

[300] Öhrn, A.; Hermida-Ramon, J. M.; Karlström, G. Method for Slater-Type Density Fitting for Intermolecular Electrostatic Interactions with Charge Overlap. I. The Model. *J. Chem. Theory Comput.* **2016**, *12*, 2298–2311.

[301] Tang, K. T.; Toennies, J. P. An Improved Simple Model for the van der Waals Potential Based on Universal Damping Functions for the Dispersion Coefficients. *J. Chem. Phys.* **1984**, *80*, 3726–3741.

[302] Meath, W. J.; Koulis, M. On the Construction and Use of Reliable Two- and Many-Body Interatomic and Intermolecular Potentials. *J. Mol. Struct. THEOCHEM* **1991**, *226*, 1–37.

[303] Gianturco, F. A.; Paesani, F.; Laranjeira, M. F.; Vassilenko, V.; Cunha, M. A.; Shashkov, A. G.; Zolotoukhina, A. F. Computed and Measured Transport Coefficients for CO-He Mixtures: Testing a Density Functional Approach. *Mol. Phys.* **1998**, *94*, 605–622.

[304] Wu, Q.; Yang, W. Empirical Correction to Density Functional Theory for van der Waals Interactions. *J. Chem. Phys.* **2002**, *116*, 515–524.

[305] Grimme, S.; Ehrlich, S.; Goerigk, L. Effect of the Damping Function in Dispersion Corrected Density Functional Theory. *J. Comput. Chem.* **2011**, *32*, 1456–1465.

[306] Rybak, S.; Jeziorski, B.; Szalewicz, K. Many-Body Symmetry-Adapted Perturbation Theory of Intermolecular Interactions. H_2O and HF Dimers. *J. Chem. Phys.* **1991**, *95*, 6576–6601.

[307] Williams, H. L.; Chabalowski, C. F. Using Kohn-Sham Orbitals in Symmetry-Adapted Perturbation Theory to Investigate Intermolecular Interactions. *J. Phys. Chem. A* **2001**, *105*, 646–659.

[308] Szalewicz, K.; Patkowski, K.; Jeziorski, B. Intermolecular Interactions via Perturbation Theory: From Diatoms to Biomolecules. *Struct. Bond.* **2005**, *116*, 43–117.

[309] Pernal, K.; Podeszwa, R.; Patkowski, K.; Szalewicz, K. Dispersionless Density Functional Theory. *Phys. Rev. Lett.* **2009**, *103*, 236201.

[310] Austin, A.; Petersson, G. A.; Frisch, M. J.; Dobek, F. J.; Scalmani, G.; Throssell, K. A Density Functional with Spherical Atom Dispersion Terms. *J. Chem. Theory Comput.* **2012**, *8*, 4989–5007.

[311] Zhao, Y.; Truhlar, D. G. Benchmark Databases for Nonbonded Interactions and Their Use to Test Density Functional Theory. *J. Chem. Theory Comput.* **2005**, *1*, 415–432.

[312] Jurečka, P.; Šponer, J.; Černýa, J.; Hobza, P. Benchmark Database of Accurate (MP2 and CCSD(T) Complete Basis Set Limit) Interaction Energies of Small Model Complexes, DNA Base Pairs, and Amino Acid Pairs. *Phys. Chem. Chem. Phys.* **2006**, *8*, 1985–1993.

[313] DFT-D3 - A dispersion correction for density functionals, Hartree-Fock and semi-empirical quantum chemical methods. http://www.thch.uni-bonn.de/tc/index.php?section=downloads&subsection=DFT-D3&lang=english (accessed Feb. 9, 2017).

[314] Tsuneda, T.; Suzumura, T.; Hirao, K. A New One-Parameter Progressive Colle–Salvetti-Type Correlation Functional. *J. Chem. Phys.* **1999**, *110*, 10664–10678.

[315] Swart, M.; Solà, M.; Bickelhaupt, F. M. Inter- and Intramolecular Dispersion Interactions. *J. Comput. Chem.* **2011**, *32*, 1117–1127.

[316] Raghavachari, K.; Trucks, G. W.; Pople, J. A.; Head-Gordon, M. A Fifth-Order Perturbation Comparison of Electron Correlation Theories. *Chem. Phys. Lett.* **1989**, *157*, 479–483.

[317] Kendall, R. A.; Dunning, Jr., T. H.; Harrison, R. J. Electron Affinities of the First-Row Atoms Revisited. Systematic Basis Sets and Wave Functions. *J. Chem. Phys.* **1992**, *96*, 6796–6806.

[318] Werner, H.-J.; Knowles, P. J.; Knizia, G.; Manby, F. R.; Schütz, M.; Celani, P.; Korona, T.; Lindh, R.; Mitrushenkov, A.; Rauhut, G.; Shamasundar, K. R.; Adler, T. B.; Amos, R. D.; Bernhardsson, A.; Berning, A.; Cooper, D. L.; Deegan, M. J. O.; Dobbyn, A. J.; Eckert, F.; Goll, E.; Hampel, C.; Hesselmann, A.; Hetzer, G.; Hrenar, T.; Jansen, G.; Köppl, C.; Liu, Y.; Lloyd, A. W.; Mata, R. A.; May, A. J.; Mcnicholas, S. J.; Meyer, W.; Mura, M. E.; Nicklass, A.; O'Neill, D. P.; Palmieri, P.; Pflüger, K.; Pitzer, R.; Reiher, M.; Shiozaki, T.; Stoll, H.; Stone, A. J.; Tarroni, R.; Thorsteinsson, T.; Wang, M.; Wolf, A. *Molpro*, version 2010.1. http://www.molpro.net.

8 Appendix

Adaptation:

This dissertation is adapted from previously published work and is reproduced with permission from:

1) Verma, P.; Xu, X.; Truhlar, D. G. Adsorption on Fe-MOF-74 for C1-C3 Hydrocarbon Separation. *J. Phys. Chem. C* **2013**, *117*, 12648–12660. DOI: 10.1021/jp402884h

2) Maurice, R.; Verma, P.; Zadrozny, J. M.; Luo, S.; Borycz, J.; Long, J. R.; Truhlar, D. G.; Gagliardi, L. Single-Ion Magnetic Anisotropy and Isotropic Magnetic Couplings in the Metal–Organic Framework Fe_2(dobdc). *Inorg. Chem.* **2013**, *52*, 9379–9789. DOI: 10.1021/ic400953e

3) Lee, K.; Isley III, W. C.; Dzubak, A. L.; Verma, P.; Stoneburner, S. J.; Lin, L.-C.; Howe, J. D.; Bloch, E. D.; Reed, D. A.; Hudson, M. R.; Brown, C. M.; Long, J. R.; Neaton, J. B.; Smit, B.; Cramer, C. J.; Truhlar, D. G.; Gagliardi, L. Design of a Metal-Organic Framework with Enhanced Back Bonding for the Separation of N_2 and CH_4. *J. Am. Chem. Soc.* **2014**, *136*, 698-704. DOI: 10.1021/ja4102979

4) Xiao, D. J.; Bloch, E. D.; Mason, J. A.; Queen, W. L.; Hudson, M. R.; Planas, N.; Borycz, J.; Dzubak, A. L.; Verma, P.; Lee, K.; Bonino, F.; Crocell, V.; Yano, J.; Bordiga, S.; Truhlar, D. G.; Gagliardi, L.; Brown, C. M.; Long, J. R. Oxidation of Ethane to Ethanol by N2O in a Metal-Organic Framework with Coordinatively-Unsaturated Iron(II) Sites. *Nat. Chem.* **2014**, *6*, 590–595. DOI: 10.1038/nchem.1956

5) Yu, H. S.; Zhang, W.; Verma, P.; He, X.; Truhlar, D. G. Nonseparable Exchange–Correlation Functional for Molecules, Including Homogeneous Catalysis Involving Transition Metals. *Phys. Chem. Chem. Phys.* **2015**, *17*, 12146–12160. DOI: 10.1039/c5cp01425e

6) Verma, P.; Vogiatzis, K. D.; Planas, N.; Borycz, J.; Xiao, D. J.; Long, J. R.; Gagliardi, L.; Truhlar, D. G. Mechanism of Oxidation of Ethane to Ethanol at Iron(IV)-Oxo Sites in Magnesium-Diluted Fe_2(dobdc). *J. Am. Chem. Soc.* **2015**, *137*, 5770-5781. DOI: 10.1021/jacs.5b00382

7) Verma, P.; Maurice, R.; Truhlar, D. G. Identifying the Interactions That Allow Separation of O_2 from N_2 on the Open Iron Sites of Fe_2(dobdc). *J. Phys. Chem. C* **2015**, *119*, 28499–28511. DOI: 10.1021/acs.jpcc.5b10382

8) Verma, P.; Maurice, R.; Truhlar, D. G. Adsorbate-Induced Changes in Magnetic Interactions in Fe_2(dobdc) with Adsorbed Hydrocarbon Molecules. *J. Phys. Chem. C*, **2016**, *120*, 9933–9948. DOI: 10.1021/acs.jpcc.6b03240

9) Borycz, J.; Paier, J.; Verma, P.; Darago, L. E.; Xiao, D. J.; Truhlar, D. G.; Long, J. R.; Gagliardi, L. Structural and Electronic Effects on the Properties of Fe_2(dobdc) upon Oxidation with N_2O. *Inorg. Chem.* **2016**, *55*, 4924–4934. DOI: 10.1021/acs.inorgchem.6b00467

10) Verma, P.; Truhlar, D. G. Does DFT+U Mimic Hybrid Density Functionals? *Theor. Chem. Acc.* **2016**, *135*, 182. DOI: 10.1007/s00214-016-1927-4

11) Verma, P.; Truhlar, D. G. HLE16: A Local Kohn–Sham Gradient Approximation with Good Performance for Semiconductor Band Gaps and Molecular Excitation Energies. *J. Phys. Chem. Lett.* **2017**, *8*, 380–387. DOI:10.1021/acs.jpclett.6b02757

12) Verma, P.; Truhlar, D. G. HLE17: An Improved Local Exchange-Correlation Functional for Computing Semiconductor Band Gaps and Molecular Excitation Energies. *J. Phys. Chem. C* **2017**, *121*, 7144-7154. DOI: 10.1021/acs.jpcc.7b01066

13) Verma, P.; Wang, B.; Fernandez, L. E.; Truhlar, D. G. Physical Molecular Mechanics Method for Damped Dispersion. *J. Phys. Chem. A* **2017**, *121*, 2855-2862. DOI: 10.1021/acs.jpca.7b02384